A CRYOGENIC MULTIAXIS RANGE-RESOLVED LASER INTERFEROMETER

ADAM JOSEPH CHRISTIANSEN
Master of Science, University of Lethbridge, 2020

A thesis submitted
in partial fulfilment of the requirements for the degree of

DOCTOR OF PHILOSOPHY

in

EARTH, SPACE, AND PHYSICAL SCIENCE

Department of Physics and Astronomy
University of Lethbridge
LETHBRIDGE, ALBERTA, CANADA

A CRYOGENIC MULTIAXIS RANGE-RESOLVED LASER INTERFEROMETER

ADAM JOSEPH CHRISTIANSEN

Date of Defence: 6th December, 2023

David A. Naylor Thesis Supervisor	Professor	PhD
Jacqueline E. Rice Thesis Examination Committee Member	Professor	PhD
Locke D. Spencer Thesis Examination Committee Member	Associate Professor	PhD
Michael R. Smith External Examiner University of Calgary	Professor Emeritus	PhD
Chad A. Povey Chair, Thesis Examination Committee	Instructor	PhD

Abstract

Building upon the successes of previous far-infrared space astronomy missions that initially featured small but cold (<4 K) or large but warm telescopes, the future path is clear: the next generation of far-infrared telescopes must be both large and cold, which requires cryogenic cooling of the mirrors, instrumentation, and detectors. The precision to which the moving cryogenic components of the instrument must be measured and controlled demands a robust low power position metrology system, and a cryogenic multiaxis range-resolved laser interferometer using a sinusoidal frequency modulation (SFM) technique was investigated to solve this problem. The development included cryogenic considerations and characterization of several fibre and optical components, calibration of the selected hardware, and verification of the technique. Simultaneous multiaxis measurements were demonstrated at ambient and cryogenic temperatures of <6 K, and the measured performance under ambient conditions showed a resolution of ∼50 pm and a stability of 0.4 nm rms in a 20 Hz bandwidth. The demonstrated performance exceeds that which is required by proposed far-infrared missions and distinguishes the SFM range-resolved laser interferometer as a leading candidate for future space-based applications.

Acknowledgments

I express great thanks to the countless members of our research group. Prof. David Naylor, who passed along immense knowledge and gave his time and support. Brad Gom, who taught me to operate the cryostats, machined several components, and offered sound advice. The late Gregory Tompkins, whose electronics work is indispensable to the research conducted by our group. Rebecca Sirota and Mason Remmer, who provided exceptional electronics support and have been good friends to me. Alicia Anderson and I, together, had learned how to operate the infrared camera for our experiments. Thank you to the entire group for making our laboratory a great environment. I would also like to thank Prof. Locke Spencer, Prof. Jacqueline Rice, and Dr. Chad Povey for the valuable conversations that we have had.

This research was supported by the New Technologies for Canadian Observatories program, in which I was supervised by Prof. Suresh Sivanandam at the University of Toronto. As part of the program, I completed an industrial internship at Blue Sky Spectroscopy Inc. and received training under the kind supervision of Dr. Sudhakar Gunuganti. Blue Sky Spectroscopy Inc. has supplied the components that I used to construct the system presented in this thesis.

Parts of this research would not be possible without several collaborators. Matthew Popelka and Dr. Andrei Stolov at OFS Fitel, LLC who supported the testing of cryogenically cycled optical fibres with the provision of fibres and mechanical, spectroscopic, and thermogravimetric analyses, and have kindly allowed me to author and publish the results of our work. Alain Cournoyer at ABB Ltd. who has granted me permission to use their FTSM in my cryogenic experiments. Prof. Felipe Guzmán,

Andrea Nelson, and Brina Martinez at Texas A&M University provided the silica resonator that I have measured. I would also like to recognize the funding agencies that supported this research: ABB Ltd., Alberta Innovates, Blue Sky Spectroscopy Inc., Canada Foundation for Innovation, Canadian Microelectronics Corporation, Canadian Space Agency, Natural Sciences and Engineering Research Council of Canada, New Technologies for Canadian Observatories, and the University of Lethbridge.

Lastly, I thank my family, especially my parents, Suzy and Darryl, who have always encouraged me, and my loving partner, Caitlyn, for her endless support and patience.

Contents

List of Tables

List of Figures

List of Abbreviations

AC	alternating current
ADC	analog-to-digital converter
API	application programming interface
BRAM	block random access memory
CAD	computer-aided design
CORDIC	coordinate rotation digital computer
CSA	Canada Space Agency
CTE	coefficient of thermal expansion
DAC	digital-to-analog converter
DC	direct current
DDR	double data rate
DFB	distributed-feedback
DFT	discrete Fourier transform
DMA	direct memory access
DSP	digital signal processing
dToF	direct time-of-flight
EOM	electro-optic modulator
ESA	European Space Agency
FC/APC	ferrule-connector angled physical contact
FC/PC	ferrule-connector physical contact
FIFO	first-in first-out
FMCW	frequency-modulated continuous-wave
FMDU	frequency-modulation-demodulation unit
FPGA	field-programmable gate array
FSI	fibre segment interferometry
FTIR	Fourier transform infrared spectroscopy
FTS	Fourier transform spectrometer
FTSM	Fourier transform spectrometer mechanism
FWHM	full width at half maximum
GPIO	general-purpose input/output

HeI	heterodyne interferometry
HoI	homodyne interferometry
HVAC	heating, ventilation, and air conditioning
ISO	Infrared Space Observatory
iToF	indirect time-of-flight
JAXA	Japan Aerospace Exploration Agency
JSON	JavaScript Object Notation
JTAG	Joint Test Action Group
JWST	James Webb Space Telescope
LD	laser diode
LiDAR	light detection and ranging
LIGO	Laser Interferometer Gravitational-Wave Observatory
LSB	least significant bit
LUT	look-up table
LVDT	linear variable differential transformer
MEMS	microelectromechanical systems
MIT	Massachusetts Institute of Technology
MPSoC	multi-processor system-on-chip
NASA	National Aeronautics and Space Administration
NEP	noise-equivalent power
OCT	optical coherence tomography
OPD	optical path difference
OPL	optical path length
PC	personal computer
PL	programmable logic domain
PRIMA	PRobe far-Infrared Mission for Astrophysics
PRN	pseudorandom number
PS	processing system domain
PTC	pulse tube cryocooler
PWM	pulse-width modulation
PZT	piezoelectric transducer
QPSK	quadrature phase shift keying
QSPI	quad serial peripheral interface

RADAR	radio detection and ranging
RAM	random access memory
RMS	root mean square
SAFARI	SPICA Far-Infrared Instrument
SFM	sinusoidal frequency modulation
SMA	SubMiniature version A
SNR	signal-to-noise ratio
SOCF	synthesis of the optical coherence function
SPICA	Space Infrared telescope for Cosmology and Astrophysics
SW	software domain
TAMU	Texas A&M University
TCP/IP	Transmission Control Protocol/Internet Protocol
TEC	thermoelectric cooler
TGA	thermogravimetric analysis
TIA	transimpedance amplifier
ToF	time-of-flight
TWI	two-wavelength interferometer
UART	universal asynchronous receiver-transmitter
UDP	User Datagram Protocol
USB	Universal Serial Bus
USB OTG	Universal Serial Bus On-the-Go
WDM	wavelength division multiplexer

List of Notations

A	phase modulation amplitude, area
A_d	phase demodulation amplitude
ΔA_min	minimum phase modulation amplitude
a	acceleration
α	linear coefficient of thermal expansion, angular acceleration
$\vec{B}$	magnetic field (flux density)
b	frictional damping coefficient
C	complex carrier, capacitance
c	vacuum speed of light, 299 792 458 m/s
D	demodulated signal
d	distance, gap
$d_\star$	degree of demodulatability
E	electric field, energy, Young's modulus
$\vec{E}$	electric field vector
ϵ	permittivity
F	force
F_D	Fourier transform of demodulated signal
F_{WU}	Fourier transform of windowed signal
f	frequency
f_0	natural frequency
f_b	beat frequency
f_{b^+}	positive beat frequency envelope
f_{b^-}	negative beat frequency envelope
f_d	Doppler frequency
f_m	modulation frequency
f_r	resonant frequency
f_s	sampling frequency
Δf	bandwidth
$\mathcal{F}$	Fourier transform

G_{mod}	laser optical frequency modulation gain
Γ	Lorentzian function full-width at half-maximum
$\mathscr{H}$	Hilbert transform
$\mathscr{H}_{32}$	32-point Hilbert transform
$\hbar$	discrete Hilbert transform coefficient
H	transfer function
η	normalized signal contribution
h	Lorentzian function height
I	optical intensity, electrical current
I_{b}	laser diode bias current
I_{M}	moment of inertia
I_{pd}	photodiode current
$I_{\mathrm{b,set}}$	laser diode bias current setpoint
J_n	order n Bessel function of the first kind
j	imaginary unit, $+\sqrt{-1}$
K	recursive running sum filter width
K_{T}	torque sensitivity
k	angular wave number, spring constant
$\vec{k}$	wavevector
L	Hann window function width, inductance, length, Lorentzian function
LP	low-pass filter
ℓ	optical path length
Λ	optical path difference
Λ_{c}	centre optical path difference
$\Delta\Lambda_{\mathrm{max}}$	maximum demodulatable change in optical path difference
$\Delta\Lambda_{\mathrm{min}}$	minimum separation in optical path differences
$\Delta\Lambda$	change in optical path difference
λ	vacuum wavelength
λ_{c}	centre vacuum wavelength
M_ℓ	multiset of interferometer optical path lengths
M_Δ	multiset of interferometer optical path differences
m	arbitrary number (often integral), mass
μ_0	vacuum magnetic permeability, $1.256\,637\,062\,12(19) \times 10^{-6}\,\mathrm{N\,A^{-2}}$

N	number of interference axes
N_p	number of primary interference axes
N_s	number of secondary interference axes
n	refractive index, discrete time signal dependent variable, arbitrary integer
n_d	stress corrosion resistance
ν	optical frequency
ν_A	optical frequency modulation amplitude
ν_a, ν_b	signal optical frequency of arbitrary axes
ν_c	centre optical frequency
$\emptyset$	empty set
P	optical power
P_D	demodulated signal power spectrum
P_{WU}	windowed signal power spectrum
π	pi, $3.141\,592\,653\ldots$
ϕ	phase
ϕ_0	initial phase
ϕ_a, ϕ_b	signal phase of arbitrary axes
$\Delta\phi$	phase difference
φ	phase due to optical path difference
$\Delta\varphi$	change in phase due to optical path difference
Q	quadrature, quality factor
R	electrical resistance, rectangular window function width
R_f	feedback resistance
R_λ	optical responsivity
r	radius, range
$\vec{r}$	position vector
ρ	resistivity
S	set of interferometer paths
S_D	set of normalized demodulatable axes
SNR	signal-to-noise ratio
saw	sawtooth function
sgn	signum function
σ	Gaussian window width, stress
σ_p	Gaussian power spectrum width

T	temperature
T_m	modulation period
ΔT	change in temperature
t	time
t'	time of signal detection
t''	time of demodulation
t''_c	central time of demodulation
tri	triangle function
θ	phase modulation function
τ	torque
τ_ad	analog-to-digital delay
τ_da	digital-to-analog delay
$\tau_\mathrm{del,bound}$	optical delivery delay from interferometer boundary
$\tau_\mathrm{del,in}$	incoming optical delivery delay
$\tau_\mathrm{del,out}$	outgoing optical delivery delay
τ_det	detector delay
τ_eo	combined electrical and optical delay
τ_f	optical time-of-flight delay
τ_meas	measurement delay
τ_mod	laser modulation delay
τ_norm	normalization delay
$\Delta\mathcal{T}_\mathrm{cool}$	change in optical transmittance after cooling
$\Delta\mathcal{T}_\mathrm{cyc}$	change in optical transmittance after thermal cycling
$\Delta\mathcal{T}$	change in optical transmittance
U	normalized photodetector signal
$U_\mathrm{tp,a}$, $U_\mathrm{tp,b}$, $U_\mathrm{tp,c}$	three-phase signals
V	voltage
V_det	photodetector voltage
V_mod	modulation voltage
v	velocity
v_opt	velocity in optical path
$v_\mathrm{opt,max}$	maximum velocity in optical path
W	Gaussian window function
W_1	single Gaussian window function
W_H	Hann window function
$W_\sqcap$	rectangular window function
w	band separation coefficient
ω	angular frequency
ω_0	natural angular frequency

x	position, generic discrete time input signal
Δx_{c}	horizontal change in central Gaussian beam position
Δx_{FWHM}	horizontal change in Gaussian beam FWHM
Δx	displacement
y	generic discrete time output signal
Δy_{c}	vertical change in central Gaussian beam position
Δy_{FWHM}	vertical change in Gaussian beam FWHM
$\mathbb{Z}$	set of integers

Chapter 1

Introduction

Precision displacement measurement techniques employing optical interferometry are widespread with countless applications including monitoring earthquakes, landslides, and volcanoes [1–4], understanding the mechanics of the middle ear [5,6], determining the ripeness of fruits [7, 8], and exploring the behaviour of tennis racquets [9]. This thesis focuses on a specific sinusoidal frequency modulation (SFM) laser range-resolved interferometry technique for obtaining precision multiaxis displacement measurements of systems operating at cryogenic temperatures.

As will be shown in this chapter, by necessity, the next generation of cryogenic space astronomy missions will be of a fully cryogenic nature ($<4\,\mathrm{K}$). At a high level, one must be able to move and measure precisely the mechanical components of the spectroscopic instrument suite at cryogenic temperatures without dissipating significant heat. In Chapter 2, I present a review of the displacement metrology systems that have been used in previous cryogenic space astronomy missions, from which it is seen that the only technique that meets the stringent requirements of cryogenic operation, increased precision, and having low thermal parasitics, is a range-resolved laser interferometer. My thesis concerns the implementation and verification of a cryogenic range-resolved laser interferometer.

1.1 Range-Resolved Interferometry

Interference is the phenomenon by which superposed waves are collectively observed to exhibit properties that differ from that of each individual wave. As is seen in Chapter 3, the superposition of fields can be summarized in terms of the intensity, I. Two interfering quasi-monochromatic waves result in an intensity described by the interference equation [10–12],

$$I(t) = I_1 + I_2 + 2\sqrt{I_1 I_2}\cos\big(\varphi(t)\big), \qquad [\mathrm{W/m^2}] \ (1.1)$$

where I_1 and I_2 are the intensities of the individual waves, φ is the phase difference between them, and t is time. Equation (1.1) illustrates how one may leverage interference to perform displacement measurements, as the phase may be written as

$$\varphi(t) = \frac{2\pi}{\lambda}\Lambda(t), \qquad [\mathrm{rad}] \ (1.2)$$

where Λ is the difference in optical path length of the paths traversed by the interfering waves and λ is the wavelength. When measuring a displacement with an interferometer, the intensity from Equation (1.1) is detected and used to determine φ, allowing the change in Λ to be computed using Equation (1.2). In practice, matters are not quite this simple, and one must appreciate the complexity of the required physical and processing systems to extract φ from a measurement of I. This thesis explores an SFM interferometry approach, which follows the underlying interference principle of Equations (1.1) and (1.2), but, as shown in Chapters 3 and 4, requires more complex signal processing to recover the phase.

Two common interferometer configurations are presented in Figure 1.1. A traditional Michelson interferometer [13] built using a cube beam splitter is shown in Figure 1.1. In this configuration, light from the laser is split by the beamsplitter cube and directed toward two mirrors, of which the top mirror is fixed and the right mirror

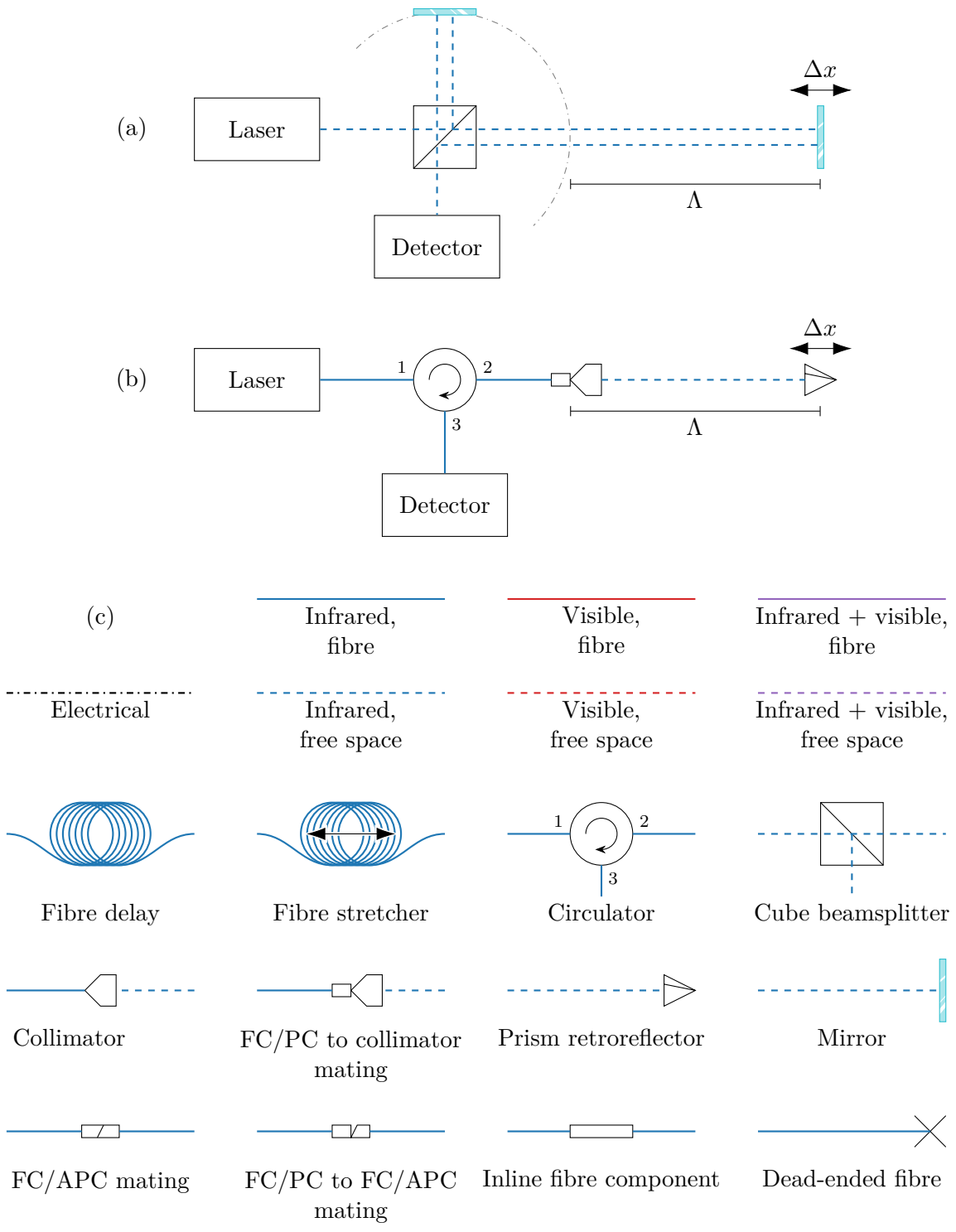

Figure 1.1: Schematics of common interferometer configurations showing a traditional Michelson interferometer (a) and a Fizeau interferometer (b). Electro-optical symbols used in this thesis are shown in (c); when used, *inline fibre components* are labeled according to their functions.

is movable. Motion of the mirror results in a change in Λ and thus φ, which may be measured to recover the displacement, Δx. The second configuration in Figure 1.1b is a Fizeau interferometer — the name often given to a low-finesse Fabry-Pérot interferometer [10, 12, 14], — which uses an inline Fresnel reflection [10] from the tip of the fibre mated to the collimator. Interferometers discussed in this thesis most often use the Fizeau configuration.

1.2 Motivation

The journey into cryogenic range-resolved interferometry began with the European Space Agency (ESA) and Japan Aerospace Exploration Agency (JAXA) led Space Infrared telescope for Cosmology and Astrophysics (SPICA) — a mission that aimed to study the formation of and evolution of galaxies, black holes, and planetary systems through high resolution spectroscopic observations in the 5 to 230 µm band [15]. The SPICA Far-Infrared Instrument (SAFARI), consisting of a low resolution grating spectrometer and high resolution Fourier transform spectrometer (FTS), was one of three proposed instruments onboard SPICA and would cover the 34 to 230 µm far-infrared range. Active cooling of the telescope optics and instrumentation was required to fully exploit the sensitivity of state-of-the-art far-infrared bolometer detectors [16], leading to three temperature zones: <8 K for the telescope optics, <4 K for the instrumentation, and ∼50 mK for the detectors. A general rule of thumb when designing space-based instrumentation is to reduce the number of moving parts. In SAFARI, a fixed grating spectrometer disperses light onto a detector array to instantaneously measure the spectrum, however, by necessity, the FTS has a moving mirror such as the interferometer shown in Figure 1.1a that must be precisely measured and controlled at <4 K while dissipating minimal thermal power. The operational principle of an FTS requires that the interference signal from the two beams that traverse the interferometer (known as the interferogram) be sampled at equal increments of

Table 1.1: Summary of SPICA SAFARI FTS motion and metrology requirements [33].

Metrology Parameter	Requirement
Uncertainty[1]	10 nm rms
Range	33.5 mm
Environment	Vacuum, <4 K
Thermal Power[2]	<1 mW

[1] 20 Hz measurement bandwidth.
[2] Total power dissipated in the cryogenic workspace.

optical path difference (OPD), thus, FTSs require precise knowledge of the OPD. The goal of my thesis is to study a new approach to measuring the OPD that is based upon a cryogenic application of range-resolved interferometry. An upper limit of 1.5 mW was allocated to the entirety of SAFARI, but with a goal of <1 mW, of which 10 % is notionally given to the displacement metrology. Other forms of metrology, including capacitive [17–19], inductive [20–28], and encoder [22–24, 29–32] sensors have been deployed in space, but cannot satisfy all of the SAFARI FTS requirements listed in Table 1.1. For this reason, a range-resolved laser interferometer — the topic discussed in this thesis — was adopted.

The University of Lethbridge is a Canada Space Agency (CSA) partner and led Canadian contributions to SAFARI before the SPICA mission was canceled in late 2020 due to undisclosed costs [34]. A SPICA-shaped hole was left in far-infrared space-based facilities, and with such a realization, the National Aeronautics and Space Administration (NASA) has proposed the PRobe far-Infrared Mission for Astrophysics (PRIMA) [35]. At the time of writing, the displacement metrology requirements for PRIMA have not been established, but are expected to be similar to those of SAFARI.

The impetus for the work presented in this thesis was to consider an approach to displacement metrology at cryogenic temperatures over relatively long ranges while dissipating minimal power, but it was quickly realized that the versatility of cryogenic multiaxis displacement metrology lends itself to countless other applications. Over

the course of my studies the objective evolved to include not only meeting the SAFARI FTS requirements, but also produce a generalized displacement metrology system to investigate applications involving simultaneous multiaxis displacement measurements under both ambient and cryogenic conditions.

1.3 Outline

This thesis is written to flow from a general view of displacement metrology into the specifics of the adopted SFM approach. A review of displacement metrology techniques gives context to the adoption of a range-resolved interferometer for cryogenic displacement measurement and prior work is briefly presented. Work on the SFM technique is split into five chapters detailing the theory, implementation, cryogenic considerations, uncertainty, and several explored applications, then concluding with a final chapter that provides a summary and outlook. The thesis outline is as follows:

Chapter 1 presents a brief introduction to range-resolved interferometry and establishes the motivation for and outline of the presented work.

Chapter 2 provides a review of displacement metrology and prior work. The purpose is to provide context for the adoption of a range-resolved interferometer and the SFM technique.

Chapter 3 presents the underlying theory of the SFM approach with a generalized model for multiaxis applications that highlights key design drivers.

Chapter 4 discusses the implementation of the SFM technique that realizes the theory presented in Chapter 3. Techniques and results are presented for the extensive required calibration.

Chapter 5 discusses the theoretical uncertainty of the SFM approach with the theory in Chapter 3 and implementation in Chapter 4 and summarizes key design drivers.

Chapter 6 presents results from the characterization of several commercial off-the-shelf fibre and optical components necessary for cryogenic applications of the SFM technique.

Chapter 7 explores several single-axis and multiaxis applications of the SFM technique in ambient and cryogenic environments, including three novel developments: (1) a strategy for determining the resolution of the SFM range-resolved laser interferometer, (2) a HeNe laser interferometer verification technique, and (3) an approach to extending the measurement range of the SFM technique beyond its conventional limit.

Chapter 8 concludes with a summarization of results and an outlook that highlights directions for future work with the SFM interferometer.

Naturally, given the subject, electro-optical systems are pervasive and require schematics that span electrical and optical domains. Unlike electronic circuits, there are no standards for drawing electro-optic systems, and often such drawings are accompanied by extensive labeling. All presented electro-optic schematics, such as Figures 1.1a and 1.1b, draw from a common set of components, and their symbols are drawn consistently following the styles and conventions in Figure 1.1c.

I was responsible for the design, development, and verification of a cryogenic multiaxis range-resolved-resolved laser interferometer based on an SFM technique. I begin by deriving a generic set of SFM interferometer equations which I then used to develop an implementation of the SFM technique supporting the real-time measurement of up to eight simultaneous displacement axes. Calibration of the selected hardware is necessary for the correct modulation and demodulation of the laser; in Chapter 4, I will discuss the experiments and data processing required to derive these calibration products. Armed with these calibration products and the underlying theory, I developed a custom digital signal processing pipeline from scratch in a field-programmable gate array (FPGA) controlled by a tightly integrated real-time operating system. I

have also developed a robust and scriptable driver to control the system and obtain displacement measurements from any personal computer (PC) running a major operating system. Further software was written for a theoretical numerical model of the technique to which the measured performance of the implemented system showed close agreement. To support cryogenic applications of a range-resolved interferometer, I also investigated several performance characteristics of optical fibres and collimators at cryogenic temperatures. Having completed all this work to assemble a cryogenic multiaxis range-resolved laser interferometer, I then explored eight unique applications of the SFM technique under both ambient and cryogenic conditions; all of which required unique and sometimes creative data processing solutions. Furthermore, these applications often required specialized mechanical components which I have designed, and custom purpose built fibres that I have prepared. These applications include three novel developments: a fibre segment interferometry technique for determining the resolution of the SFM range-resolved laser interferometer, a wave division multiplexing interferometer to verify the SFM technique against a HeNe laser, and a strategy that exploits the multiaxis nature of the technique to extend the SFM measurement range beyond the conventional single-axis limit. I set out to show that an SFM range-resolved laser interferometer is well-suited for future far-infrared space astronomy missions. The measured performance not only meets but exceeds the stringent displacement metrology requirements of the SPICA SAFARI FTS outlined in Table 1.1. The SFM technique has been demonstrated as a leading candidate for precise and robust displacement measurements in cryogenic space-based applications and represents an improvement of several orders of magnitude over the metrology employed by previous space missions.

Chapter 2

Review of Displacement Metrology Techniques

This chapter presents a review of common displacement measurement techniques that is used to motivate the adoption of a range-resolved laser interferometer for cryogenic applications in infrared space astronomy. Several optical ranging and displacement measurement techniques are reviewed to build a corpus of performance parameters and show where the adopted sinusoidal frequency modulation (SFM) approach lies in the parameter space. From these reviews, it is clear that the family of fibre-fed laser interferometer techniques is the solution. In my master's thesis I studied a three-phase fibre-fed laser interferometer system that provided the necessary precision, but suffered from poor performance at low speeds. That study provided the impetus for the adoption of the SFM approach, the cryogenic implementation and validation of which is the focus of this thesis.

2.1 Displacement Metrology Techniques

In this section, displacement metrology techniques that have been or could be used in space, including capacitive, inductive, encoder, and interferometric sensors, are reviewed in the context of cryogenic space-based applications. A summary table of key performance metrics and trade-offs is provided at the end of the section in Table 2.1. This review summarizes and provides updates to Chapter 2 of my master's thesis [36]. Each subsection is kept brief with a focus on relevant performance characteristics and

cryogenic considerations; operational principles of the techniques can be found in the literature [37–44].

2.1.1 Capacitive Sensors

Modifications to the configuration of a capacitor can be used to measure displacement through a change in capacitance. The capacitance, C, of a parallel plate capacitor is given by [45]

$$C = \frac{\epsilon A}{d}, \qquad \text{[F]} \quad (2.1)$$

where ϵ is the electric permittivity of the dielectric between the plates of the capacitor, A is the area of the plates, and d is the separation between plates. From Equation (2.1), there are three basic configurations (ignoring edge effects) for which the capacitance may be varied as a function of displacement: moving dielectric, axial moving plate, and lateral moving plate, which modify ϵ, d, and A, are shown from left to right in Figure 2.1a, respectively.

Extremely sensitive capacitance micrometers have demonstrated measurements of 10^{-14} m, while practical capacitive sensors have an accuracy of 5 ppm [41]. Commercially available devices can offer <1 nm resolution in bandwidths up to 100 kHz [37,46]. The largest capacitive sensors achieve ranges of 8 to 10 mm [38, 41]. Zero power is dissipated at the point of measurement [41]. In a cryogenic space-based application there are two primary aspects of power dissipation to consider: the power dissipation of the payload in the cryogenic workspace and the power consumption of the service module in the warm part of the spacecraft. The maximum 1 mW power dissipation requirement for the SPICA Far-Infrared Instrument (SAFARI) Fourier transform spectrometer (FTS) in Table 1.1 concerns the former, as this 1 mW budget includes both the motion *and* measurement of a cryogenic scanning mechanism.

Applications that can maintain plate alignment over the full travel range can best use the axial moving plate configuration which offers the greatest accuracy but

moving dielectric and lateral moving plate sensors are better suited to longer range applications [37]. While nonlinearities are introduced primarily through tilting and bowing of the plates due to mounting stress [37, 41], high linearities on the order of 10 ppm can be achieved. All capacitor configurations in Figure 2.1a exhibit similar sensitivities to tilt deformities, but the lateral moving plate configuration is most sensitive to bowing, as both the distance and angle between the plates changes as a function of displacement. Sensitivity to nearby electric fields and contamination of the air gap can reduce accuracy and linearity but may be mitigated by the introduction of a guard electrode and keeping the sensor in a shielded housing [37, 38, 47].

The Infrared Space Observatory (ISO) employed capacitance micrometry in the control of its cryogenic Fabry-Pérot etalons [17–19]. Four Fabry-Pérot interferometers

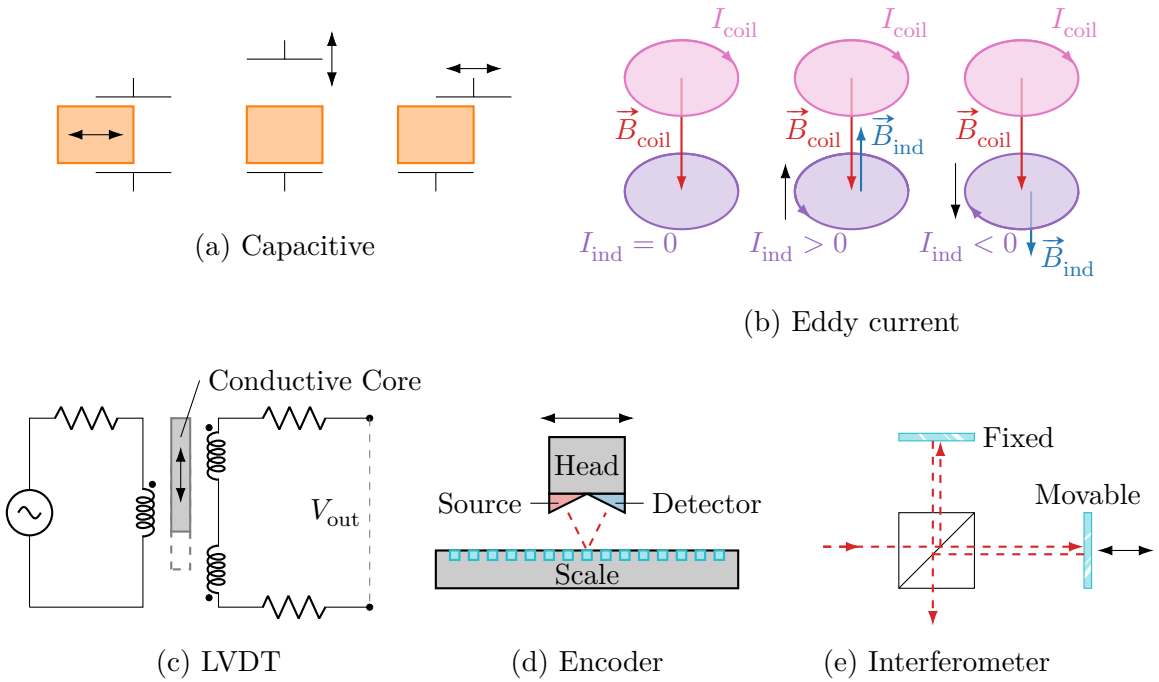

Figure 2.1: Illustration of displacement metrology techniques discussed in this section. Black arrows show the direction of motion. The following are depicted: (a) capacitive sensors in (left to right) moving dielectric, axial moving plate, and lateral moving plate configurations; (b) eddy current sensors in stationary, converging, and diverging states; (c) example LVDT excitation circuit; (d) optical encoder read-head moving along a glass scale; and (e) a single-axis Michelson interferometer.

were flown onboard ISO: two in the Short-Wavelength Spectrometer and two in the Long-Wavelength Spectrometer. The two interferometers in the Long-Wavelength Spectrometer, the FPS and FPL, achieved resolutions of $\leq$22.4 and $\leq$29.8 nm over the ranges of 91.8 and 122.2 µm, respectively, at $\sim$3.2 K.

2.1.2 Eddy Current Sensors

When a coil is excited by a current, I_{coil}, to produce a magnetic field, $\vec{B}_{\text{coil}}$, the induced current, I_{ind}, in a target conducting sheet or some distance away, is such that the induced magnetic field, I_{ind}, opposes the initial change in magnetic field [45]. This property, known as Lenz's law, is illustrated in Figure 2.1b and shows three cases (stationary, converging, and diverging targets) that may be exploited to determine position from the target response to a change in displacement assuming that I_{coil} is AC. The displacement is determined via changes in the mutual inductance between the source coil and the target, and in practice, an AC excitation signal up to several MHz is used [42].

Eddy current sensors are sensitive to stray magnetic fields, but are relatively unaffected by air gap contamination compared to other non-contact techniques such as capacitive and interferometric strategies [37, 42]. Contamination is generally not of concern in cryogenic applications, however, stray magnetic fields may be present. Eddy current sensors transfer thermal energy through Joule (and induction) heating which must be considered in cryogenic applications.

Commercial eddy current sensors are available with ranges of approximately 100 µm up to 80 mm. Resolutions of 10 nm are possible with ranges of approximately 250 µm, while larger sensors with ranges up to 80 mm generally have resolutions on the order of microns. Overall, this is an accuracy of approximately 0.1 % at lower bandwidths, which can reach up to 100 kHz [37, 48, 49]. Although power requirements for an eddy current sensor interface is often at the forefront of the specifications, the power dis-

sipated by the sensor itself is not often stated. For example, Nabavi et al. describes an approach achieving a resolution of ∼250 nm over a range of 1.5 mm in a 1 kHz measurement bandwidth with 9.5 mW power consumption for the interface [50] and Pimenta et al. demonstrate a 200 µW eddy current proximity sensor with a reduced 500 µm range [51]. The power dissipated by eddy currents in a conducting sheet can be estimated by [52]

$$P = \frac{\pi^2 B_\mathrm{p}^2 t^2 f^2 m}{6\rho d}, \qquad \text{[W]} \quad (2.2)$$

where P is power, B_p is the peak magnetic field resulting from sinusoidal excitation, t is the thickness of the sheet, f is the excitation frequency, m is the mass of the sheet, ρ is the resistivity of the sheet, and d is the density of sheet. In vacuum, excitation of the coil generates a magnetic field given by $B_\mathrm{p} = \mu_0 NIA/2\pi r^3$ [45] where μ_0 is the vacuum magnetic permeability, N is the number of turns in the coil, I is the excitation current, A is the area of the coil, and r is the distance from the centre of the coil to the conducting sheet. Assuming reasonable excitation parameters of $N = 20$, $I = 10\,\mathrm{mA}$, $A = 100\,\mathrm{mm}^2$, and using $r = 33.5\,\mathrm{mm}$ from the stroke of the SAFARI FTS [33, 42, 53], B_p is estimated at 500 nT. Using this B_p estimate in Equation (2.2) along with estimates of $d = 100\,\mu\mathrm{m}$, $f = 10\,\mathrm{MHz}$, and an aluminum sheet of $m = 10\,\mathrm{g}$, $\rho = 2.7 \times 10^{-8}\,\Omega\,\mathrm{m}$, and $D = 2700\,\mathrm{kg/m}^3$ gives a power dissipation estimate of ∼60 µW in the conducting sheet.

The Composite Infrared Spectrometer onboard Cassini [20] employed a differential eddy current sensor at 170 K [21] for the linear scan mechanism of its FTS. The sensor operated over a displacement range of 15 mm and resolution reported as <1 % of the range (and therefore, <150 µm). Although not a space mission, Sagar et al. report on an eddy current sensor achieving 40 µm resolution and 0.1 % accuracy over a 1.5 mm linear range at 4.2 K [54].

2.1.3 Linear Variable Differential Transformers

The linear variable differential transformer (LVDT) is a second type of inductive displacement sensor. Figure 2.1c shows the operation of a simplified LVDT. The left circuit provides an excitation current that is coupled into the right circuit via the three inductors to produce an induced voltage, V_{out}, at the output. A conductive core passing through the inductors changes the coupling from the excitation circuit (left side) to the read out circuit (right side) based on its position. The displacement of the core may then be determined via the measurement of V_{out} [37, 38].

LVDTs in low range applications (<500 µm) can achieve resolutions of 5 nm; larger LVDT sensors with 500 mm ranges deliver resolutions of 1 µm [37]. Measurement bandwidth is generally limited to 1 kHz, as greater excitation frequencies produce eddy currents in the core that adversely impact performance [38]. LVDTs can achieve nonlinearities of <1 % and accuracy of 0.25 % [37]. Like eddy current sensors, LVDTs are susceptible to external magnetic fields [55] and Joule and induction heating, but are also insensitive to contaminants such as oil and dirt in the air gap [42]. Although LVDTs are considered a contactless sensor due to the air gap, often the sensor housing has mechanical contact to keep the core centred between the coils unless used in an application where the alignment of the core and coils is maintained over the entire ranges by design.

The Spitzer Space Telescope employed a pair of redundant LVDTs in the cryogenic scanning mirror mechanism for its multi-band imaging photometer at ≤13 K [25–28]. The sensors measure the position of a rotary mirror mechanism which pivots over a range of 15° in a ∼10 Hz bandwidth. The SPIRE instrument onboard Herschel employed a Heidenhain optical encoder [56] along with an LVDT that could provide redundant position measurement [22]. The LVDT had a limited range and dissipated 0.112 mW of thermal power but was never used in normal operation.

2.1.4 Encoders

Encoders consist of two main components: a precisely constructed scale and a read-head that traverses its length. The scale encodes either absolute displacement by assigning a unique pattern to each position along the scale or incremental displacement with periodic patterns. Figure 2.1d depicts an optical encoder which typically consists of a glass scale that is illuminated and scanned by the read-head as it moves along the length of the scale. For an incremental encoder, a second scale is required to obtain direction information, which may be identical to the first but offset by 90° to produce a quadrature signal. An optical encoder design is shown in Figure 2.1d, but other strategies such as magnetic [57, 58], capacitive [59, 60], and microwave (also called electromagnetic) [61] encoders operate on the same principle. Encoders have historically been popular, and a 2010 survey in Japan found that over 70 % of precision positioning applications use encoders [62, 63]. Optical encoders are discussed since they have been employed in cryogenic space astronomy missions.

The range of an optical encoder is limited by the length of the scale, which in principle, can be built arbitrarily long. High resolution encoders achieve resolutions of <10 nm and accuracies of 5 ppm, and at reduced ranges, may achieve accuracies of 0.5 ppm; bandwidths can exceed 100 kHz [37]. The use of encoders in cryogenic space astronomy applications poses several challenges. First, the scale length must be at least the maximum displacement to be measured, consequently, the mass increases in proportion to the maximum displacement and requires greater cooling power to reach a target temperature. Second, as encoders are large, it may be difficult to place an encoder in the cryogenic workspace along with the other cryogenic hardware. Third, depending on the scanning mechanism of a cryogenic FTS, an encoder may not be easily retrofitted. There are two practical ways to mount the encoder: the scale fixed and the read-head moved, or the read-head fixed and the scale moved. Typically, the scale is fixed and the read-head is mounted to the moving mechanism. The change

to the dynamics of the scanning mechanism by the added mass of the read-head may need to be considered early in the design of the instrument. Fourth, the fragile glass scales are at risk of damage when subject to large launch forces [30].

Optical encoders have been used on the Herschel [23, 24], AKARI [29, 30], and James Webb Space Telescope (JWST) [64] missions. Herschel used a modified Heidenhain LIP401A moiré fringe encoder with a 2 µm step size that demonstrated an accuracy of 10 nm at cryogenic temperatures [65,66]. A modified Heidenhain LIP401P encoder was flown on AKARI and with an accuracy of 1 µm at temperatures of ∼3 K [30]. Heidenhain encoders typically dissipate up to 1 W of power [56], but the thermal power dissipation of the modified encoder was 1.2 mW at cryogenic temperatures [22]. The JWST employs a computational pattern recognition optical encoder which analyzes images of linear and rotary scales for absolute displacement measurements [31]. Evaluation of the encoder performance at 100 K showed an accuracy of 60 nm rms [32].

2.1.5 Interferometers

Interferometers encode displacement information as the phase of an optical signal; a concept introduced in Section 1.1. Although there are many range-resolved interferometry techniques, the Michelson interferometer [10, 11, 13] shown in Figure 2.1e is used to provide a generic introduction. In this approach, quasi-monochromatic light input from the left is split by a cube beamsplitter. A reference beam traverses the path with the fixed upper mirror and the signal beam traverses the path to the right with a movable mirror. When the right mirror is displaced, the relative phase between the reference and signal beams changes and a phase shift is observed in the output beam at the bottom of the beamsplitter. Measurement of the output signal allows one to recover the wrapped phase difference between the two beams, which can provide displacement over a limited range within one wavelength. One must generate

more phase information to determine larger displacements, which can be done with strategies such as the introduction of more beams in three-phase techniques discussed in Sections 2.3.1 and 2.3.2 or modulation of the laser optical frequency in the SFM technique in Section 2.3.3 and Chapter 3 onward. In practice, the Michelson interferometer of Figure 2.1e is rarely used in displacement measuring applications due to the sensitivity to displacement of the reference mirror.

Commercially available interferometers can measure ranges of up to 60 m [67], although some commercial interferometers relying on frequency modulation may have smaller measurement ranges [68]. Interferometers offered by Renishaw achieve resolutions of 39 pm [69], which corresponds to $\ll 1$ ppm. The practical bandwidth is dictated by the photodetection and processing electronics can exceed 1 MHz and the optical power of probing beams can be <1 mW [67].

In addition to the excellent range, resolution, and accuracy, often exceeding the techniques discussed in Sections 2.1.1 to 2.1.4 [37], interferometers confer several functional advantages over other measurement techniques. Interferometers are intrinsically non-contact and when fibre-coupled are easy to install or retrofit. Since the components that form the interferometer itself (i.e., lens and reflector) are passive, the foremost mechanical consideration for deploying an interferometer in harsh environments is that that these components can survive and retain their functionality under such conditions. This makes an interferometer an excellent choice for cryogenic applications as the laser, detector, and associated signal processing hardware can be situated external to the measurement environment, thereby limiting the thermal power dissipation in the cryogenic workspace by the probing photons which enter but do not exit together, along with any parasitic power arising from conduction along the fibre or transmission of unwanted thermal radiation from the fibre. In this way, the power dissipated by the laser and signal processing hardware is kept well away from the cryogenic workspace. Furthermore, although not desirable in far-infrared space-based

astronomical instrumentation, all but the reflector can be external to the cryostat and the beam passed through a window or the position of a target inside a cryostat can be measured relative to a window by exploiting multisurface reflections [70].

In atmosphere, free space interferometers are affected by fluctuations in refractive index of air dependent on temperature, pressure, and humidity, that can lead to an apparent change in displacement, however, this is not of concern in a cryogenic application under vacuum. Interferometers generally require a direct line-of-sight and are susceptible to beam breakage; maintaining alignment of the probing beam is critical to minimize the cosine (i.e., the angle between the measurement and translation vectors is non-zero) and Abbe (i.e., pitch and yaw in the motion) errors [41]. Interferometers are also among the most expensive displacement measurement systems.

While no cryogenic infrared space astronomy mission to date has flown a range-resolved laser interferometer, interferometers have been used in the cryogenic testing of astronomical instrumentation. Notable examples in related work include the testing of a novel angle-scanned Fabry-Pérot interferometer for astronomical instrumentation [71, 72], characterization and control of a novel stiffness-compensated scanning mechanism [73], and thermal expansion properties of carbon fibre reinforced polymer composites for space telescope mirrors from room to cryogenic temperatures [74, 75].

2.1.6 Summary

The performance of each technique discussed in this chapter is summarized in Table 2.1. Recall that the SAFARI metrology requirement, outlined in Table 1.1, calls for 10 nm rms accuracy in a measurement bandwidth of 20 Hz over a range of 33.5 mm. Additionally, the total system must be cryogenic and dissipate no more than 1 mW of thermal power, and the metrology itself on the order of 0.1 mW. Sections 2.1.1 to 2.1.5 introduced concepts in capacitive, inductive, encoder, and interferometric displacement sensors. From a review of Table 2.1, the best sensor technology for the

Table 2.1: Comparison of displacement metrology techniques updated from Chapter 2 of my master's thesis [36]. In the *Pros/Cons* column, pros and cons are respectively marked with + and −; trade-offs are evaluated in the context of a cryogenic space-based application.

Type	Performance		Pros/Cons	Space Missions
Capacitive Section 2.1.1	Range Bandwidth Resolution Accuracy Thermal Power	10 mm 100 kHz <1 nm 5 ppm 0 mW	+ High bandwidth + High resolution + High accuracy − Short range − Stress-induced nonlinearity − Susceptible to electric fields	ISO [17–19]
Eddy Current Section 2.1.2	Range Bandwidth Resolution Accuracy Thermal Power[1]	80 mm 100 kHz 10 nm 0.1 % <0.1 mW	+ High bandwidth + High resolution − Low accuracy − Susceptible to magnetic fields	Cassini [20, 21]
LVDT Section 2.1.3	Range Bandwidth Resolution Accuracy Thermal Power	500 mm 1 kHz 5 nm 0.25 % 0.112 mW [22]	+ Long range + High resolution + Robust − Low accuracy − Susceptible to magnetic fields	Herschel [22–24] Spitzer [25–28]
Encoder (Optical) Section 2.1.4	Range Bandwidth Resolution Accuracy Thermal Power	>1 m >100 kHz <10 nm 5 ppm 1.2 mW [22]	+ Long range + High bandwidth + High resolution + High accuracy − Thermal loading (mass) − Fragile	Herschel [22–24] AKARI [29, 30] JWST [31, 32, 64]
Interferometer Section 2.1.5	Range Bandwidth Resolution Accuracy Thermal Power[1]	>1 m >100 kHz <1 nm <1 ppm <0.1 mW	+ Long range + High bandwidth + High resolution + High accuracy − Susceptible to beam breakage	None to date SPICA (Canceled) [15] PRIMA (Proposed) [35]

[1] Estimate based on reasonable operating conditions.

SAFARI FTS becomes clear. Capacitive sensors cannot satisfy the required range while eddy current and LVDT sensors lack the required accuracy. Encoders can meet the measurement requirements, but the drawbacks of large size, fragility, and thermal power dissipation exceeding the entire thermal power budget of the SAFARI FTS are prohibitive for the adoption of an encoder. The thermal power budget of 1 mW for the SAFARI FTS includes both motion *and* measurement of a scanning mechanism; notionally, 90 % is assigned to motion and 10 % to metrology. It can be seen from Table 2.1 that the only candidate that meets these requirements is an interferometer, and for these reasons, SAFARI has adopted a frequency modulation range-resolved interferometer to provide position metrology at <4 K [33]. The development, including

cryogenic considerations, characterization and calibration, and applications of a cryogenic multiaxis sinusoidal frequency modulation (SFM) range-resolved interferometer is presented from Chapter 3 onward.

2.2 Optical Displacement Metrology Techniques

Optical sensors are employed in numerous applications with measurands including strain [76–80], temperature [78, 80, 81], and vibration [79, 82], along with more exotic applications, such as determining the ripeness of fruits [7, 8] and the study and conservation of paintings [83, 84]. This section focuses on a number of optical techniques for position measurement, including those in Figure 2.2. The field of displacement metrology is very large, and as part of this thesis, I have performed a comprehensive literature search to survey the parameter space of range and resolution. The goal of this section is not to explain how these techniques work, but instead provide an overview of each and present the summary table (Table 2.2) and summary plot (Figure 2.3) that I have constructed to compare the performance of each technique on as equal a footing as possible.

2.2.1 Time-of-Flight

Time-of-flight (ToF) sensing provides absolute ranging based on the round-trip ToF from the source to an object and back and can be classified as either direct time-of-flight (dToF) or indirect time-of-flight (iToF) [85–89]. dToF is in principle equivalent to starting a stopwatch when the signal is transmitted and stopping it when the return signal is received [90], as shown in Figure 2.2a, while iToF ranging techniques determine time-of-flight through phase measurements [88,89,91,92]. Pulsed light sources are common in dToF methods [93–96] as they enable the use of single photon avalanche diodes with arrival time resolutions on the order of 10^{-11} s [97] — sub-femtosecond temporal resolution can be achieved by locking to an Rb atomic

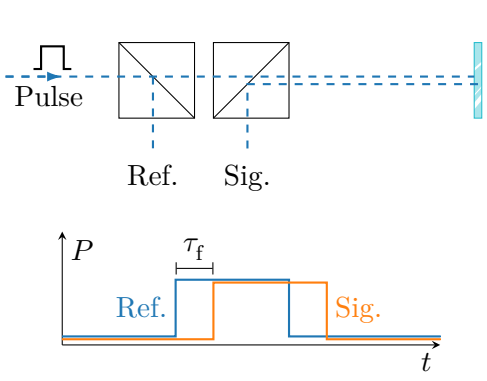

(a) Time-of-flight (direct)

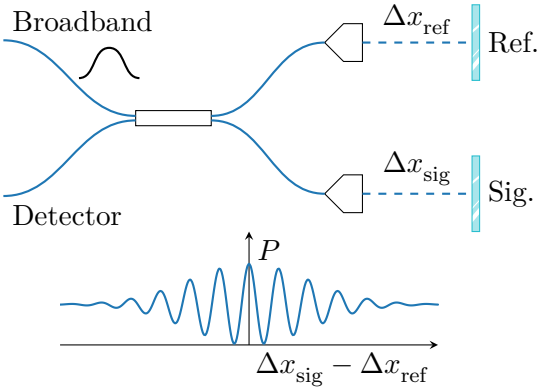

(b) White light interferometer

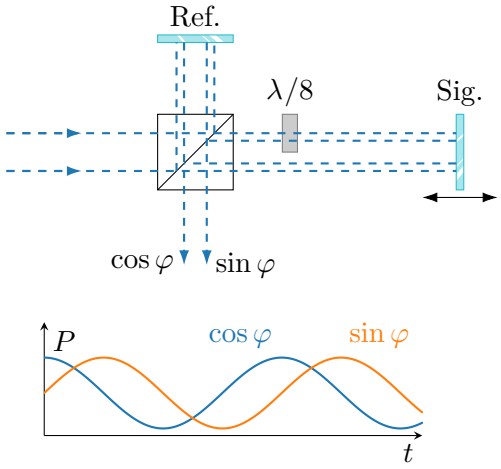

(c) Homodyne interferometer

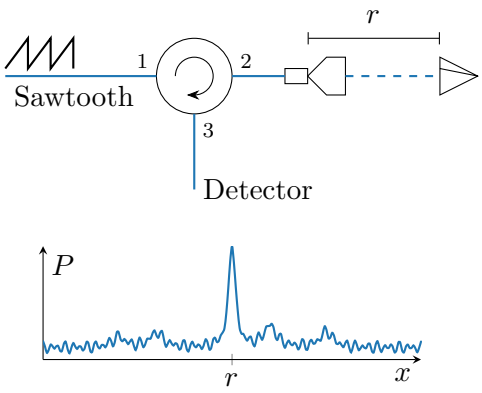

(d) Heterodyne interferometer

Figure 2.2: Operating principles of select ranging techniques discussed in this section. Each diagram shows a schematic of the approach and a plot with the detected optical power, P. A pulsed dToF implementation (a) which measures the round-trip time-of-flight delay, τ_f, between the rising edges of the reference and signal optical power as a function time, t. A fibre-fed white light interferometer (b) with an injected broadband source; the reference mirror is scanned a displacement Δx_{ref}, and the position of the signal mirror, Δx_{sig}, is known to be equal to Δx_{ref} when the brightest interference fringe is observed. A homodyne interferometer (c) which directly generates a quadrature signal by introducing a double-passed $\lambda/8$ delay in one of the probing beams to impart a $\pi/2$ phase shift. A fibre-fed heterodyne interferometer (d) with a sawtooth optical frequency modulated interrogating beam and reference Fresnel reflection [10] from the FC/PC fibre tip in the collimator measures a range, r, corresponding to the peak in the position, x.

clock [98, 99]. The automotive industry is a major driver for 3D imaging ToF sensors [92, 100, 101] which require scalable imaging technologies to keep up with evolving demands [102–105]. ToF sensors also have applications in non-line-of-sight sensing of occluded objects and scenes [106, 107]. While dToF sensors have greater range and rejection of non-target objects than iToF sensors, they require higher power for the readout electronics; iToF approaches have been integrated into miniaturized, low power modules, and are acceptable for short range applications on the order of $\sim$10 m or less [89, 108–110].

2.2.2 Optical Coherence

A white light interferometer that exploits the low coherence of a broadband source [111–113] is shown in Figure 2.2b. A bright fringe is produced when the optical lengths of the reference and measurement paths are equal so that the optical path difference (OPD) is zero [11,12]. The position of the scanning mirror is known by some other sensor, and the absolute distance to the measurement target can be recovered [114–117]. Optical coherence tomography (OCT) is commonly used for non-invasive imaging of structures such as tissues, veins, and retinae [114, 118–121]; cancer diagnostics [122], and fingerprint recognition [123, 124]. OCT systems often employ a scheme such as the white light interferometer shown in Figure 2.2b [116, 125–127] and in medical applications employ near infrared light for its tissue penetration depth [119]. Techniques based upon a moving reference mirror as shown in Figure 2.2b are limited in range by the mechanical stroke of the reference arm, however, modifications to the optical interrogation can be used to extend the measurement range. Synthesis of the optical coherence function (SOCF) schemes synthesize coherence along the OPD, usually via laser modulation [128–134]. These long range techniques are often used in fibre characterization and fault location where features due to Rayleigh scattering and Fresnel reflections are detected [135, 136].

2.2.3 Homodyne Laser Interferometry

In 1892, using an interferometer of his design, Albert A. Michelson sought to define the length standard of the metre, and without the aid of computers, counted one metre to be 1 553 164.13 wavelengths of the 644 nm cadmium red emission line in air at 760 mmHg and 15 °C. This definition stood until 1960 when the metre was redefined in terms of the orange 606 nm emission line of krypton 86 [137–140]. To obtain a displacement measurement, the additional phase information required to determine the direction of travel in homodyne interferometry (HoI) can be generated using several strategies, such as introducing a phase delay as shown in Figure 2.2c, encoding the quadrature components as orthogonal polarization states [141–145], and using a 3×3 [146] or 4×4 fibre optic coupler [147]. In prior work, I developed a differential three-phase technique with a 3×3 fibre coupler (discussed briefly in Section 2.3.2) that was demonstrated at cryogenic temperatures [36, 148]. HoI provides incremental displacement, but absolute ranging is possible with a slowly swept wavelength that avoids heterodyne interference [149]. By discretely modulating the phase without changing the frequency, simultaneous multiplexed measurements may be performed with HoI: for example, using pseudorandom numbers (PRN) codes to phase modulate with a four-point stepping pattern of 0, 90, 180, and 270° [150], akin to quadrature phase shift keying (QPSK) [151].

2.2.4 Heterodyne Laser Interferometry

Heterodyne interferometry (HeI) involves the mixing of two or more frequencies. Two-wavelength interferometer (TWI) or multiwavelength interferometry eliminate interference order ambiguity over a limited range by examining the synthetic wavelength of the beat frequency [152–155]. A different style of multiple wavelength interferometer based on wave-division multiplexing and a phasemeter tracks the phase between heterodyne frequencies generated by two frequency-shifted lasers [156, 157].

Digital modulation using PRN codes can also be applied in HeI approaches by matching the phase modulation to the delay of the interferometer [158,159]. Absolute ranging using a technique such as sawtooth modulation of the optical frequency as shown in Figure 2.2d is used in absolute ranging applications [160]. Overviews of sawtooth and triangular modulation schemes are presented in Sections 3.5.1 and 3.5.2. Triangular optical frequency modulation can be exploited to provide information about absolute range and velocity and is commonly employed in frequency-modulated continuous-wave (FMCW) light detection and ranging (LiDAR)s [161–164]. Sinusoidal optical frequency modulation (which is thoroughly discussed from Chapter 3 onward) can be used for absolute ranging [162] and incremental displacement measurement [165,166]. The latter is investigated in this thesis.

2.2.5 Commercial Displacement Measuring Interferometers

While the optical displacement metrology techniques reviewed so far in this section exist within academic research, it is important to consider commercial systems that are readily available at the time of writing. Although the systems discussed in this section may also be grouped under the homodyne and heterodyne interferometry discussions in Sections 2.2.3 and 2.2.4, respectively, they are presented in their own category due to their idiosyncrasies. Commercial interferometers often have different ranging characteristics based on sensor heads (i.e., lens and/or detectors) and signal processing units, which allows companies to offer customizable solutions at different price points to appeal to a broader customer base. Furthermore, the reported resolution does not often correspond to the smallest resolvable change in displacement that can be measured, but instead, to the least significant bit (LSB) of a digital position readout that may not be meaningful. Commercial interferometers from Attocube [167–169], SmarAct [68,170–172], Zygo [173–176], and Renishaw [67,69,177–179] are considered.

Table 2.2: Performance of optical displacement measurement and ranging techniques. After reviewing the papers referenced in this section, I have constructed this table and accompanying plot in Figure 2.3 to compare the various techniques on as equal a footing as possible. The *Class* column names the technique and the *Notes* column includes additional information such as unique features or capabilities. *Range* and *Resolution* columns show the best *demonstrated* values, not theoretical limits. The *Type* column may contain $\rightarrow$ or Δ to denote absolute or incremental measurements, respectively. The dotted horizontal line separates systems reported in academia (above) from commercially available units (below). Entries appear in the same order as the text.

Source	Year	Class	Notes	Range	Resolution	Type
Kilpelä et al. [93]	2001	dToF	44 W laser pulse	34.5 m	∼2 mm	→
Liang et al. [94]	2014	dToF	Multiple repetition rate	∼1.5 km	<1 cm	→
Warburton et al. [95]	2007	dToF	Pulse pattern	330 m	4 mm	→
Hiskett et al. [96]	2008	dToF	Random pulse pattern	∼2.2 km	3.5 mm	→
Lee et al. [98, 99]	2012	dToF	Rb atomic clock locking	∼700 m	∼23.7 nm	→
Lee et al. [102]	2019	dToF	Back-illuminated pixels	27 m	<4.5 cm	→
Ximenes et al. [103]	2019	dToF	Back-illuminated pixels	300 m	15 cm	→
Perenzoni et al. [104]	2017	dToF	Imaging or single point	1 km	3 cm	→
Brooks et al. [106]	2019	dToF	Non-line-of-sight	<3 m	—[1]	→
Nam et al. [107]	2021	dToF	Non-line-of-sight imaging	3.5 m	8 cm	→
Horio et al. [108]	2022	iToF	Amplitude modulation	9.3 m	<20 cm	→
Dutton et al. [109]	2015	iToF	Short pulse	600 mm	38 mm rms	→
Stoppa et al. [110]	2004	iToF	Multipulse, imaging	8 m	<100 µm	→
Swanson et al. [116]	1992	OCT	Single pixel	7.5 mm	17 µm	→
Dubois et al. [125]	2018	OCT	Line scan camera	500 µm	1.1 µm	→
Li et al. [126]	2020	OCT	Low-cost, MEMS mirror	2 mm	9 µm	→
Kakuma et al. [127]	2008	OCT	Discretely swept source	12 mm	28 µm	→
Hotate et al. [128]	1993	SOCF	Proposed SOCF	<1 m	10 mm	→
Xue et al. [129]	2021	SOCF	External modulation	50 km	1.4 m	→
Kashiwagi et al. [130]	2009	SOCF	Temporal gating	1 km	19 cm	→
Mizuno et al. [132]	2010	SOCF	Double modulation	1.5 km	27 cm	→
Saida et al. [134]	1998	SOCF	Pulse window	5 km	6 cm	→
Požar et al. [143, 144]	2001	HoI	Polarization	1 mm	<1 nm	Δ
Pisani [145]	2009	HoI	Polarization, folding > 100	<1 nm	20 fm/$\sqrt{\text{Hz}}$	Δ
Christiansen et al. [36, 148]	2020	HoI	Differential three-phase	2.5 cm	2.3 nm rms	Δ
Smith et al. [149]	2009	HoI	Tuned Fabry Pérot	50 nm	2 pm	Δ
Sutton et al. [150]	2012	HoI	PRN QPSK	<1 µm	0.8 pm/$\sqrt{\text{Hz}}$	Δ
Thurner et al. [154]	2013	HeI	TWI, gas cell	25 µm	1 nm	→
Lin et al. [155]	2004	HeI	TWI, perturbation feedback	∼4.8 mm	∼5 nm[3]	→
Zhang et al. [156, 157]	2022	HeI	Two-wavelength, phasemeter	9.1 µm	220 pm/$\sqrt{\text{Hz}}$	Δ
de Vine et al. [158]	2009	HeI	PRN digital phase shifting	<5 µm	5 pm/$\sqrt{\text{Hz}}$	Δ
Kissinger et al. [159]	2013	HeI	PRN, delayed demodulation	<3 mm^2	∼0.6 nm/$\sqrt{\text{Hz}}$[2]	Δ
Shi et al. [160]	2019	HeI	Sawtooth, Hilbert transform	6.7 m	76.8 µm	→
Shi et al. [163]	2014	HeI	Triangular, linearization	8.7 m	50 µm	→
Jang et al. [164]	2023	HeI	Triangular FMCW LiDAR	3 m	6 mm	→
Sakai et al. [165]	1987	HeI	SFM, external modulation	<1 mm[3]	100 pm/$\sqrt{\text{Hz}}$[2]	Δ
Kissinger et al. [166]	2015	HeI	SFM, LD bias modulation	3.5 µm	∼0.8 nm^2	Δ
This Thesis	2023	HeI	SFM, cryogenic	300 mm	∼50 pm	Δ
Attocube [167–169]	—	HeI	Acetylene gas cell	5 m	1 pm[4]	Δ
SmarAct [68, 170–172]	—	HeI	SFM	<5 m	1 pm[4]	Δ
Zygo [173–176]	—	—[1]	HeNe, heterodyne	21.2 m	0.15 nm[4]	Δ
Renishaw [67, 69, 177–179]	—	HoI	HeNe	60 m	38.6 pm[4]	Δ

[1] Not provided by the source.
[2] Provided by the source in non-length units and converted based on context.
[3] Not provided by the source; calculated or estimated from context.
[4] Resolution provided by digital output; not necessarily the minimum resolvable displacement.

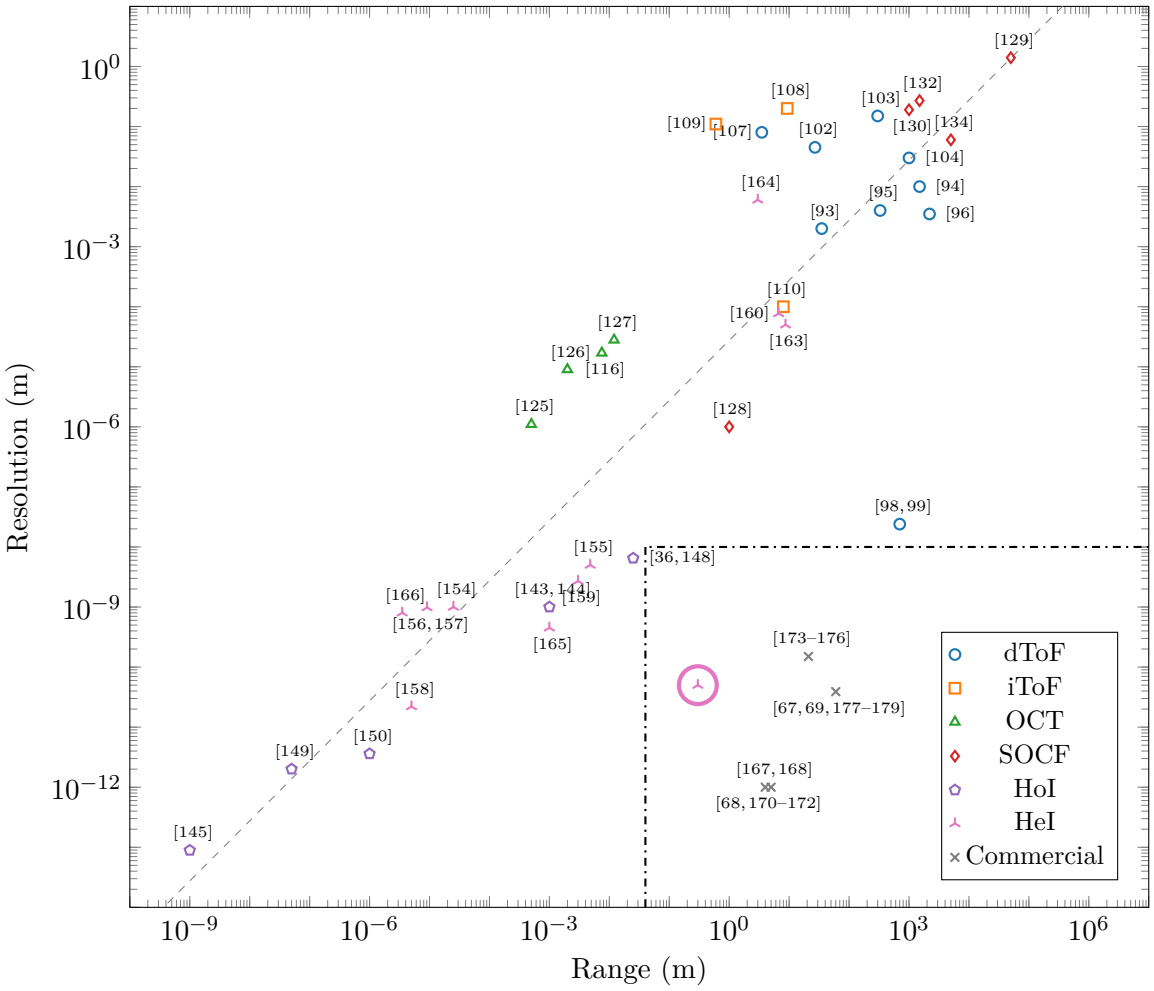

Figure 2.3: Visualization of the range and resolution of the techniques listed in Table 2.2. To obtain this plot, some modifications to the resolutions in Table 2.2 are required. Entries with a "simple" unit (e.g., nm) are plotted as is; entries carrying an RMS unit are notionally assumed sinusoidal and converted to an equivalent peak-to-peak value (e.g., 1 nm rms is taken as 2.8 nm); entries with a sensitivity (i.e., $\mathrm{m}/\sqrt{\mathrm{Hz}}$) are taken over the 20 Hz bandwidth requirement of the SPICA SAFARI FTS outlined in Table 1.1 (e.g., $1\,\mathrm{nm}/\sqrt{\mathrm{Hz}}$ is taken as 4.5 nm). Entries with missing ranges or resolutions are excluded. Like Table 2.2, the best *demonstrated* performance is plotted, not theoretical limits. Point labels are citations; the pink circled trident point is the performance demonstrated by the SFM technique in this thesis. The dashed gray line shows the geometric mean of all Resolution/Range ratios, which is 27 ppm; the dash dotted box in the lower right is the region bounded by the SPICA SAFARI FTS requirements from Table 1.1.

2.2.6 Summary

This section has served to present an overview of the many different types of optical displacement metrology techniques and estimates of their measured performances. The results are summarized in Table 2.2 and Figure 2.3, which compare the parameter space of range and resolution. The *Resolution* column in Table 2.2 highlights inconsistencies in reporting, as it includes "simple" units (i.e., nm), root mean square (RMS) uncertainties (i.e., nm rms), and sensitivities (i.e., $\mathrm{nm}/\sqrt{\mathrm{Hz}}$). Furthermore, a column for measurement bandwidth has not been included as it is not often reported in the literature. In the visualization of Figure 2.3, the best performing techniques lie in the lower right and the worst in the upper left; in general, most techniques fall along the dashed line that represents the average resolution/range trade-off of 27 ppm. There is also generally a clustering of each technique where ToF and SOCF are long range and low resolution, OCT is mid range and mid resolution, and interferometry is low to mid range and high resolution.

The location of the SAFARI FTS requirements outlined in Table 1.1 is denoted by the dash dotted box in the lower right of this parameter space — all techniques that fall within this region are HoI and HeI. There are two techniques that lie just outside this region. The first is the dToF approach reported by Lee et al. with a femtosecond laser locked to an Rb atomic clock [98, 99], which lies just above the box and does not meet the required resolution. The second is the three-phase interferometer from prior work — the subject of my master's thesis [36] — which lies to the left of the box and does not meet the required range. In principle, the three-phase technique can measure much greater ranges, however, the comparisons in Table 2.2 and Figure 2.3 show the best *demonstrated* performance, and the three-phase approach was never used to measure displacements greater than 2.5 cm. Furthermore, the three-phase approach was not adopted due its poor DC performance discussed in Sections 2.3.1 and 2.3.2.

The techniques that have been demonstrated to meet the SAFARI FTS requirements are the sinusoidal frequency modulation (SFM) technique discussed in this thesis (the pink circled trident point in Figure 2.3) and the commercially available displacement measurement interferometers. It is perhaps no surprise that the commercially available systems fall in the lower right region of the plot where the highest performing techniques reside, however, one may be sceptical of these values due to the varying definitions of resolution. The performance of the SFM technique presented in this thesis was demonstrated, with the resolution characterized in Section 7.7 and the largest measured range in Section 7.8. From this survey of optical displacement metrology techniques there is clearly no "one size fits all" solution, but in the context of the SAFARI FTS, the SFM range-resolved laser interferometer presented in this thesis is a leading candidate.

2.3 Prior Work in Cryogenic Range-Resolved Interferometry

The foray into cryogenic range-resolved laser interferometry began with the three-phase approach [36, 180] presented in Section 2.3.1, which was extended to the differential scheme in Section 2.3.2. The shortcomings of three-phase laser interferometry motivated the adoption of the sinusoidal frequency modulation (SFM) technique discussed in Section 2.3.1, for which a prototype was demonstrated at ambient and cryogenic temperatures [36, 148]. All of these techniques were presented in my master's thesis [36], and so this thesis focuses exclusively on the development of the SFM technique for cryogenic and multiaxis applications. From Chapter 3 onward, the SFM technique introduced in this section is investigated as a candidate for cryogenic displacement metrology.

2.3.1 Three-Phase Range-Resolved Interferometry

Three-phase homodyne laser interferometry is based upon the Clarke transformation, proposed by Edith Clarke, which is commonly used in electrical engineering to convert between two- and three-phase power [181]. Although Edith Clarke did not initially receive her deserved recognition — which in no small part was due to sexism in the 20$^{\text{th}}$ century field of engineering — she received the Society of Women Engineers Achievement Award in 1954 [182], just five years before her passing, and in 2015, was inducted into the National Inventors Hall of Fame [183]. Furthermore, Edith Clarke broke several barriers for women in electrical engineering by becoming the first woman to earn a master of science in electrical engineering from MIT, the first woman professionally employed as an electrical engineer in the United States of America, and the first female electrical engineering professor in the United States of America.

In a three-phase interferometer, the three normalized interference signals, $U_{\text{tp,a}}$, $U_{\text{tp,b}}$, and $U_{\text{tp,c}}$, are defined in terms of the OPD dependent phase, φ, as

$$\begin{bmatrix} U_{\text{tp,a}}(t) \\ U_{\text{tp,b}}(t) \\ U_{\text{tp,c}}(t) \end{bmatrix} = \begin{bmatrix} \cos\big(\varphi(t)\big) \\ \cos\big(\varphi(t) - 2\pi/3\big) \\ \cos\big(\varphi(t) + 2\pi/3\big) \end{bmatrix}. \tag{2.3}$$

Equation (2.3) is defined such that $U_{\text{tp,b}}$ lags and $U_{\text{tp,c}}$ leads $U_{\text{tp,a}}$, and $U_{\text{tp,a}}$ is taken as the reference signal. Figure 2.4a shows how three-phase signals encode a particular phase. To obtain quadrature from three-phase, one may apply the Clarke transfor-

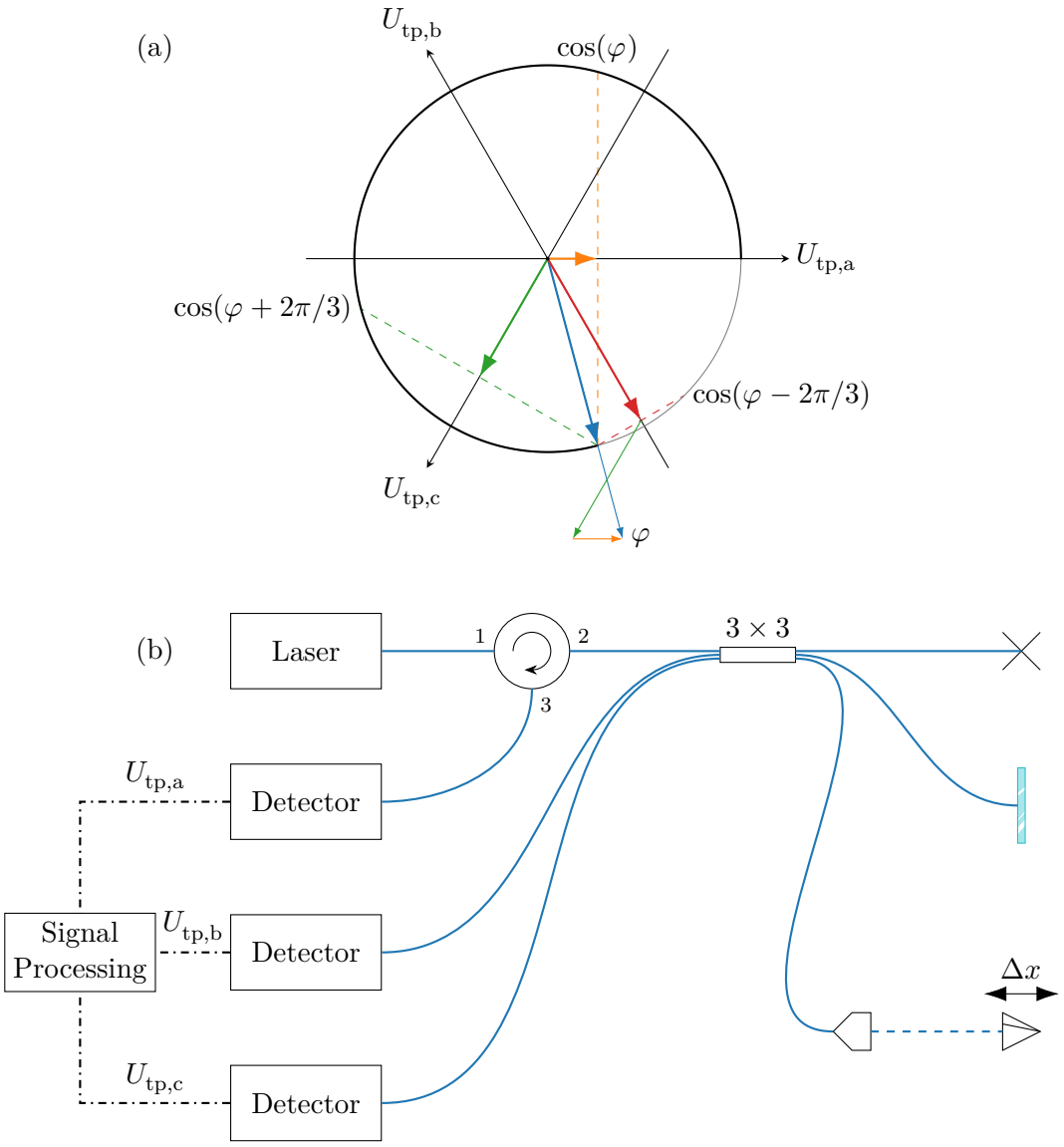

Figure 2.4: Three-phase interferometer encoding and configuration in a three-phase interferometer. Three-phase signals (a) used to encode an OPD carrying a wrapped phase of $\varphi = 19\pi/12$. The three-phase vectors for $U_{\text{tp,a}}$, $U_{\text{tp,b}}$, and $U_{\text{tp,c}}$ in orange, green, and red, respectively, sum to the resultant in blue at an angle φ. The total length of the resultant vector is 3/2, and it is scaled to fit within the unit circle. Chords drawn for $U_{\text{tp,a}}$, $U_{\text{tp,b}}$, and $U_{\text{tp,c}}$ show that their intersection coincides with the scaled resultant vector. In the three-phase interferometer configuration (b), laser light is split into three signals by the 3×3 coupler: one is dead-ended, one is directed to a reference mirror, and one to probe the target. The reference and probing beam return and pass through the coupler again in the reverse direction, which spreads each signal across the three output fibres, and the three interference signals in Equation (2.3) are detected.

mation, given by

$$\begin{bmatrix} U_{\mathrm{tp,a}}(t) \\ U_{\mathrm{tp,b}}(t) \\ U_{\mathrm{tp,c}}(t) \end{bmatrix} \underbrace{\begin{bmatrix} 2/3 & -1/3 & -1/3 \\ 0 & \sqrt{3}/3 & -\sqrt{3}/3 \\ 1/3 & 1/3 & 1/3 \end{bmatrix}}_{\text{Clarke transformation}} = \begin{bmatrix} \cos\big(\varphi(t)\big) \\ \sin\big(\varphi(t)\big) \\ 0 \end{bmatrix}. \tag{2.4}$$

It can be seen by Equation (2.4) that the Clarke transformation produces quadrature accompanied by a zero signal. The zero signal only takes on a value of 0 when the three-phase signals are ideal, that is, mutually phase separated by exactly $2\pi/3$ and equal in amplitude.

Figure 2.4b shows one possible implementation of three-phase interferometer. There are several factors present in this interferometer that led to non-ideal three-phase interference signals. First, a 3×3 coupler was used to split the laser intensity and impart $2\pi/3$ phase shifts to each output. Couplers are typically constructed in the fused biconical taper topology which have unique gains and phase shifts on each port unless manufactured with perfect symmetry [11, 184]. Second, one of the returning three-phase signals passes through a circulator, which contributes a unique insertion loss to one of the three signals. Third, the detectors and amplification circuitry have unique gains and offsets. These non-idealities were successfully handled with appropriate calibration and phase shift irregularities at the 3×3 coupler were found to be negligible [36].

The implementation of the three-phase interferometer required three photodetectors, each seated in a circuit with three operational amplifiers for a total of nine amplifiers, each of which must be calibrated to correctly apply the Clarke transformation. The three amplifiers in each circuit were used for offset adjustment, transimpedance amplification, and gain adjustment. Since part of the OPD is in fibre, this design is sensitive to length fluctuations along the fibres, which are often thermal. This is

partly mitigated by keeping the fibres in the same enclosure, however, it is not guaranteed that the fibres are isothermal with respect to each other. Furthermore, $1/f$ noise in the photodetection circuitry leads to poor DC performance when the target is stationary (i.e., the interference fringe rate at the photodetectors is 0 Hz). At DC, the amplified signals wandered and were interpreted as interference fringes by the digital signal processing (DSP) system, leading to drifts in the recovered displacement.

2.3.2 Differential Three-Phase Range-Resolved Interferometry

An immediate improvement to the three-phase interferometer discussed in Section 2.3.1 is to modify the configuration so that the fixed reference reflector in Figure 2.4b can be used to provide a differential measurement. Figure 2.5 shows two changes to the design. First, the introduction of a custom paired fibre in which the fibre segments are kept close together in stainless armor reduces differential temperature fluctuations in the fibres, as their proximity makes temperature induced changes in length common-mode. Secondly, a retroreflector was added to the backside of the target to be probed. As the target moves, the length of one optical path increases and the other decreases, and this differential nature gives an immediate $2\times$ improvement in resolution over the original three-phase design in Section 2.3.1. Although the introduction of the paired fibre grants some protection against temperature fluctuations, there is no improvement in the DC performance. The maximum velocity is halved due to doubling of the interference fringe rate that accompanies the doubled folding factor of the interferometer, a necessary trade-off for the increased resolution.

2.3.3 Sinusoidal Frequency Modulation Range-Resolved Interferometry

The driving factor for abandoning the three-phase approach in favour of the heterodyne sinusoidal frequency modulation (SFM) technique was the poor DC performance of the three-phase system. With optical frequency modulation the signal power is shifted away from 0 Hz, thereby eliminating drift due to $1/f$ noise that was

observed in the three-phase interferometer and improving DC sensitivity. Furthermore, simultaneous measurements of multiple axes are possible using a single laser and detector since differing OPDs in the interferometer leads to signals in different frequency bands that can be simultaneously demodulated. The SFM approach is in general less susceptible to noise in the interference signal as the derived quadrature signal is found by time averaging the product of the interference signal and a carrier tuned to a specific OPD. An SFM interferometer can generally be constructed with fewer optical components than a three-phase interferometer using the design shown in Figure 2.6.

The SFM approach is not without drawbacks. The signal processing and calibration have significantly greater complexity than the three-phase technique. With respect to the three-phase interferometers of Sections 2.3.1 and 2.3.2, there is a reduction in the measurable range and velocity, as is shown in Sections 3.2 and 3.3. Displacements may only be tracked over short ranges as demodulation goes out-of-band when the OPD deviates from its central value, however, a strategy to overcome

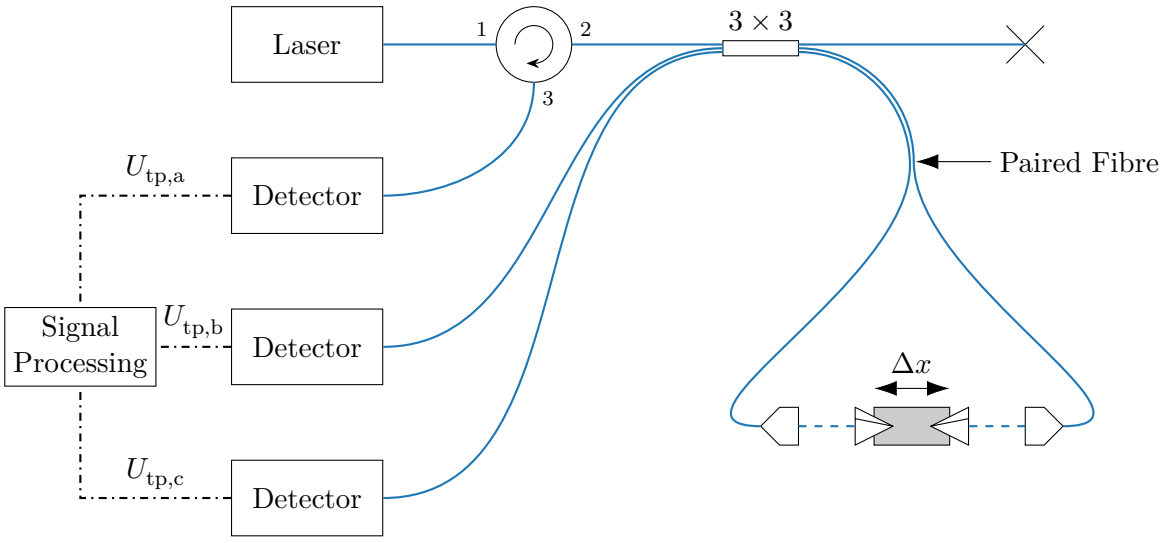

Figure 2.5: Configuration of a differential three-phase interferometer. Operation is like that of Figure 2.4b, except the fixed mirror has been replaced with a second probing beam to a reflector on the backside of the target.

this limitation is presented in Section 7.8. For photodetector amplifiers with similar cutoff frequencies, the maximum measurable velocity with an SFM interferometer is always less than that of a three-phase interferometer since modulation of the laser increases the rate of interference fringes at the detector.

In prior work I verified a single-axis proof of concept of the SFM technique at cryogenic temperatures [36]. This thesis further develops the SFM approach with a generalized theoretical model in Chapter 3 that enables the extension to simultaneous measurements of multiple axes as discussed in Chapter 4.

2.3.4 Summary

Table 2.3 summarizes the trade-offs between the three-phase and SFM approaches discussed in Sections 2.3.1 to 2.3.3. With respect to performance characteristics, the only drawback in transitioning from the initial three-phase approach to the SFM technique is the reduction in range and velocity. Additional complexities in signal processing and calibration were considered a small price to pay to enjoy the benefits of the SFM technique. The foray into range-resolved laser interferometry was to provide cryogenic displacement metrology for cryogenic space-based far-infrared FTSs where ranges and velocities are small, typically <10 cm and <1 cm/s, respectively. Although

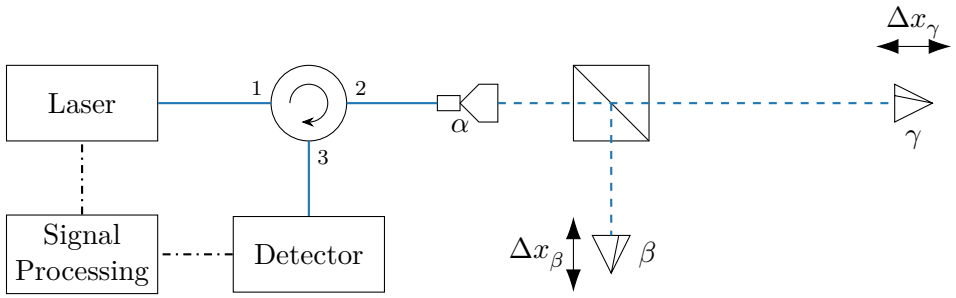

Figure 2.6: Configuration of an SFM interferometer. Laser light is passed through a circulator and partially reflected off the face of an FC/PC terminated fibre at α. The beam probes two moving retroreflectors at β and γ, which reflect light back to the collimator. There are three OPDs which can be simultaneously measured: $\alpha\beta$, $\alpha\gamma$, and $\beta\gamma$.

the maximum SFM range and velocity are less than that of the three-phase, the SFM technique prevails in robustness of performance especially at low velocities and in step-and-integrate operating modes often found in FTS.

2.4 Conclusions

This chapter presents a review of displacement metrology techniques that either have been or could be employed in cryogenic space astronomy applications, and the results are summarized in Table 2.1. Furthermore, a comprehensive literature survey of optical displacement measurement and ranging techniques was performed to construct the comparisons in Table 2.2 and Figure 2.3. It has been shown that the stringent Space Infrared telescope for Cosmology and Astrophysics (SPICA) SAFARI FTS displacement metrology requirements of precision, range, and operation at $<4\,\mathrm{K}$ with low power dissipation (Table 1.1) can only be met by a laser-based metrology system. While the three-phase laser interferometer, which was the subject of my master's thesis, held much promise, its poor performance at low velocities could not be overcome. It was realized that the signal of interest must be moved away from DC. The shortcomings of the three-phase system pointed the way forward to the adoption

Table 2.3: Summary of three-phase and SFM interferometer pros and cons.

Technique	Pros	Cons
Three-Phase (Section 2.3.1)	Few optical components Simple signal processing Long range, high velocity	Poor DC performance 3 detectors, 9 amplifiers, calibration Single-axis
Differential Three-Phase (Section 2.3.2)	2× resolution improvement Simple signal processing Long range, high velocity	Poor DC performance Many optical components (custom) 3 detectors, 9 amplifiers, calibration Single-axis
SFM (Section 2.3.3)	High DC sensitivity Less susceptible to electrical noise Multiaxis Few optical components 1 detector, 1 amplifier	Complex signal processing Extensive calibration Short range, low velocity

of the sinusoidal frequency modulation (SFM) technique. The central theme of this thesis is the development and cryogenic validation of the SFM technique.

Chapter 3

Multiaxis Sinusoidal Frequency Modulation Interferometry Theory

Chapter 2 concluded that the sinusoidal frequency modulation (SFM) technique in principle can meet the stringent displacement metrology requirements of the Space Infrared telescope for Cosmology and Astrophysics (SPICA) SPICA Far-Infrared Instrument (SAFARI) Fourier transform spectrometer (FTS) given in Table 1.1. In this chapter, I review the underlying principles of SFM theory which builds upon the previously published works of Sakai et al. [165] and Kissinger et al. [166]. A unique feature of my thesis is a cryogenic multiaxis application of the SFM technique. The practical implementation details are discussed in Chapter 4. To make the text more readable only key results are presented in this chapter, however, the complete derivations of steps in the procedure are given in Appendix A.

3.1 Single-Axis Interferometry

Before delving into the multiaxis SFM model in Section 3.2, a simplified overview of a single-axis interferometer is presented. In this section, results are simply stated, as the equations in Section 3.2 reduce to the single-axis equations for the $|S| = 2$ interferometer in Figure 3.1 where S is the set of paths through the interferometer. The purpose of this section is to provide a short and digestible overview of the SFM technique, so the equations are presented for a single-axis interferometer configuration with omission of the delays that arise in a practical implementation.

3.1.1 Modulation

A laser, such as a semiconductor distributed-feedback (DFB) laser diode (LD), is modulated so that its optical frequency is sinusoidally swept at a modulation frequency, f_m, with an optical frequency modulation amplitude, ν_A, about a centre optical frequency, ν_c. The instantaneous optical frequency of the laser can be expressed as

$$\nu(t) = \nu_\mathrm{A} \sin\big(2\pi f_\mathrm{m} t\big) + \nu_\mathrm{c}, \qquad \text{[Hz]} \quad (3.1)$$

where t is time. The phase, ϕ, of a signal carrying a frequency $\nu(t)$ from Equation (3.1) is given by $2\pi \int \nu(t)\ \mathrm{d}t$. Having an initial phase of ϕ_0 at $t = 0$, the phase for some $t \geq 0$ is

$$\phi(t) = \phi_0 + \frac{\nu_\mathrm{A}}{f_\mathrm{m}}\big[1 - \cos(2\pi f_\mathrm{m} t)\big] + 2\pi\nu_\mathrm{c} t. \qquad \text{[rad]} \quad (3.2)$$

There are two paths that the signal may take through the interferometer in Figure 3.1: the shorter path follows the reflection from a reference surface, α, and the longer traverses the round-trip to the target and back, β. The signal that traverses the longer path is delayed by the time-of-flight, $\tau_\mathrm{f}(t)$, and carries frequency and phase of $\nu(t - \tau_\mathrm{f}(t))$ and $\phi(t - \tau_\mathrm{f}(t))$ by Equations (3.1) and (3.2), respectively. The phase difference, $\Delta\phi$, between the two paths may be found via $\phi(t) - \phi(t - \tau_\mathrm{f}(t))$, and is

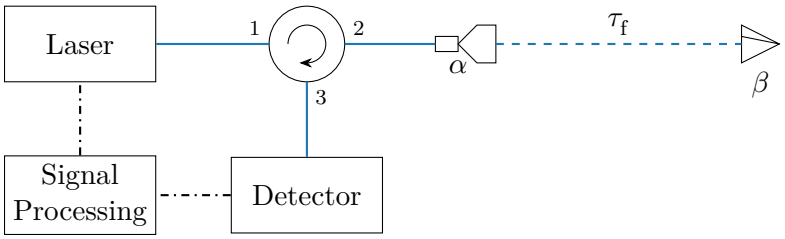

Figure 3.1: Schematic of a single-axis interferometer. At α, a $\sim$4 % Fresnel reflection [10] provides a reference signal; the target is the retroreflector at β. The round-trip time-of-flight delay, τ_f, is the time for the signal to travel from the collimator at α to the retroreflector at β and back.

given by

$$\Delta\phi(t) = \underbrace{\underbrace{\frac{2\nu_{\mathrm{A}}}{f_{\mathrm{m}}}\sin\big(\pi f_{\mathrm{m}}\tau_{\mathrm{f}}(t)\big)}_{A(t)}\sin\left(2\pi f_{\mathrm{m}}\left[t-\frac{1}{2}\tau_{\mathrm{f}}(t)\right]\right)}_{\theta(t)} + \underbrace{2\pi\nu_{\mathrm{c}}\tau_{\mathrm{f}}(t)}_{\varphi(t)}, \qquad \text{[rad] (3.3)}$$

where $A(t)$ is the phase modulation amplitude, $\theta(t)$ is the phase modulation, and $\varphi(t)$ is the optical path difference (OPD) dependent phase.

The time-of-flight delay can be expressed as $\tau_{\mathrm{f}}(t) = \Lambda(t)/\mathrm{c}$, where Λ is the OPD of the interferometer and c is the vacuum speed of light. The modulation amplitude can then be approximated as

$$A \approx \frac{2\pi\nu_{\mathrm{A}}\Lambda_{\mathrm{c}}}{\mathrm{c}} \quad \text{when} \quad \Lambda_{\mathrm{c}} \ll \frac{c}{\pi f_{\mathrm{m}}}. \qquad \text{[rad] (3.4)}$$

where $\Lambda_{\mathrm{c}} = (\max\Lambda + \min\Lambda)/2$ is the central OPD of the interferometer. Although A is time varying, there are a range of OPDs where the constant approximation of A in Equation (3.4) is valid. Changes in OPD result in this approximation going out-of-band and limit the measurement range, which is explored throughout Chapter 5. A novel technique to overcome this limitation is explored in Section 7.8.

The phase modulation, $\theta(t)$ in Equation (3.3), is the change in phase of the signal primarily due to the modulation of the laser *and* OPD, while the OPD dependent phase, $\varphi(t)$, depends *only* on the OPD of the interferometer. These two phase terms are given by

$$\theta(t) = A(t)\sin\left(2\pi f_{\mathrm{m}}\left[t'-\frac{1}{2}\tau_{\mathrm{f}}(t)\right]\right), \qquad \text{[rad] (3.5a)}$$

$$\varphi(t) = \frac{2\pi\nu_{\mathrm{c}}\Lambda(t)}{\mathrm{c}}. \qquad \text{[rad] (3.5b)}$$

The individual phase components in Equations (3.5a) and (3.5b) allow Equation (3.3) to be written in the compact form

$$\Delta\phi(t) = \theta(t) + \varphi(t). \qquad \text{[rad]} \tag{3.6}$$

Equation (3.6) highlights the key to the SFM technique, namely that the phase is separated into two terms: one of which is approximately known, $\theta(t)$, and the other is unknown, $\varphi(t)$. A demodulation scheme may be used to recover the OPD dependent phase, $\varphi(t)$, via a carrier that approximates $\theta(t)$.

3.1.2 Demodulation

After detection of the signal carrying the phase difference $\Delta\phi(t)$ from Equation (3.6), demodulation is performed on the normalized interference signal, $U(t)$. A normalization procedure is presented later in Section 4.5.1. The normalized signal is given by

$$U(t) = \cos\Delta\phi(t). \tag{3.7}$$

A complex carrier is generated to carry a phase that approximates $\theta(t)$. A demodulation amplitude, A_{d}, is selected in the carrier generation, and is chosen to equal A from Equation (3.4). The parameterization of the carrier over A_{d} is important in the extension to multiple axes introduced in Section 3.2, as each axis is demodulated by a carrier having a unique A_{d}. The carrier is given by

$$C(t, A_{\mathrm{d}}) = \exp\left[-\mathrm{j}A_{\mathrm{d}}\sin\left(2\pi f_{\mathrm{m}}\left[t - \frac{1}{2}\tau_{\mathrm{f}}(t)\right]\right)\right]. \tag{3.8}$$

where $\mathrm{j}^2 = -1$.

The carrier in Equation (3.8) uses $-\mathrm{j}$ rather than $+\mathrm{j}$. Suppose that when the OPD increases, the recovered phase changes by some amount, $\Delta\varphi$. When $-\mathrm{j}$ is used, the recovered phase *increases* by $\Delta\varphi$, and when $+\mathrm{j}$ is used, the recovered phase *decreases*

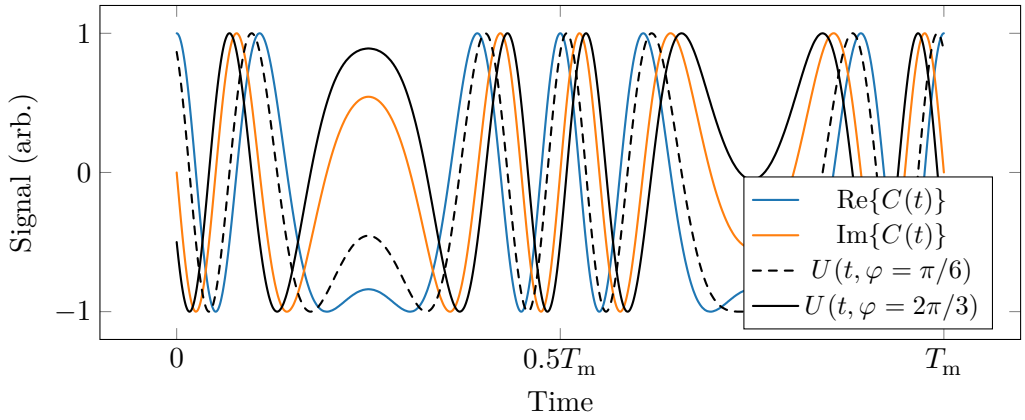

Figure 3.2: Demonstration of demodulation that highlights the selection of −j over +j in the carrier. When φ increases by $\pi/2$, it shifts the normalized signal, U, away from the real part of the carrier toward the imaginary part in the positive (anticlockwise) direction around the unit circle. The selection of −j in the carrier allows recovery a phase that increases with increasing OPD. When +j is used, a phase increase of $\pi/2$ shifts U the opposite direction, and the recovered phase decreases when the OPD increases.

by $\Delta\varphi$, thus, −j is chosen so that a positive change in OPD results in a positive change in phase after demodulation. This effect is illustrated in Figure 3.2, which shows how U moves along C from the dashed to solid black curve as the OPD dependent phase increases.

While U may be demodulated directly by C, a window function is used to reduce the baseband contribution of U and C to the demodulated signal. Following the work of Kissinger [185] and Kissinger et al. [166], a Gaussian window is selected with a frequency of $2f_\mathrm{m}$, given by

$$W(t, \sigma) = \sum_{m \in \mathbb{Z}} \exp\left[-\frac{1}{2\sigma^2} \left(\frac{t - \frac{1}{2}\tau_\mathrm{f}(t)}{T_\mathrm{m}} - \frac{m}{2} \right)^2 \right], \tag{3.9}$$

where σ is the window width expressed as the standard deviation and $\mathbb{Z}$ is the set of integers. The value $\sigma = 0.0225$ is used as recommended by Kissinger [185] and explored throughout Chapter 5. The window selects the highest frequency regions of U and C, which, for example, are the regions near 0, $T_\mathrm{m}/2$, and T_m, in Figure 3.2,

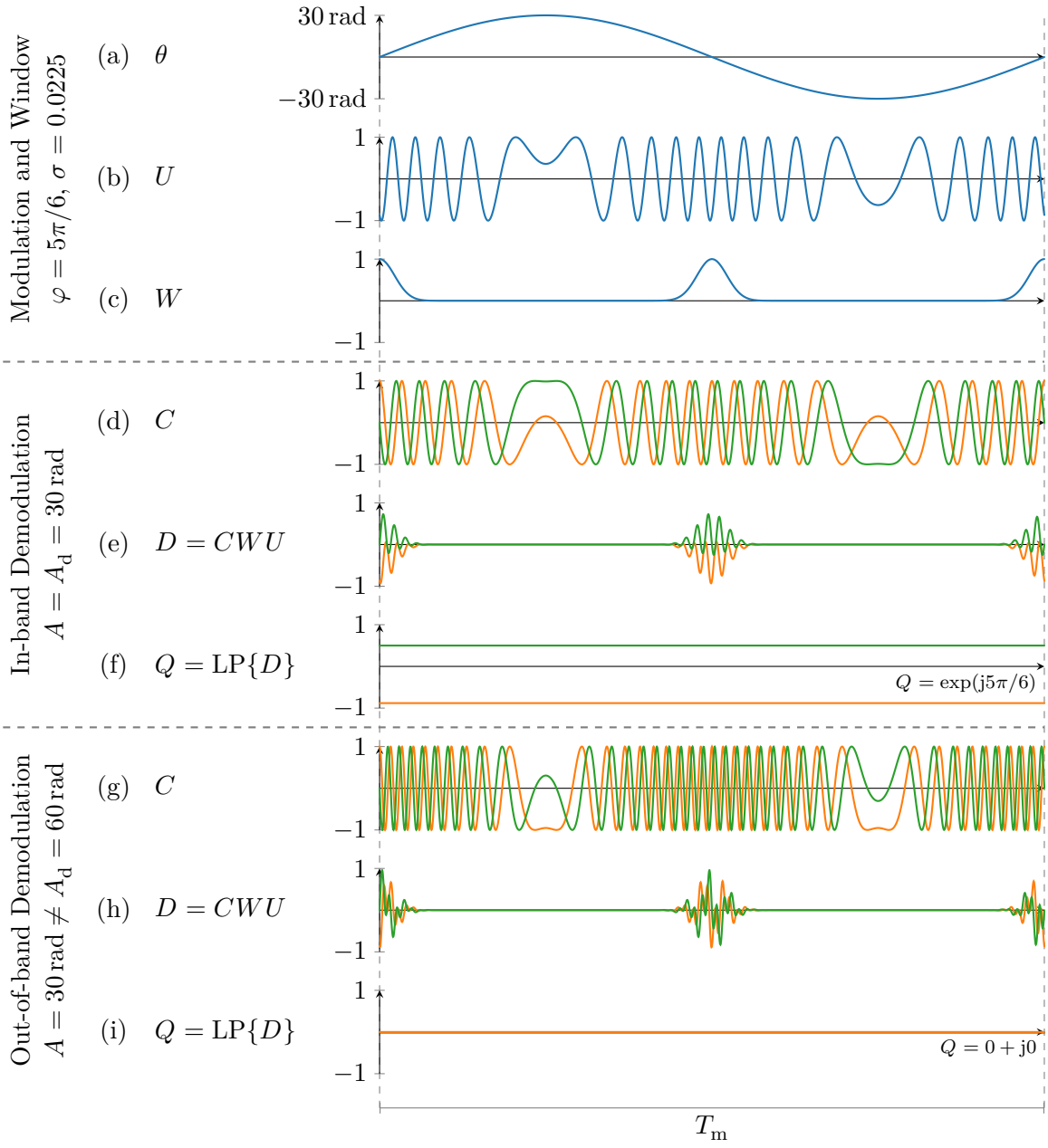

Figure 3.3: Simulation of modulation and both in and out-of-band demodulation over one modulation period for a single-axis interferometer with $\varphi = 5\pi/6$. In (a), phase modulation by $A = 30\,\mathrm{rad}$ is shown which produces the normalized signal in (b). The window function in (c) is used for demodulation. In-band demodulation where $A_\mathrm{d} = A$ is shown in (d), (e), and (f), while out-of-band demodulation where $A_\mathrm{d} = 60\,\mathrm{rad} \neq A$ is shown in (g), (h), and (i), The φ value is recovered as a quadrature signal for in-band demodulation in (f), and no quadrature signal is recoverable for out-of-band demodulation in (i). Plots (b) through (i) are shown with arbitrary vertical axis units; complex signals are plotted with the real in orange and imaginary in green.

where $T_{\mathrm{m}} = 1/f_{\mathrm{m}}$ is the modulation period. Although the Gaussian window was selected, other window functions are briefly explored in Section 3.3.3.

The normalized signal, carrier, and window from Equations (3.7) to (3.9), respectively, are multiplied to obtain a demodulated signal given by

$$D(t, \sigma, A_{\mathrm{d}}) = W(t, \sigma)C(t, A_{\mathrm{d}})U(t). \tag{3.10}$$

The baseband of the demodulated signal gives the *overlap* of U and C, which in turn, allows the OPD dependent phase to be recovered as a quadrature signal via low-pass filtering of D in Equation (3.10). Quadrature, Q, is given by

$$Q(t) = \mathrm{LP}\{D(t)\} = \exp[\mathrm{j}\varphi(t)], \tag{3.11}$$

and carries exclusively the OPD dependent phase term; LP denotes low-pass filtering. Figure 3.3 shows the simulated demodulation for in-band ($A_{\mathrm{d}} = A$) and out-of-band ($A_{\mathrm{d}} \neq A$) cases. The simulation illustrates the ability to simultaneously demodulate multiple axes discussed in Section 3.2. A carrier that is in-band for one axis recovers Q from Equation (3.11) and is out-of-band for the others. Out-of-band demodulation for other axes results in $Q = 0$ and contribute nothing to the quadrature signal resolved in-band.

Phase unwrapping of the quadrature signal in Equation (3.11) allows the optical displacement to be computed. Using the centre wavelength, $\lambda_{\mathrm{c}} = \mathrm{c}/\nu_{\mathrm{c}}$, the optical displacement is given by

$$\Delta\Lambda(t) = \frac{\lambda_{\mathrm{c}}}{2\pi}\varphi(t). \qquad [\mathrm{m}] \tag{3.12}$$

3.2 Multiaxis Interferometry

The simplified single-axis equations discussed in Section 3.1 set the framework to introduce the generalized multiaxis SFM model in this section. The multiaxis SFM

equations presented in this section form the model that is used for the rest of this thesis.

3.2.1 Multiaxis Layout

In Section 3.1, a single-axis interferometer was discussed where the number of axes, N, is 1, however, there is some ambiguity on what is meant by an N-axis interferometer when $N > 1$. The SFM approach concerns *demodulatable* axes, which are formed between any two non-identical optical paths through an interferometer. Consider the multiaxis interferometer depicted in Figure 3.4, having three optical paths: α reflects from the fibre tip reference; β traverses the round-trip of the cube beamsplitter and bottom prism retroreflector; and γ traverses the round-trip of the cube beamsplitter and right prism retroreflector. In the traditional sense, this interferometer has two axes, $\alpha\beta$ and $\alpha\gamma$, with respect to the reference at α; however, there are three *demodulatable* axes, $\alpha\beta$, $\alpha\gamma$, and $\beta\gamma$, which may be resolved.

As a generalization, all optical paths through an interferometer are members of a set S. Axes are pairwise combinations from S, thus, there are

$$N = \binom{|S|}{2} = \frac{|S|\big(|S|-1\big)}{2} \tag{3.13}$$

axes, where $|S|$ is the cardinality of S. The interferometer in Figure 3.4 is described by $S = \{\alpha, \beta, \gamma\}$, giving $N = 3$ demodulatable axes by Equation (3.13). It is not

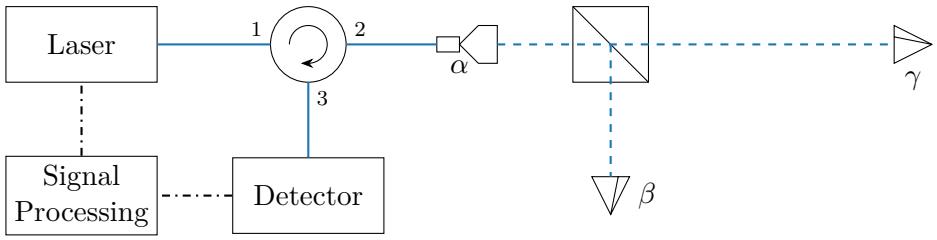

Figure 3.4: A three-axis interferometer constructed using the ∼4 % Fresnel reflection [10] from an FC/PC terminated fibre. Fresnel reflection from the beamsplitter cube is assumed negligible due to inefficiencies in the free space optics.

Table 3.1: Relationship between the size of S and the number of demodulatable axes in an interferometer. Since at least two paths are required to form an axis, N is zero for $|S| = 0$ and $|S| = 1$.

$\|S\|$	0	1	2	3	4	5	6	7	8	9	10
N	0	0	1	3	6	10	15	21	28	36	45

possible for an interferometer to be designed with an arbitrary number of axes, as only specific values of N exist; Table 3.1 shows the number of demodulatable axes for several values of $|S|$. The number of demodulatable axes increases rapidly as N grows quadratically with $|S|$. Growth in the number of axes poses an important design consideration, as one may find that large $|S|$ interferometers are polluted by axes that are not desired, and simply exist as artefacts of those that are.

3.2.2 Timing

Propagation of all signals contribute to phase delays and must be considered carefully. The single-axis equations presented earlier in Section 3.1 considered only the necessary time-of-flight delay, τ_{f}; however, there are several other time delays that are incurred along the signal path. These delays all come into effect at the time of demodulation, as the carrier must be timed to coincide with the interference signal. There are three significant instances in time which must be taken into consideration:

1. The base time, t, at which the signal processing system begins to modulate the laser.
2. The reference detection time, t', at which the first photons emitted from the laser due to modulation started at time t reach the detector. As there are multiple paths through an interferometer, t' is taken to be the time when the photons through the *shortest* optical path reach the detector.
3. The demodulation time, t'', at which the signal detected at t' is demodulated.

Figure 3.5 depicts a single-axis interferometer configuration that highlights where each delay is incurred:

- τ_{da} is the digital-to-analog delay in generating the modulation signal,
- τ_{mod} is the modulation delay for the optical frequency of the laser to respond to the modulation signal,
- $\tau_{\mathrm{del,out}}$ is the outgoing optical delivery delay from the laser to the interferometer delivery optics,
- $\tau_{\mathrm{del,bound}}$ is the round-trip optical delivery delay of the interferometer, from the boundary of the interferometer to the boundary of the nearest axis,
- $\tau_{\mathrm{f}}(t)$ is the round-trip time-of-flight delay of the axis OPD,
- $\tau_{\mathrm{del,in}}$ is the incoming optical delivery delay between the boundary of the interferometer delivery optics and the detector,
- τ_{det} is the detection delay,
- τ_{ad} is the delay of the analog-to-digital conversion in the signal processing electronics, and
- τ_{norm} is the signal processing delay of the normalization procedure up to the point that the signal is demodulated. Signal normalization is introduced in Section 3.2.6 and further developed in Chapters 4 and 5.

The delivery delays, $\tau_{\mathrm{del,out}}$, $\tau_{\mathrm{del,bound}}$, and $\tau_{\mathrm{del,in}}$, are defined in the most general terms possible so that the same definitions may be used in all interferometer configurations.

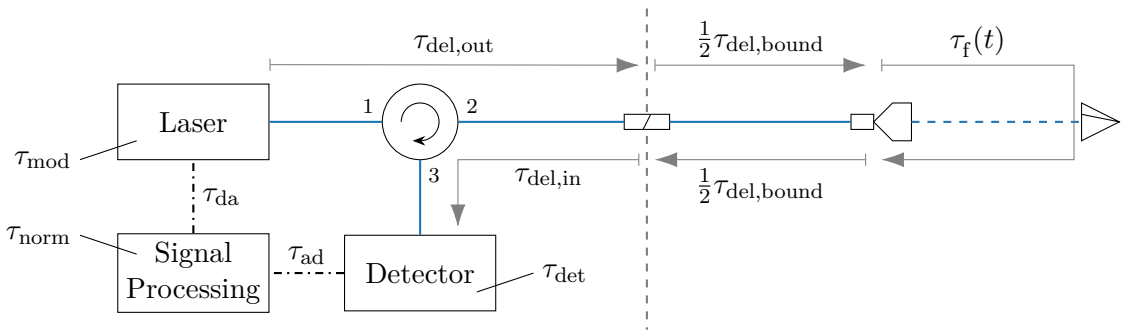

Figure 3.5: One possible single-axis interferometer configuration. The delays of the system are shown where they are incurred. $\tau_{\mathrm{del,bound}}$ is split into two, as for this particular interferometer, one half of the delay is incurred in each direction. The dashed gray line splits the signal processing and probing signal generation on the left from the interferometer optics on the right.

Although it is simpler to say that $\tau_{\text{del,out}}$, $\tau_{\text{del,bound}}$, and $\tau_{\text{del,in}}$ are the delays from the laser to a reference reflector and the reference reflector to the detector, respectively, this definition applies only to a subset of interferometer configurations, such as the single-axis Michelson interferometer [13] in Figure 3.5. The generalized definitions allow mapping the delays to other interferometer configurations, such as the Mach-Zehnder interferometer [10] in the fibre segment interferometry (FSI) experiment of Section 7.3. Figure 3.5 is split vertically by the dashed line isolating the signal processing on the left from the interferometer optics on the right. This distinction is important when discussing the implementation in Chapter 4, where the modulation and demodulation hardware on the left side is fixed and the reconfigurable interferometer optics on the right side varies with application.

Separation of the delivery delays allows them to be determined experimentally, which is discussed in Section 4.4. Using the above definitions, t' and t'' can be expressed as

$$t' = t - \tau_{\text{da}} - \tau_{\text{mod}} - \tau_{\text{del,out}} - \tau_{\text{del,bound}} - \tau_{\text{del,in}}, \quad \text{[s]} \tag{3.14a}$$

$$t'' = t - \tau_{\text{da}} - \tau_{\text{mod}} - \tau_{\text{del,out}} - \tau_{\text{del,bound}} - \tau_{\text{del,in}} - \tau_{\text{det}} - \tau_{\text{ad}} - \tau_{\text{norm}}. \quad \text{[s]} \tag{3.14b}$$

Note that τ_{f} is omitted from Equations (3.14a) and (3.14b) as t' and t'' concern only the *shortest* path through the interferometer, which by definition has a time-of-flight delay $\tau_{\text{f}} = 0$. In all equations that follow, τ_{f} is explicitly written, while the presence of any other delay is implied by t, t', and t''.

3.2.3 Modulation

In the extension to multiple axes, parameters are labeled using members from S. Optical paths in S are assigned letters from the Greek alphabet, such as α, β, γ, etc., while placeholder paths are denoted by English letters, having labels of a, b, c, and

so on. Although S has been called a set and is treated with set semantics throughout this analysis, the assignment of labels to the values in S have an implied order. The labels are assigned such that path α is shorter than path β, path β is shorter than path γ, and so on (i.e., the lexicographic ordering of the labels *increases* with optical path length). Several results depend on the difference of time-of-flight delays, and the implied ordering ensures that the time-of-flight differences that commonly arise (e.g., $\tau_{\mathrm{f},\beta} - \tau_{\mathrm{f},\alpha}$, $\tau_{\mathrm{f},b} - \tau_{\mathrm{f},a}$) are positive. Whether the labeling of S is ordered or not has little impact as out of order differences simply negate the phase difference, however, this ordering rule is upheld so that an increase in OPD for an axis is also an increase of its OPD dependent phase.

A laser, such as a semiconductor DFB LD, is modulated to produce a sinusoidal optical frequency of $\nu(t)$, given by Equation (3.1). The interference of two signals forming an axis, ab, is detected after the optical signal undergoes delays of $\tau_{\mathrm{f},a}(t')$ and $\tau_{\mathrm{f},b}(t')$ for the a and b paths, respectively. The interfering signals in ab have optical frequencies of

$$\nu_a(t') = \nu\big(t' - \tau_{\mathrm{f},a}(t')\big), \qquad \text{[Hz]} \ (3.15a)$$

$$\nu_b(t') = \nu\big(t' - \tau_{\mathrm{f},b}(t')\big). \qquad \text{[Hz]} \ (3.15b)$$

Note that t' is used rather than t, since the signals are examined at the time interference is detected, which occurs at t'. The signal frequencies from Equation (3.15) carry phases found via $2\pi \int \nu(t)\ \mathrm{d}t$ that are respectively given by

$$\phi_a(t') = \phi_0 + \frac{\nu_\mathrm{A}}{f_\mathrm{m}}\left[1 - \cos\Big(2\pi f_\mathrm{m}\big[t' - \tau_{\mathrm{f},a}(t')\big]\Big)\right] + 2\pi\nu_\mathrm{c}\big[t' - \tau_{\mathrm{f},a}(t')\big], \quad \text{[rad]} \ (3.16a)$$

$$\phi_b(t') = \phi_0 + \frac{\nu_\mathrm{A}}{f_\mathrm{m}}\left[1 - \cos\Big(2\pi f_\mathrm{m}\big[t' - \tau_{\mathrm{f},b}(t')\big]\Big)\right] + 2\pi\nu_\mathrm{c}\big[t' - \tau_{\mathrm{f},b}(t')\big]. \quad \text{[rad]} \ (3.16b)$$

The phase difference for each pair a and b in S contributes a component $\Delta\phi_{ab} = \phi_a - \phi_b$ to the interference signal, where ϕ_a and ϕ_b are given by Equation (3.16). Using the simplification in Appendix A.1, $\Delta\phi_{ab}$ may be written as

$$\Delta\phi_{ab}(t') = \underbrace{\underbrace{\frac{2\nu_{\mathrm{A}}}{f_{\mathrm{m}}}\sin\Big(\pi f_{\mathrm{m}}\big[\tau_{\mathrm{f},b}(t') - \tau_{\mathrm{f},a}(t')\big]\Big)}_{A_{ab}(t')}\sin\left(2\pi f_{\mathrm{m}}\left[t' - \frac{1}{2}\big[\tau_{\mathrm{f},b}(t') + \tau_{\mathrm{f},a}(t')\big]\right]\right)}_{\theta_{ab}(t')} + \underbrace{2\pi\nu_{\mathrm{c}}\big[\tau_{\mathrm{f},b}(t') - \tau_{\mathrm{f},a}(t')\big]}_{\varphi_{ab}(t')}. \qquad \text{[rad]} \quad (3.17)$$

The phase modulation amplitude, $A_{ab}(t')$, is the angular disturbance of the ab axis due to modulation of the laser. Although expressed in terms of $\tau_{\mathrm{f},a}$ and $\tau_{\mathrm{f},b}$ in Equation (3.17), A_{ab} can also be written as a function of the OPD,

$$A_{ab}(t') = \frac{2\nu_{\mathrm{A}}}{f_{\mathrm{m}}}\sin\left(\frac{\pi f_{\mathrm{m}}\Lambda_{ab}(t')}{\mathrm{c}}\right), \qquad \text{[rad]} \quad (3.18)$$

where $\Lambda_{ab}(t') = \mathrm{c}[\tau_{\mathrm{f},b}(t') - \tau_{\mathrm{f},a}(t')]$ is the OPD of the ab axis. The modulation amplitude is time dependent as the OPD may change, but when the OPD does not deviate far from its central value, Equation (3.18) can be approximated as

$$A_{ab} \approx \frac{2\pi\nu_{\mathrm{A}}\Lambda_{\mathrm{c},ab}}{\mathrm{c}} \quad \text{when} \quad \Lambda_{\mathrm{c},ab} \ll \frac{c}{\pi f_{\mathrm{m}}}, \qquad \text{[rad]} \quad (3.19)$$

where $\Lambda_{\mathrm{c},ab} = (\max\Lambda_{\mathrm{c},ab} + \min\Lambda_{\mathrm{c},ab})/2$ is the central OPD between the limits of travel. The result in Equation (3.19) shows that the modulation frequency has a negligible effect on the phase modulation amplitude and that A_{ab} is dictated by ν_{A} and $\Lambda_{\mathrm{c},ab}$.

While A_{ab} gives the phase modulation amplitude, the overall phase modulation due to the frequency modulation of the laser is given by

$$\theta_{ab}(t') = A_{ab}(t') \sin\left(2\pi f_{\mathrm{m}}\left[t' - \frac{1}{2}\big[\tau_{\mathrm{f},b}(t') + \tau_{\mathrm{f},a}(t')\big]\right]\right). \qquad \text{[rad]} \ (3.20)$$

The OPD of the interferometer contributes a phase component proportional to the displacement in optical path, which is ultimately the phase component recovered in the demodulation step. The OPD dependent phase is given by

$$\varphi_{ab}(t') = 2\pi\nu_{\mathrm{c}}\big[\tau_{\mathrm{f},b}(t') - \tau_{\mathrm{f},a}(t')\big] = \frac{2\pi\nu_{\mathrm{c}}\Lambda_{ab}(t')}{\mathrm{c}}. \qquad \text{[rad]} \ (3.21)$$

Equation (3.17) can be expressed in terms of Equations (3.20) and (3.21) to obtain a short form of the phase difference,

$$\Delta\phi_{ab}(t') = \theta_{ab}(t') + \varphi_{ab}(t'), \qquad \text{[rad]} \ (3.22)$$

that bears similarity to the single-axis phase difference shown in Equation (3.6). Overall, the equations in this section are nearly identical to the single-axis equations Section 3.1.1 with a and b subscripts introduced. One obtains the single-axis equations by choosing $S = \{\alpha, \beta\}$ and realizing that $\tau_{\mathrm{f},\alpha} = 0$ as it is the reference. The theme of the single-axis equations bearing close resemblance to the path annotated multiaxis equations holds for the rest of the section.

3.2.4 Beat Frequency

A beat frequency, $f_{\mathrm{b},ab}(t') = \nu_a(t') - \nu_b(t')$, is observed at the detector for the ab axis due to the interference of heterodyne signals carrying frequencies ν_a and ν_b. Although the beat frequency is an important quantity that arises in Section 3.3, it is not of particular use in the time domain modulation and demodulation equations — nonetheless, the beat frequency is presented here as it is the next step along the

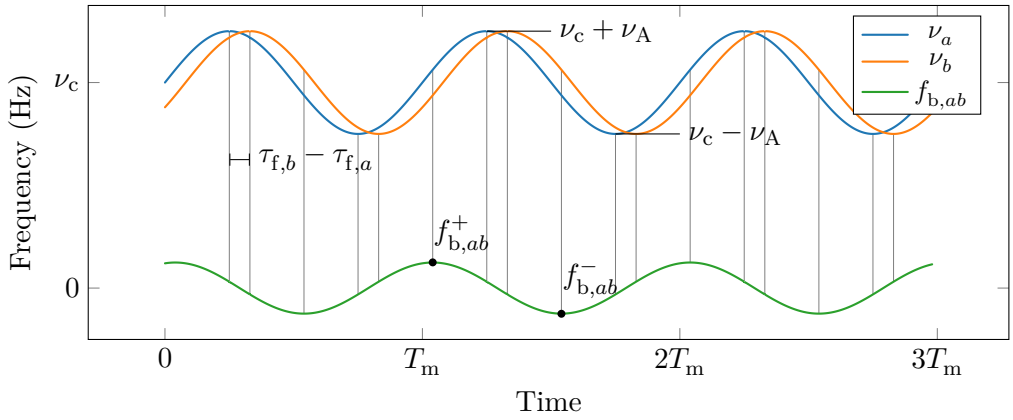

Figure 3.6: Beat frequency of two interfering sinusoidal SFM signals separated by a constant time-of-flight delay. Before demodulation, the Gaussian kernels of the window function are centred on the extrema in the beat frequency to select parts of the signal around $f^+_{b,ab}$ and $f^-_{b,ab}$.

signal path. A derivation of the beat frequency is presented in greater detail in Appendix A.2, and f_b is given by

$$f_{b,ab}(t') = A_{ab}(t') f_m \cos\left[2\pi f_m \left(t' - \frac{1}{2}\left[\tau_{f,b}(t') + \tau_{f,a}(t')\right]\right)\right]. \quad \text{[Hz]} \quad (3.23)$$

The beat frequency of Equation (3.23) is plotted in Figure 3.6 for two interfering signals carrying different time-of-flight delays. It can be seen that the largest positive beat frequency occurs when both ν_a and ν_b are increasing together, for example, near T_m; the largest negative beat frequency occurs when both ν_a and ν_b are decreasing together, for example, near $3T_m/2$.

Of particular interest are the maxima and minima of f_b, denoted by f_b^+ and f_b^-, respectively. Their exact values are found in Equation (A.17) and given by $f_b^+(t') = A_{ab}(t') f_m$ and $f_b^-(t') = -A_{ab}(t') f_m$, but may be approximated by

$$f^+_{b,ab} = -f^-_{b,ab} \approx \frac{2\pi \nu_A f_m \Lambda_{c,ab}}{c} = A_{ab} f_m \quad \text{when} \quad \Lambda_{c,ab} \ll \frac{c}{\pi f_m}, \quad \text{[Hz]} \quad (3.24)$$

which requires the same condition on $\Lambda_{c,ab}$ as the approximation of A_{ab} in Equation (3.19). Although the beat frequency is not used in the derivation or application

of the demodulation procedure, the form $f_{\mathrm{b}}^{+} = Af_{\mathrm{m}}$ from Equation (3.24) emerges in the frequency domain analysis presented in Section 3.3 and comparison against other (non-sinusoidal) modulation profiles in Section 3.5.

3.2.5 Intensity

For a single-axis interferometer with $S = \{\alpha, \beta\}$, the intensity at the detector is given by the two-beam interference equation [10]

$$I(t') = I_0(t') + I_{\alpha\beta}(t') \cos \Delta\phi(t'), \qquad [\mathrm{W/m^2}] \ (3.25)$$

where $I_0 = I_\alpha + I_\beta$ is the offset intensity $I_{\alpha\beta} = 2\sqrt{I_\alpha I_\beta}$ is the interference term, and I_α and I_β are the intensities of the two individual beams. It is assumed that the light is quasimonochomatic and that the coherence length of the laser is much greater than any paths through the interferometer. The specifications of the selected laser can be found in Table C.5, and the coherence length is $\sim$3 km [10, 186]. For a multiaxis interferometer, it is shown in Appendix A.3 that the intensity at the detector is

$$I(t') = I_0(t') + \sum_{\{a,b\} \subseteq S} I_{ab}(t') \cos \Delta\phi_{ab}(t'), \qquad [\mathrm{W/m^2}] \ (3.26)$$

where $I_0 = \sum_{a \in S} I_a$ and I_{ab} is the interference term for the ab axis. The summation is taken over pairwise *combinations* of paths through the interferometer, which is mathematically expressed as $\{a, b\} \subseteq S$. The set of combinations contains all axes, and thus has cardinality N from Equation (3.13). When $N = 2$, the multiaxis intensity in Equation (3.26) devolves into the single-axis case in Equation (3.25).

An optical power, $P(t')$, is collected by the detector. The power takes an analogous form to Equation (3.26), given by

$$P(t') = P_0(t') + \sum_{\{a,b\} \subseteq S} P_{ab}(t') \cos \Delta\phi_{ab}(t'), \qquad [\mathrm{W}] \ (3.27)$$

where P_0 captures the offset power due to the first sum of Equation (3.26) and P_{ab} is the power due to each interference term I_{ab} in the second sum.

3.2.6 Demodulation

Bias current modulation of a LD results in modulation of both optical frequency *and* power [187]. A photodetector and amplification circuitry produce a voltage proportional to the incident optical power, and the detector voltage is sampled and normalized in signal processing to remove its change in power due the modulation of the laser. At the time of demodulation, the normalized signal ideally takes the form of

$$U(t'') = \sum_{\{a,b\}\subseteq S} \eta_{ab} \cos \Delta\phi_{ab}(t''), \tag{3.28}$$

where η_{ab} is the normalized signal contribution arising from P_{ab} in Equation (3.27) and t'' is the demodulation time from Equation (3.14b). Each η value contributes a fraction of the total signal power, and are thus

$$\eta_{ab} = \frac{\left\langle P_{ab}(t'')\right\rangle}{\sum_{\{c,d\}\subseteq S}\left\langle P_{cd}(t'')\right\rangle}, \tag{3.29}$$

where $\langle \ldots \rangle$ denotes a time averaged value. This normalization strategy ensures that $|\max(U)| \leq 1$. The normalization procedure is an implementation detail discussed in Section 4.5.1; for this chapter, the ideal normalized signal described Equations (3.28) and (3.29) is used to discuss the demodulation procedure.

Equation (3.22) shows that $\Delta\phi_{ab}$ is composed of two phase components: θ_{ab} and φ_{ab}. The former is due primarily to the modulation of the laser and the latter is dictated by the OPD, thus θ_{ab} is the carrier phase and φ_{ab} is the baseband phase.

The normalized signal is demodulated using a complex carrier given by

$$C_{ab}(t'', A_\mathrm{d}) = \exp\left[-\mathrm{j}A_\mathrm{d}\sin\left(2\pi f_\mathrm{m}\left[t'' - \frac{1}{2}\left[\tau_{\mathrm{f},b}(t'') + \tau_{\mathrm{f},a}(t'')\right]\right]\right)\right] \tag{3.30}$$

where A_d is the demodulation amplitude. The carrier has a phase term that bears resemblance to θ_{ab} from Equation (3.20), but with A_{ab} replaced by A_d. A selection of A_d is made so that the phase of C_{ab} approximates θ_{ab} and *in-band* demodulation may extract φ_{ab}. When $A_\mathrm{d} \neq A_{ab}$, the demodulation is *out-of-band*, and the phase cannot be recovered. There is not a single point where the demodulation goes out-of-band, but rather a gradual decrease in the ability to extract φ_{ab}, which is explored throughout Chapter 5. When all axes have unique A values, an arbitrary axis may be demodulated simply through the selection of A_d in Equation (3.30). It is this property that enables simultaneous multiaxis displacement measurements.

Since the recovered phase, φ_{ab}, is the baseband component of U, a windowing function is applied before demodulation to eliminate baseband contributions from the low frequency regions of U itself, which are the regions of the signal near $T_\mathrm{m}/4$ and $3T_\mathrm{m}/4$ in Figure 3.2. Following Kissinger [185], a Gaussian window was selected having the form

$$W_{ab}(t'', \sigma) = \sum_{m\in\mathbb{Z}} \exp\left[-\frac{1}{2\sigma^2}\left(\frac{t'' - \frac{1}{2}[\tau_{\mathrm{f},b}(t'') + \tau_{\mathrm{f},a}(t'')]}{T_\mathrm{m}} - \frac{m}{2}\right)^2\right], \tag{3.31}$$

where the window width expressed as standard deviation of a Gaussian distribution is $\sigma = 0.0225$. This σ value is used at the recommendation of Kissinger [185] and its consequences are explored throughout Chapter 5; some alternative window functions are briefly discussed in Section 3.3.3. Like Equation (3.30), W is a function of t'' from Equation (3.14b), because U, C, and W must have like phases at the time of demodulation, which occurs at t''.

In practice, the $\frac{1}{2}(\tau_{\mathrm{f},b}+\tau_{\mathrm{f},a})$ term in Equations (3.28), (3.30) and (3.31) is negligible when $\frac{1}{2}(\tau_{\mathrm{f},b}+\tau_{\mathrm{f},a}) \ll T_{\mathrm{m}}$. Under this assumption, the approximation $t'' \approx t'' - \frac{1}{2}(\tau_{\mathrm{f},b} + \tau_{\mathrm{f},a})$ can be made. In the implementation of a multiaxis interferometer, acceptable performance can be achieved using the central demodulation time,

$$t''_{\mathrm{c}} = t'' - \frac{1}{2}\underbrace{\Big[\max\big\{\tau_{\mathrm{f},b} \;\big|\; b \in S\big\} + \min\big\{\tau_{\mathrm{f},a} \;\big|\; a \in S\big\}\Big]}_{\text{Central time-of-flight delay}} \approx t'', \qquad \text{[s]} \tag{3.32}$$

which takes into consideration the delays of all axes. When the time-of-flight delays for every axis are much less than T_{m}, the envelopes of the beat frequencies, f_{b}^{+} and f_{b}^{-}, occur near each other in time for each axis, and application $W(t''_{\mathrm{c}})C(t''_{\mathrm{c}})$ selects and demodulates the signal around each beat frequency extrema. Using the single t''_{c} rather than $t'' - \frac{1}{2}(\tau_{\mathrm{f},b}+\tau_{\mathrm{f},a})$ for each axis simplifies signal processing and provides acceptable performance with negligible effects on timing, as the times t''_{c} and $t'' - \frac{1}{2}(\tau_{\mathrm{f},b} + \tau_{\mathrm{f},a})$ typically differ on the order of a single sampling interval of the signal processing system for small OPDs. The remaining demodulation equations are presented in terms of t'' to preserve generality.

The demodulated signal, D, is computed from Equations (3.28), (3.30) and (3.31) as

$$D_{ab}(t'', \sigma, A_{\mathrm{d}}) = W_{ab}(t'', \sigma)C_{ab}(t'', A_{\mathrm{d}})U(t''), \tag{3.33}$$

which is a complex signal carrying the phase φ_{ab} as quadrature in its baseband. The quadrature signal, Q, is recovered by low-pass filtering Equation (3.33), giving

$$Q_{ab}(t'') = \mathrm{LP}\big\{D_{ab}(t'', \sigma, A_{\mathrm{d}})\big\} = \exp\big[\mathrm{j}\varphi_{ab}(t'')\big]. \tag{3.34}$$

In practice, there is some crosstalk between axes where signal power from two or more axes are present in the demodulated baseband. In a multiaxis interferometer, *ab* and *cd* axes are not individually demodulatable when the time-of-flight differences

for ab and cd are similar. When $\tau_{\mathrm{f},b} - \tau_{\mathrm{f},a} \approx \tau_{\mathrm{f},d} - \tau_{\mathrm{f},c}$, and thus $\Lambda_{ab} \approx \Lambda_{cd}$ and $A_{ab} \approx A_{cd}$, crosstalk is present between the ab and cd axes as their frequency bands overlap. Strategies for band placement are discussed in Section 3.4, while an analysis of crosstalk itself is presented in Section 5.3.

The OPD dependent phase of Equation (3.34) can be unwrapped to obtain φ_{ab} using a technique such as the one presented in Section 4.5.3. The optical displacement is

$$\begin{aligned}\Delta\Lambda_{ab}(t'') &= \frac{\lambda_{\mathrm{c}}}{2\pi}\varphi_{ab}\left(t - \tau_{\mathrm{da}} - \tau_{\mathrm{mod}} - \tau_{\mathrm{del,out}} - \tau_{\mathrm{del,bound}} - \frac{1}{2}\left[\tau_{\mathrm{f},b}(t'') + \tau_{\mathrm{f},a}(t'')\right]\right) \\ &= \frac{\lambda_{\mathrm{c}}}{2\pi}\varphi_{ab}\left(t'' - \frac{1}{2}\left[\tau_{\mathrm{f},b}(t'') + \tau_{\mathrm{f},a}(t'')\right] + \underbrace{\tau_{\mathrm{del,in}} + \tau_{\mathrm{det}} + \tau_{\mathrm{ad}} + \tau_{\mathrm{norm}}}_{\tau_{\mathrm{meas}}}\right) \\ &\approx \frac{\lambda_{\mathrm{c}}}{2\pi}\varphi_{ab}(t'' + \tau_{\mathrm{meas}}),\end{aligned} \qquad \text{[m]} \quad (3.35)$$

where τ_{meas} represents the measurement delay due to the return path and signal processing.

The modulation frequency and wavelength impose a maximum velocity in optical path. Phase changes larger than $\pm\pi$ cannot be unwrapped, and a minimum of two quadrature points is required to represent a change in optical path corresponding to a displacement of λ_{c}, giving a maximum velocity in optical path of

$$v_{\mathrm{opt,max}} = \frac{1}{2}\lambda_{\mathrm{c}} f_{\mathrm{m}}. \qquad \text{[m/s]} \quad (3.36)$$

3.3 Frequency Domain Analysis

While an implementation of the SFM technique uses the time domain equations from Section 3.2, the frequency domain provides details that aid in understanding the performance and selecting demodulation parameters. The jump from a single-axis to three-axis interferometer is the largest complication in the theory, and without loss of generality, analysis of the three-axis interferometer shown in Figure 3.7 is sufficient

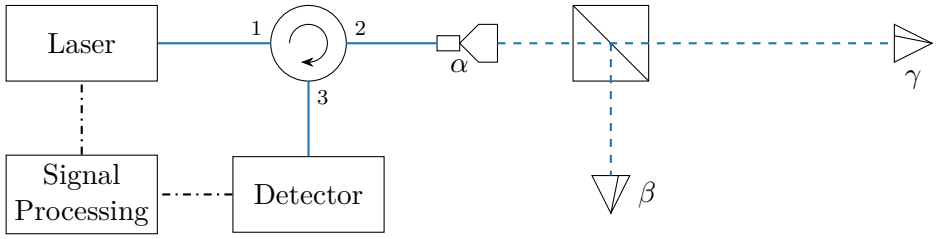

Parameter	Value
ν_c	193 THz
ν_A	3 GHz
f_m	25 kHz

Axis	Λ (cm)	A (rad)
$\alpha\beta$	67	42
$\alpha\gamma$	231	145
$\beta\gamma$	164	103

Figure 3.7: A three-axis interferometer constructed using the ∼4 % Fresnel reflection [10] from an FC/PC terminated fibre. Fresnel reflection from the beamsplitter cube is assumed negligible due to inefficiencies in the free space optics. The interferometer design and tabulated parameters are used in all examples provided in this section.

to generalize to any number of axes. Examples presented in this section use the three-axis interferometer design and parameters in Figure 3.7.

The interferometer in Figure 3.7 has three labeled axes: $\alpha\beta$, $\alpha\gamma$, and $\beta\gamma$, and are analyzed in terms of the phase modulation amplitudes, The OPDs of the axes are $\Lambda_{\alpha\beta}$, $\Lambda_{\alpha\gamma}$, and $\Lambda_{\beta\gamma}$. There is some redundancy, as the OPDs bear the relationship $\Lambda_{\beta\gamma} = \Lambda_{\alpha\gamma} - \Lambda_{\alpha\beta}$, and thus the phase modulation amplitudes exhibit an analogous relationship $A_{\beta\gamma} = A_{\alpha\gamma} - A_{\alpha\beta}$.

3.3.1 Windowing

The signal bandwidth after windowing can be used to inform the selection of OPDs for a multiaxis interferometer. In Appendix A.4.1, an exact solution to the power spectrum of the windowed interference signal is derived, which is the magnitude

squared of the WU Fourier transform, F_{WU}, given by

$$F_{WU}(f) = \frac{\sqrt{2\pi}\sigma}{f_{\mathrm{m}}} \sum_{\{a,b\}\subseteq S} \sum_{m\in\mathbb{Z}} \eta_{ab} \Bigg[\sum_{\substack{n\in\mathbb{Z} \\ \text{even}}} \cos(\varphi_{ab}) J_{|n|}(A_{ab}) \exp\left(-\frac{2\pi^2\sigma^2}{f_{\mathrm{m}}^2}[f - nf_{\mathrm{m}}]^2\right) \exp\left(-\frac{\mathrm{j}m\pi}{f_{\mathrm{m}}}[f - nf_{\mathrm{m}}]\right) + \mathrm{j} \sum_{\substack{n\in\mathbb{Z} \\ \text{odd}}} \mathrm{sgn}(n) \sin(\varphi_{ab}) J_{|n|}(A_{ab}) \exp\left(-\frac{2\pi^2\sigma^2}{f_{\mathrm{m}}^2}[f - nf_{\mathrm{m}}]^2\right) \exp\left(-\frac{\mathrm{j}m\pi}{f_{\mathrm{m}}}[f - nf_{\mathrm{m}}]\right) \Bigg], \tag{3.37}$$

where J_n is the order n Bessel function of the first kind, sgn is the signum function, and $\tau_{\mathrm{f},a}$, $\tau_{\mathrm{f},b}$, and φ_{ab} are constant for all $\{a, b\}$ in S. For the purposes of this analysis, Equation (3.37) is not easy to work with, and instead, an approximation of the power spectrum envelope is determined. From the procedure in Appendix A.4.2, the windowed power spectrum, $|\mathcal{F}\{WU\}(f)|^2$, may be approximated by

$$P_{WU}(f) \approx \frac{2\pi\sigma^2}{f_{\mathrm{m}}^2} \sum_{\{a,b\}\subseteq S} \eta_{ab}^2 \Bigg[\exp\left(-\frac{4\pi^2\sigma^2}{f_{\mathrm{m}}^2}[f - A_{ab}f_{\mathrm{m}}]^2\right) + \exp\left(-\frac{4\pi^2\sigma^2}{f_{\mathrm{m}}^2}[f + A_{ab}f_{\mathrm{m}}]^2\right) \Bigg]. \tag{3.38}$$

where f is the spectral frequency. The approximation is valid when $\sigma \ll 1$, as explained in Appendix A.4. Time domain representations of a normalized interference signal and window are shown in Figure 3.8a, and their power spectra in Figure 3.8b. Table 3.2 shows the locations of the numbered peaks in Figure 3.8b. The peak locations correspond to the maximum beat frequencies, f_{b}^+ and f_{b}^-, for each axis. When the modulation property of the Fourier transform was employed in the derivation of Equation (3.38), the Gaussian was modulated by a cosine carrying a frequency of $A_{ab}f_{\mathrm{m}} = f_{\mathrm{b},ab}^+$, which results in the centring of Gaussian peaks about each beat frequency. It should be noted that Equations (3.37) and (3.38) have different scaling

Table 3.2: Peaks of the windowed signal in Figure 3.8b. For clarity, the ± symbols are omitted from each value.

Number	Amplitude (rad)	Frequency
3	$A_{\alpha\beta} = 42$	$A_{\alpha\beta} f_{\mathrm{m}}$
2	$A_{\beta\gamma} = 103$	$A_{\beta\gamma} f_{\mathrm{m}}$
1	$A_{\alpha\gamma} = 145$	$A_{\alpha\gamma} f_{\mathrm{m}}$

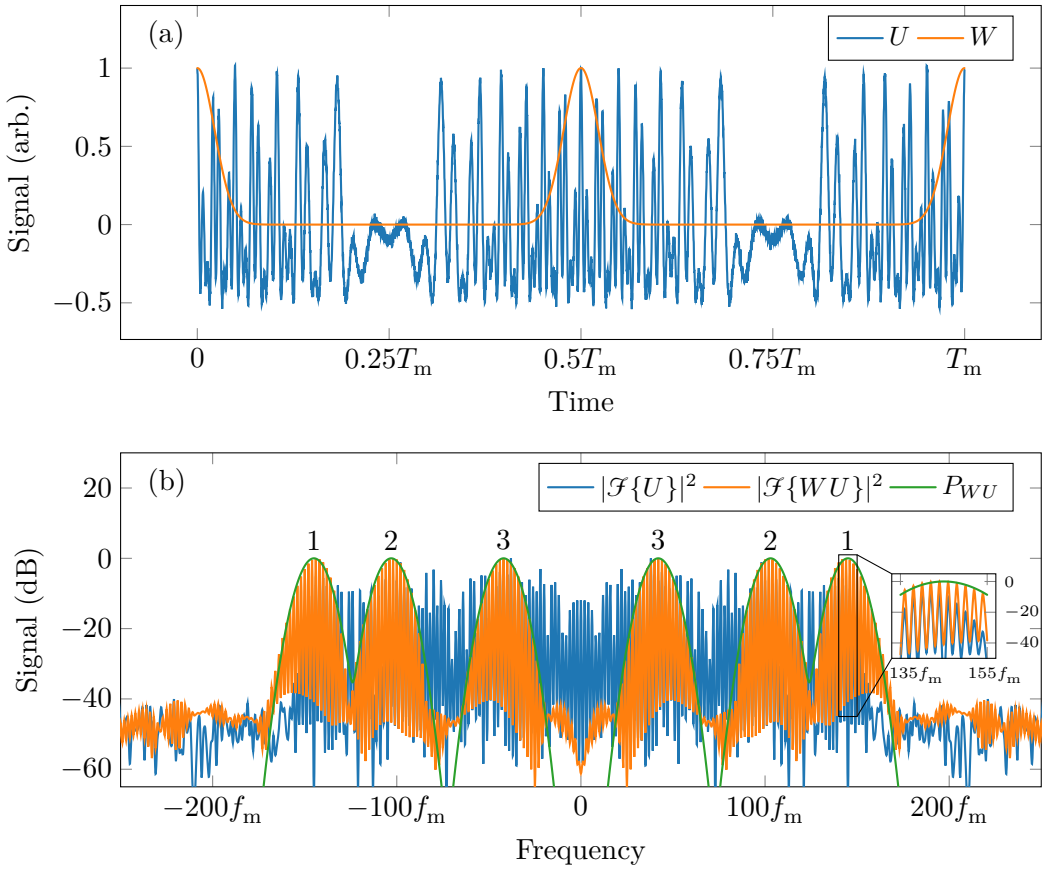

Figure 3.8: The normalized interference signal from a three-axis interferometer in Figure 3.7 is shown in (a) and its power spectrum in (b). The simulated windowed power spectrum $|\mathcal{F}\{WU\}|^2$ uses the complete windowed signal, WU, over one modulation period, while the approximation of the P_{WU} signal is computed using W_1 in F_{WU} from Equation (A.39). The three distinct numbered peaks correspond to the phase carriers in each axis and are summarized in Table 3.2. Gaussian random noise was added to the normalized interference signal to achieve a signal-to-noise ratio of 1000 which is representative of interferometers discussed in Chapter 7.

factors, but when plotted on a normalized scale (as are all power spectra plots in this thesis), Equation (3.38) approximates the envelope in Equation (3.37).

The Gaussian components of Equation (3.38) have a width, expressed as standard deviation, σ_{p}, dictated by the modulation frequency and inversely proportional to the window width in the time domain, given by

$$\sigma_{\mathrm{p}} = \frac{f_{\mathrm{m}}}{2\sqrt{2}\pi\sigma}. \tag{3.39}$$

The bandwidth, Δf, is the width of the signal in the frequency domain and is defined via Equations (3.38) and (3.39). As the frequency deviates from the mean value of one of the Gaussian components centred at $\pm A_{ab} f_{\mathrm{m}}$, or alternatively, $f^{+}_{\mathrm{b},ab}$ and $f^{-}_{\mathrm{b},ab}$, the bandwidth is taken to be the width of the Gaussian function at that point. It should be noted that this width is neither standard deviation, full width at half maximum (FWHM), nor any other well-defined metric. The bandwidth is defined generally in terms of an acceptable choice of band separation coefficient, w, in

$$\Delta f = 2w\sigma_{\mathrm{p}} = \frac{w f_{\mathrm{m}}}{\sqrt{2}\pi\sigma}. \quad \text{[Hz]} \tag{3.40}$$

What defines an *acceptable* choice of w is rather subjective, however, the selection $w = 2.5$ is recommended based on the discussion in Section 5.3. An acceptable choice of w is one for which the band centred at $A_{ab} f_{\mathrm{m}}$ does not overlap with any other bands over the bandwidth given by Equation (3.40). This is a key design driver for a multiaxis interferometer which dictates the minimum separation between the constituent OPDs of a multiaxis interferometer based on the choice of w.

The bandwidth dictates ΔA_{min}, the minimum allowed interferometer phase modulation amplitude *and* the minimum phase modulation amplitude separation between interferometer axes, such that the signal can be demodulated. The first demodulatable band must occur well away from the baseband of the signal, at least $\Delta f = \Delta A_{\mathrm{min}} f_{\mathrm{m}}$

away, thus, the minimum modulation amplitude is

$$\Delta A_{\min} = \frac{\Delta f}{f_{\mathrm{m}}} = \frac{2w\sigma_{\mathrm{p}}}{f_{\mathrm{m}}} = \frac{w}{\sqrt{2}\pi\sigma}. \qquad \text{[rad]} \ (3.41)$$

In an interferometer implementation, it is useful to consider the mechanical constraints on the interferometer, thus a minimum demodulatable OPD, $\Delta\Lambda_{\min}$, is generally more useful than the minimum modulation amplitude. In addition to the minimum demodulatable OPD, $\Delta\Lambda_{\min}$ also describes the minimum OPD separation between axes. Letting A equal $\Delta A_{\min}$ in Equations (3.19) and (3.41), the minimum demodulatable OPD is

$$\Delta\Lambda_{\min} \approx \frac{w\mathrm{c}}{2\sqrt{2}\pi^2\nu_{\mathrm{A}}\sigma} \quad \text{when} \quad \Lambda \ll \frac{c}{\pi f_{\mathrm{m}}}. \qquad \text{[m]} \ (3.42)$$

The result in Equation (3.42) drives the selection of OPDs when constructing an interferometer. For all a, b, c, and d in S, the following conditions must hold for *every* OPD to be demodulatable:

1. Minimum OPD: $\Lambda_{ab} \geq \Delta\Lambda_{\min}$,
2. Minimum OPD separation: $|\Lambda_{ab} - \Lambda_{cd}| \geq \Delta\Lambda_{\min}$.

The same conditions may also be written for A and $\Delta A_{\min}$, but are redundant. These conditions must hold for *every* axis to be demodulatable — a property which is referred to as *total demodulatability*. Some applications may not require that all axes be demodulatable, as it may be impractical in cases where $|S|$, and thus N, are large. In such cases, *partial demodulatability* may be favourable. Both total and partial demodulatability are discussed in Section 3.4.

3.3.2 Demodulation

To analyze the demodulated signal, $D(t'', \sigma, A_{\mathrm{d}})$, an approximation of $\mathcal{F}\{D\}(f)$ and power spectrum is established in a similar fashion to Equations (3.38), (A.41)

and (A.42). Although an exact solution for the demodulated power spectrum could be derived following a similar procedure to the one presented in Appendix A.4.1 for the exact windowed spectrum in Equation (3.37), that is not required for this analysis, and the approximation is instead adopted. As shown in Appendix A.5, when $A_{ab} - A_\mathrm{d}$ and $A_{ab} + A_\mathrm{d}$ are unique for all a and b in S and the Gaussian peaks in the demodulated signal are sufficiently spaced, the demodulated power spectrum may be approximated as

$$\begin{aligned} P_D(f, A_\mathrm{d}) \approx & \frac{2\pi\sigma^2}{f_\mathrm{m}^2} \sum_{\{a,b\}\subseteq S} \eta_{ab}^2 \exp\left[-\frac{4\pi^2\sigma^2}{f_\mathrm{m}^2}\big(f - [A_{ab} + A_\mathrm{d}]f_\mathrm{m}\big)^2\right] \\ & + \frac{2\pi\sigma^2}{f_\mathrm{m}^2} \sum_{\substack{\{a,b\}\subseteq S \\ A_{ab}\not\approx A_\mathrm{d}}} \eta_{ab}^2 \exp\left[-\frac{4\pi^2\sigma^2}{f_\mathrm{m}^2}\big(f - [A_{ab} - A_\mathrm{d}]f_\mathrm{m}\big)^2\right] \\ & + \frac{2\pi\sigma^2}{f_\mathrm{m}^2} \sum_{\substack{\{a,b\}\subseteq S \\ A_{ab}\not\approx A_\mathrm{d}}} \eta_{ab}^2 \exp\left[-\frac{4\pi^2\sigma^2}{f_\mathrm{m}^2}\big(f + [A_{ab} - A_\mathrm{d}]f_\mathrm{m}\big)^2\right] \\ & + \frac{2\pi\sigma^2}{f_\mathrm{m}^2} \sum_{\{a,b\}\subseteq S} \eta_{ab}^2 \exp\left[-\frac{4\pi^2\sigma^2}{f_\mathrm{m}^2}\big(f + [A_{ab} + A_\mathrm{d}]f_\mathrm{m}\big)^2\right] \\ & + \frac{8\pi\sigma^2}{f_\mathrm{m}^2} \sum_{\substack{\{a,b\}\subseteq S \\ A_{ab}\approx A_\mathrm{d}}} \eta_{ab}^2 \exp\left[-\frac{4\pi^2\sigma^2}{f_\mathrm{m}^2} f^2\right], \end{aligned} \tag{3.43}$$

where the summation conditions of $A_{ab} \approx A_\mathrm{d}$ and $A_{ab} \not\approx A_\mathrm{d}$ denote in-band and out-of-band demodulation, respectively. The limits of the second and third summations filter out those cases where $A_{ab} \approx A_\mathrm{d}$, and these cases are deferred to the fifth summation that represents the signal baseband. Like Equation (3.38), the approximation is valid when $\sigma \ll 1$, as explained in Appendix A.5. When demodulation is in-band for the ab axis, $A_{ab} - A_\mathrm{d} \approx A_\mathrm{d} - A_{ab} \approx 0$, producing a Gaussian centred at $f = 0$ in the fifth summation. Power spectra computed by Equation (3.43) for a three-axis interferometer are shown in Figure 3.9. Each axis contributes components at two frequencies, $A_{ab} - A_\mathrm{d}$ and $A_{ab} + A_\mathrm{d}$, outlined in Table 3.3. For interferometers with adequate OPD and modulation amplitude separation, there is exactly one $\{a, b\}$ in S for which in-band demodulation produces baseband component at $A_{ab} - A_\mathrm{d}$.

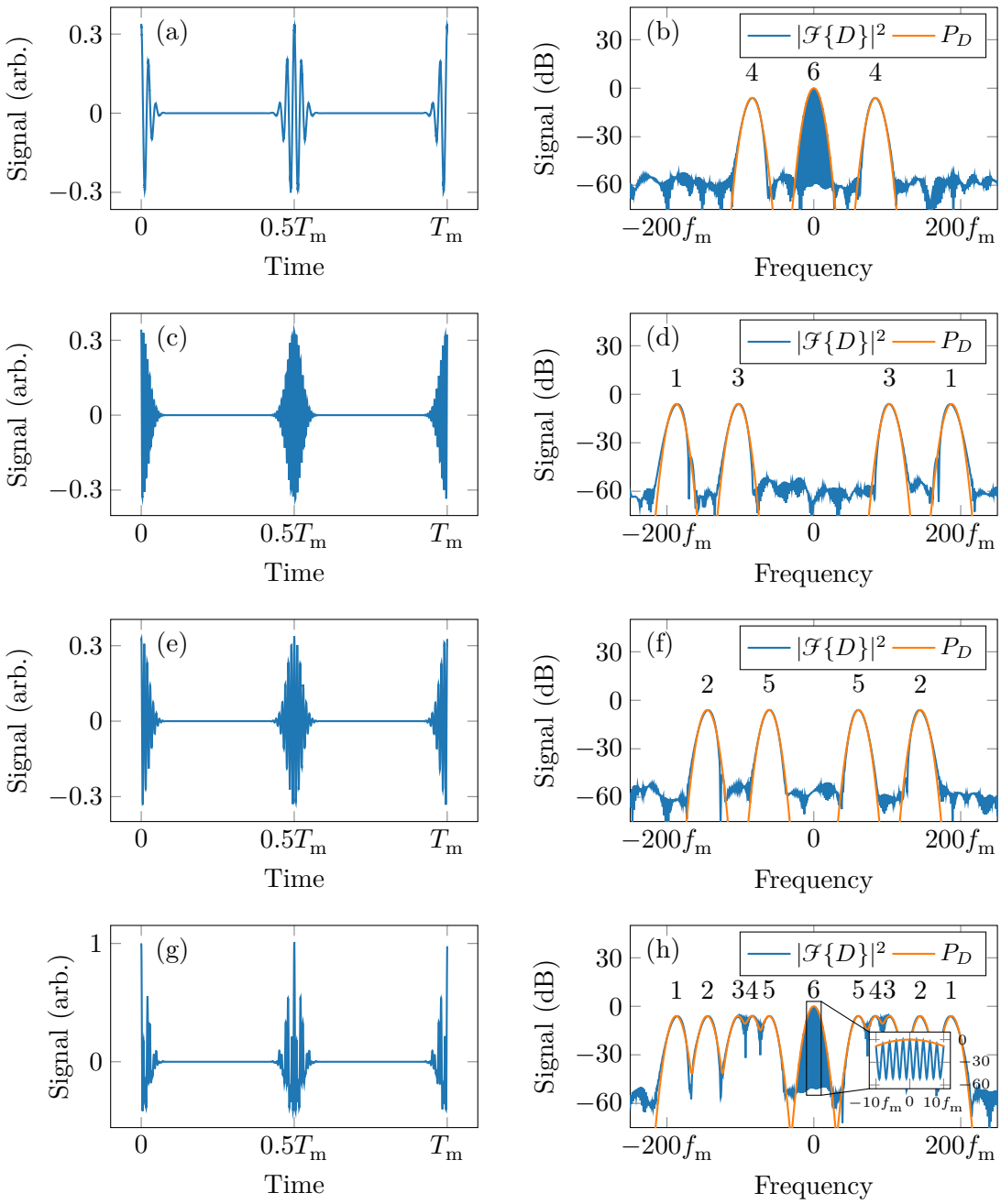

Figure 3.9: Demodulation power spectra for the three-axis interferometer shown in Figure 3.7. The $\alpha\beta$, $\alpha\gamma$, and $\beta\gamma$ axes have modulation amplitudes of 42, 145, and 103 rad, respectively, and the demodulation amplitude is selected such that $A_\mathrm{d} = A_{\alpha\beta} = 42\,\mathrm{rad}$. Time domain signals and power spectra are shown for the isolated $\alpha\beta$ axis in (a) and (b), $\alpha\gamma$ axis in (c) and (d), $\beta\gamma$ axis in (e) and (f), and all axes in (g) and (h). The $|\mathcal{F}\{D\}|^2$ curves are simulated, and P_D curves are computed via Equation (3.43). (h) shows that peak 6 is uniquely in the baseband and its OPD dependent phase can be recovered; peaks are summarized in Table 3.3. Gaussian random noise was added to the normalized interference signals to achieve a signal-to-noise ratio of 1000 which is representative of interferometers discussed in Chapter 7.

Table 3.3: Peaks of the power spectra in Figure 3.9 for in-band demodulation.

Number	Amplitude (rad)	Frequency
6	$A_{\alpha\beta} - A_{\mathrm{d}} = 0$	$\pm(A_{\alpha\beta} - A_{\mathrm{d}})f_{\mathrm{m}} = 0$
5	$A_{\beta\gamma} - A_{\mathrm{d}} = 61$	$\pm(A_{\beta\gamma} - A_{\mathrm{d}})f_{\mathrm{m}}$
4	$A_{\alpha\beta} + A_{\mathrm{d}} = 84$	$\pm(A_{\alpha\beta} + A_{\mathrm{d}})f_{\mathrm{m}}$
3	$A_{\alpha\gamma} - A_{\mathrm{d}} = 103$	$\pm(A_{\alpha\gamma} - A_{\mathrm{d}})f_{\mathrm{m}}$
2	$A_{\beta\gamma} + A_{\mathrm{d}} = 145$	$\pm(A_{\beta\gamma} + A_{\mathrm{d}})f_{\mathrm{m}}$
1	$A_{\alpha\gamma} + A_{\mathrm{d}} = 187$	$\pm(A_{\alpha\gamma} + A_{\mathrm{d}})f_{\mathrm{m}}$

In Figures 3.9b and 3.9h there exists a comb structure under the power spectrum in the baseband due to the $2f_{\mathrm{m}}$ frequency of the window function. Shifting g by $T_{\mathrm{m}}/2$ within a modulation period is equivalent to repeating g at a frequency of $2f_{\mathrm{m}}$. For the discrete Fourier transform over one modulation period, such as the simulated spectra in Figures 3.9b, 3.9d, 3.9f and 3.9h, the frequency resolution is equal to f_{m}, so the spectra are sampled at the points mf_{m} where m is an integer. If g and G are time and frequency domain representations of a signal, respectively, using the result from Equation (A.50), then

$$\left|\mathcal{F}\left\{g(t) + g\left(t - \frac{T_{\mathrm{m}}}{2}\right)\right\}(f)\right|^2 = \begin{cases} 4\left|G(f)\right|^2 & m \text{ even} \\ 0 & m \text{ odd.} \end{cases} \tag{3.44}$$

The form of the power spectrum in Equation (3.44) explains the comb structure under the baseband in Figures 3.9b, 3.9d, 3.9f and 3.9h caused by the $2f_{\mathrm{m}}$ frequency of the window. Figure 3.9h shows a zoomed region near $f = 0$ in Figure 3.9h to better show the comb with the attenuated signals at the interstices. Quadrature is encoded in the baseband of this signal, which is the tooth of the comb centred at $f = 0$ with width $2f_{\mathrm{m}}$. In practice, the imperfect matching of A_{d} to the phase modulation amplitude of the desired signal results in small components at $\pm f_{\mathrm{m}}$, and quadrature should be extracted via low-pass filtering with a maximum cutoff frequency of $f_{\mathrm{m}}/2$. From the zoom in Figure 3.9h, it may seem that filtering with a cutoff frequency of f_{m}

is adequate as the first interstices of the comb structure tend to zero at $\pm f_{\mathrm{m}}$, however, it is not sufficient in practice. When A_{d} is not perfectly matched to A_{ab}, the comb interstices carry a small amount of power that can leak into the filtered baseband; a cutoff frequency of $f_{\mathrm{m}}/2$ or less reduces these effects. Throughout Chapter 5, effects of imperfect demodulation where A_{d} does not exactly equal A_{ab} are examined.

Peaks arising from demodulation may be near each other, as the demodulation sum term for one axis may be near the difference term for another. For well separated axes, these peaks do not occur near the baseband at $f = 0$, but may occur well away, such as peaks 3, 4, and 5 in Figure 3.9. Unlike the placement of bands in the windowed signal, such as those in P_{WU} shown in Figure 3.8b, overlapping bands in the demodulated signal are acceptable as they lie well away from the baseband. Figure 3.9b shows the power spectrum resulting from in-band demodulation for the isolated $\alpha\beta$ axis, while Figures 3.9d and 3.9f show out-of-band demodulation for the respective isolated $\alpha\gamma$ and $\beta\gamma$ axes. The combined power spectrum in Figure 3.9h shows that only the contribution from $\alpha\beta$ occupy the baseband, thereby allowing a quadrature signal representative of its encoded phase to be extracted.

Figure 3.9 and Table 3.3 are missing one feature. When U is not normalized and is carries a non-zero offset, there is a peak in the power spectrum at $\pm A_{\mathrm{d}} = \pm 42\,\mathrm{rad}$ due to the signal offset. The feature is not observed in Figure 3.9 since the simulated U signal has zero offset. The feature arising at A_{d} has little effect since it is always well away from the baseband provided that every axis follows the rules imposed by $\Delta\Lambda_{\mathrm{min}}$.

3.3.3 Alternative Windows

When selecting a window function, one must take into consideration two factors:

1. The window function must eliminate the signal baseband. Quadrature is encoded in the baseband of the demodulated signal, and the windowed signal baseband should be removed for improved performance.
2. The window function must be narrow and exhibit rapid asymptotic decay in the frequency domain so that the windowed signal does not leak into adjacent bands.

Sakai et al. [165] report on a rectangular window function, and Kissinger et al. recommends a Gaussian window [166] — the latter was adopted in this work. Brief analyses of these two windows are presented, along with a third window, the commonly used Hann function [188].

For simplicity, single instance rather than repeated window functions are considered. The single instance Gaussian window function is given by W_1 in Equation (A.38). A rectangular window function, $W_\sqcap$, with the definition

$$W_\sqcap(t,R) = \begin{cases} 1 & |t| < R/2 \\ 1/2 & |t| = R/2 \\ 0 & \text{otherwise,} \end{cases} \tag{3.45}$$

where R is the width of the function. The Hann function, with length L, is typically defined with amplitude $1/L$, however, the window functions discussed are normalized to have unity amplitude, and the Hann window function, W_H, is given by

$$W_\mathrm{H}(t,L) = \begin{cases} \cos^2(\pi t/L) & |t| \leq L/2 \\ 0 & \text{otherwise.} \end{cases} \tag{3.46}$$

In Figure 3.10a, the time domain representations for W_1, $W_\sqcap$, and W_H are shown, with widths of $\sigma = 0.0225$, $R = 4\sigma$, and $L = 5\sigma$, respectively. The Fourier transforms of the $W_\sqcap$ and W_H are well known [188,189], and for their definitions Equations (3.45)

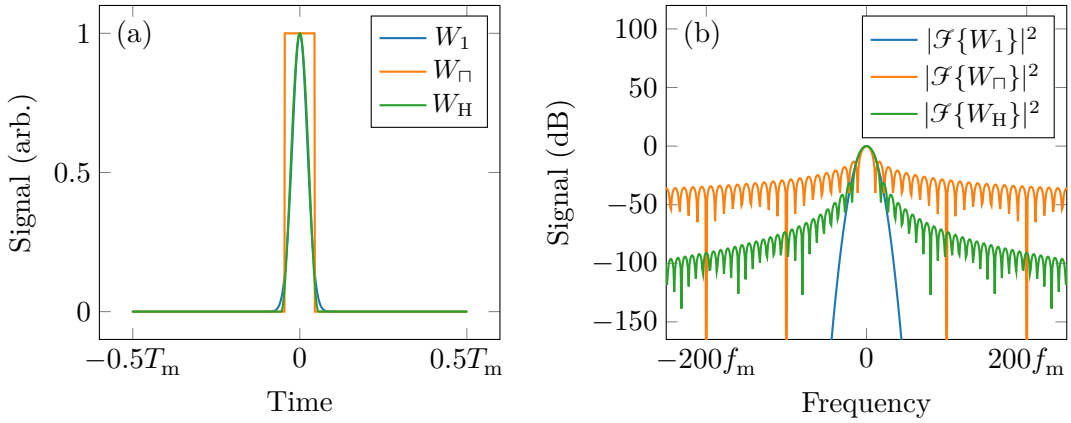

Figure 3.10: Comparison of Guassian, rectangular, and Hann window functions in time (a) and frequency (b) domains. Widths of the Gaussian, rectangular, and Hann functions are $\sigma = 0.0225$, $R = 4\sigma$, and $L = 5\sigma$, respectively, and are chosen to produce window functions of similar visual width. The Gaussian window function does not show any sidelobe behaviour.

and (3.46), respectively, are given by

$$\mathcal{F}\{W_\sqcap(t,R)\}(f) = R\,\mathrm{sinc}(Rf) \tag{3.47a}$$

$$\mathcal{F}\{W_H(t,L)\}(f) = \frac{L\,\mathrm{sinc}(Lf)}{2(1-L^2f^2)}, \tag{3.47b}$$

where $\mathrm{sinc}(x) = \sin(\pi x)/\pi x$. Equations (3.47a) and (3.47b) are simply squared to produce the power spectra in Figure 3.10b.

From Equation (A.32) the Fourier transform of a Gaussian is known to be Gaussian, and thus its power spectrum is Gaussian; Equations (3.47a) and (3.47b) show that the Fourier transforms of rectangular and Hann functions are sinc and sinc-like, respectively, and produce power spectra with a sinc^2 component. Despite the Gaussian power spectrum having a larger main lobe, it does not possess sidelobes like the rectangular and Hann functions due to their sinc^2-like power spectra. The single lobed Gaussian is desirable as it does not have sidebands which can leak signal power into adjacent bands occupied by other axes. Furthermore, the Gaussian has a much more rapid asymptotic decay than the rectangular and Hann windows which

decay at 6 dB/octave and 18 dB/octave [188, 190], respectively, while the Gaussian window decays quadratically, and quickly exceeds 100 dB/octave near $2\sigma_{\mathrm{p}}$ ($\sim 31 f_{\mathrm{m}}$ in Figure 3.10b). These results should not give one the false sense that the Gaussian window shows no sidelobe behaviour. The Gaussian function must be generated over an infinite interval to be purely Gaussian in frequency otherwise it exhibits sinc-like sidelobes due to truncation with a rectangular function. The employed Gaussian window width of $\sigma = 0.0225$ is sufficiently small relative to a modulation period that sidelobes are negligible; performance of different σ valus in the demodulation is explored throughout Chapter 5.

3.4 Total and Partial Demodulation

The placement of bands in the windowed signal, such as those shown in Figure 3.8b, dictates which axes are demodulatable. Depending on the selection of OPDs, and thus the phase modulation amplitude, A, for each axis, some (or even all), axes may not be demodulatable. *Total demodulatability* is when all axes can be uniquely demodulated, and is the name given to the case where all OPDs and demodulation amplitudes are adequately separated by $\Delta\Lambda_{\mathrm{min}}$ and ΔA_{min}, respectively. When two or more axes are not well separated, this condition leads to *partial demodulatability*, where only a subset of axes may be demodulated, as the bands in the windowed signal have significant overlap.

In practice, the OPDs of an interferometer are not exact multiples of $\Delta\Lambda_{\mathrm{min}}$, but to simplify the analysis in this section, it is assumed that OPDs are integer multiples of $\Delta\Lambda_{\mathrm{min}}$. Under this assumption, the demodulatability may be analyzed using set theory, and algorithms for prescribing interferometer configurations with a desired demodulatability can be developed.

The multiset of normalized optical path lengths (OPL), M_ℓ, is used to generate the multiset of normalized OPDs for all axes, M_Δ. In this language, OPLs are the optical

lengths traversed by each signal within the confines of the interferometer described by $\ell_a = \mathrm{c}\tau_{\mathrm{f},a}$, and the OPDs are $\Lambda_{ab} = \ell_b - \ell_a$. The multiset of normalized OPLs is given by

$$M_\ell = \left\{ \frac{\ell_a}{\Delta\Lambda_{\min}} \middle| a \subseteq S \right\}. \tag{3.48}$$

Based on the definition in Equation (3.48), M_ℓ is a multiset of non-negative integers which represent the multiples of $\Delta\Lambda_{\min}$ defining the OPLs in the interferometer. Since the optical paths begin at the interferometer boundary, there always exists a shortest path, $\ell = 0$ in M_ℓ. By definition, $|M_\ell| = |S|$, as M_ℓ contains one normalized OPL for every path in S.

When constructing an interferometer, one generally has control over the physical size, and thus the selection of M_ℓ. To achieve total demodulatability, it is not sufficient for M_ℓ to exhibit a multiplicity of one for each member, as more careful consideration is required to ensure that all OPDs are unique. The pairwise differences of the members of M_ℓ give the multiset of all normalized OPDs, M_Δ, via

$$M_\Delta = \left\{ \ell_b - \ell_a \middle| \{a, b\} \subseteq M_\ell \right\}, \tag{3.49}$$

Equation (3.49) illustrates the importance of OPL selection, as multiple a and b may exist in M_ℓ that produce equal $|\ell_b - \ell_a|$, resulting in two axes occupying the same band. Because M_Δ is generated from M_ℓ, M_Δ is also a multiset of non-negative integers and has cardinality $|M_\Delta| = N$.

3.4.1 Degree of Demodulatability

In a totally demodulatable interferometer, all members in M_Δ are non-zero and have multiplicities of 1. When any members of M_Δ are 0 (when the OPD is zero) or have multiplicities of 2 or greater (when two or more axes occupy the same band), then the interferometer is partially demodulatable. In extreme cases when all members of

M_Δ are either 0 or have multiplicities greater than 2, the interferometer exhibits no demodulatability. The set of demodulatable axes is then

$$S_{\mathrm{D}} = \left\{ m \middle| m \in M_\Delta \wedge \text{multiplicity}(m) = 1 \wedge m \neq 0 \right\}. \tag{3.50}$$

To summarize the fraction of axes that may be demodulated and to describe interferometers in the following examples, the degree of demodulatability, $d_\star$, is formed and given by

$$d_\star = \frac{|S_{\mathrm{D}}|}{N}. \tag{3.51}$$

The degree of demodulatability describes 3 classes of interferometer:

1. $d_\star = 1$: the interferometer is totally demodulatable,
2. $0 < d_\star < 1$: the interferometer is partially demodulatable,
3. $d_\star = 0$: the interferometer has no demodulatability.

When constructing an interferometer with a desired degree of demodulatability, based upon Equations (3.48) to (3.51), one must devise M_ℓ such that it generates M_Δ with the target $d_\star$. In Section 3.2.1, N was observed to grow quadratically with the cardinality of S, which consume the finite bandwidth available to the interference signals. For large N interferometers, one may employ *band overloading*, where 2 or more axes that are not of interest are placed in the same band.

For this discussion, the concepts of *primary* and *secondary* axes are used to describe different cases for demodulatability. Primary axes are those which include the shortest OPL corresponding to $\ell = 0$ for some ℓ in M_ℓ, while secondary axes are those that do not. For example, the $\alpha\beta$ and $\alpha\gamma$ axes in Figure 3.4 are primary, and the $\beta\gamma$ axis is secondary. For this interferometer, the zero length path is ℓ_α. The number of

primary axes, N_p, and secondary axes, N_s, are given by

$$N_\mathrm{p} = |S - 1|, \tag{3.52a}$$

$$N_\mathrm{s} = \frac{(|S| - 1)(|S| - 2)}{2}, \tag{3.52b}$$

$$N = N_\mathrm{p} + N_\mathrm{s}. \tag{3.52c}$$

The primary axes are simply the number of pairs of axes that can be formed with the shortest path (that by convention is always labeled α), for which Equation (3.52a) shows that there are $|S|-1$ other paths to pair. The number of secondary axes is equal to the remaining number of axes, which is $N - N_\mathrm{p}$, written in terms of S in Equation (3.52b). For completeness, the total number of axes is shown in Equation (3.52c), which is equal to the definition in Equation (3.13).

3.4.2 Interferometer Configurations

Table 3.4 shows the minimal interferometer configurations that achieve a desired degree of demodulatability. There are infinitely many configurations with a given demodulatability — take the $|S| = 2$ case of Table 3.4 for instance, for which any $M_\ell = \{0, m\}$ where $m \geq 1$ satisfies the $d_\star = 1$ and $d_\star \geq N_\mathrm{p}/N$ conditions. As there are infinitely many configurations for any given demodulatability condition, only the configurations which satisfy a given condition and have the least $\max(M_\ell)$ are shown in Table 3.4.

The algorithm used to determine M_ℓ with $d_\star = 1$ for the configurations in Table 3.4 is a brute force approach, where all possible M_ℓ are generated, and Equations (3.49) to (3.51) are applied to filter the configurations which do not achieve $d_\star = 1$. This algorithm rapidly slows as $|S|$ grows, and configurations for large interferometers are computationally hard. In most applications, demodulatability of all primary axes is required and the demodulatability of secondary axes is irrelevant, for instance,

Table 3.4: Minimal interferometers that can be constructed for a desired number of axes and demodulatability. All solutions were found via numerical simulation using Equations (3.48) to (3.50). The three $d_\star$ conditions for generating M_ℓ, from left to right, are total demodulatability, partial demodulatability where all primary axes are demodulatable, and partial demodulatability where all secondary axes are demodulatable, respectively. There are no secondary axes in the case where $|S| = 2$.

$\lvert S\rvert$	N	M_ℓ with least $\max(M_\ell)$		
		$d_\star = 1$ Total	$d_\star \geq N_\mathrm{p}/N$ Primary axes	$d_\star \geq N_\mathrm{s}/N$ Secondary axes
2	1	$\{0, 1\}$	$\{0, 1\}$	—
3	3	$\{0, 1, 3\}$ $\{0, 2, 3\}$	$\{0, 1, 3\}$ $\{0, 2, 3\}$	$\{0, 1, 3\}$ $\{0, 2, 3\}$
4	6	$\{0, 1, 4, 6\}$ $\{0, 2, 5, 6\}$	$\{0, 1, 3, 5\}$ $\{0, 3, 4, 5\}$	$\{0, 1, 4, 6\}$ $\{0, 2, 5, 6\}$
5	10	$\{0, 1, 4, 9, 11\}$ $\{0, 2, 7, 8, 11\}$ $\{0, 2, 7, 10, 11\}$ $\{0, 3, 4, 9, 11\}$	$\{0, 1, 3, 5, 7\}$ $\{0, 4, 5, 6, 7\}$	$\{0, 1, 4, 9, 11\}$ $\{0, 2, 7, 8, 11\}$ $\{0, 2, 7, 10, 11\}$ $\{0, 3, 4, 9, 11\}$
6	15	$\{0, 1, 4, 10, 12, 17\}$ $\{0, 1, 4, 10, 15, 17\}$ $\{0, 1, 8, 11, 13, 17\}$ $\{0, 1, 8, 12, 14, 17\}$ $\{0, 2, 7, 13, 16, 17\}$ $\{0, 3, 5, 9, 16, 17\}$ $\{0, 4, 6, 9, 16, 17\}$ $\{0, 5, 7, 13, 16, 17\}$	$\{0, 1, 3, 5, 7, 9\}$ $\{0, 5, 6, 7, 8, 9\}$	$\{0, 1, 4, 10, 12, 17\}$ $\{0, 1, 4, 10, 15, 17\}$ $\{0, 1, 8, 11, 13, 17\}$ $\{0, 1, 8, 12, 14, 17\}$ $\{0, 2, 7, 13, 16, 17\}$ $\{0, 3, 5, 9, 16, 17\}$ $\{0, 4, 6, 9, 16, 17\}$ $\{0, 5, 7, 13, 16, 17\}$
7	21	$\{0, 1, 4, 10, 18, 23, 25\}$ $\{0, 1, 7, 11, 20, 23, 25\}$ $\{0, 1, 11, 16, 19, 23, 25\}$ $\{0, 2, 3, 10, 16, 21, 25\}$ $\{0, 2, 5, 14, 18, 24, 25\}$ $\{0, 2, 6, 9, 14, 24, 25\}$ $\{0, 2, 7, 13, 21, 22, 25\}$ $\{0, 2, 7, 15, 21, 24, 25\}$ $\{0, 3, 4, 12, 18, 23, 25\}$ $\{0, 4, 9, 15, 22, 23, 25\}$	$\{0, 1, 3, 5, 7, 9, 11\}$ $\{0, 6, 7, 8, 9, 10, 11\}$	$\{0, 1, 4, 10, 18, 23, 25\}$ $\{0, 1, 7, 11, 20, 23, 25\}$ $\{0, 1, 11, 16, 19, 23, 25\}$ $\{0, 2, 3, 10, 16, 21, 25\}$ $\{0, 2, 5, 14, 18, 24, 25\}$ $\{0, 2, 6, 9, 14, 24, 25\}$ $\{0, 2, 7, 13, 21, 22, 25\}$ $\{0, 2, 7, 15, 21, 24, 25\}$ $\{0, 3, 4, 12, 18, 23, 25\}$ $\{0, 4, 9, 15, 22, 23, 25\}$

using the interferometer in Figure 3.4 to track the displacements of two independently moving targets β and γ. There are two simple ways to achieve partial demodulatability for all primary axes using band overloading.

The first strategy is that all normalized OPLs, except the shortest (which is zero by definition), are odd. When M_Δ is computed, all primary axes have odd normalized lengths with multiplicities of 1, while all secondary axes have even normalized lengths with multiplicities of 1 or greater. Formally, this strategy is written

$$M_\ell = \Big\{0\Big\} \cup \left\{ 2x+1 \middle| x \in \mathbb{Z} \wedge 1 \leq x < N_\mathrm{p} - 1 \right\}. \tag{3.53}$$

where $\mathbb{Z}$ is the set of integers. Using this strategy, some secondary axes have normalized length multiplicities greater than 1 when $|S| > 3$. For example, in Table 3.4, a minimal solution for the demodulatability of all primary axes in the $|S| = 4$ case is $M_\ell = \{0, 1, 3, 5\}$, which produces $M_\Delta = \{1, 2, 2, 3, 4, 5\}$. The normalized OPDs of the primary and secondary axes are $\{1, 3, 5\}$ and $\{2, 2, 4\}$, respectively. This interferometer has $d_\star = 2/3$ since all primary axes are demodulatable along with the longest secondary axis.

The second strategy for generating a configuration where all primary axes are demodulatable is to make the first non-zero normalized path length equal to $N_\mathrm{p} = |S| - 1$, and increment the normalized lengths by 1 for the next $|S| - 2$ paths, written as

$$M_\ell = \Big\{0\Big\} \cup \left\{ x \in \mathbb{Z} \wedge N_\mathrm{p} \leq x < 2N_\mathrm{p} - 1 \right\}. \tag{3.54}$$

This strategy is the second minimal solution for demodulatability of primary axes in Table 3.4. For example, again consider the $|S| = 4$ configuration, having $M_\ell = \{0, 3, 4, 5\}$ generate $M_\Delta = \{1, 1, 2, 3, 4, 5\}$. The primary axes are $\{3, 4, 5\}$ and the secondary axes are $\{1, 1, 2\}$, again giving $d_\star = 2/3$.

The M_ℓ selection strategies shown in Equations (3.53) and (3.54) represent the first and second minimal M_ℓ configurations for $|S| \geq 3$ in Table 3.4. In effect, these configurations overload bands by placing two or more secondary axes into the same band. Large $|S|$ interferometers may pollute the bandwidth with axes that need not be measured, so one or more bands may be freed by devising a $d_\star < 1$ configuration which places extra axes in the same bands.

Table 3.4 is valuable in the design phase for selecting OPDs in simple multiaxis interferometers, however, constraints on the system may bring about exotic configuations in which only some primary and some secondary axes are demodulatable. For example, consider $M_\ell = \{0, 2, 3, 5\}$ which generates $M_\Delta = \{1, 2, 2, 3, 3, 5\}$ having $d_\star = 1/3$ where the primary axes of M_Δ are $\{2, 3, 5\}$ and the secondary axes are $\{1, 2, 3\}$. Only the normalized OPDs of 5 and 1 are demodulatable, which are, respectively, primary and secondary axes.

Table 3.4 shows that the configurations achieving total demodulatability and partial demodulatability of secondary axes are identical. Secondary axes provide a redundant measurement with respect to the primary axes, as knowledge of all primary axes allows one to derive secondary axis displacement; if all secondary axes are required to be demodulatable, then all primary axes must also be demodulatable. Note that the converse is false and the relationship is asymmetric, as all primary axes may be demodulatable without demodulatability of all secondary axes.

The case where $d_\star = 0$ was mentioned, but not developed, as it is not of practical use. For a three-axis interferometer, consider $M_\ell = \{0, 1, 1\}$, giving $M_\Delta = \{0, 1, 1\}$. When generating S_D from this M_Δ using Equation (3.50), it is found that $S_\mathrm{D} = \emptyset$. One member of M_Δ is 0, and the other has a multiplicity of 2, so all members of M_Δ fail the filtering predicate of Equation (3.50), resulting in $d_\star = 0$.

3.5 Comparison of Common Modulation Schemes

The SFM technique outlined in this chapter uses sinusoidal frequency modulation, however, there are other modulation schemes that are commonly used, namely sawtooth and triangle modulation. The underlying models of sawtooth and triangular modulation are briefly presented in this section to explore their use cases and trade-offs.

3.5.1 Sawtooth Frequency Modulation

A brief derivation of the sawtooth modulation equations is presented in this section, while greater detail is provided in Appendix A.6. Sawtooth frequency modulation is based on the periodic sawtooth function. Using the floor function, $\lfloor x \rfloor$, the saw function may be written as

$$\mathrm{saw}(x) = 2(x - \lfloor x \rfloor) - 1, \tag{3.55}$$

which oscillates between -1 to 1 with an oscillatory factor of 1 (compared to 2π for trigonometric functions). Using the sawtooth function from Equation (3.55), the modulated optical frequency is given by

$$\nu(t) = \nu_{\mathrm{A}} \mathrm{saw}(f_{\mathrm{m}} t) + \nu_{\mathrm{c}}. \qquad \text{[Hz]} \tag{3.56}$$

The beat frequency is expressed as the difference $\nu_a(t' - \tau_{\mathrm{f},a}(t')) - \nu_b(t' - \tau_{\mathrm{f},b}(t'))$ using ν from Equation (3.56). In Appendix A.6, the positive and negative beat frequencies, f_{b}^{+} and f_{b}^{-}, are derived in Equations (A.54) and (A.55) and given by

$$f_{\mathrm{b},ab}^{+}(t') = 2\nu_{\mathrm{A}} f_{\mathrm{m}} \big[\tau_{\mathrm{f},b}(t') - \tau_{\mathrm{f},a}(t')\big], \qquad \text{[Hz]} \tag{3.57a}$$

$$f_{\mathrm{b},ab}^{-}(t') = 2\nu_{\mathrm{A}} f_{\mathrm{m}} \big[\tau_{\mathrm{f},b}(t') - \tau_{\mathrm{f},a}(t')\big] - 2\nu_{\mathrm{A}}. \qquad \text{[Hz]} \tag{3.57b}$$

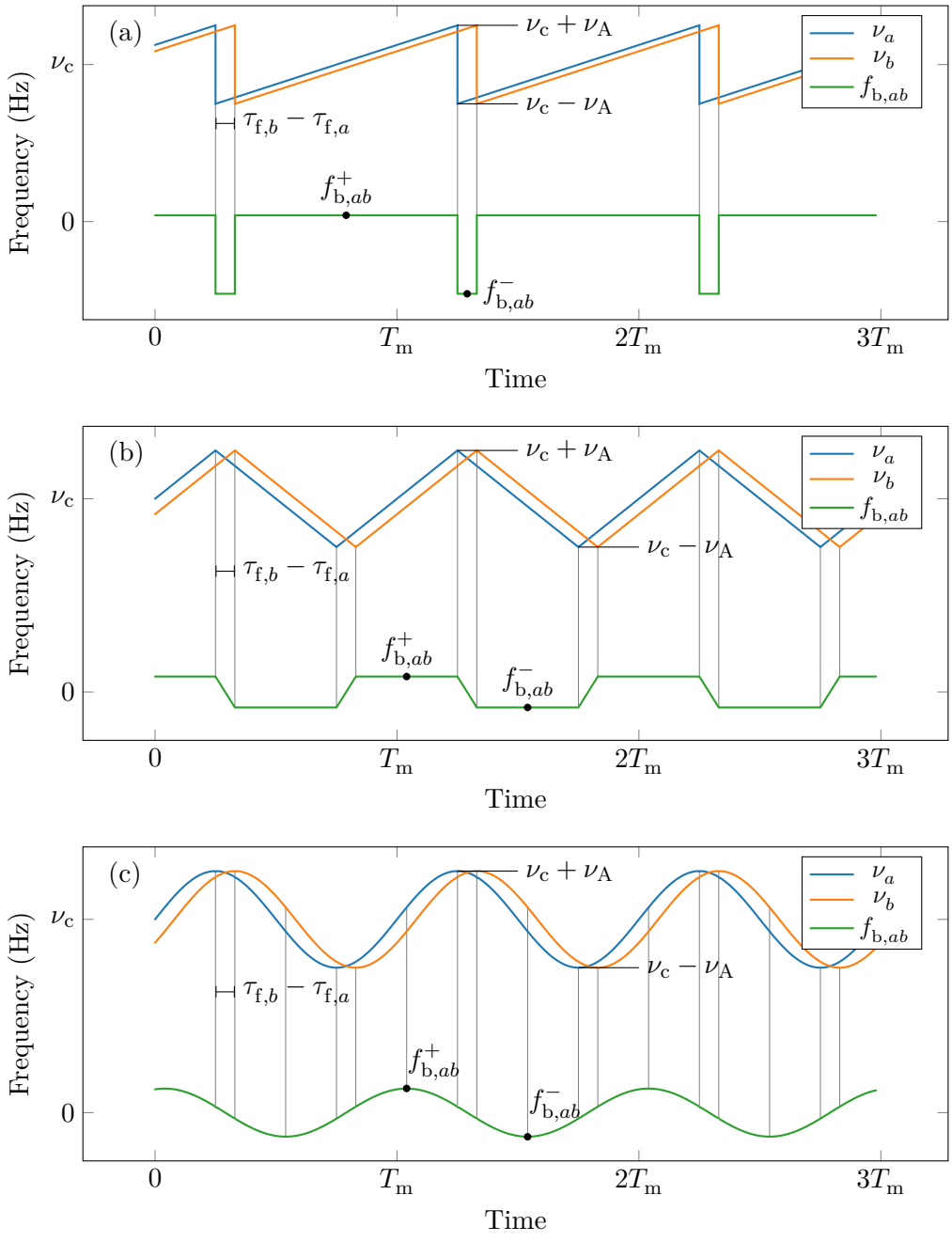

Figure 3.11: Comparison of sawtooth (a), triangular (b), and sinusoidal (c) frequency modulation beat frequencies with constant time-of-flight delays.

The sawtooth modulation technique is often used in absolute ranging paired with a Fourier transform or fringe counting algorithm [191–193]. When a measurement of f_{b}^{+} is obtained, Equation (3.57a) may be applied to determine the OPD as

$$\Lambda_{ab}(t'') = \frac{\mathrm{c}}{2\nu_{\mathrm{A}}} \frac{f_{\mathrm{b},ab}^{+}(t'')}{f_{\mathrm{m}}}. \qquad \text{[m]} \ (3.58)$$

A measurement of f_{b}^{-} in Equation (3.57b) is generally not of particular use because it is ephemeral for all but very large OPDs. The technique also allows simultaneous measurements of multiple axes, provided that all axes possess different OPDs so that they produce unique beat frequencies that can be resolved by Equation (3.58).

3.5.2 Triangular Frequency Modulation

Like the sawtooth modulation discussion in Section 3.5.1, a summary of the triangular modulation equations is presented and while the derivation is found in Appendix A.7. Triangular modulation is similar to the sawtooth modulation scheme discussed in Section 3.5.1, but there is a negative modulation slope rather than a discontinuity. Like the saw function, a triangular periodic function is defined in terms of the floor function,

$$\mathrm{tri}(x) = \begin{cases} 4(x - \lfloor x \rfloor) - 1 & x - \lfloor x \rfloor \leq \frac{1}{2} \\ 4(\lfloor x \rfloor - x) + 3 & x - \lfloor x \rfloor > \frac{1}{2} \end{cases}, \qquad (3.59)$$

that again oscillates between -1 to 1 with an oscillatory factor of 1 (compared to 2π for trigonometric functions). Using Equation (3.59), the optical frequency of a triangularly modulated signal is

$$\nu(t) = \nu_{\mathrm{A}} \mathrm{tri}(f_{\mathrm{m}} t) + \nu_{\mathrm{c}}. \qquad \text{[Hz]} \ (3.60)$$

The beat frequency envelopes, f_{b}^{+} and f_{b}^{-}, are found when both interfering frequencies, $\nu_a(t' - \tau_{\mathrm{f},a}(t'))$ and $\nu_b(t' - \tau_{\mathrm{f},b}(t'))$ using ν from Equation (3.60), simultaneously show positive or negative slopes. These beat frequencies are given by

$$f_{\mathrm{b},ab}^{+}(t') = 4\nu_{\mathrm{A}} f_{\mathrm{m}} \big[\tau_{\mathrm{f},b}(t') - \tau_{\mathrm{f},a}(t')\big], \qquad \text{[Hz]} \ (3.61a)$$

$$f_{\mathrm{b},ab}^{-}(t') = -4\nu_{\mathrm{A}} f_{\mathrm{m}} \big[\tau_{\mathrm{f},b}(t') - \tau_{\mathrm{f},a}(t')\big]. \qquad \text{[Hz]} \ (3.61b)$$

which are illustrated in Figure 3.11b.

From Equations (3.61a) and (3.61b), there is a symmetry that $f_{\mathrm{b}}^{+} = -f_{\mathrm{b}}^{-}$, however, only when the target is stationary. From the relativistic Doppler effect used in radio detection and ranging (RADAR) systems, a Doppler frequency of $f_{\mathrm{d}} = 2v/\lambda_{\mathrm{c}} = v_{\mathrm{opt}}/\lambda_{\mathrm{c}}$ is observed, where v is the velocity of the target [194]; the beam undergoes a single reflection so $v_{\mathrm{opt}} = 2v$ is the velocity in optical path. After Doppler shifting, the modified beat frequencies

$$f_{\mathrm{b},ab}^{+\prime} = f_{\mathrm{b},ab}^{+} + f_{\mathrm{d},ab}, \qquad \text{[Hz]} \ (3.62a)$$

$$f_{\mathrm{b},ab}^{-\prime} = f_{\mathrm{b},ab}^{-} + f_{\mathrm{d},ab} = -f_{\mathrm{b},ab}^{+} + f_{\mathrm{d},ab}. \qquad \text{[Hz]} \ (3.62b)$$

The triangular modulation scheme is employed in many frequency-modulated continuous-wave (FMCW) light detection and ranging (LiDAR) systems [195–197] and absolute ranging applications [62, 163] that exploit Equation (3.62) to simultaneous measure position and velocity of a target.

The Doppler shifted beat frequencies from Equation (3.62) are measured, and both the position and velocity may be determined. The position is found from the difference of these frequencies, $f_{\mathrm{b},ab}^{+\prime} - f_{\mathrm{b},ab}^{-\prime} = 2f_{\mathrm{b},ab}^{+}$, while the velocity is found from

the sum $f^{+\prime}_{\mathrm{b},ab} + f^{-\prime}_{\mathrm{b},ab} = 2f_{\mathrm{d},ab}$. The OPD and velocity in optical path are given by

$$\Lambda_{ab}(t'') = \frac{\mathrm{c}}{8\nu_{\mathrm{A}}} \frac{f^{+\prime}_{\mathrm{b},ab}(t'') - f^{-\prime}_{\mathrm{b},ab}(t'')}{f_{\mathrm{m}}}. \quad \text{[m]} \tag{3.63a}$$

$$v_{\mathrm{opt},ab}(t'') = \frac{\lambda_{\mathrm{c}}}{2}\left[f^{+\prime}_{\mathrm{b},ab}(t'') + f^{-\prime}_{\mathrm{b},ab}(t'')\right]. \quad \text{[m/s]} \tag{3.63b}$$

In the derivations of Equations (3.63a) and (3.63b) the ab subscript to denote each axis was carried through, however, multiaxis measurements are challenging as it is difficult to pair the f^{+}_{b} and f^{-}_{b} terms for each axis. Typical LiDAR systems use a single-axis and a pointing mechanism to enable measurements of multiple targets [198, 199].

3.5.3 Sinusoidal Frequency Modulation

While sinusoidal modulation has been discussed in greater depth throughout this chapter, several key points are repeated here. The beat frequency of an SFM interferometer was presented earlier in Figure 3.6 and is plotted once more in this section in Figure 3.11c for easy comparison with discussions in Sections 3.5.1 and 3.5.2 on sawtooth and triangular modulation, respectively.

The greatest difference between sinusoidal and the sawtooth or triangular modulation schemes is that sinusoidal modulation is better suited to incremental displacement measurements, whereas sawtooth and triangular modulation are often employed in absolute ranging. Incremental encoding of a quadrature signal in the SFM technique offers the greatest resolution and highest sampling rate. First, a sinusoidal profile is better suited to high-speed laser modulation via bias current injection than a sawtooth profile, as discontinuities associated with the latter elicit a distorted response from the LD [200]. Second, the resolution of sawtooth and triangular modulation schemes respectively outlined in Sections 3.5.1 and 3.5.2 depend on the length of the recorded sample. While it is possible to use sinusoidal modulation for absolute

ranging, the linear sawtooth and triangular modulation result in narrower frequency domain features, offering greater spatial resolution than the windowed spectra with broad Gaussian peaks, such as those observed in Figure 3.8.

3.6 Conclusions

In this chapter, the underlying principles of the SFM technique, which can be found in the literature, have been presented. I have derived these equations myself in such a way that they can be used to prescribe the design of a practical multiaxis interferometer configuration. A generalized model for a multiaxis range-resolved SFM laser interferometer was formulated in time and frequency domains. Due the laser optical frequency modulation, each interferometer axis carries two phase components: one primarily influenced by the modulation of the laser and the other dependent on the OPD. With approximate knowledge of the OPD, the interference signal may be demodulated to recover the OPD dependent phase, and thus, the displacement may be measured. By exploiting the proportionality between interference beat frequency and OPD, simultaneous measurements of multiple axes are possible by selecting interferometer configurations with well separated OPDs, thereby placing the demodulatable axes in unique frequency bands. The end-to-end implementation of the SFM technique discussed in this chapter is presented in Chapter 4 and includes the laser diode (LD), digital-to-analog converter (DAC), LD controller, fibres, fibre components, detector, electronics, analog-to-digital converter (ADC), and digital signal processing (DSP) hardware and software components.

Chapter 4

Multiaxis Sinusoidal Frequency Modulation Interferometer Implementation

This chapter describes the implementation of a multiaxis range-resolved sinusoidal frequency modulation (SFM) laser interferometer based upon the model presented in Chapter 3. Several aspects of the implementation are outlined, which include: the selected hardware; the software and digital signal processing (DSP) designs; the extensive calibration of the laser optical frequency modulation characteristics and signal delays introduced in Section 3.2.2; and an overview of the preparation of custom fibre optic patch cords that are required to achieve specific, demodulatable optical path differences (OPD) in the experiments of Chapter 7.

4.1 Hardware

The implementation of the interferometer can be separated into electrical and optical aspects. An electrical system consisting of the laser, detector, and signal processing hardware provides a means of signal modulation and demodulation, while the optical system includes components such as fibres, beamsplitters, and reflectors that form the interferometer itself. The electrical and optical aspects are largely independent, with the only crossover requirement being that the electrical system must have prior knowledge of the signal delays in the optics. Focus is given to the

electrical system in this section, as its design is invariant among all interferometers that are presented.

4.1.1 Frequency-Modulation-Demodulation Unit

From this point forward, the electrical system is referred to as the frequency-modulation-demodulation unit (FMDU), which consists of the laser, fibre optic circulator, detector, and signal processing hardware. The assembled FMDU in Figure 4.1 provides a single bidirectional optical port which feeds the interferometer optics with an SFM signal and returns the signal to detector. Specifications for the FMDU components are given in Appendix C.1 and a list of all components in the FMDU in Table C.1.

The signal processing system is implemented in a Xilinx Zynq-7000 multi-processor system-on-chip (MPSoC) [201] on a Digilent Eclypse Z7 development board [202] (whose specifications are given in Table C.2). The signal processing implementation details are presented in Section 4.5. Two high-speed SYZYGY ports [203] on the board are interfaced with 14 bit 100 MHz dual-channel Digilent Zmod AWG 1411 digital-to-analog converter (DAC) [204] and Zmod Scope 1410-105 analog-to-digital converter (ADC) [205] expansion cards (refer to Tables C.3 and C.4 for respective specifications). The primary DAC channel provides a bias current modulation signal to the laser diode (LD) controller that in turn modulates the optical frequency of the laser. Although the secondary DAC channel has no formal use in the implementation, it provides a means to view intermediate signals and was particulary useful during development. Both channels of the ADC are used for measurement. The primary channel samples the interference signal from the detector that is used in demodulation, while the secondary channel is used to simultaneously sample an arbitrary signal. Having the ability to simultaneously sample another signal and preserve its phase relationship with the demodulated displacement signals improves the versatility of the system

and enables applications such as the HeNe laser interferometer verification strategy in Section 7.5, cryogenic force feedback accelerometer in Section 7.6, and cryogenic characterization of a silica resonator in Section 7.7.

The laser is a 1550 nm discrete mode Eblana Photonics EP1550 NLW 14-pin butterfly LD with 100 kHz linewidth [186, 206]. A Koheron CTL200 digital LD controller [207] is used for current and temperature control of the LD. Respective LD and LD controller specifications are given in Tables C.5 and C.6. The MPSoC board

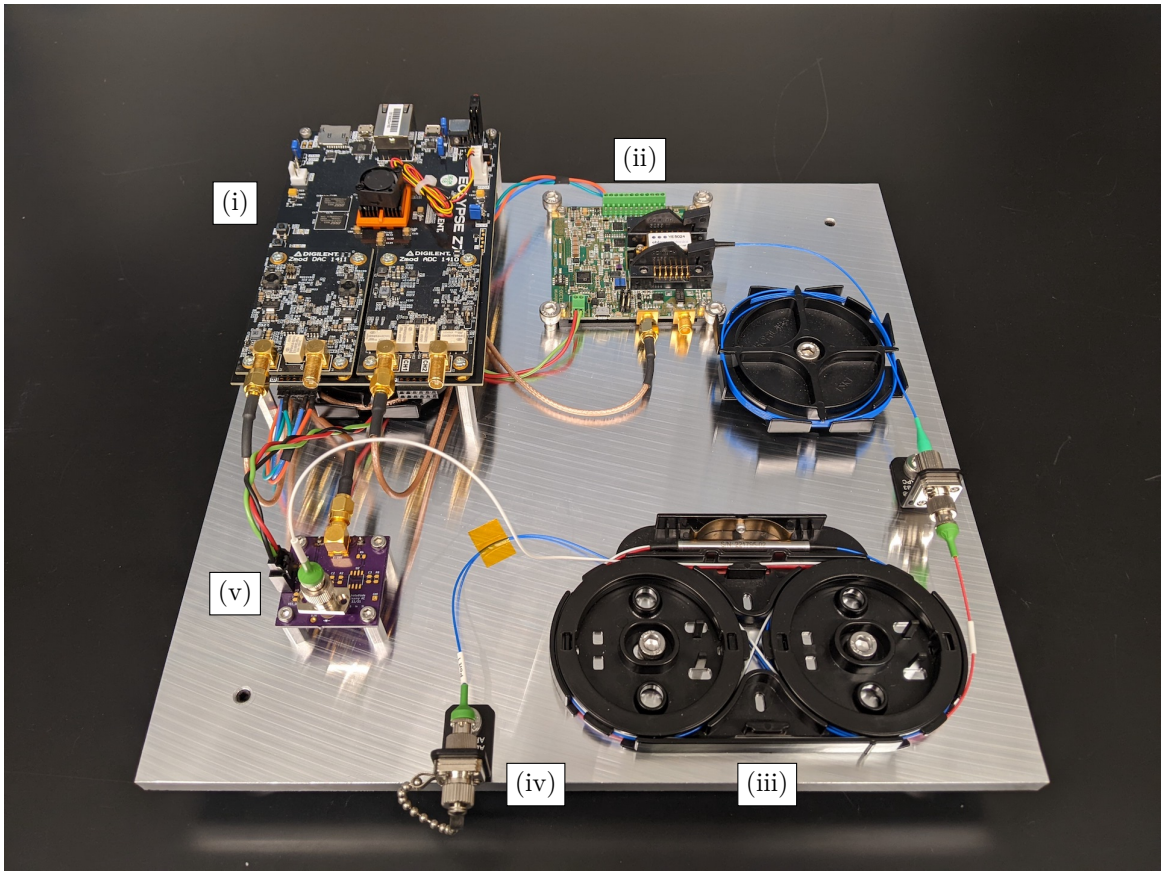

Figure 4.1: FMDU assembled on an aluminum plate. The signal processing system (i) provides an analog modulation signal to the LD controller (ii). An SFM signal is delivered to circulator (iii) which redirects it to the interferometer port (iv). The signal probes an external interferometer and returns through the same port (iv) where it passes through the circulator (ii) and is redirected to the detector and amplifier (v). The FMDU digitizes the ampified detector signal and demodulates it to recover the displacement in real-time. Components of the FMDU were provided by Blue Sky Spectroscopy Inc.

manages the LD controller configuration and state over serial communication while providing an analog modulation signal through the DAC. Calibration of the LD and LD controller parameters is presented in Section 4.3. The probing beam makes outgoing and return passes through a Thorlabs 6015-3-APC circulator [208], and the interference signal is detected by a Thorlabs FGA01FC InGaAs photodiode [209] in a custom amplifier circuit. Photodiode specifications are given in Table C.7.

4.1.2 Photodetector and Amplifier

A custom transimpedance amplifier (TIA) circuit is used to amplify the signal from the Thorlabs FGA01FC InGaAs photodiode. The TIA is built around an Analog Devices AD8009 high slew rate operational amplifier [210]; a schematic of the circuit is shown in Figure 4.2 and specifications for the operational amplifier are given in Table C.8. The amplifier feedback has a resistance of $R_\mathrm{f} = 1\,\mathrm{k\Omega}$ and capacitance of $C = 10\,\mathrm{pF}$ giving a cutoff frequency of 16 MHz. These R_f and C values were chosen so that the detector output voltage, V_det, uses close to the full range of the ADC while still providing a high speed response. The transfer function, H, is given by

$$H(\mathrm{j}\omega) = \frac{V_\mathrm{det}}{I_\mathrm{pd}} = -\frac{R_\mathrm{f}}{1 + \mathrm{j}\omega R_\mathrm{f} C}, \qquad \text{[V/A]} \quad (4.1)$$

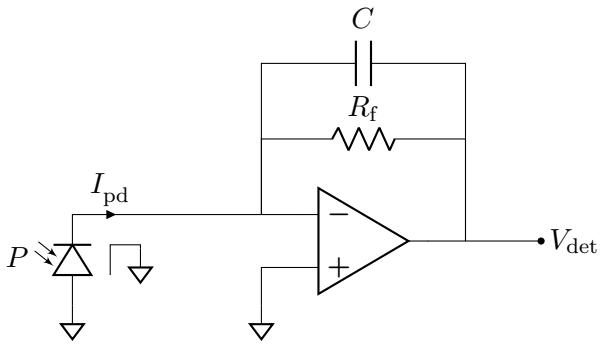

Figure 4.2: Schematic of the photodetector and amplifier circuit. Voltage sources and decoupling capacitors are omitted. The clockwise ground arrow beside the photodiode indicates that the case is grounded.

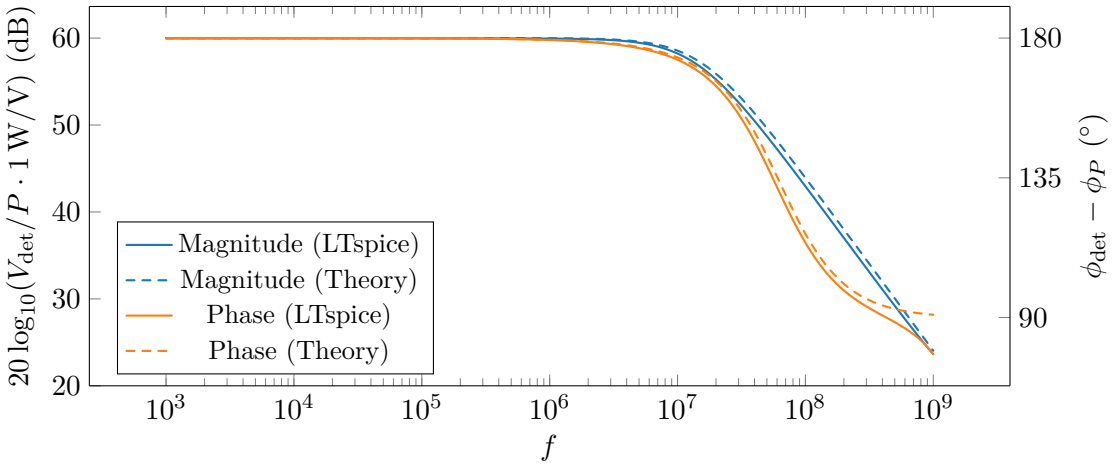

Figure 4.3: Bode magnitude and phase plots for the photodetector amplifier. Simulated curves were produced in LTspice XVII; theoretical curves are from Equation (4.2). The 60 dB gain below the cutoff indicates that the output is 1 V for every 1 mW of optical power collected by the detector. ϕ_{det} and ϕ_P are the phases of V_{det} and P, respectively.

where ω is angular frequency, and I_{pd} is the photodiode current. Equation (4.1) may be expressed in terms of the optical power on the detector, P, giving

$$H(\text{j}\omega) = \frac{V_{\text{det}}}{P} = -R_\lambda \frac{R_\text{f}}{1 + \text{j}\omega R_\text{f} C}, \qquad \text{[V/W]} \ (4.2)$$

where $R_\lambda = 1.003\,\text{A/W}$ is the responsivity of the Thorlabs FGA01FC photodiode at 1550 nm and can be assumed constant over the optical frequency modulation range with negligible error in the magnitude of the transfer function [209].

Bode plots for V_{det}/P are shown in Figure 4.3. Simulated curves are generated from an LTspice XVII [211] design that includes decoupling capacitors and a model of the AD8009 operational amplifier and theoretical curves are calculated from Equation (4.2). The LTspice model shows a different phase behaviour than the transfer function near 1 GHz, which is beyond the conventional range of the SFM signals and is not considered further.

4.2 Software

The software implementation spans three domains: the programmable logic domain (PL), which is the field-programmable gate array (FPGA) fabric of MPSoC; the processing system domain (PS), which is the processor in the MPSoC; and the software domain (SW), which is the user software on a personal computer (PC). PL and PS nomenclature is adopted from Xilinx [201]. The architecture of the FMDU software in Figure 4.4 shows the interactions and flows of data between the components of the system. While the PL implementation can be considered as hardware since FPGAs are a class of reconfigurable *hardware*, the PL *implementation* is discussed alongside software due to its tight coupling with and extension of the PS implementation.

To give some context of the work that I conducted, over 22 000 lines of code were required *just* for the FMDU implementation. This does *not* include the calibration discussed in this chapter, the numerical modeling in Chapter 5, the acqusition and analysis programs required for the cryogenic characterization of optical fibres and components in Chapter 6, or the data processing software for the applications in Chapter 7. The code discussed here is simply for operating the FMDU to obtain displacement measurements and can be broken down as follows:

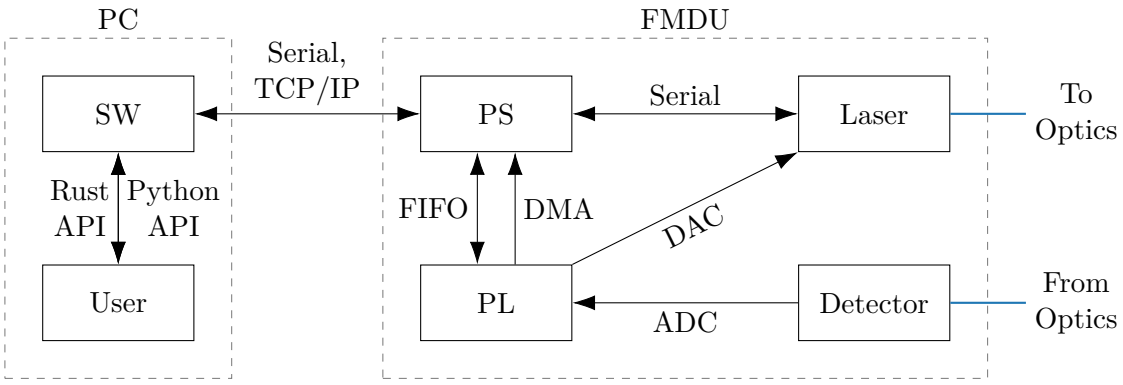

Figure 4.4: Architecture of the FMDU software showing interaction and data flows between the system components.

- PL (∼8700 lines): control the LD controller, DAC, ADC; perform the DSP required for demodulation; generate digital quadrature outputs; and pass the demodulated phase values to the PS.
- PS (∼8900 lines): Control the PL, compute pregenerated signals required for modulation and demodulation; communicate with the SW over the network for control of the FMDU; stream the recovered phase values to the SW.
- SW (∼4900 lines): Communicate with the PS to control the FMDU; receive and buffer the phase values from the PS; provide a simple and easy to use interfaces for controlling the FMDU.

Several processes were employed during development to give confidence in the correctness of the FMDU implementation. Automated regression testing was used to assist in the prevention of committing errors into the codebase. Due to the nature of the hardware involved, hardware integration tests were manually configured and run to verify correct interfacing between the FMDU and other hardware components of the system, such as the PC, LD controller, DAC, and ADC. Furthermore, the measurements obtained in Chapter 7 using the FMDU implementation were compared against the numerical models explored in Chapter 5, to which close agreement was shown.

4.2.1 Programmable Logic Domain

The FMDU is an embedded system consisting of the PL and PS that interface with the LD controller and the photodetection circuit. Both PL and PS domains run concurrently in an MPSoC, enabling high speed work to be performed by reconfigurable hardware in the PL and less demanding work on the conventional processor in the PS.

Two communication channels between the PL and PS are employed. A bidirectional first-in first-out (FIFO) queue is used to pass modulation parameters and state

from the PS to PL and vice versa. Modulation and demodulation waveforms are precomputed by the PS using the equations in Section 3.2 and handed off to the PL over the FIFO where they are stored in block random access memory (BRAM) look-up tables. The PL produces a LD modulation voltage on one of the available DAC channels by cycling through the samples of the stored modulation waveform. After the interference signal is detected and sampled by the ADC, the digital signal is received by the PL, where it is normalized and demodulated (procedures for which are discussed in Section 4.5). The phase of the demodulated signal is unwrapped and passed to the PS over a one-way direct memory access (DMA) channel to the PS, where it is packaged and transferred to the SW on a PC. In total, eight parallel demodulation pipelines are implemented, which enables simultaneous demodulation of up to eight axes. The choice of support for eight axes is limited by the size of the hardware — a greater number of axes is possible with an MPSoC having greater available BRAM storage in the FPGA to store the large modulation and demodulation look-up tables. Alternatively, one may also support a greater number of axes by increasing the minimum allowed modulation frequency, as lower modulation frequencies result in larger look-up tables. Considering this trade-off, a minimum modulation frequency of 25 kHz was selected for the current implementation as it leaves sufficient space for the simultaneous demodulation of up to eight axes. Most applications in Chapter 7 use three or fewer axes, however, the novel range fragmentation technique in Section 7.8 uses seven.

The FMDU employs dual-channel DACs and ADCs, but only one channel of each is required for modulation and demodulation. Within the FPGA, care was taken to delay-compensate a signal sampled on the secondary ADC channel for the time consumed by the normalization and demodulation procedures, allowing for an analog voltage measurement to be recorded simultaneously with the recovered optical displacements. The secondary ADC signal may be read in place of the last axis, allowing

Table 4.1: Truth table for computing digital quadrature from a fixed-point value. Only fractional values of the fixed-point numbers are considered and are partitioned into four ranges. The X bits indicate *don't care* in the truth table and are shown for generality; the a and b bits (indicated by the positions under the table) are the only bits that matter for the computation and are select to be the most significant fractional bits.

Range of Fractional Value	Fixed-Point Binary	Cosine	Sine
0.00 to 0.2499...	...XXX.00XXX...	1	1
0.25 to 0.4999...	...XXX.01XXX...	0	1
0.50 to 0.7499...	...XXX.10XXX...	0	0
0.75 to 0.9999...	...XXX.11XXX...	1	0
	...XXX.*ab*XXX...		

for either up to eight axes or up to seven axes and one analog voltage to be simultaneously measured. The simultaneous voltage measurement is exploited by some applications discussed in Chapter 7, including the HeNe laser interferometer strategy in Section 7.5 and the cryogenic characterization of a silica resonator in Section 7.7. A secondary DAC channel is available, but it was not implemented to have any functionality for the end user. During development the availability of a second DAC channel was invaluable for conveniently debugging internal signals using an oscilloscope.

The PL can generate digital quadrature outputs for up four axes to feed other devices (limited by available GPIO pins), such as a displacement servo controller, each having a base resolution in optical path of $\lambda_c/4$. Quadrature is generated from the unwrapped phase, which is represented by a fixed-point number in normalized units, where 1 unit is equivalent to 2π rad. In this representation, the cosine and sine of quadrature can be generated from the first two fractional bits of the number. From Table 4.1, cosine is simply a XNOR b and sine is NOT a. Furthermore, quadrature may easily be multiplied before output to increase the quadrature resolution by changing which bits are taken for a and b. Shifting by k bits increases the quadrature resolution by a factor of 2^k. The increase in resolution, however, comes at the cost of a 2^k reduction in the maximum measurable velocity from Equation (3.36). Above this

velocity the quadrature output is unable to follow the motion, resulting in skipped quadrature counts.

For example, at 100 kHz modulation about a central wavelength of 1550 nm, the maximum OPD velocity than can be tracked by the FMDU is ∼8 cm/s by Equation (3.36). The FMDU unwraps the phase over $\pm\pi$ which is a maximum optical displacement step of $\lambda_c/2$. Devices that interface with a digital quadrature readout cannot tolerate a missing quadrature count, and will introduce errors at velocities above $v_{\text{opt,max}}/2$, where the factor of 2 arises due to the digital quadrature step size. In the present case, the maximum OPD velocity that can be relayed over digital quadrature is ∼4 cm/s. Using quadrature multiplication with a shift of two, the step resolution is increased by a factor of four to $\lambda_c/16$, which results in a maximum velocity limit that is reduced by a factor of four to $v_{\text{opt,max}}/8 \approx 1\,\text{cm/s}$.

4.2.2 Processing System Domain

The PS is coupled with the PL and serves as an intermediary between the PL and the SW running on a PC. Most tasks performed by the PS are commands issued from the SW that are forwarded to the PL to control the hardware. To achieve good real-time performance, the PL software is built upon FreeRTOS [212] using preemptive task scheduling.

A non-volatile flash memory is present on the Eclypse Z7 development board for storing the bootloader, PS program, and PL configuration. The bootloader, PS program, and PL configuration occupy about 400 kB (or 4 MB with debugging symbols) of the available 16 MB storage space. The remaining space may be used by the application. Extra storage is used for two sets of data: device calibration settings and user parameters, each taking about 1 kB of storage space. The device settings are determined when the system is assembled and include calibration data for the optical and electrical components of the FMDU, such as the laser modulation and delay parame-

ters discussed in Sections 4.3 and 4.4, respectively, along with data from component specification sheets and characterization reports. These calibration data are hidden behind a private application programming interface (API), but the user configuration data, such as the device hostname on the network, modulation frequency, frequency modulation amplitude, and the interferometer OPDs, can be modified at any time.

Modulation and demodulation equations from Section 3.2 are implemented in the PS and computed from the calibration and user parameters to generate waveforms that are handed off to the PL. The act of modulating the laser optical frequency is a shared responsibility between the PS and PL. The LD controller settings and state are controlled over serial by the PS, and the PS signals to the PL when it is safe to inject the modulation voltage from the DAC.

A PC running the SW can communicate with the PS via USB serial or TCP/IP over the network. The serial connection may be useful for debugging, but is not useful in practice as the baud rate is too low to stream displacement data and requires the FMDU be situated near the PC. Communication over the network is possible using a TCP/IP connection, which supports much greater data rates and allows the FMDU to be accessed remotely. When streaming high volumes of data, one may prefer to use UDP, which has a lower overhead than TCP/IP; however, this performance improvement comes at a cost, as UDP cannot recover lost packets. For this reason, TCP/IP was selected for its robustness and its ability to achieve reasonably high speeds. Over the local network, the FMDU achieved streaming rates of just over 500 kHz. As this is the maximum total rate, if multiple axes are streamed, their combined rates cannot exceed this limit, e.g., two axes at 250 kHz or five axes at 100 kHz.

4.2.3 Software Domain

The SW is the interface to the FMDU that an end user integrates into their custom software on a PC. The underlying FMDU driver is written in 100 % safe Rust [213], and APIs in Rust and Python [214] are provided for the user. Rust, being a systems programming language, was selected due to its performance and ease of integration with Python via PyO3 [215] for scripting on any operating system supported by the Rust compiler, which includes Windows, macOS, and Linux. There is no single program that makes up the control software, but rather a library with a simple interface that can be integrated into projects as needed. An example script is shown in Figure 4.5, which demonstrates connecting to the FMDU, recording multiaxis data, and producing a plot.

Internally, the SW owns a worker thread which performs all communication with the FMDU. A handle encapsulating the worker thread is given to the user, who may use the public API to send and receive messages for controlling the FMDU and receiving data. The advantage of this design is that receiving data is a non-blocking operation since the worker thread buffers the received data, allowing the main thread controlled by the user to do other work while the data is collected. Additionally, the Python API provides the collected data directly as NumPy [216] arrays that can be passed to other numerical procedures. The entire design of the SW API is to provide a minimal but complete set of methods that simplify control and usability of the FMDU.

The largest challenge with streaming data from the PL through the PS and into the SW are bottlenecks with packing and unpacking the data. Both the serial and TCP/IP interfaces to the FMDU utilize the same JavaScript Object Notation (JSON) serialization scheme for sending commands and data. JSON is a trade-off between performance, flexibility, and ease of use. As JSON is text-based, it is not well suited for transmitting numeric and binary data, but is good for constructing and debugging

```python
import time
import matplotlib.pyplot as plt
import numpy as np
import fmdu

# Connect to the FMDU using its hostname on the network.
with fmdu.connect('fmm000') as fm:
  fm.write_config(
    opd=[0.3, 1.2],     # OPDs of 2 axes in metres.
    stream_axes=[0, 1], # Stream both axes.
    mod_freq=100e3)     # Modulation frequency in Hz.
  # Warm up the laser.
  fm.power_on()
  time.sleep(10)
  # Stream the data from both axes. Another thread buffers
  # the data so other work can be performed while receiving.
  fm.start()
  time.sleep(10) # Record 10 seconds of data.
  fm.power_off()
  # Receive the data. This can be called multiple times
  # to implement something like a live plot.
  data = fm.recv()
  # The data is striped between axis 0 and axis 1 and must
  # be reshaped to get each displacement.
  a0, a1 = data.reshape((len(data) // 2, 2)).transpose()
  # Generate time values from the 100 kHz sampling rate.
  t = np.arange(len(a0)) / 100e3
  # Make a plot. The measurement is provided in metres,
  # so it is converted to micrometres.
  plt.plot(t, 1e6 * a0, label='Axis 0')
  plt.plot(t, 1e6 * a1, label='Axis 1')
  plt.xlabel('Time (s)')
  plt.ylabel('Optical Displacement (µm)')
  plt.legend()
  plt.show()
```

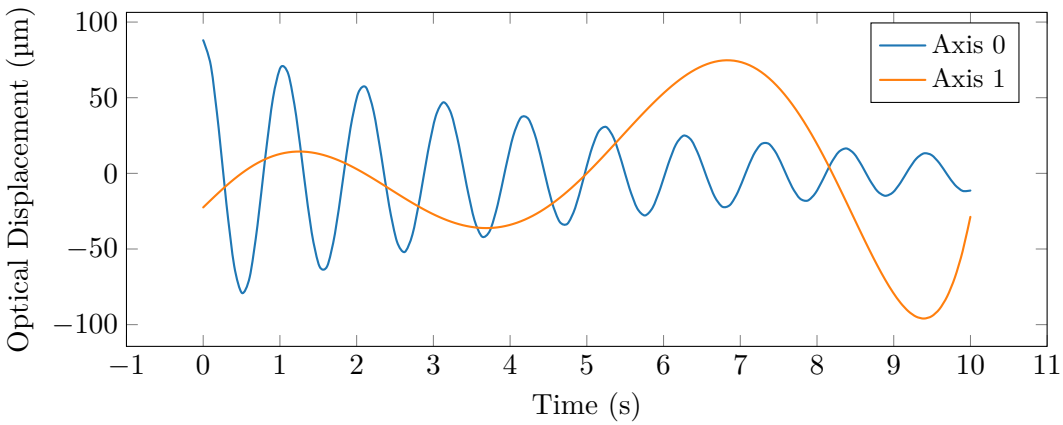

Figure 4.5: A minimal Python program that uses the FMDU driver to simultaneously sample two axes and produce a plot. An example plot that the program may output is shown.

basic commands. There is significant overhead in the serialization of numeric data to a text-based format, however, a trick is employed in the PL to alleviate pressure on the PS. Internally, the PL accumulates the unwrapped phase in 48 bit fixed-point numbers. Before sending the phase values over DMA to the PS, they are Base64 encoded natively in the PL. Using the FPGA for Base64 encoding is advantageous, since a streaming Base64 encoder may be implemented over a single clock period. As Base64 encoding increases the data size by a factor of 4/3, a single 48 bit phase measurement is expressed in exactly 64 bits. Phase data from several parallel channels can then be transferred over DMA with 8 byte alignment and no padding, meaning that the PS can simply drop the phase data into a prebuilt JSON structure without any additional processing. When received by the SW, the overhead of deserializing the JSON and Base64 is negligible since the worker thread spends most of its time in idle. A total displacement sample rate of 500 kHz was achieved. The bottleneck limiting the data rate is the TCP/IP stack in the PS, so there is no benefit in sacrificing the debugging and ease of use advantageous of JSON serialization for a more compact binary format.

When the PS streams normalized phase data to the SW, the central wavelength, λ_c, is included. The SW can recover the optical displacement by scaling the phase with the wavelength. Phase data is represented by a 48 bit fixed point number with a 16 bit radix. Since there are 32 integral bits, a measurement range of $2^{32}\lambda_c = 6.7\,\text{km}$ optical is possible with $\lambda_c = 1550\,\text{nm}$. This range is significantly greater than any change in OPD discussed in this thesis. Since 32 bit numbers with 16 fractional and 16 integral bits may only represent ranges of 10 cm optical, so 48 bit values were selected. With 16 bit fractions, a readout resolution of $\lambda_c/2^{16} = 23.6\,\text{pm}$ is achieved. This value is *not* the smallest displacement that can be resolved, which in Section 7.3 was determined to be $\sim$50 pm.

4.3 Laser Calibration

Knowledge of the laser optical frequency modulation amplitude, ν_{A}, and the centre optical frequency, ν_{c}, are required to demodulate the interference signal and recover displacement. In this section, ν_{c} is measured directly and a technique for experimentally determining ν_{A} as a function of f_{m} is presented.

4.3.1 Laser Diode Calibration

Measurements of the LD optical power, frequency, and wavelength were recorded at several laser bias currents at thermistor setpoints of 12.5, 10, and 8.1 kΩ, which are approximately temperatures of 20, 25, and 30 °C, respectively. The temperature values are not exactly known, but were approximated from the Steinhart-Hart equation [217],

$$T(R) = \frac{1}{C_1 + C_2 \ln(R) + C_3 \ln(R)^3}, \qquad \text{[K]} \quad (4.3)$$

where T is temperature, R is the thermistor resistance given in Ω, and C_1, C_2, and C_3 are known as the Steinhart-Hart coefficients. The Steinhart-Hart coefficients were not calibrated for this LD; assumed values of $C_1 = 1.125 \times 10^{-3}\,\mathrm{K}^{-1}$, $C_2 = 2.347 \times 10^{-4}\,\mathrm{K}^{-1}$, and $C_3 = 0.855 \times 10^{-7}\,\mathrm{K}^{-1}$ were chosen based on the nominal coefficients used by ILX Lightwave LD controllers [218]. Not knowing the exact relation between T and R is acceptable as measurements at different temperatures were obtained simply to demonstrate the effects of temperature on the LD parameters. In the implementation, the LD is always operated at a thermistor setpoint of 10 kΩ, which is approximately 25 °C by Equation (4.3).

Optical power was recorded using a Keysight N7744A optical power meter [219], while frequency and wavelength were recorded with an EXFO WA-1500-NIR wavemeter [220] adjusted to vacumm values (refer to Tables C.13 and C.14 for specifications). Uncertainties in optical power measurements are ±4.5 %; frequency and wavelength measurements have respective uncertainties of ±25 MHz and ±0.3 pm. A linear least-

Table 4.2: Calibrated laser power, frequency, and wavelength coefficients for Equation (4.4). The laser power is fitted to a line, so it does not have higher-order coefficients.

k	C_{Pk} (W/A^k)	$C_{\nu k}$ (Hz/A^k)	$C_{\lambda k}$ (m/A^k)
0	$-1.413(10) \times 10^{-3}$	$193.4780(1) \times 10^{12}$	$1549.491(1) \times 10^{-9}$
1	$3.561(7) \times 10^{-2}$	$-8.00(26) \times 10^{10}$	$6.42(26) \times 10^{-10}$
2	—	$-8.00(22) \times 10^{11}$	$6.39(21) \times 10^{-9}$
3	—	$-6.50(59) \times 10^{11}$	$-5.15(58) \times 10^{-9}$

squares fit was applied to the power measurements, and third order polynomial least-squares fits to the frequency and wavelength measurements (both fitting order are standard for these measurements), giving

$$P(I_{\mathrm{b,set}}) = C_{P0} + C_{P1} I_{\mathrm{b,set}}, \qquad \text{[W]} \quad (4.4a)$$

$$\nu(I_{\mathrm{b,set}}) = C_{\nu 0} + C_{\nu 1} I_{\mathrm{b,set}} + C_{\nu 2} I_{\mathrm{b,set}}^2 + C_{\nu 3} I_{\mathrm{b,set}}^3, \qquad \text{[Hz]} \quad (4.4b)$$

$$\lambda(I_{\mathrm{b,set}}) = C_{\lambda 0} + C_{\lambda 1} I_{\mathrm{b,set}} + C_{\lambda 2} I_{\mathrm{b,set}}^2 + C_{\lambda 3} I_{\mathrm{b,set}}^3. \qquad \text{[m]} \quad (4.4c)$$

where $I_{\mathrm{b,set}}$ is the non-modulated LD bias current setpoint in A, yielding: the optical power, P, in W; the optical frequency, ν, in Hz, and the vacuum wavelength, λ, in m. The polynomial coefficients of C_{xk} are given in Table 4.2. Fits were applied for the measurements at 50 mA and above, as the LD threshold current was found to be just below 40 mA which is consistent with the nominal 40 mA threshold current for this LD [186]). The measurements are shown in Figure 4.6.

To first order, the laser power is unaffected by temperature, however, as the temperature increases, elongation of the cavity leads to the significant change in frequency and wavelength shown in Figures 4.6b and 4.6c, respectively. As the bias current is modulated, the laser frequency is in turn modulated due to temperature changes in the diode [200]. An LD may simultaneously be bias current modulated and frequency stabilized using minute bias and temperature adjustments when locked to an absorption

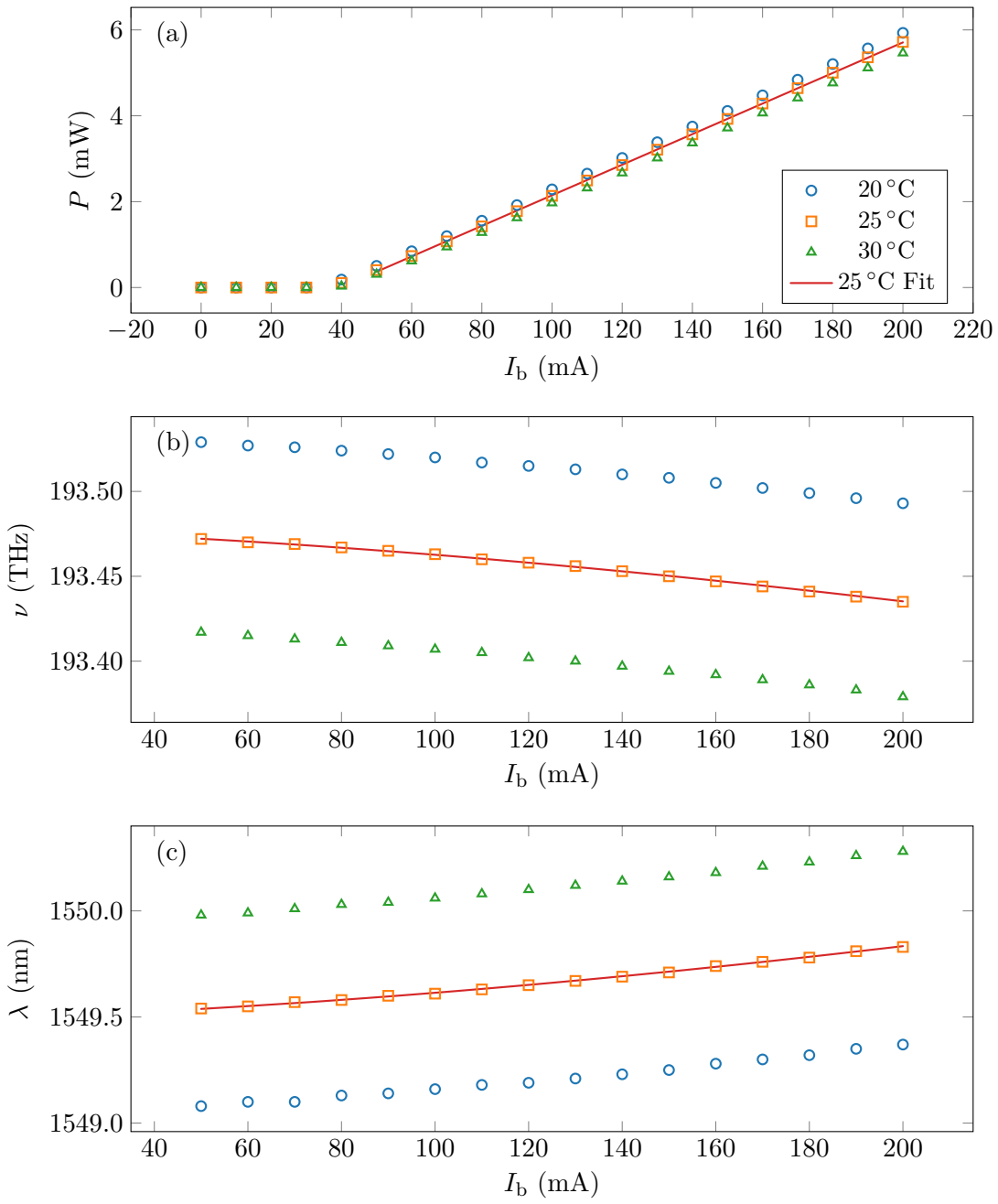

Figure 4.6: Measurements of laser power (a), frequency (b), and wavelength (c). In (a), the laser threshold current is observed near 40 mA. Fits from Equation (4.4) are plotted over the 50 to 200 mA range, which is the range for which the laser power was sufficient to obtain frequency and wavelength measurements. Only the 25 °C series are fitted, as that is the temperature at which the laser is operated in the implementation. The legend in (a) applies to all plots. Error bars are omitted due to their small scale; measurement uncertainties are: ±4.5 % in optical power, ±25 MHz in optical frequency, ±0.3 pm in wavelength.

line of a gas cell [221] or gas-filled hollow-core fibre [222,223]. Section 5.5 demonstrates a laser frequency stabilization scheme that was investigated for SFM interferometry. Although laser stabilization was achieved using this approach, it was not adopted for this implementation due to restrictions imposed on the optical frequency modulation amplitude, ν_{A}, in Equation (3.1).

Laser power modulation is not corrected using Equation (4.4a), and is instead corrected in real-time using an automatic normalization procedure in the PL. In ideal modulation, the laser power would not change as the modulated bias current, I_{b}, deviates from the setpoint. Because of the linear relationship observed in Figure 4.6a, care should be taken to keep I_{b} above the threshold current so that the laser output is continuous. Furthermore, the amplitude modulation depth is larger when modulating near the threshold current than the maximum current at 200 mA. For example, if a 20 mA modulation range is required, then modulating over 50 to 70 mA has an amplitude modulation depth of 41 % in the detector voltage, V_{det}, while modulating over 160 to 180 mA has a depth of 8 %. Section 5.4 shows that the impact of power modulation is small on the uncertainty of the recovered displacement, however, a procedure to remove the power modulation envelope is discussed in Section 4.5.1.

Since the frequency and wavelength shown in Figures 4.6b and 4.6c are well approximated by cubic functions of the LD bias current, achieving sinusoidal *optical frequency* modulation requires that the generated LD *bias current* modulation, $I_{\mathrm{b}}(t)$, is not sinusoidal. Figure 4.7 shows a simulation for typical values of I_{b}, ν_{c}, and ν_{A}, using Equation (4.4b). In Figure 4.7a, the simple sinusoidal bias modulation results in a non-sinusoidal optical frequency modulation shown in Figure 4.7b, but the calibrated non-sinusoidal bias modulation results in a sinusoidal optical frequency modulation in the respective figures. The calibrated modulation scheme is found by generating the desired frequency modulation profile using Equation (4.4b) and performing a binary search to determine the bias current that produces the frequency at each point. A bi-

nary search is viable as Figure 4.7b shows that the frequency decreases monotonically with I_b over the measured 50 to 200 mA range.

4.3.2 Optical Frequency Modulation Gain

When an LD is bias current modulated at some modulation frequency, f_m, the optical frequency modulation amplitude, ν_A, which is the departure from the centre optical frequency, decreases as f_m is increased [224]. An analog voltage modulation signal, V_{mod}, is provided to the LD controller which in turn modulates the laser bias current about a setpoint, $I_{b,set}$, with a nominal gain of 25 mA/V [207]. The individual responses of the LD controller and the LD are not easily measured, however, their combined effects are, giving the calibration product required for the SFM technique. In this section, only the magnitude response of the laser modulation is characterized; the delay (i.e., phase) response is characterized in Section 4.4. The goal of characterizing the magnitude response is to obtain the modulation gain, G_{mod}, in Hz/V, which gives the laser optical frequency modulation amplitude, ν_A, as a function of the modulation parameters.

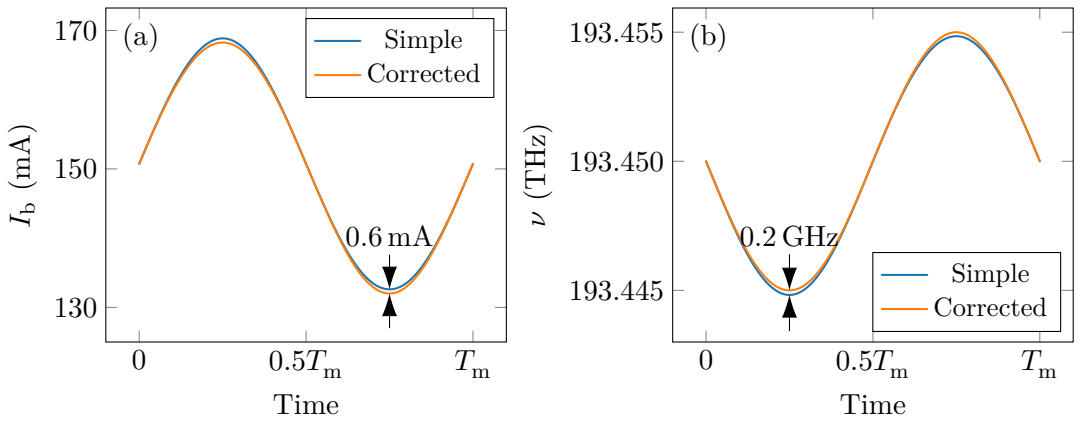

Figure 4.7: Comparison of LD bias current modulation (a) and the resulting optical frequency modulation (b) about $\nu_c = 193.450$ THz with amplitude $\nu_A = 5$ GHz. Simple modulation is sinusoidal in current, but not optical frequency; calibrated modulation is sinusoidal in optical frequency, but not current; absolute differences at the peaks are labeled on each plot. These simulations do not account for modulation frequency dependent losses discussed in Section 4.3.2.

Several single-axis interferometers were constructed according to Table 4.3 with varying OPDs. Each configuration is operated with different bias current setpoints and bias modulation amplitudes. In each case, the bias modulation is adjusted so that the optical frequency modulation of ν is sinusoidal using the technique discussed in Section 4.3.1. The detector signal, V_{det}, was recorded and windowed with W from Equation (3.9), to obtain the power spectrum of WV_{det} discussed in Section 3.3.1. From Figure 3.8b, the location of the Gaussian peaks in the power spectrum are known to occur at the beat frequencies $f_{\mathrm{b}}^{+} = Af_{\mathrm{m}}$ and $f_{\mathrm{b}}^{-} = -Af_{\mathrm{m}}$. Using Equation (3.24), the optical frequency modulation amplitude can be found as

$$\nu_{\mathrm{A}} \approx \frac{\mathrm{c} f_{\mathrm{b}}^{+}}{2\pi\Lambda f_{\mathrm{m}}}. \qquad \text{[Hz]} \ (4.5)$$

In Figure 4.8, the procedure for finding ν_{A} from V_{det} using Equation (4.5) is shown. The power spectrum of the sampled V_{det} and overlayed W in Figure 4.8a is shown in Figure 4.8b and is consistent with the spectra presented in Section 3.3.1. The locations of the peaks of the power spectrum are $\pm Af_{\mathrm{m}}$, and ν_{A} may be computed from Equation (4.5). This measurement was repeated for several values of f_{m} to obtain ν_{A} as a function of f_{m}, which is used to calculate G_{mod} by

$$G_{\mathrm{mod}} = \frac{2\nu_{\mathrm{A}}(f_{\mathrm{m}})}{\max\{V_{\mathrm{mod}}\} - \min\{V_{\mathrm{mod}}\}}. \qquad \text{[Hz/V]} \ (4.6)$$

The collected data is plotted in Figure 4.9 on a log-log axis. Since the measurements form a straight line, a power law least-squares fit was selected. Inspection of the plot shows that the gain increases with $I_{\mathrm{b,set}}$, and is relatively unchanged with the modulation depth, thus, the curve can be represented by a power law in f_{m} and scaled by $I_{\mathrm{b,set}}$. A gain expression of $\alpha I_{\mathrm{b,set}} f_{\mathrm{m}}^{\beta}$ was found, where fits of α and β yield

$$G_{\mathrm{mod}}(I_{\mathrm{b,set}}, f_{\mathrm{m}}) = (3.61(21) \times 10^{11}\,\mathrm{Hz/V/A}) I_{\mathrm{b,set}} (1\,\mathrm{Hz}^{-1} f_{\mathrm{m}})^{-0.276(5)}. \qquad \text{[Hz/V]} \ (4.7)$$

Table 4.3: Parameters for laser modulation gain characterization. *Name* is a unique identifier given to the test configuration by which it is referenced in the text. *Depth* is a qualitative description of the modulation amplitude which is incorporated into the *Name* and better described by the V_{mod} *Amp.* and I_{b} *Amp.*, which are the modulation voltage and corresponding bias current modulation amplitudes. V_{mod} *Amp.* is the average voltage modulation amplitude of V_{mod}, computed as $(\max\{V_{\mathrm{mod}}\} - \max\{V_{\mathrm{mod}}\})/2$, and I_{b} *Amp.* is the corresponsing average bias current modulation amplitude. Since the V_{mod} *Amp.* varies by over an order of magnitude among the configurations, the OPD is adjusted accordingly to produce a reasonable beat frequency.

Name	$I_{\mathrm{b,set}}$ (mA)	Depth	V_{mod} Amp. (mV)	I_{b} Amp. (mA)	OPD (m)
140L	140	Low	44.1(1)	0.551(11)	17.48(19)
140M	140	Mid	373.1(5)	4.66(9)	1.63(2)
140H	140	High	747.0(9)	9.34(19)	1.02(2)
160L	160	Low	39.1(1)	0.488(10)	17.48(19)
160M	160	Mid	343.5(5)	4.29(9)	1.63(2)
160H	160	High	689.1(9)	8.61(17)	1.02(2)
180L	180	Low	37.5(1)	0.468(9)	17.48(19)
180M	180	Mid	323.0(5)	4.04(8)	1.63(2)
180H	180	High	645.1(9)	8.06(16)	1.02(2)

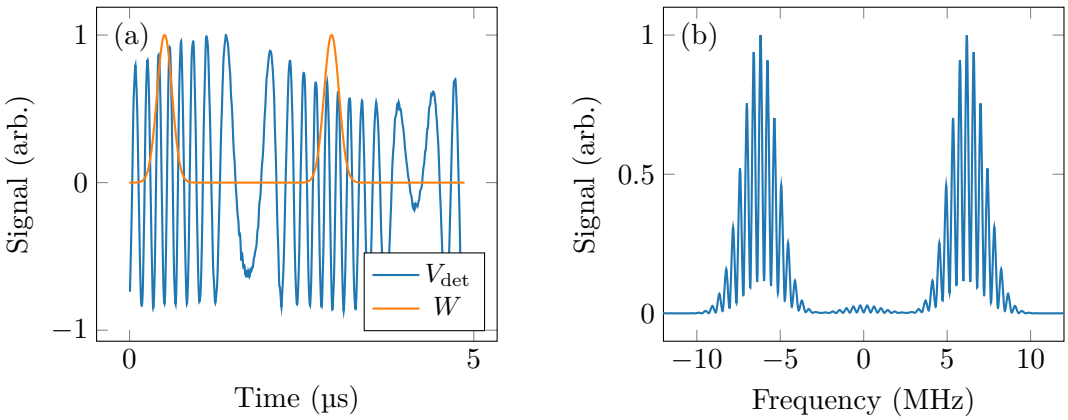

Figure 4.8: Procedure for measurement of the modulation gain at $f_{\mathrm{m}} = 206.186\,\mathrm{kHz}$ for a 1.02(2) m OPD and $I_{\mathrm{b,set}} = 180\,\mathrm{mA}$. The detector signal in (a) is windowed and a power spectrum of WV_{det} is plotted in (b). The two large peaks of the Gaussian power spectrum occur at $f_{\mathrm{b}}^{+} = -f_{\mathrm{b}}^{-} = 6.6(4)\,\mathrm{MHz}$, corresponding to $\nu_{\mathrm{A}} = 1.5(1)\,\mathrm{GHz}$ by Equation (4.5). and $G_{\mathrm{mod}} = 2.31(15)\,\mathrm{GHz/V}$ by Equation (4.6). The smaller peak centred around 0 Hz is due to the slight offset in the V_{det} signal.

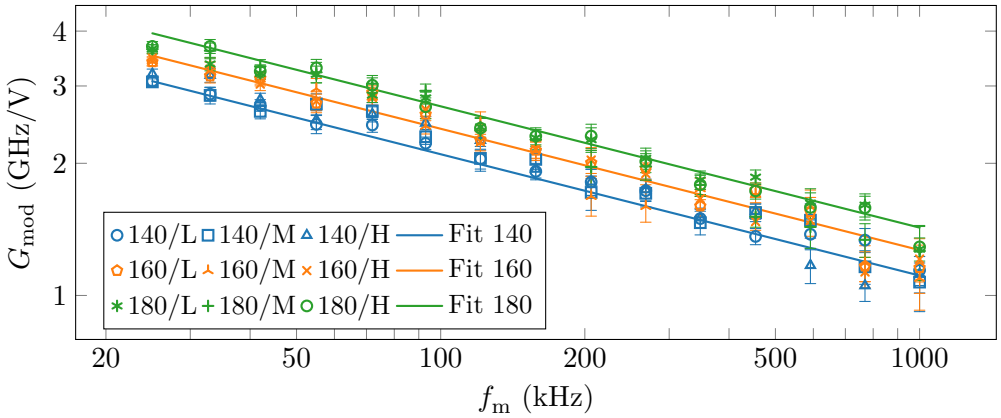

Figure 4.9: Measurement of the modulation gain for the LD controller with the power law least-squares fit from Equation (4.7). Legend entries correspond to the *Name* column in Table 4.3 which gives the testing configuration. These measurements are used to obtain the fitted modulation gain, G_{mod}, in Equation (4.7).

Equation (4.7) is programmed into the FMDU and is one of the many calibrations required for the generation of modulation parameters. Arrival at Equation (4.7) was tedious, as the procedure outlined in Figure 4.8 had to be performed 135 times, however, the result is valuable. Knowledge of Figure 4.8 grants the ability to operate the laser at any bias current setpoint and modulation amplitude. This flexibility has been useful in practice. Typically the laser is operated at a high $I_{\mathrm{b,set}}$ in the 160 to 180 mA range to reduce the amplitude modulation depth of the interference signal. For some interferometers, the optical losses are so small that the detector voltage saturates the ADC, in which case $I_{\mathrm{b,set}}$ may simply be reduced and the modulation gain is still followed by Equation (4.7).

4.4 Signal Delay

The optical and electrical signal propagation delays must be accounted for to demodulate the interference signal. Knowledge of each individual delay introduced in Section 3.2 and Figure 3.5 is not required, as it is only the total combined delay that matters for demodulation. Signal processing delays in the FPGA are determined from DSP implementation are thus known. Other delays, such as those introduced by the

DAC, ADC, laser, and detector, cannot be derived, and must be determined. Since the desired calibration product is the total combined delay, several delays may be merged into a single measurement. Merging delay measurements provides two benefits: the number of calibration measurements is reduced and delays that are difficult to measure individually may be measured as part of a greater delay in which they are contained. The latter is particularly useful, since DAC and ADC delay measurements are difficult to measure individually, but trivial when combined, and the same is true for the laser modulation and detector delays.

4.4.1 Digitization Delay

The digitization delay summarizes the electrical propagation delays of the DAC and ADC. To measure the combined delay, $\tau_{\mathrm{da}} + \tau_{\mathrm{ad}}$, the DAC generates a sinusoidal signal that is fed directly into the ADC. At the positive zero crossings of the wave given to the DAC, a counter is started that increments every clock cycle until the corresponding zero-crossing is observed in the sampled signal from the ADC. The FPGA clock is 100 MHz, which matches the sampling frequencies of DAC and ADC, giving a sampling resolution of 10 ns.

Modulation frequencies of $f_{\mathrm{m}} = 25,\ 100,\ 200,\ 225,\ 250,\ 333,\ 500$, and 1000 kHz were investigated, and 1000 measurements were recorded at each setting. All measurements were evenly distributed between 360 and 370 ns, and the digitization delay is taken at the centre value of

$$\tau_{\mathrm{da}} + \tau_{\mathrm{ad}} = 365(5)\,\mathrm{ns}. \tag{4.8}$$

Equation (4.8) has an uncertainty range of 10 ns which is equal to the sampling period of the ADC and DAC. The delay contribution from Equation (4.8) is only one constituent of the total delay, and two others must be determined to obtain the effective total delay in Section 4.4.4.

4.4.2 Modulation, Delivery, and Detection Delays

To measure the combined delay of modulation of the LD controller and LD, optical delivery delay of the fibres within the FMDU, and the detector, modulation was performed at different frequencies and different interferometer configurations. The interferometer configurations are identical to those in Table 4.3 for the laser modulation gain characterization presented in Section 4.3.2. The same dataset was used for the LD modulation gain calibration in Section 4.3.2, and the interferometer configurations in Table 4.3 were used for this characterization.

Figure 4.10a shows a plot for the modulation signal at $f_{\mathrm{m}} = 206.186\,\mathrm{kHz}$, and the total measured delay is marked by the interval drawn on the plot. The delay is the time between the turnaround point of V_{mod} to the turnaround point in the phase modulation of V_{det}. This delay is given by $\tau_{\mathrm{mod}} + \tau_{\mathrm{del,out}} + \tau_{\mathrm{del,bound}} + \tau_{\mathrm{f}} + \tau_{\mathrm{del,in}} + \tau_{\mathrm{det}}$, and the desired delay measurement is,

$$\tau_{\mathrm{eo}}(f_{\mathrm{m}}) = \tau_{\mathrm{mod}}(f_{\mathrm{m}}) + \tau_{\mathrm{del,out}} + \tau_{\mathrm{del,in}} + \tau_{\mathrm{det}}(f_{\mathrm{m}}), \qquad [\mathrm{s}] \ (4.9)$$

where τ_{eo} is the combined delay of the analog electronics and optics in the FMDU. In Equation (4.9), τ_{mod} and τ_{det} are functions of f_{m} because the analog components of the LD controller and the detector impart a frequency dependent phase shift. The delays of $\tau_{\mathrm{del,bound}}$ and τ_{f} are not included in Equation (4.9), since those are not permanent components of the FMDU, but rather delays specific to an arbitrary interferometer configuration. The configuration dependent delivery delay of the $2.17(1)\,\mathrm{m}$ fibre, $\tau_{\mathrm{del,bound}} = 21.1(2)\,\mathrm{ns}$, and time-of-flight delays, τ_{f}, must be subtracted from the measured value to obtain τ_{eo}.

Using the technique in Figure 4.10a for obtaining measurements of τ_{eo}, the delays at several frequencies are plotted in Figure 4.10b. Like the modulation gain in Section 4.3.2, the delay is linear on a log-log axis, indicating that the relationship is a

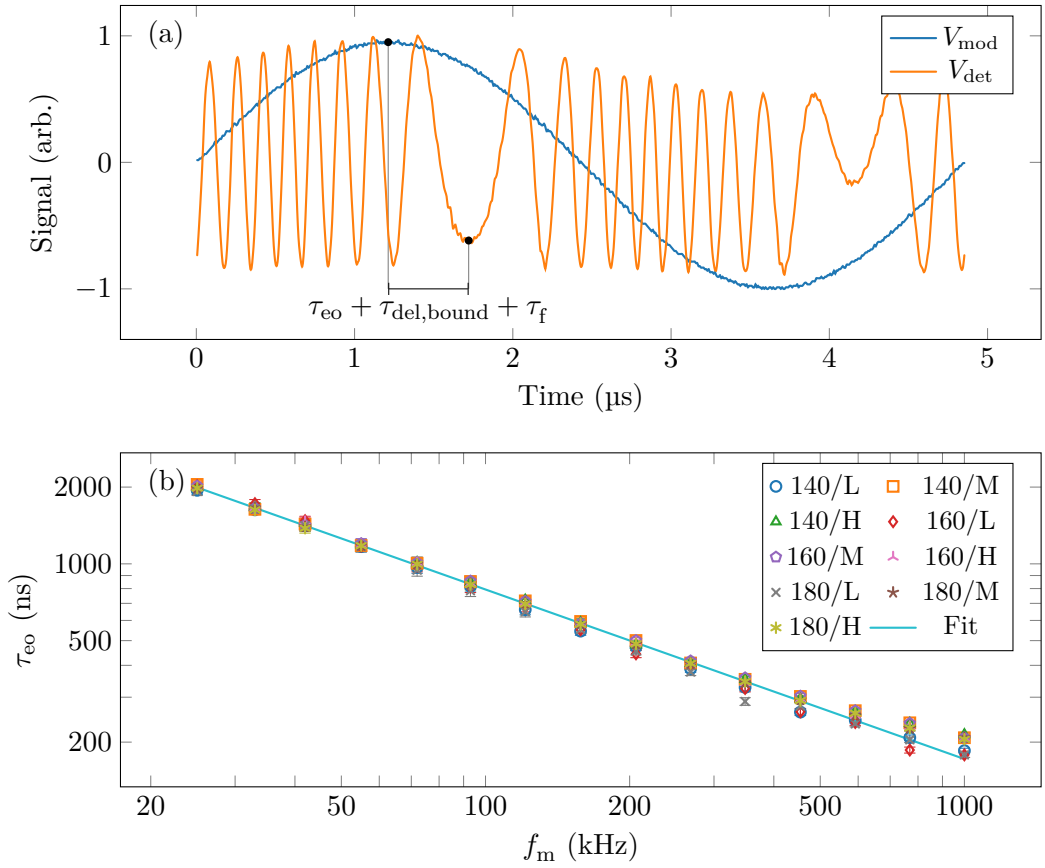

Figure 4.10: Measurement procedure and calibration curves for the modulation, delivery, and detection delays. (a) shows the measurement procedure for obtaining the combined modulation, delivery, and detector delays at $f_{\mathrm{m}} = 206.186\,\mathrm{kHz}$. This is the same dataset as Figure 4.8, however, the procedure is adjusted to measure the delay rather than the modulation gain. (b) shows the he calibration curve for τ_{eo} with a power law fit from Equation (4.10). The same dataset was used for the LD modulation gain calibration in Section 4.3.2 and legend entries are the names of the interferometer configurations in Table 4.3.

power law. A power law fit was obtained and plotted in Figure 4.10b, given by

$$\tau_{\mathrm{eo}}(f_{\mathrm{m}}) = (1.45(23) \times 10^{-3}\,\mathrm{s})(1\,\mathrm{Hz}^{-1} f_{\mathrm{m}})^{-0.665(3)}. \qquad [\mathrm{s}] \quad (4.10)$$

The delay in Equation (4.10) is included in the effective calibrated delay summarized in Section 4.4.4.

4.4.3 Normalization Delay

The normalization delay is the time from when a sample is returned from the ADC to when it is demodulated. As part of the FPGA design, constituent delays of the normalization delay are constrained based on the performance of each DSP step before demodulation, and each delay can be determined directly from the design. Table 4.4 shows the delay of each signal processing component; while each DSP step is discussed in greater detail in Section 4.5, the delays are all that are required for this discussion. A single recursive running sum low-pass and two recursive running sum high-pass filters are used for filtering high frequencies and offset removal, having respective widths of K_{LP}, K_{HP1}, and K_{HP2}. A 32-point Hilbert transform combined with a recursive running sum low-pass filter having a width of K_{norm} is used to extract the signal envelope in the amplitude normalization step. The filter implementation is discussed in Section 4.5.1, and filter schematics are shown in Figure 4.11. Steps of the normalization procedure may be disabled, so the total delay depends on both the filter widths and which components are enabled. Filtering configurations and recommendations are explored in Sections 4.5.1 and 5.4.

Table 4.4: Constituents of the normalization delay measured in clock cycles. The Hilbert transform procedure cannot be disabled and always consumes 22 clock cycles; other components depend on the filter widths, K.

Component	Clock Cycles	
	Enabled	Disabled
Low-pass filter	$\lfloor K_{\mathrm{LP}}/2 \rfloor + 3$	0
High-pass filter 1	$\lfloor K_{\mathrm{HP1}}/2 \rfloor + 3$	0
High-pass filter 2	$\lfloor K_{\mathrm{HP2}}/2 \rfloor + 3$	0
Hilbert transform	22	—
Amplitude Normalization	$\lfloor K_{\mathrm{norm}}/2 \rfloor + 71$	0

The normalization delay may be found as the sum of each step in Table 4.4. Assuming that all filters and normalization are enabled, the normalization delay is

$$\tau_{\text{norm}} = \left(\left\lfloor \frac{K_{\text{LP}}}{2} \right\rfloor + \left\lfloor \frac{K_{\text{HP1}}}{2} \right\rfloor + \left\lfloor \frac{K_{\text{HP2}}}{2} \right\rfloor + \left\lfloor \frac{K_{\text{norm}}}{2} \right\rfloor + 102 \right) \times 10\,\text{ns}. \tag{4.11}$$

In practice, Equation (4.11) is not implemented directly, and each constituent delay is conditionally included based on whether that signal processing step is enabled; these adjustments are straightforward using Table 4.4. The normalization delay from Equation (4.11) is the final component of the total delay in Section 4.4.4.

4.4.4 Effective Delay

All delays discussed in this section are those due to the components selected for the FMDU and the signal processing implementation. Using Equations (4.8), (4.10) and (4.11), the constituent delays can be combined,

$$\begin{aligned} \tau_{\text{da}} + \tau_{\text{eo}} + \tau_{\text{ad}} + \tau_{\text{norm}} = {} & 1385(5)\,\text{ns} + (1.45(23) \times 10^6\,\text{ns})(1\,\text{Hz}^{-1} f_{\text{m}})^{-0.665(3)} \\ & + \left(\left\lfloor \frac{K_{\text{LP}}}{2} \right\rfloor + \left\lfloor \frac{K_{\text{HP1}}}{2} \right\rfloor + \left\lfloor \frac{K_{\text{HP2}}}{2} \right\rfloor + \left\lfloor \frac{K_{\text{norm}}}{2} \right\rfloor \right) \times 10\,\text{ns}, \\ & [\text{ns}] \end{aligned} \tag{4.12}$$

where f_{m} is taken in Hz. Equation (4.12) is programmed into the FMDU and computed based on the modulation and filtering settings. This equation assumes that all signal processing steps are enabled, but in practice, a modified form is used to adjust the delay when steps are omitted. With Equation (4.12), the FMDU is able to operate in both the base time, t, and central total common-mode shifted time, t''_{c}, from Equation (3.32). The delay calibration in Equation (4.12) allows the FMDU to provide optical frequency modulation of the LD in t and demodulation of the transmitted interference signal occurring later at $t'' \approx t''_{\text{c}}$ by compensating for the delay contributions from the electronics, optics, and signal processing.

4.5 Digital Signal Processing

The digital signal processing (DSP) procedure implemented in the FPGA of the FMDU demodulates the sampled detector voltage, V_{det}, to recover the OPD dependent phase, φ (Equations (3.5b) and (3.21)), that ultimately gives the measured displacement. This process includes three steps: normalization that transforms V_{det} into a normalized SFM signal, U, (Section 4.5.1); the demodulation of U to obtain a wrapped phase difference, $\Delta\varphi$, (Section 4.5.2); and phase unwrapping of $\Delta\varphi$ to obtain the unwrapped OPD dependent phase, φ. (Section 4.5.3).

FPGA manufacturers provide "cores" as part of their development tools, which in essence, form a standard library for the hardware, much like how software programming languages include standard libraries with commonly used constants, functions, algorithms, and data structures. For some applications, it is then possible to program an FPGA without writing a single line of code by simply integrating the provided cores into a design. Due to the specialized processing required for the SFM technique, nearly all the code for the normalization, demodulation, and phase unwrapping was handwritten and consisted of ∼8700 lines of code including production and testing modules. Two Xilinx coordinate rotation digital computer (CORDIC) cores [225, 226] were used for the square root in the normalization and the arctangent to recover phase from the demodulated quadrature. The advantage of a handwritten DSP pipeline is that the latency of every component can be tightly controlled so that the normalization delay, τ_{norm}, discussed in Section 4.4.3 is correctly compensated.

4.5.1 Normalization

The normalization step prepares V_{det} for demodulation by producing U, which is representative of V_{det} but with the following applied: filtering of high frequencies, elimination of the DC and power modulation offsets, and removal of the amplitude modulation introduced by the bias current modulation of the LD. The procedure is

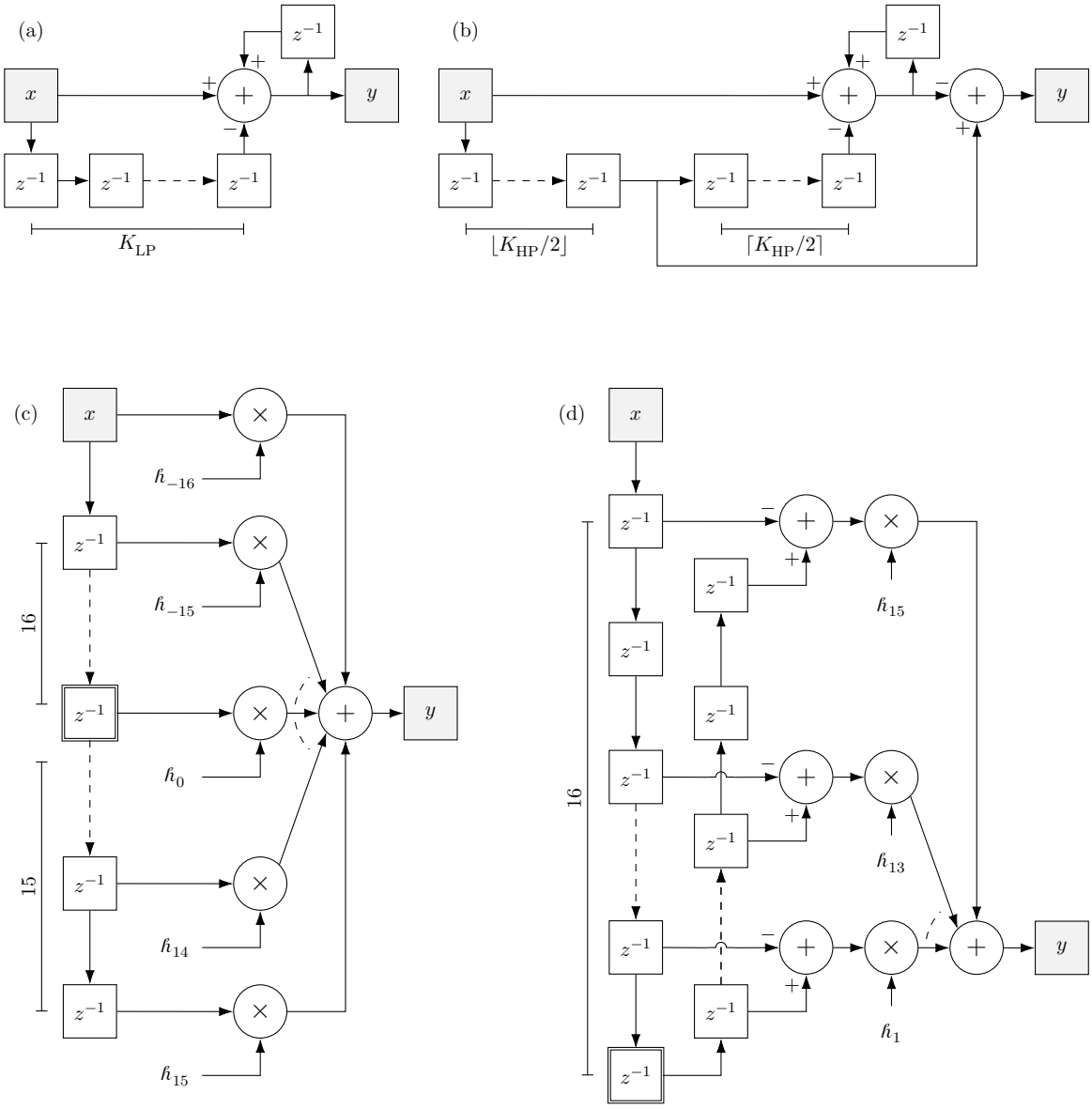

Figure 4.11: Topologies for several implemented signal processing components. Recursive running sum filters in (a) and (b) show low-pass and high-pass filters with widths of K_{LP} and K_{HP}, respectively. A 32-point Hilbert transform with expanded coefficients is shown in (c); the same filter is shown in (d) with the (implemented) folded topology that eliminates even $\hbar_n = 0$ terms and leverages the $\hbar_n = -\hbar_n$ symmetry to reduce the number of multiplications by a factor of four. Dashed arrows indicate where repeated components are omitted; x are inputs; y are outputs; z^{-1} is a unit delay; non-boxed values are constants; double-bordered nodes are highlighted for reference in the text.

shown in Figure 4.12 with the following substeps that may be individually enabled: low-pass filtering of high frequencies (LP), first stage high-pass filtering for DC and modulation offset removal (HP1), second stage high-pass filtering (HP2), and correction of the signal power modulation envelope (amplitude normalization) based on a Hilbert transform. A second high-pass filter is included to optionally increase the roll-off when enabled.

Low-pass and high-pass filters are implemented using recursive running sums shown in Figure 4.11a and Figure 4.11b. The high-pass filter is implemented by subtracting a low-pass filtered value from the input signal. In the FPGA these are implemented using circular buffers in BRAM for the long delay lines. The filtering width, K, is realized by modifying the pointers into the buffer. Although the filters have a simple implementation, the buffering requires many on-chip resources. The FMDU supports the demodulation of up to eight simultaneous axes, this number being limited by the available BRAM on chip.

The Hilbert transform takes as an input a real signal and yields a real signal with the frequency components of the input phase shifted by $\pi/2$ [227]. This property is leveraged in amplitude normalization to obtain a complex valued signal where the imaginary part is equal to the real part phase shifted by $\pi/2$ so that the instantaneous amplitude can be determined from the magnitude. The discrete Hilbert transform [228] of signal, x, may be written as

$$\mathcal{H}\{x\}[n] = x[n] * \hbar_n = \sum_{m=-\infty}^{\infty} x[n-m]\hbar_m \tag{4.13}$$

where $*$ is convolution and $\hbar_n$ are the discrete Hilbert transform coefficients given by

$$\hbar_n = \begin{cases} 0 & n \text{ even} \\ \frac{2}{\pi n} & n \text{ odd.} \end{cases} \tag{4.14}$$

By noticing that $\hbar_n = -\hbar_{-n}$ and that $\hbar_n = 0$ for even n, the Hilbert transform can then be rewritten as

$$\mathcal{H}\{x\}[n] = \sum_{m>0,\text{ odd}}^{\infty} \big(x[n-m] - x[n+m]\big)\hbar_m. \tag{4.15}$$

As a real implementation in the FPGA is limited by the size of the hardware, a 32-point Hilbert transform defined over m from -16 to 15 is taken, which can be written as

$$\mathcal{H}_{32}\{x\}[n] = \sum_{m=-16}^{15} x[n-m]\hbar_m \tag{4.16a}$$

$$= \sum_{m>0,\text{ odd}}^{15} \big(x[n-m] - x[n+m]\big)\hbar_m. \tag{4.16b}$$

An implementation of the discrete Hilbert transform from Equation (4.16a) with 32 coefficients is shown in Figure 4.11c. The *folded* second form of the 32-point Hilbert transform in Equation (4.16b) is shown in Figure 4.11d, where folding of the delay

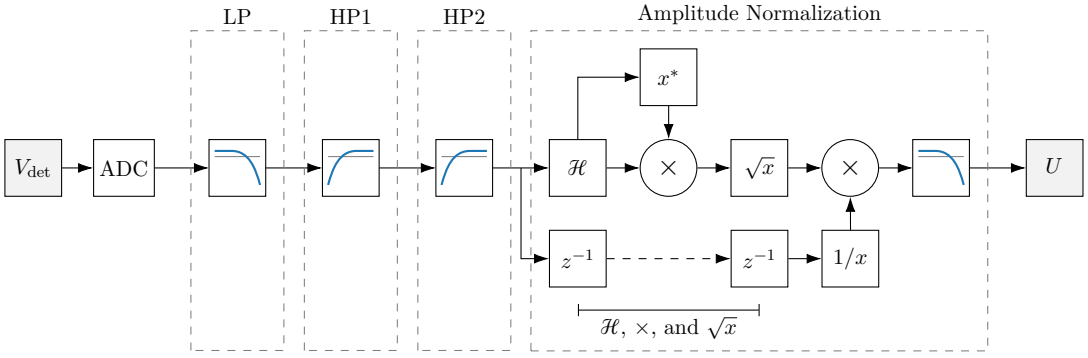

Figure 4.12: Topology of the filtering and normalization step. $\mathcal{H}$ is a Hilbert transform, x^* is complex conjugation, z^{-1} is a unit delay, and $1/x$ is a multiplicative inverse. Substeps are denoted by the dashed boxes and can be individually enabled or disabled: LP is low-pass filtering; HP1 and HP2 are high-pass filtering. Although the Hilbert transform defined in the text takes as input a real signal and gives a real signal as output, for simplicity in the diagram, $\mathcal{H}$ outputs a complex number where the real part is the original signal and the imaginary part is the input with a $\pi/2$ phase shift.

line to exploit that $\hbar_n = -\hbar_{-n}$ and $\hbar_n = 0$ for even n reduces the required number of multiplications by a factor of four. The latter (Figure 4.11d) is implemented in the FPGA, where the real part is taken from the double bordered node corresponding to the $n = 0$ term and the imaginary part is taken from the output, y.

4.5.2 Demodulation

Signal demodulation is performed by multiplying a complex carrier, C, from Equations (3.8) and (3.30), the window function, W, from Equations (3.9) and (3.31), and U produced from the normalization step in Section 4.5.1, followed by low-pass filtering and decimation. These steps are shown in Figure 4.13. The carriers and window functions are precomputed by the PS and passed to the PL where they are stored in circular BRAM buffers like the filters described above. The PL streams the delay-compensated carrier for each axis to the demodulation pipeline where they are multiplied into U and subsequently low-pass filtered and decimated.

As discussed in Section 3.3.2, the demodulated signal must be low-pass filtered with a cutoff at $f_\mathrm{m}/2$. This is prohibitively expensive using the low-pass filter in Figure 4.11a and then taking one sample every second modulation period. Given the sampling frequency of $f_\mathrm{s} = 100\,\mathrm{MHz}$ and typical modulation frequency of $f_\mathrm{m} = 100\,\mathrm{kHz}$, employing a recursive running sum low-pass filters requires a BRAM buffer with at

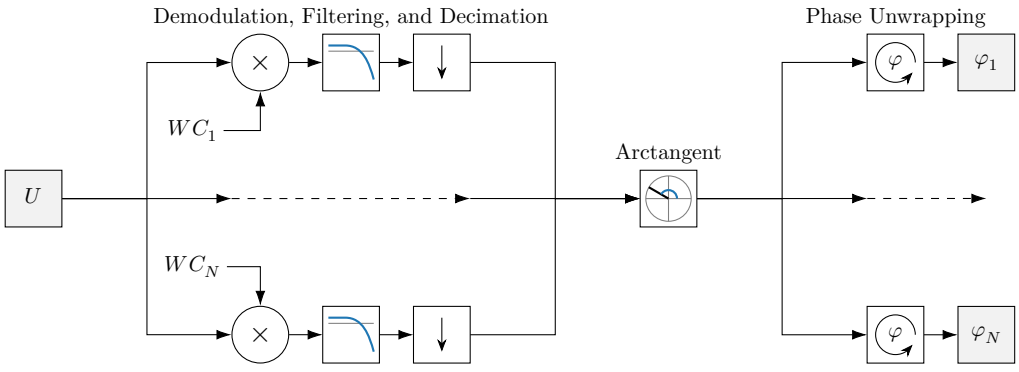

Figure 4.13: Topology of the demodulation and phase unwrapping steps covering the demodulation process outlined in Section 3.2.6. Dashed arrows indicate where repeated components are omitted; ↓ denotes decimation.

least $2f_s/f_m = 2000$ samples *per axis*. To circumvent this issue, filtering and decimation are combined into a specialized filter that exploits the fact that an equivalent recursive running sum low-pass filter would consider all samples over two modulation periods to produce an output that is then decimated to a rate of $f_m/2$. The specialized filter employs two interleaved accumulators that sum all samples over two modulation periods and produces an equivalent output to a recursive running sum filter downsampled to f_m while occupying a small (and constant) space regardless of the modulation frequency. Since the accumulator-based filters are interleaved and decimate to $f_m/2$, the overall sampling rate of the quadrature recovered by the demodulation is equal to f_m.

4.5.3 Phase Unwrapping

After a quadrature signal is obtained from the demodulation procedure described in Section 4.5.2, it is converted to a phase using an arctangent. Figure 4.13 shows that one arctangent module is shared between all axes. Like the issue with recursive running sum filters described above, the arctangent has a large footprint and the FPGA did not have enough logic resources for all eight demodulation pipelines to each have their own integrated arctangent. Fortunately, the arctangent has a large idle time due to decimation of the quadrature and one arctangent can be shared among all axes. The quadrature samples are taken from the demodulation pipelines for each axis and serialized into a single stream that can be passed through the fully pipelined arctangent. The computed phases are subsequently re-parallelized and fanned out to individual processes for phase unwrapping.

The phase unwrapping procedure processes the point-to-point OPD dependent wrapped phase differences, $\Delta\varphi$. To track displacements greater than one wavelength

of the laser, the phase is unwrapped to obtain φ using the basic unwrapping algorithm

$$\varphi[n+1] = \varphi[n] + \Delta\varphi[n] + \begin{cases} 2\pi & \Delta\varphi[n] < -\pi/2 \\ -2\pi & \Delta\varphi[n] > \pi/2 \\ 0 & \text{otherwise.} \end{cases} \quad \text{[rad]} \tag{4.17}$$

In the FMDU implementation, the phase is represented by normalized radians where the value 2π rad corresponds to the normalized value of 1. The unwrapped phase corresponds to the fractional number of wavelengths representing the change in OPD. This number is transferred out of the PL in the FPGA using DMA to the PS. The normalized phase values and the calibrated central wavelength, λ_c, based on the modulation and LD parameters, are packaged by the PS and streamed to a PC where the change in OPD is recovered from the product of λ_c and φ.

4.6 Fibre Preparation, Termination, and Polishing

When configuring a multiaxis interferometer, one must take care to set up axes from optical paths with specific lengths, as discussed in Chapter 3, and particularly, Section 3.4. In some cases, it is necessary to introduce an added delay so that the OPDs produce demodulatable axes. Delays can be added in fibre, which enables space efficient delays to be added in situations that are difficult to achieve in free space. Commercially available fibre patch cords are typically delivered in increments of 50 cm and 100 cm, and while it is possible to purchase custom length fibre patch cords, they are expensive and usually delivered with ∼10 cm tolerance. By terminating fibres in-house, arbitrary fibre patch cord lengths can be produced with <1 cm tolerance in one day. The laboratory is equipped with the fibre termination and splicing supplies outlined in Appendix C.4; fibre termination parts are listed in Table C.16 and select specifications of the arc fusion splicer in Table C.17. Equipment part numbers are

omitted to keep this section readable, and Appendix C.4 should be referred to for details on the fibre preparation equipment.

Termination and polishing of both ferrule-connector physical contact (FC/PC) and FC/APC ferrules are performed in-house. FC/PC terminations are plane polished orthogonal to the fibre axis and give ∼4 % Fresnel reflections [10] when the beam is launched into free space. FC/APC terminations are plane polished at 8° to the fibre axis normal so that Fresnel reflections do not stay guided in the core. In most interferometer configurations discussed, an FC/PC termination is used in the reference path and FC/APC terminations are used everywhere else.

When terminating a fibre, the fibre jacket and coating is stripped using a furcation/buffer stripper, and the FC/PC or FC/APC ferrule and connector are epoxied to the fibre. Figure 4.14a shows Thorlabs SMF-28-J9 fibre [229] epoxied into a Thorlabs 30126A9 FC/APC ferrule [230]. The fibre is single-mode at 1550 nm and conforms to the ITU-T G.652 fibre design [231]. A long pot life epoxy is injected into the 126 µm bore of a ferrule connector and the 125 µm fibre is pushed through; the tolerance on the

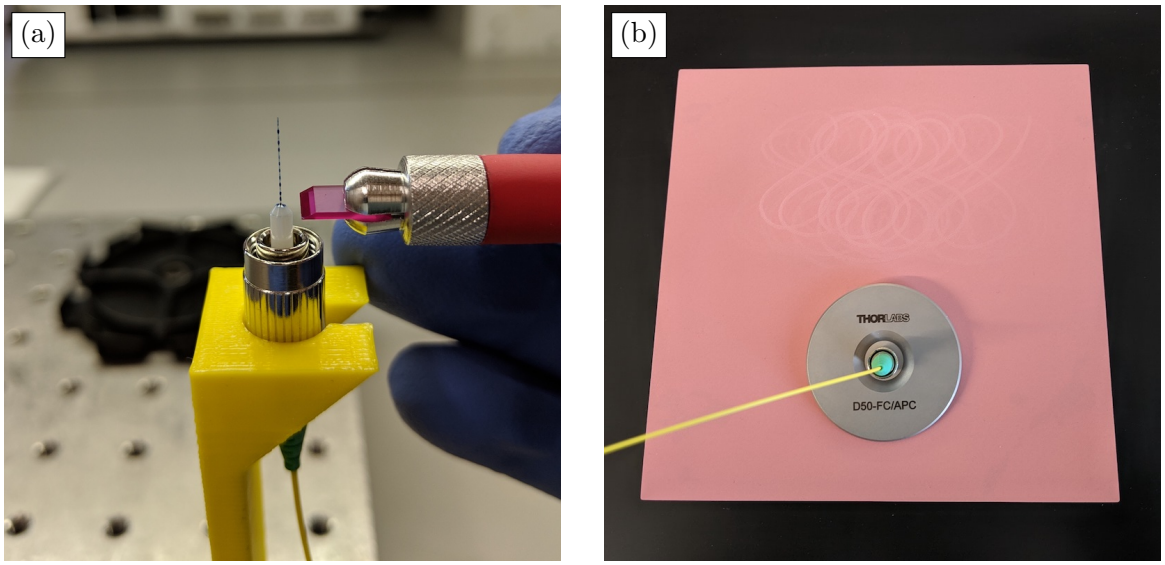

Figure 4.14: (a) Cleaving of an epoxied fibre in an FC/APC connector using a ruby scribe and (b) polishing of an FC/APC connector using a ferrule-connector angled physical contact (FC/APC) polishing puck on 3 µm lapping film

radii is small to ensure that concentricity of the fibre within the ferrule. Figure 4.14a shows the fibre after curing with beads of blue epoxy were deposited along the length of the fibre from its insertion into the epoxied ferrule. The fibre protruding from the ferrule is cleaved with a ruby scribe and polished on successively finer diamond lapping films with 30, 6, 3, 1, and 0.02 µm grits. Figure 4.14b shows the polishing of an FC/APC connector. A polishing puck holds the FC/APC ferrule at the correct angle against the lapping film. The lapping film is placed on a Thorlabs NRS913A polishing pad [232] to provide a soft surface for polishing that slightly radiuses the ferrule for better contact between the cores of two connectors when inserted into a mating sleeve. The fibre is polished in a figure-eight pattern across the film, which

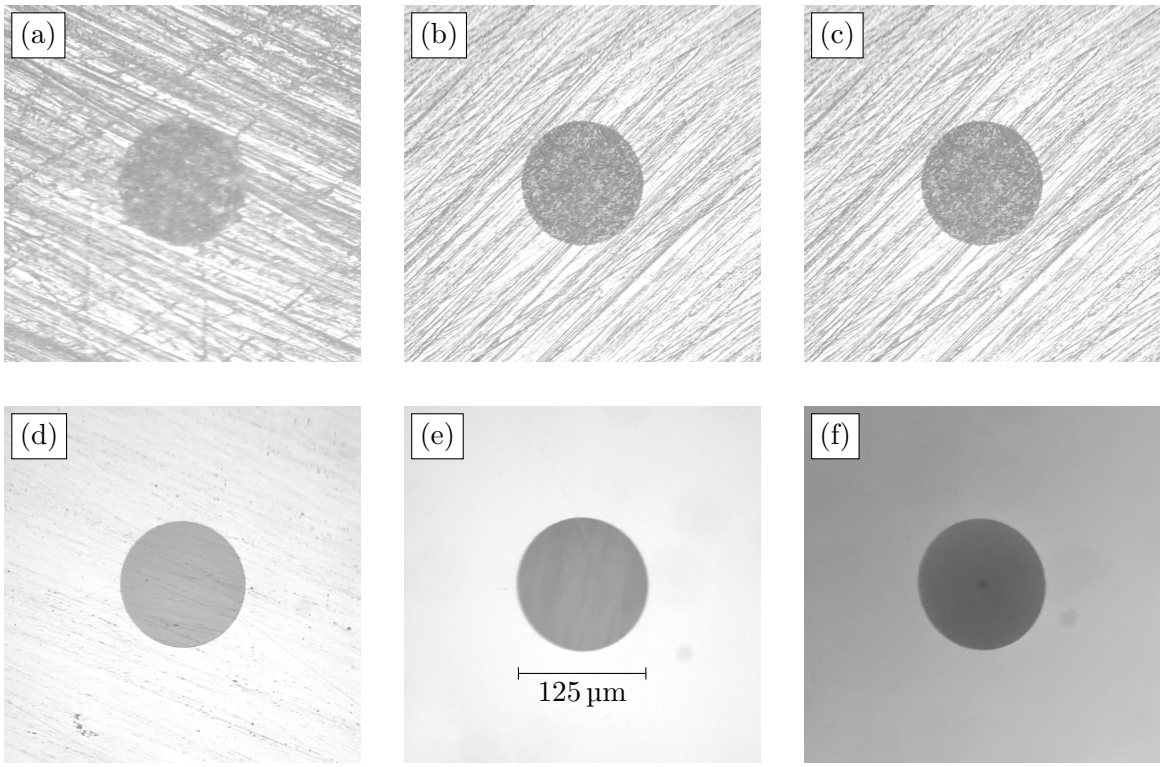

Figure 4.15: Polishing of an FC/PC connector. Images (a), (b), (c), and (d), show the connector face with direct illumination after each polishing phase with 30, 6, 3, and 1 µm lapping film, respectively; the final finish after 0.02 µm lapping film is shown in (e) with direct and in (f) oblique illumination. The core visible in the centre of the cladding in (f). The fibre is Thorlabs SMF-28-J9 with 8.2 µm and 125 µm core and cladding diameters, respectively [229].

is visible above the puck. For FC/PC termination, the same procedure is followed, except a polishing puck that holds the fibre perpendicular to the polishing surface is used.

Figure 4.15 shows images of Thorlabs SMF-28-J9 fibre [229] in a Thorlabs 30126C9 FC/PC ferrule [233] after each polishing phase. The images were recorded through a Thorlabs FS201 [234] fibre inspection microscope with an optical magnification of 200×. In Figures 4.15a to 4.15e, the 125 µm cladding of the fibre is visible; in Figure 4.15f, the fibre face is illuminated from a different angle and the 8.2 µm core can be seen at the centre of cladding. Fibre splices are not shown in this section, however, an Inno Instrument View 7 arc fusion splicer [235] was utilized to construct the fibre attenuator used in Section 6.5 and tapered fibres in Section 7.5.

4.7 Conclusions

In this chapter, I have described a real-time multiaxis implementation of the SFM technique introduced in Chapter 3. The implementation is referred to as the frequency-modulation-demodulation unit (FMDU) for the rest of this thesis. I was responsible for the design, procurement, and integration of the hardware and software, and extensive calibration of the hardware components. The hardware breaks along two lines, one of which is the hardware associated with the DSP (FPGA, DAC, and ADC), and the other is the hardware associated with the photonics (LD, LD controller, optics, custom fibres, and custom detector). Similarly, the software has two principal components. The first is the digital signal processing to perform the computation of the demodulation procedure outlined in Chapter 3 as fast as possible, and the second the control software which interfaces with the FMDU to obtain the end result. To put this chapter in context of the work conducted in this thesis, it represents over half the effort in implementing the SFM technique in hardware and

software and lays the framework for applying it to eight applications discussed in Chapter 7.

Chapter 5

Multiaxis Sinusoidal Frequency Modulation Interferometry Uncertainty Analysis

In this chapter I present an uncertainty analysis of the sinusoidal frequency modulation (SFM) technique based on simulations. The goal of this chapter is to explore the following:

1. The phase uncertainty of a typical interferometer presented in the applications of Chapter 7.
2. The optical path difference (OPD) separation required in a multiaxis interferometer to suppress uncertainty contributions due to crosstalk to a desired level.
3. The improvement gained by correcting the optical power modulation arising from bias current modulation of the laser diode (LD) discussed in Section 4.3.1.

5.1 In the Literature

This section summarizes results obtained by Kissinger et al. [166, 185] that are drawn on in this thesis. The results presented in the sections on this chapter that follow (i.e., Sections 5.2 to 5.5) represent original work to this thesis.

5.1.1 Window Width

The Gaussian window proposed by Kissinger et al. confers two principal advantages over the rectangular window used by Sakai et al. [165]: the Gaussian window

function results in little to no sidelobes [185] and does not require that the window width or OPDs be tuned so that an integral number of oscillations occur in the selected region of the signal [166] These advantages combined allow arbitrarily spaced OPDs that satisfy the minimum OPD separation rules in Equation (3.42). Kissinger determined that $\sigma = 0.0225$ is the optimal Gaussian window width as it minimizes the baseband suppression ratio, which is the ratio between the signal level at the highest order nodes and DC in Figures 3.9d and 3.9e. A value of $\sigma = 0.0225$ is assumed in this thesis, but variations in σ are explored in this section to demonstrate the effects.

5.1.2 Quantization

By simulation, Kissinger showed that the phase uncertainty amplitude of cyclic nonlinearities is bit width limited with the greatest linearity at $\sigma = 0.0225$ and that the phase uncertainty amplitude approximately halves for every 1 bit increase in the digital signal processing (DSP) bit width [185]. In the frequency-modulation-demodulation unit (FMDU) implementation, the DSP bit width is limited by the 14 bit analog-to-digital converter (ADC), however, the numeric representation of the fixed-point numbers in DSP is large enough at every stage so that the least significant bits (LSB) are never truncated.

5.2 Modulation and Demodulation Parameters

Phase uncertainties are simulated for a single-axis interferometer to understand uncertainty contributions that depend on SFM modulation and demodulation parameters. A general example of the procedure is illustrated in Figure 5.1: the demodulation of a simulated interference signal results in the quadrature in Figure 5.1a with the phase uncertainty 18 mrad rms in Figure 5.1b and Lissajous plot of the phase in Figure 5.1c. The analysis in this section consists of several simulations like that of Figure 5.1 to quantify effects related to the optical frequency modulation amplitude,

ν_{A}, the modulation frequency, f_{m}, the OPD, Λ, and Gaussian window width, σ. To consistently quantify the behaviours, all results are presented as an average of the phase uncertainty over a phase range of 2π under the specified conditions.

The simulations in this section are all run for a realistic SNR $= 10^3$ of the interference signal before demodulation. As part of the applications explored in Section 7.1 and Section 7.4, the signal-to-noise ratios (SNR) of practical multiaxis and single-axis interferometers were estimated at ∼1000 and ∼1200, respectively. SNR is defined as [236]

$$\mathrm{SNR} = \frac{P_{\mathrm{signal}}}{P_{\mathrm{noise}}} = \left(\frac{s}{n}\right)^2, \tag{5.1}$$

where P_{signal} is the average power of the signal, P_{noise} is the average power of the noise, s is the root mean square (RMS) amplitude of the signal, and n is the RMS amplitude

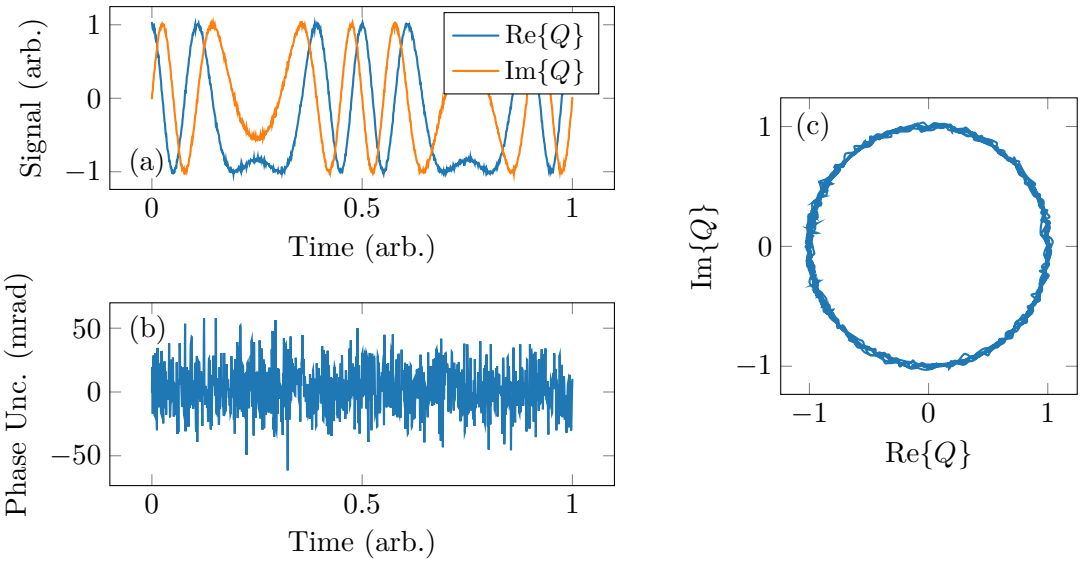

Figure 5.1: Phase uncertainties in an SFM quadrature signal with in-band demodulation at $f_{\mathrm{m}} = 100\,\mathrm{kHz}$ and $\nu_{\mathrm{A}} = 1.5\,\mathrm{GHz}$ moving a short distance about an OPD of $\Lambda = 1\,\mathrm{m}$. For visualization purposes, a large Gaussian random noise is added to the interference signal before demodulation such that SNR $= 10$ (in practice, the SNR is 10^3 but 10 is used in these plots for visualization purposes). The quadrature signal in (a) recovered using the SFM technique carries a sinusoidal OPD dependent phase. Uncertainties in the quadrature are shown in (b), averaging to 18 mrad rms over the entire time. A Lissajous figure is plotted in (c) in which the phase uncertainty is visible.

of the noise. The introduced noise is Gaussian random with a mean of zero, so the standard deviation of the noise is equal to the RMS, thus, by Equation (5.1), the noise is generated with an RMS amplitude of $n = s/\sqrt{\text{SNR}}$.

One must keep in mind that the SPICA Far-Infrared Instrument (SAFARI) Fourier transform spectrometer (FTS) requirements outlined in Table 1.1 call for 10 nm rms uncertainty in a 20 Hz bandwidth, which at a wavelength of 1550 nm in a typical double-passed interferometer like most of Chapter 7, corresponds to a phase uncertainty of 81 mrad rms. The example of Figure 5.1 shows 18 mrad rms with an SNR of 10, which already exceeds the SAFARI FTS requirement. In this context, an SNR of 10^3 is considered as it is representative of the interferometers explored in Chapter 7.

5.2.1 Optical Frequency Modulation Amplitude

The optical frequency modulation amplitude, ν_A, was varied for select OPDs. An interferometer was simulated with $f_\text{m} = 100\,\text{kHz}$, $\sigma = 0.0225$, and sampling frequency $f_\text{s} = 100\,\text{MHz}$ for OPDs of 0.5, 1, and 2 m over optical frequency modulation

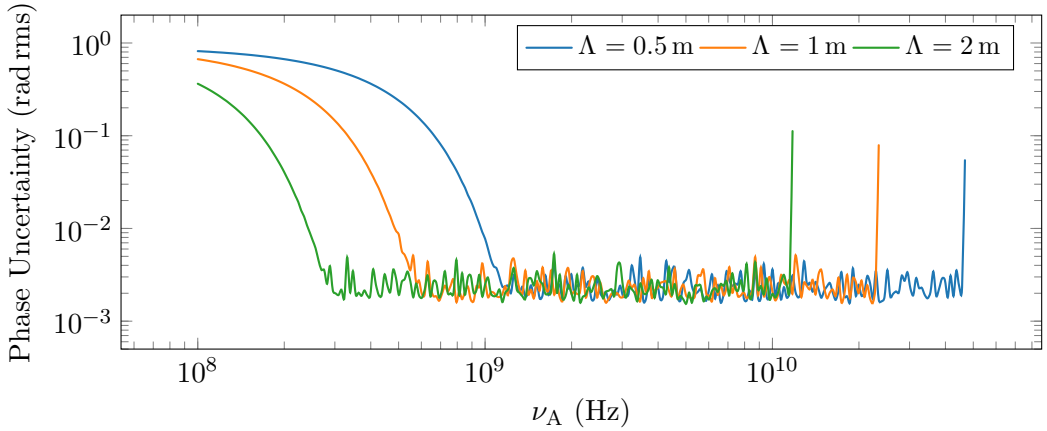

Figure 5.2: Simulation of optical frequency modulation amplitude effects on phase uncertainty with SNR = 10^3 of the interference signal. Parameters of $f_\text{m} = 100\,\text{kHz}$, $\sigma = 0.0225$, and $f_\text{s} = 100\,\text{MHz}$ were used for OPDs of 0.5, 1, and 2 m. Curves for each simulation are plotted up to the Nyquist frequency where the beat frequency, f_b^+, exceeds half the sampling rate, $f_\text{s}/2$, and can be seen on the right side of the plot where the uncertainty sharply increases. Over the flat (i.e., in-band) regions the average uncertainty is 2.4 mrad rms.

amplitudes over a range centred on the typically used 1.5 GHz value in Chapter 7. Simulated results are shown in Figure 5.2. The knees where the curves plateau occur at ν_A values of approximately 1.2, 0.6, and 0.3 GHz for the OPDs of 0.5, 1, and 2 m, respectively. These ν_A values all map to the same $A \approx 12.5$ rad. In the flat regions where demodulation is in-band, the average phase uncertainty is 2.4 mrad rms with a 0.7 mrad rms standard deviation.

The $A \approx 12.5$ rad determined above *could* be the minimum phase modulation amplitude separation for a single-axis interferometer, ΔA_{min}, defined in Section 3.3.1, however, this is not sufficient in a multiaxis interferometer. While demodulation is in-band at these points corresponding to $A \approx 12.5$ rad for this isolated single-axis simulation, it must be doubled in the presence of multiple axes to ensure that the Gaussian frequency bands do not overlap as shown in the crosstalk analysis of Section 5.3.

Although not plotted, as SNR $\to \infty$, the flat region of the model bottoms out at $\sim 10^{-15}$ rad rms due to the numeric representation. This value is nonsensical in practice, however, in the context of the model, it suggests that the SFM technique does not have inherent nonlinearities and corroborates the results reported by Kissinger [185] that are summarized in Section 5.1.2. The baseline of $\sim 10^{-15}$ rad rms as SNR $\to \infty$ is consistent for all presented models, but will not be mentioned again in this section.

5.2.2 Modulation Frequency

The modulation frequency was varied for several OPDs to simulate the practical effects of the modulation frequency on the phase uncertainty with a finite sampling rate. An interferometer was simulated with $\nu_A = 1.5$ GHz, $\sigma = 0.0225$, and $f_s = 100$ MHz for OPDs of 0.5, 1, and 2 m over a range of modulation frequencies. Figure 5.3 shows consistent behaviour for all three OPDs. At the $f_m = 100$ kHz

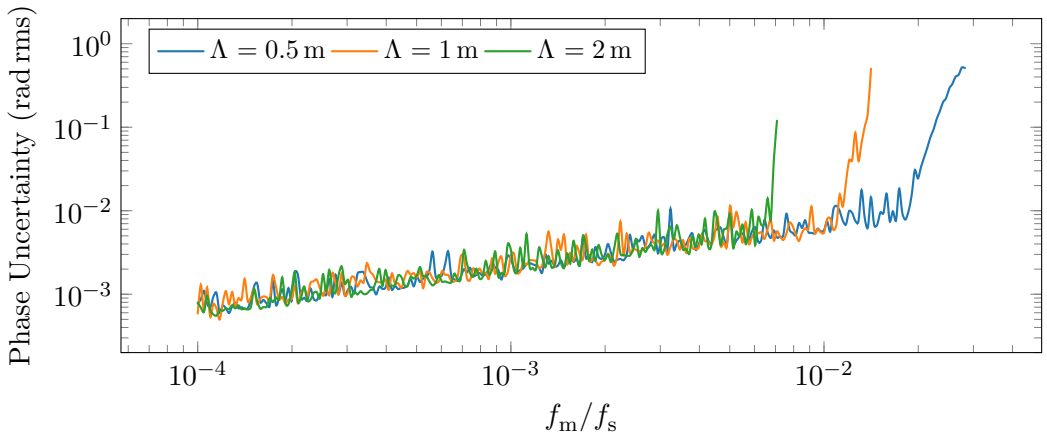

Figure 5.3: Simulation of modulation frequency effects on phase uncertainty with SNR $= 10^3$ of the interference signal. Parameters of $\nu_\mathrm{A} = 1.5\,\mathrm{GHz}$, $\sigma = 0.0225$, and $f_\mathrm{s} = 100\,\mathrm{MHz}$ were used for OPDs of 0.5, 1, and 2 m. Curves for each simulation are plotted up to the Nyquist frequency where the beat frequency, f_b^+, exceeds half the sampling rate, $f_\mathrm{s}/2$, and can be seen on the right side of the plot where the uncertainty sharply increases. The uncertainty in all curves starts at ∼0.7 mrad rms around $f_\mathrm{m}/f_\mathrm{s} = 10^{-4}$ and increases to ∼5 mrad rms at $f_\mathrm{m}/f_\mathrm{s} = 5 \times 10^{-3}$; at $f_\mathrm{m}/f_\mathrm{s} = 10^{-3}$ (the typical value in applications of Chapter 7) the uncertainty is 2.4 mrad.

modulation used in all applications presented in Chapter 7, the phase uncertainty is 2.4 mrad with a standard deviation of 0.7 mrad, which is identical to the uncertainty determined in Section 5.2.1. Furthermore, these results suggests that greatly oversampling the detector output signal reduces the phase uncertainty, however, this may not be economical in practice.

5.2.3 Window Width

Using the typical modulation parameters of $\nu_\mathrm{A} = 1.5\,\mathrm{GHz}$, $f_\mathrm{m} = 100\,\mathrm{kHz}$, and $f_\mathrm{s} = 100\,\mathrm{MHz}$ from applications in Chapter 7, the effects of window width, σ, at several OPDs are evaluated for SNR $= 10^3$ to obtain the data shown in Figure 5.4. The interferometer OPD is fixed at $\Lambda = 1\,\mathrm{m}$ and the OPD encoded by the carrier is varied over 0 to 2 m to yield the OPD deviation on the horizontal axes of Figure 5.4 for a range of σ values; the OPD deviation is the difference between the OPD of the interferometer and the OPD of the carrier used in demodulation. Figure 5.4b plots

cross sections from Figure 5.4a at selected σ values of 0.007 12, 0.0225, and 0.0712 that span one decade.

Figure 5.4 shows that the window can be tuned as a trade-off between phase uncertainty and range. The $\sigma = 0.00712$ case offers improved range by flattening the curve at the cost of an increase in average phase uncertainty, the default $\sigma = 0.0225$ offers balanced performance between range and phase uncertainty, while the $\sigma = 0.0712$ case suggests that a negligible improvement in uncertainty can be gained at the cost of a significantly reduced range. Furthermore, $\sigma = 0.0225$ corresponds to the low phase uncertainty region of Figure 5.4a and agrees with the results from Kissinger [185] summarized in Section 5.1.1 insomuch as the $\sigma = 0.0225$ window width offers a large range with relatively low phase uncertainty. Within ±10 cm of zero OPD deviation, the $\sigma = 0.0225$ and SNR $= 10^3$ curve has an average 2.6 mrad rms phase uncertainty with 0.8 mrad rms standard deviation and agrees closely to the results from Sections 5.2.1 and 5.2.2.

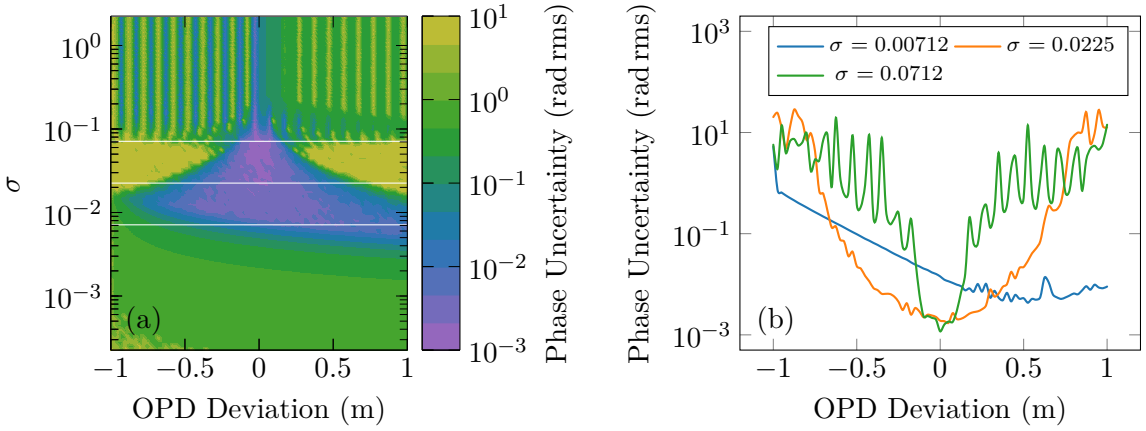

Figure 5.4: Simulation of window width and OPD effects on phase uncertainty with SNR $= 10^3$ of the interference signal. Parameters of $\nu_A = 1.5$ GHz, $f_m = 100$ kHz, and $f_s = 100$ MHz were used. The axis is kept fixed at an OPD of 1 m while the carrier is "slid" along it for the modulation amplitude at the given OPD deviation. The carrier is perfectly in-band at an OPD deviation of zero. The white horizontal lines from bottom to top in (a) are the $\sigma = 0.007\,12$, 0.0225, and 0.0712 cross sections plotted in (b). The $\sigma = 0.0225$ curve has an uncertainty of 2.6 mrad rms over a ±10 cm OPD deviation.

5.2.4 Summary

The analyses in Sections 5.2.1 to 5.2.3 all show that the phase uncertainty for the typical interferometer configurations in Chapter 7 having $\nu_A = 1.5\,\text{GHz}$, $f_m = 100\,\text{kHz}$, OPDs on the order of 1 m, and SNR $\approx 10^3$ exhibit theoretical phase uncertainties in the range of 2.4 to 2.6 mrad rms, which exceeds the SAFARI FTS requirements that imply 81 nm rms in a double-passed interferometer. Over the range of window widths investigated, an overall trade-off between the window width, phase uncertainty, and range was observed. The optimal width of $\sigma = 0.0225$ reported by Kissinger [185] was corroborated and the results showed that increasing the window width results in an increased measurement range with greater uncertainty and decreasing the width offers a slight uncertainty reduction at the cost of a greatly reduced range. The average value of 2.5 mrad rms corresponds to an OPD uncertainty of 0.6 nm rms at $\lambda_c = 1550\,\text{nm}$, and in the double-pass Fizeau interferometer configuration used for displacement measurements in Chapter 7, represents a 0.3 nm rms displacement uncertainty. This should be compared to the results in Section 7.4, which in atmosphere demonstrate 0.5 nm rms in a 50 kHz bandwidth and 0.4 nm rms in a 20 Hz bandwidth and exceeds the SAFARI FTS uncertainty requirement by over an order of magnitude.

5.3 Crosstalk

Multiaxis interferometers experience crosstalk due to leakage of the signal power from one band to another, crosstalk effects were examined in a simulation with two conflicting interferometer axes. The laser modulation was simulated with $f_m = 100\,\text{kHz}$ and $\nu_A = 1.5\,\text{GHz}$ — the same as the simulations presented in Section 5.2 and most applications of Chapter 7 — and a reference axis was placed at an OPD of $\Lambda_1 = 1\,\text{m}$. An interference signal was simulated at a sample rate $f_s = 100\,\text{MHz}$ and was demodulated by a carrier in-band for Λ_1. The contribution to the interference

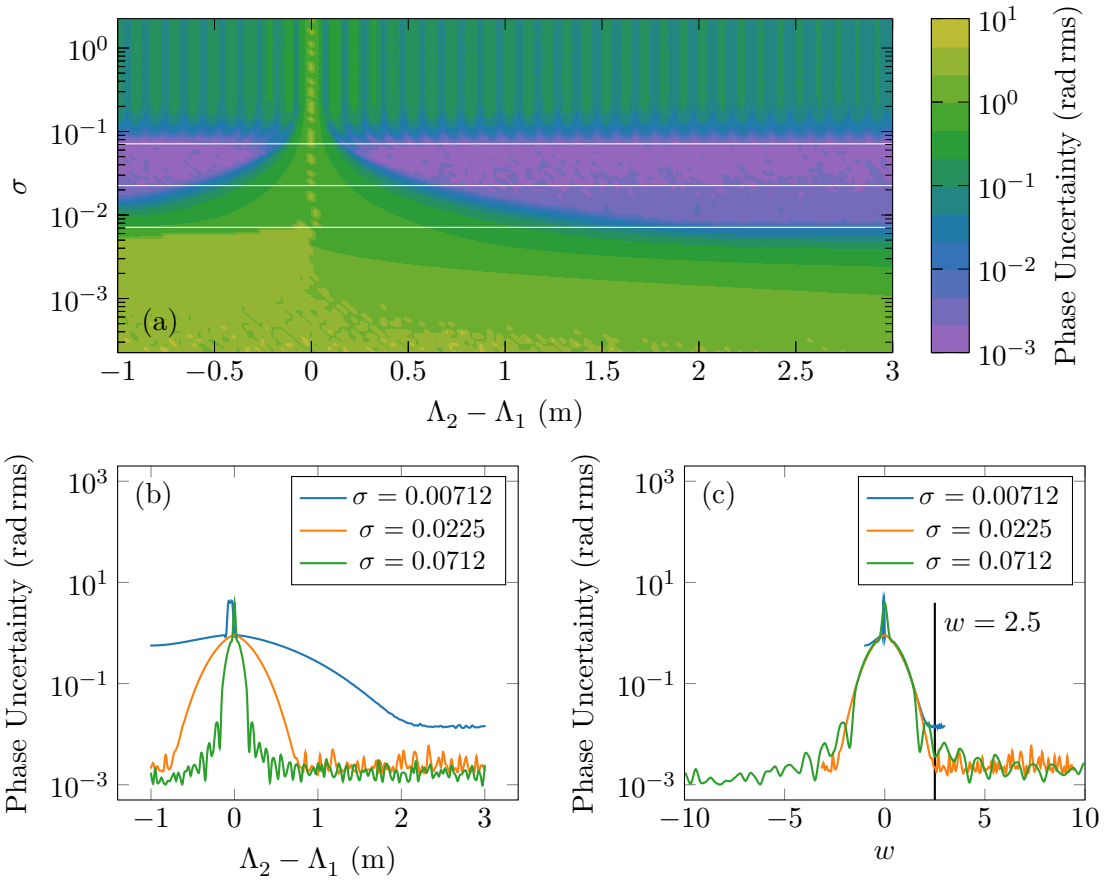

Figure 5.5: Simulation of crosstalk phase uncertainty as a function of window width and OPD of two axes using $\nu_A = 1.5\,\text{GHz}$, $f_m = 100\,\text{kHz}$, and $f_s = 100\,\text{MHz}$ for an interference signal with SNR $= 10^3$. One axis is kept fixed at an OPD of $\Lambda_1 = 1\,\text{m}$ while the other, Λ_2, is "slid" along it. The axis of Λ_1 OPD is demodulated in-band by a fixed carrier and the axes overlap when the OPD offset is zero. The horizontal white lines in the heatmap of (a) correspond to σ values of 0.007 12, 0.0225, and 0.0712 (from bottom to top) plotted in (b) and (c). Curves from (b) are replotted in (c) as a function of w the band separation coefficient, w, computed by Equation (5.2) using $\Delta\Lambda_{\text{min}} = \Lambda_2 - \Lambda_1$. From the $\Lambda_2 - \Lambda_1 \geq 0.8\,\text{m}$ range in (b) corresponding to the $w \geq 2.5$ range in (c) where crosstalk effects are minimal, the phase uncertainty for the $\sigma = 0.0225$ case is 2.5 mrad rms.

signal from a second axis was added, where the OPD of the axis, Λ_2, was varied, and in effect, was "slid" along Λ_1 such that they overlap at 1 m where $\Lambda_2 - \Lambda_1 = 0$ corresponding to the point in Figure 5.5 where the crosstalk is greatest.

Figure 5.5a shows the phase uncertainty for Λ_2 over 0 to 4 m (i.e., $\Lambda_2 - \Lambda_1$ over -1 to 3 m) and σ taken over 0.0225×10^{-2} to 0.0225×10^{2}, which spans four decades

centred at 0.0225. Figures 5.5b and 5.5c show cross sections of Figure 5.5a indicated by the white horizontal lines denoting the σ values taken over one decade at 0.007 12, 0.0225, and 0.0712. The curves in Figures 5.5b and 5.5c illustrate how the phase uncertainty plateaus as the crosstalk diminishes. Regardless of σ, there is a sharp increase in phase uncertainty when $\Lambda_2 \approx \Lambda_1$ as these two axes occupy the same frequency band. When the OPDs change to deviate by merely a few centimetres, Λ_2 moves sufficiently out-of-band for a sharp drop in phase uncertainty, after which, the phase uncertainty further reduces.

Figure 5.5b can be used to estimate the minimum OPD separation, $\Delta\Lambda_{\text{min}}$, and appropriate band separation coefficient, w, in Equation (3.42). Recall that $\Delta\Lambda_{\text{min}}$ is a subjective minimum OPD separation between axes, and w is a unitless coefficient that dictates the band separation, and thus OPD separation. The $\sigma = 0.0225$ cross section plateaus on the phase uncertainty of 2.5 mrad rms with a 0.9 mrad rms standard deviation at $\Lambda_2 - \Lambda_1 = 0.8\,\text{m}$ — the same uncertainty was shown for all simulations in Section 5.2. An estimate on the lower bound for an appropriate w is obtained by writing Equation (3.42) as

$$w \approx \frac{2\sqrt{2}\pi^2\nu_{\text{A}}\sigma\Delta\Lambda_{\text{min}}}{\text{c}} \quad \text{when} \quad \Lambda \ll \frac{c}{\pi f_{\text{m}}}, \tag{5.2}$$

and taking a $\Delta\Lambda_{\text{min}} = 0.8\,\text{m}$ as the point where the effects of crosstalk diminish, which is the point that delimits the range of the Λ_1 axis and is shown by the vertical line in Figure 5.5c. By Equation (5.2), an estimate of $w = 2.5$ is found based on the modulation parameters implies that $\Delta A_{\text{min}} = 25\,\text{rad}$ in agreement with the discussion in Section 5.2.1. The range of an axis, which is the maximum demodulatable change in OPD, is then estimated by

$$\Delta\Lambda_{\text{max}} \approx \Delta\Lambda_{\text{min}} \approx \frac{w\text{c}}{2\sqrt{2}\pi^2\nu_{\text{A}}\sigma} \quad \text{when} \quad \Lambda \ll \frac{c}{\pi f_{\text{m}}}. \qquad \text{[m]} \tag{5.3}$$

Figure 5.5c replots Figure 5.5b with w on the horizontal axis rather than $\Lambda_2 - \Lambda_1$, and the horizontal span differs due to $w \propto \sigma$. Equation (5.2) is used to determine w, where $\Delta\Lambda_{\text{min}} = \Lambda_2 - \Lambda_1$. The plot in this form shows that the approximation of w above is valid for all cases since the shapes of the plots adjust based on the product $\sigma\Delta\Lambda_{\text{min}}$; the $w = 2.5$ line is drawn vertically in Figure 5.5c for positive w. As described in Section 3.3, the value of w is a choice on what provides an *acceptable* uncertainty level, but $w = 2.5$ represents a separation where crosstalk is eliminated, and the phase uncertainty is the same as that for the isolated single-axis interferometer investigated in Section 5.2. Figure 5.5c represents a key design driver since a w value can be selected from a desired phase uncertainty to determine the required OPD separation between the interferometer axes.

5.4 Filtering and Amplitude Normalization

Optical frequency modulation is achieved via bias current modulation of the LD, which as discussed in Section 4.3.1, has the side effect that the optical power is also modulated. The filtering and amplitude normalization processing steps discussed in Section 4.5 provide low-pass filtering to increase the SNR, high-pass filtering to remove the signal offset, and amplitude normalization to eliminate the signal envelope. These steps are applied to V_{det}, the photodetector amplifier readout voltage to obtain U of Equation (3.28), which is the normalized interference signal that ultimately undergoes demodulation.

Models in Sections 5.2 and 5.3 considered cases for a nominal SNR $= 10^3$ (which is representative of interferometer configurations in Sections 7.1 and 7.4) and SNR $= \infty$. The models in this section were applied to an SNR range of 10^1 to 10^5 that spans two decades on either side of the realistic SNR $= 10^3$. Three models were investigated:

1. **Unity**: the interference signal, U, from Equation (3.28) with *unity* amplitude and zero offset.

2. **Practical**: a signal representative of V_{det} in the applications presented in Chapter 7 having non-unity amplitude and non-zero offset.
3. **Normalized**: The practical signal with normalization applied.

The names in boldface are used to refer to each of the models for the rest of this section. The unity model provides the best-case phase uncertainty for a given SNR and the practical model provides the phase uncertainty when no corrections are applied so that the normalized model can be evaluated within the context of these two limits.

Simulation results in this section are all for a single-axis interferometer with the modulation and demodulation parameters $f_{\text{m}} = 100\,\text{kHz}$, $\nu_{\text{A}} = 1.5\,\text{GHz}$, and $\sigma = 0.0225$ for an interferometer having an OPD $\Lambda = 1\,\text{m}$. The parameters are the same as those used throughout Sections 5.2 and 5.3 and are representative of the interferometer configurations in Chapter 7. Steps of the demodulation procedure from Section 4.5.1 are shown in Figure 5.6. For reference, the unity interference signal and $\sigma = 0.0225$ window function are plotted; the window shows the regions of the signal that are selected for demodulation. Low-pass filtering was omitted, but HP1 and HP2 show successively better offset removal after high-pass filtering with respective

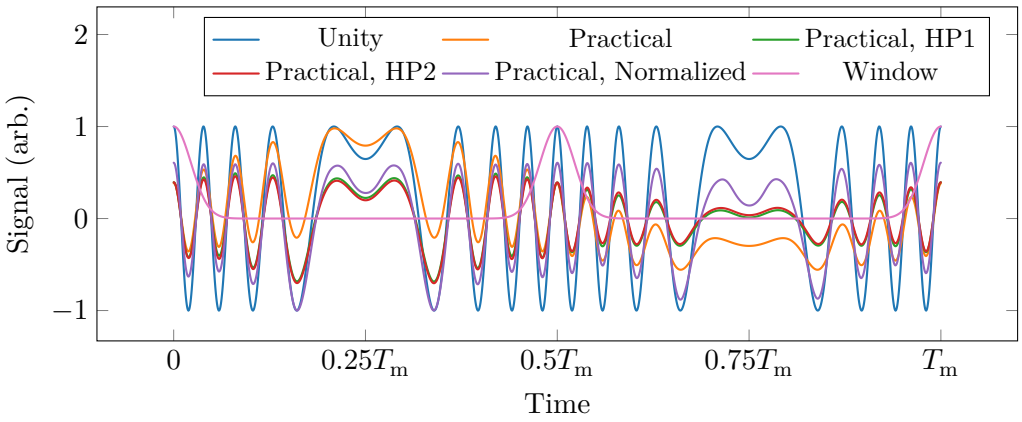

Figure 5.6: Normalization procedure for an $A = 26\,\text{rad}$ practical signal, showing the unity, practical, first and second high-pass filtered, normalized signals. The key region is under the window function, as this part of the signal is selected for demodulation; the *Practical, Normalized* signal shows a near constant amplitude over this these intervals.

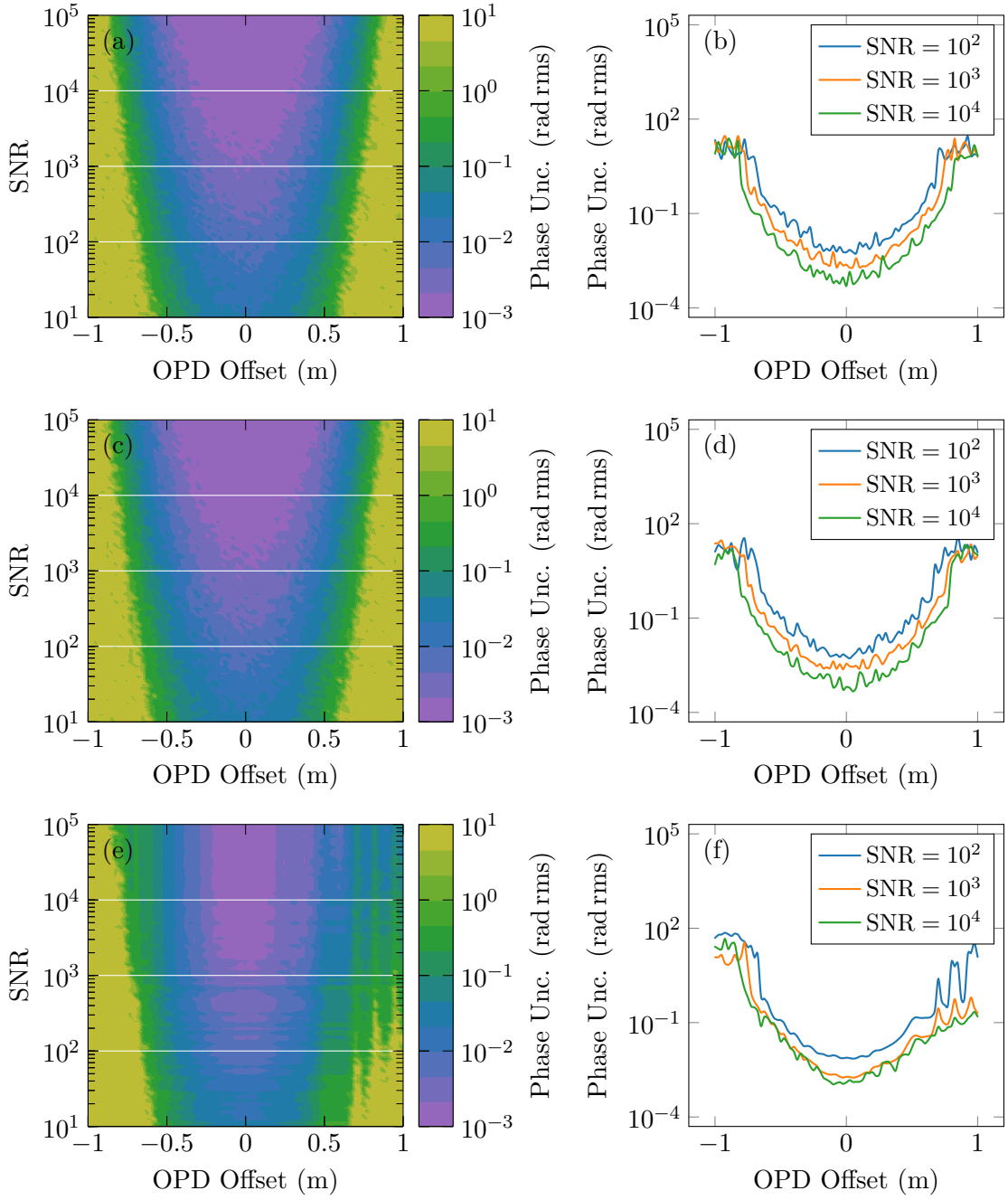

Figure 5.7: Phase uncertainties of unity, practical, and normalized interference signals for a single-axis interferometer with the parameters $f_{\mathrm{m}} = 100\,\mathrm{kHz}$, $\nu_{\mathrm{A}} = 1.5\,\mathrm{GHz}$, and $\sigma = 0.0225$. Demodulation of unity, practical, and normalized are plotted in (a), (c), and (e), with the cross sections along the white lines plotted in (b), (d), and (f), respectively. A $\sim$4 % improvement from the practical model to the unity can be achieved over the $\pm 0.1\,\mathrm{m}$ range for SNRs in 10^3 to 1.2×10^3; the normalized model achieves this improvement but is comparable or worse everywhere else.

widths of one half and one quarter the number of points in a modulation period. After amplitude normalization, the envelope is ideally removed from the second high-pass filtered signal. The amplitude normalized signal is distorted where the signal frequency is low at $0.25T_{\mathrm{m}}$ and $0.75T_{\mathrm{m}}$, however, the amplitude is consistent in the regions selected by the window at 0, $0.5T_{\mathrm{m}}$, and T_{m}.

Figure 5.7 shows that the phase uncertainty for the unity (Figures 5.7a and 5.7b) and practical (Figures 5.7c and 5.7d) models are similar over almost the entire space, however, a minimal $\sim$4 % improvement from the practical model with respect to the unity model can be achieved over the ± 0.1 m range for SNRs in 10^3 to 1.2×10^3 (which covers the SNRs measured in Sections 7.1 and 7.4). The normalized model (Figures 5.7e and 5.7f) realizes this small improvement over that range but shows comparable or worse performance over the rest of the explored parameters space. While these results show that normalization offers a small improvement over the parameter space that is representative of many applications in Chapter 7, the increase in phase uncertainty nearly everywhere else is a disadvantage. Furthermore, normalization can only be applied to single-axis interferometers as the Hilbert transform described in Section 4.5 does not yield the desired effect in the presence of multiple phase carriers. For these reasons, normalization is not used in any applications of Chapter 7.

The automatic amplitude normalization was investigated as an alternative strategy to that proposed by Kissinger [185] in which the power modulation envelope is compensated by a corrected carrier whose envelope is the multiplicative inverse. In Chapter 4, an extensive calibration of the FMDU components was required, and the corrected carrier represents yet another calibration product. Given the marginal reduction in phase uncertainty offered by the normalization strategy and the high cost of added complexity and latency DSP, adoption of the simpler corrected carrier approach is worth the extra calibration product. It is important to consider the scale of these results, as a $\sim$4 % improvement on the 2.5 mrad rms simulated phase uncertainty

for interferometer configurations in Chapter 7 is a negligible improvement and shows demodulation of an unnormalized interference signal with an uncorrected carrier is already close to the best achievable phase uncertainty.

5.5 Laser Wavelength Stability

Fluctuations in the laser centre optical frequency, ν_c, result in an uncertainty in the OPD dependent phase, φ. Recall from Equations (3.5b) and (3.21) that the OPD dependent phase is given by

$$\varphi = \frac{2\pi\nu_c\Lambda}{c}, \qquad \text{[rad]} \quad (5.4)$$

thus, fluctuations in ν_c lead to a phase shift, even if the OPD, Λ, is unchanged. Stabilization of the laser frequency to an absorption line of a gas cell was investigated as a solution to this issue.

Figure 5.8 shows the configuration of the laser frequency stabilization loop. An Eblana NLW 1550 nm LD [186] was installed in a Koheron CTL200 digital LD controller [207] and connected to 1×2 fibre coupler. Half the light from the coupler passes through a Wavelength References $H^{13}C^{14}N$ gas cell [237] and the other half through a variable attenuator that was adjusted to match the loss of the gas cell. Both signals are collected by Koheron PD100B-DC balanced photodetectors [238]. The output from the balanced photodetectors is fed to a Koheron PI200-T laser servo controller [239] that provides feedback signals to the LD controller for current and temperature tuning to keep the output of the balanced detectors at 0 V, which by slight adjustment of the variable attenuator, is the level corresponding to the side of an absorption line. Respective LD, LD controller, gas cell, balanced detectors, and servo controller specifications are given in Tables C.5, C.6 and C.18 to C.20.

The laser frequency was successfully stabilized to an absorption line and modulated using the external modulation input on the laser servo controller. A major drawback of this approach is the modulation must stay within the steep region on one half of the

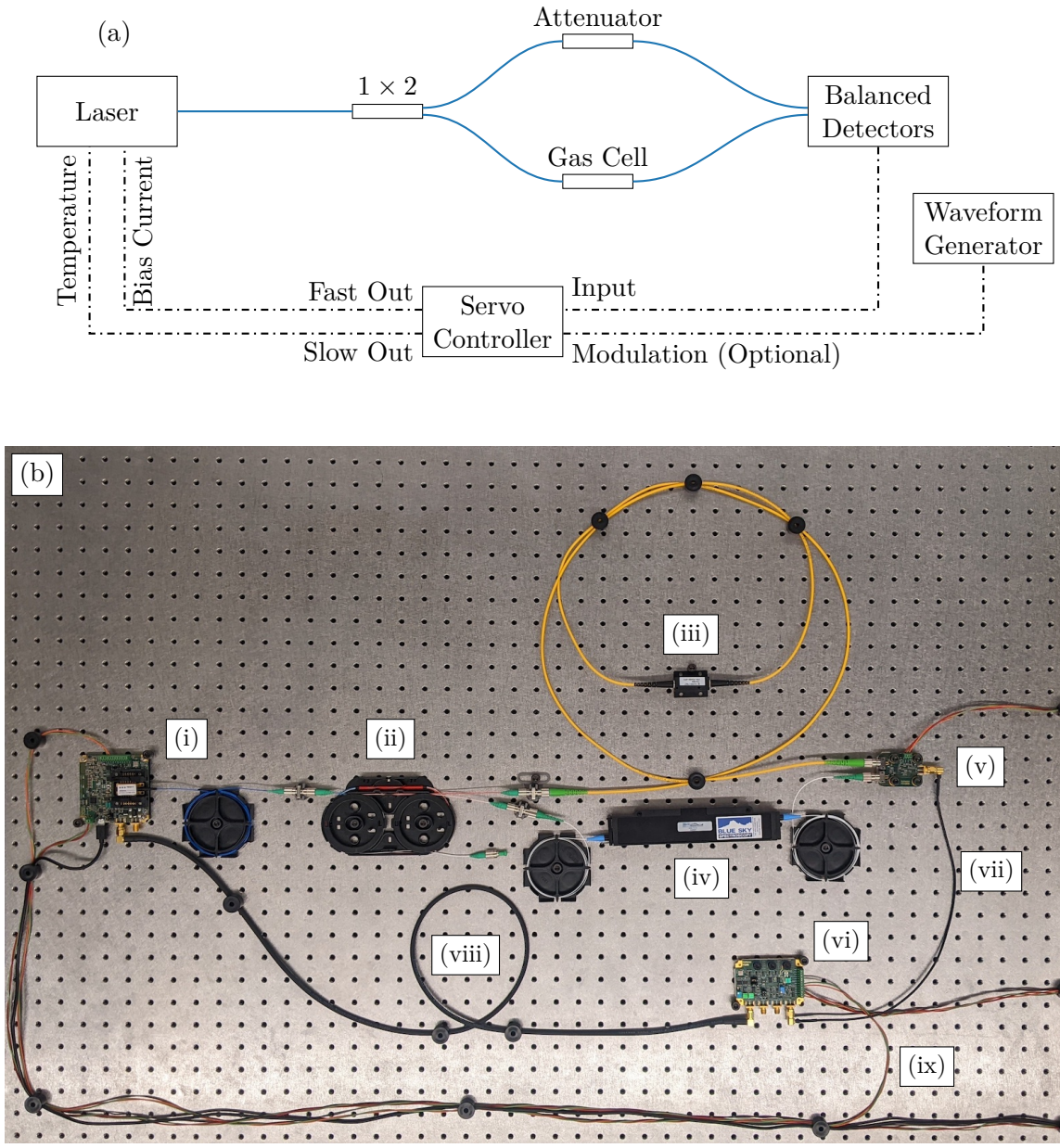

Figure 5.8: Schematic (a) and construction (b) of the laser wavelength stabilization loop. Components in (b) are: (i) laser and controller; (ii) 2 × 2 coupler; (iii) variable attenuator; (iv) $H^{13}C^{14}N$ gas cell; (v) balanced photodetectors; (vi) laser servo controller; (vii) photodetector output to servo input; (vii) fast integrator output from the servo to the laser bias current; (ix) slow integrator output from the servo to the laser temperature control. Cabling exiting the right side are power connections for the laser, photodetector, and servo, along with the USB connection to the LD controller. The (optional) waveform generator and external modulation input to the servo controller from (a) are not included. The LD, LD controller, gas cell, balanced detectors, and servo controller were provided by Blue Sky Spectroscopy Inc.

line. Figure 5.9 shows the balanced photodetectors signal for laser optical frequency modulation about the 1548.955 55(4) nm absorption line [240] using a 0.01 Hz triangle wave. The optical power modulation of the LD can be seen from the upper envelope of the V_{det} voltage from the balanced detectors with the absorption line midway through the sweep. Since one must stabilize the frequency to the side of an absorption line for the greatest sensitivity, a restriction on the modulation range is imposed. The laser has a frequency tuning coefficient of approximately $-250\,\text{GHz/A}$ (obtained from a linear fit to Figure 4.6b) and the LD controller has a gain of 25 mA/V. The sides of the absorption lines then correspond to a maximum modulation amplitude of $\nu_{\text{A}} \approx 300\,\text{MHz}$. This is not an issue in and of itself, however, the typical optical frequency modulation amplitude used in the applications of Chapter 7 is $\nu_{\text{A}} = 1.5\,\text{GHz}$, which is about five times greater than the $\sim$300 MHz restriction imposed by the gas cell.

Since the phase modulation amplitude, A, is proportional to $\nu_{\text{A}}\Lambda$, as seen in Equations (3.4) and (3.19), this wavelength stabilization scheme can be used, but only with greater OPDs. For the Fizeau interferometer configuration used in most applications presented in Chapter 7, this can be achieved by increasing the lens to target distance or by adding a delay fibre before the lens. The former is often not possible or not easily achieved, especially in a cryogenic environment, and the latter

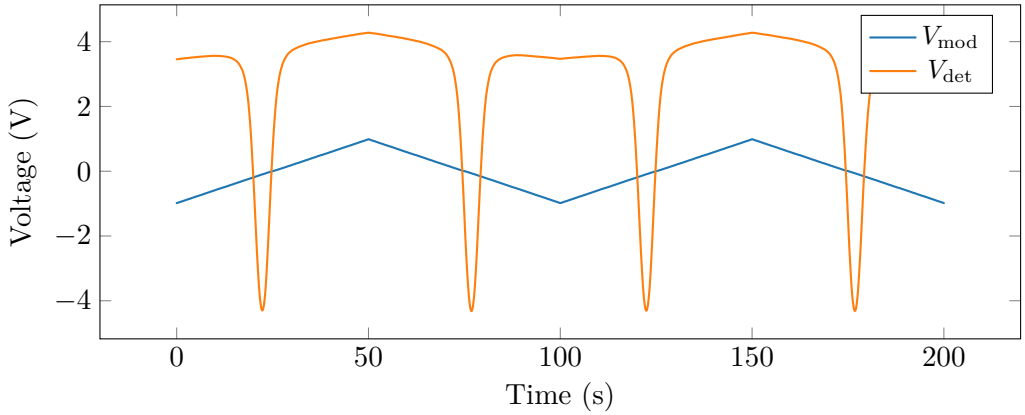

Figure 5.9: The laser swept with a 0.01 Hz triangle wave through the 1548.955 55(4) nm line [240] of an $H^{13}C^{14}N$ gas cell. V_{mod} is the modulation voltage fed to the LD controller and V_{det} is the output from the balanced detectors.

introduces noise into the measurement as seen in Sections 7.3 and 7.7. Furthermore, in a multiaxis interferometer, the OPD separation between every axis must also be increased by a factor of five which poses additional challenges in multiaxis applications like those presented in Section 7.2 where the largest OPD is ∼3 m. For these reasons, laser frequency stabilization was not included in the implementation of the SFM technique.

One must carefully consider the trade-offs of the performance gained by laser frequency stabilization using a gas absorption line against the relatively high cost of the required components with respect to the performance achieved using temperature stabilization. A measurement over a 48 h period in atmosphere using a temperature stabilized laser in Section 7.4 showed a maximum displacement change of 3.2 µm over a 50 cm length. The measured fluctuations showed evidence of diurnal characteristics that were external to the laser itself and affected the entire testing environment. These results indicate that the optical frequency of the laser is highly stable over extended periods even without a feedback mechanism such as the absorption line locking described in this section.

5.6 Conclusions

At the beginning of the chapter, three principal aspects regarding phase uncertainty in the SFM technique were outlined for investigation via numerical modeling. First, a theoretical estimate of the phase uncertainty achieved by a typical single-axis interferometer configuration in the applications of Chapter 7. Second, and exploration of crosstalk was conducted to establish design drivers for the minimum OPD separation between axes. Third, an investigation of the effects of the amplitude normalization procedure on the phase uncertainty.

The analyses in Section 5.2 showed a theoretical phase uncertainty of 2.5 mrad rms is achieved with the SNR = 10^3 representative of interferometer configurations in

Chapter 7. In a two-pass interferometer with a 1550 nm laser, this corresponds to 0.3 nm rms displacement uncertainty and has close agreement to the results of Section 7.4 which demonstrate 0.5 nm rms in a 50 kHz bandwidth and 0.4 nm rms in a 20 Hz bandwidth in atmosphere.

An analysis of the crosstalk between axes conducted in Section 5.3 in conjunction with the results from Section 5.2 gave recommendations for w, the band separation coefficient, which dictates the minimum demodulatable OPD and the minimum OPD separation between axes. It was found that $w = 2.5$ provides an acceptable minimum demodulatable OPD by Equation (3.42) by which the uncertainty contributions due to crosstalk are eliminated.

Modeling of the normalization procedure in Section 5.4 showed that a $\sim$4 % improvement in phase uncertainty can be gained from applying corrections to the demodulation. The automatic amplitude normalization scheme outlined in Section 4.5.1 was simulated and showed that it can realize this small improvement over a limited range of the explored parameter space. It was concluded that the corrected carrier strategy proposed by Kissinger [185] is a better alternative for applying amplitude corrections to the demodulation and avoids the increase in DSP complexity for a negligible improvement. Section 5.2 outlined that a phase uncertainty of 81 mrad rms is required to satisfy the SAFARI FTS displacement uncertainty requirement from Table 1.1. In this context, corrections are not required, as the measured 0.4 nm rms (3 mrad rms) uncertainty in a 20 Hz bandwidth without amplitude normalization in Section 7.4 closely agrees with the modeled 2.5 mrad rms uncertainty.

As an aside from the main goals of this chapter, Section 5.5 investigated a laser frequency stabilization scheme where the laser frequency was locked to the absorption line of an $H^{13}C^{14}N$ gas cell. While a laser was successfully locked and modulated about a point on the absorption spectrum, the technique was not incorporated into the SFM implementation. The optical frequency modulation range limited by the

width of an absorption line was four times smaller than the optical frequency modulation amplitude used in most applications of Chapter 7 and presented new challenges with meeting the minimum OPD requirements. Nonetheless, as will be shown in Section 7.4, using only a temperature stabilized laser, the implementation of the SFM technique shows great stability over several days measurements.

Chapter 6

Cryogenic Characterization of Optical Components

Working from a modest budget, I had to use commercial off-the-shelf components, so the first step was to thermally cycle the individual components to identify best practices for a range-resolved laser interferometer. The cryogenic characterization of select optical fibres, fibre coatings, fibre mating strategies, and fibre collimators was performed. A summary of the characterization results is presented in Section 6.6 and evaluated in the context of cryogenic range-resolved laser interferometry applications such as those investigated in Chapter 7.

Mechanical strength, coating integrity, and optical transmittance testing of fibres in Sections 6.1 to 6.3, respectively, were performed under contract with OFS [241] as part of an industrial internship at Blue Sky Spectroscopy Inc. [242]. I led this investigation resulting in Christiansen et al. [243], and by default, all presented work in Sections 6.1 to 6.3 was completed by me other than specifically noted results provided by OFS.

6.1 Mechanical Strength of Optical Fibres

Fibres employed in cryogenic applications often undergo many temperature cycles. One is concerned about the differential behaviour of the coating and glass when cooled, and an investigation into the mechanical properties of fibres was performed to determine whether the fibre coating material affects the overall strength after cryo-

genic temperature cycling. Optical fibres are typically coated with acrylate to protect the outside of the glass from stress and abrasion that lead to microscopic flaws along the fibre [244]. Applications in high temperature and harsh environments, such as oil and gas downhole sensing, may employ polyimide coatings which provide better protection of the fibre [245]. The behaviour of these coatings are largely unexplored at cryogenic temperatures and were evaluated to determine whether acrylate or polyimide coatings offer improved strength (in this section and Section 6.2) and optical performance (in Section 6.3).

All fibre samples were prepared by OFS, either dual acrylate coated OFS AllWave ZWP BF07090 fibre [246] or polyimide coated OFS ClearLite BF05717-01 [247], having coating diameters in the range of 240 to 245 µm and 150 to 155 µm as illustrated in Figures 6.1a and 6.1b, respectively. In total, six fibre samples were prepared — three acrylate coated, three polyimide coated, and all 20 m in length. OFS kept one acrylate-polyimide pair as a control study, and the other pairs were temperature cycled. The fibre samples were gently cycled in pairs from room temperature to 4 K and back at a descent rate of ∼2 K/min and ascent rate of ∼0.2 K/min at the steepest parts; one pair underwent one thermal cycle and the other underwent three. Others have tested the strength of fibres immersed in liquid nitrogen [248] by which the samples were rapidly cooled from room temperature to ∼77 K, however, in this study, care was taken to slowly cool the fibres which provides less of an instantaneous shock. Both acrylate and polyimide fibres of a pair were wound around a custom aluminum bobbin, as shown in Figure 6.1c, so that they are cycled under the same conditions. Figure 6.1d shows the bobbin in the cryostat with a Lake Shore Cryotronics Cernox CU thermometer [249]. All temperature excursions to ∼4 K had dwell times of ≥12 h, and bobbin temperatures are plotted in Figure 6.1e. After cycling, the samples were returned to OFS for mechanical strength testing. The coating integrity of the cycled fibres was also analyzed and presented in Section 6.2.

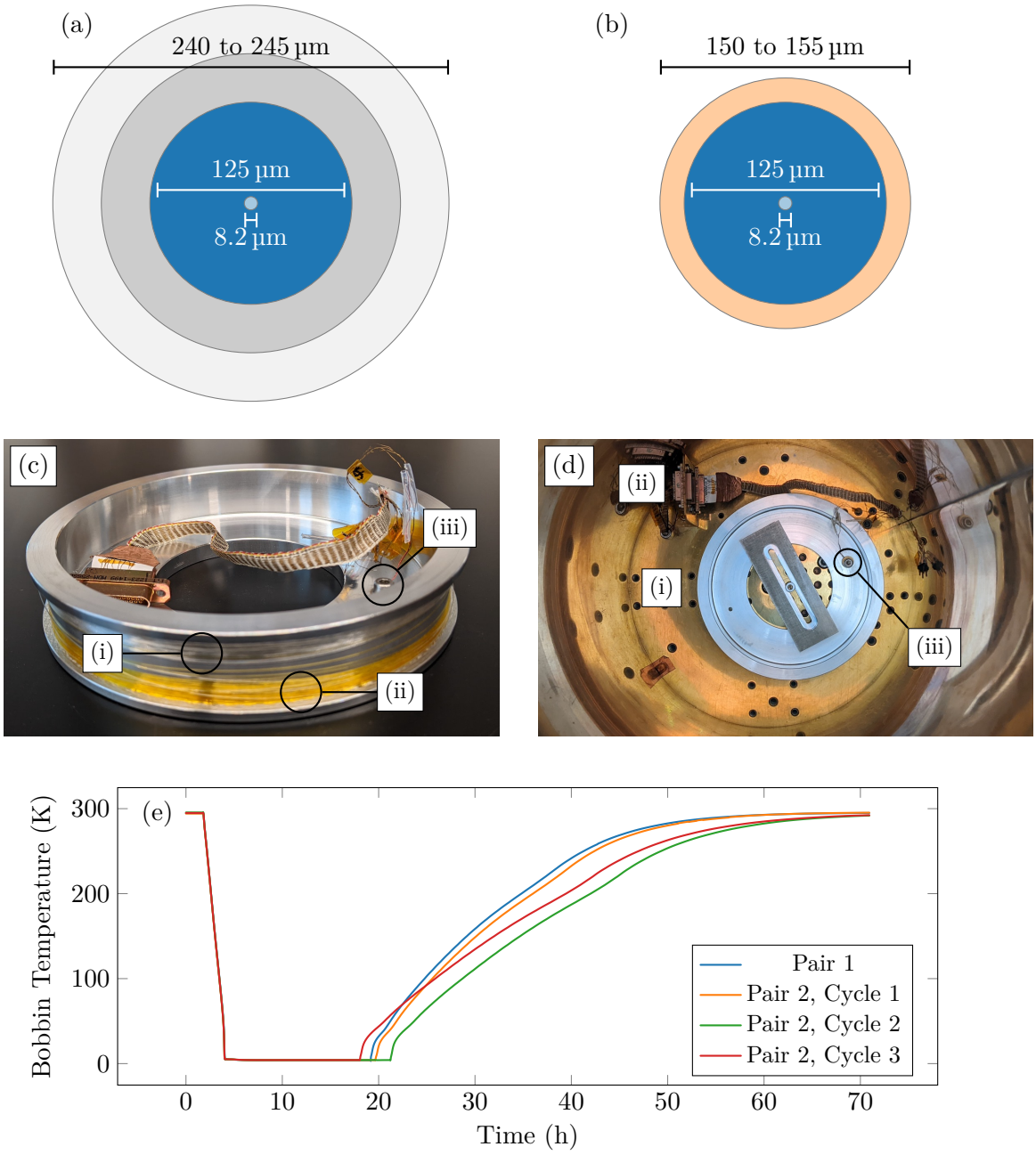

Figure 6.1: Fibre cross sections are shown to scale: the glass core, glass cladding, and dual acrylate coating (a) and glass core, glass cladding, and polyimide coating (b). Fibre samples wound on a custom aluminum bobbin (c) and installed in a cryostat (d). In (c), acrylate (i) and polyimide (ii) coated fibres are wound on the bobbin and a thermometer (iii) is attached. In (e), the bobbin (i) installed on the 4 K plate of a cryostat and a cable from the cryostat wiring (ii) connects to the thermometer (iii). Bobbin temperatures for each temperature cycle of the mechanical strength and coating integrity tests are plotted in (e).

Optical microscope images of the fibre coatings in Figure 6.2a provided by OFS show no visible evidence of coating degradation. Measurements of mechanical strength and fatigue of optical fibre were be determined via two-point testing, pictured in Figures 6.2b and 6.2c, which may also reveal evidence of microcracking and delaminations of the coating from the glass. The fibre is characterized on a microscopic scale in two-point bend testing, as the segment of fibre involved is very short [251]. OFS provided bend testing data using a Fiber Sigma two-point bend tester [250] at strain rates of 0.08, 0.57, 4, and 28 %/min after preconditioning at 23(2) °C and 50(5) % RH for at least 24 hours, 5 to 20 strength measurements were recorded for each fibre sample.

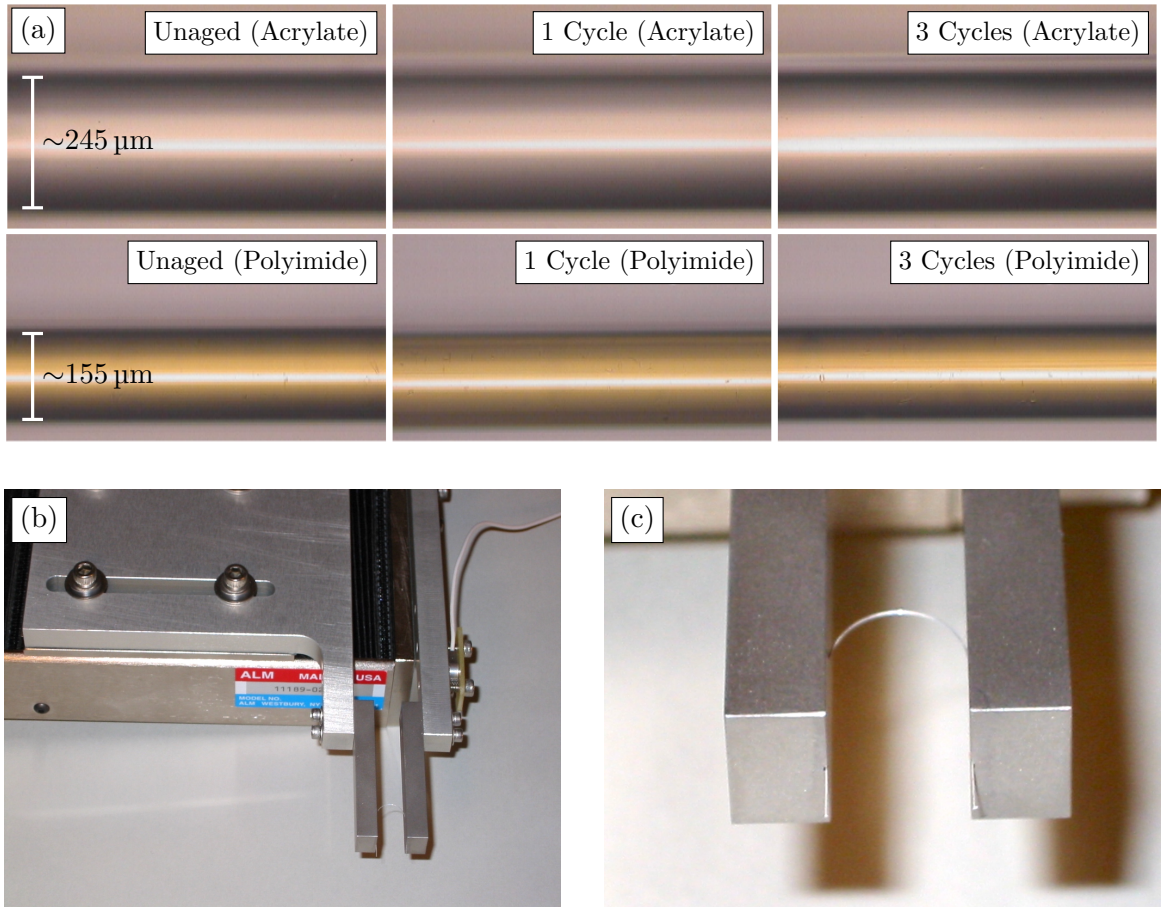

Figure 6.2: Optical images of unaged and temperature cycled acrylate and polyimide coated fibres (a); Images were provided by OFS and captured with a Nikon Optiphot optical microscope. Fiber Sigma two-point bend tester (b) and zoom on fibre (c); bend tester images are from the Fiber Sigma website [250], retrieved 22nd September, 2023.

Table 6.1: Summary of mechanical strength testing results. The tabulated values were provided by OFS and are calculated with industry standard significance and uncertainty. The uncertainty in n_d corresponds to a 95 % confidence interval.

Coating	Acrylate			Polyimide		
Aging Condition	Unaged	1 Cycle	3 Cycles	Unaged	1 Cycle	3 Cycles
Strength (GPa)	5.17	5.20	5.14	5.60	5.62	5.60
Weibull Slope	59	85	67	85	105	84
n_d	19.8(11)	19.7(6)	19.5(12)	23.6(10)	23.3(8)	24.2(12)

Strength and stress corrosion measurement results provided by OFS with industry standard significance and uncertainty are presented in Table 6.1

Fracture stress measurements obtained during strength testing can be described by Weibull distributions [252]. Respective median strength magnitudes were found to be ∼5.2 and ∼5.6 GPa for acrylate and polyimide samples, shown in Table 6.1, which correspond to 50 % cumulative failure probability. The Weibull slope is obtained from the linearization of the fracture stress cumulative failure probability, thus, narrow distributions correspond to high Weibull slopes [253]. Weibull slopes in the 15 to 30 (or greater) range represent fibres with high strength and low variability, while lesser slopes indicate lower strength and higher variability, and extremely low slopes (<4) are fibres that are filtered out by proof testing [253]. The acrylate and polyimide samples were proof tested at 100 and 200 kpsi (∼690 and ∼1380 MPa), respectively, as part of the preparation, so that fibres having lesser Weibull slopes were filtered out. All samples exhibited Weibull slopes exceeding 30, as shown in Table 6.1, indicating that 4 K excursions did not degrade the strength of the fibres.

Using two-point bend testing, the coating-glass system can be characterized while ignoring defects that were filtered by proof testing. The two-point bend measurements were used to determine the stress corrosion resistance, n_d, which is a measure of how long a fibre can survive at a given tensile or bending stress; greater n_d values correspond to reduced fatigue (i.e., crack growth rate) [254] and longer times to failure

[255]. Per industry standards, OFS requires that n_d values must meet or exceed 18. All tested acrylate and polyimide coated samples exhibited n_d values greater than 18 and did not show significant degradation after cycling, indicating that cryogenic excursions did not weaken the fibres to stress corrosion.

The tested properties were necessarily evaluated at room temperature on fibre samples after cryogenic cycling, and cycling the fibres did not introduce mechanical defects of measurable significance at room temperature. Although Table 6.1 shows better strength performance for polyimide, both acrylate and polyimide coated fibres showed no evidence of strength degradation, making both suitable for use in cryogenic applications.

6.2 Coating Integrity of Optical Fibres

The cryogenically cycled fibres from Section 6.1 not only underwent mechanical strength testing, but also analysis of the coating materials. This was a continuation of the study with OFS using the cycled fibre samples from Section 6.1. Coatings were analyzed using Fourier transform infrared spectroscopy (FTIR) and thermogravimetric analysis (TGA), shown in Figure 6.3, to determine changes in coating chemistry and integrity.

Coating spectra were obtained and provided by OFS using attenuated total reflection spectroscopy [256, 257]. A Thermo-Fischer iS50 FTIR Spectrometer [258] with internal reflection elements of ZnSe and Ge and liquid nitrogen cooled detector was used to record spectra with a resolution of $<0.09\,\mathrm{cm}^{-1}$. Although the FTIR spectrometer provides broad spectral coverage over 15 to $27\,000\,\mathrm{cm}^{-1}$, the spectra for the secondary acrylate and polyimide coatings shown in Figures 6.3a and 6.3b, respectively, are restricted to a subset of wavenumbers with features of the polymers used.

The provided subsets of the FTIR spectra from OFS show the carbonyl (1730 cm^{-1}), urethane (1530 cm^{-1}), and acrylate (1410 cm^{-1}) groups of the acrylate coating in Figure 6.3a, and an imide peak (1360 cm^{-1}) of the polyimide coating in Figure 6.3b. There is no significant change in the spectral peak intensities over the aging conditions for acrylate and polyimide coatings, and the spectra are nearly identical. The absence of differences in the coating spectra indicates that there were no alterations to the coating chemistry due to temperature cycling. While Figures 6.3a and 6.3b show spectra for the secondary acrylate and polyimide coatings, primary coating spectra

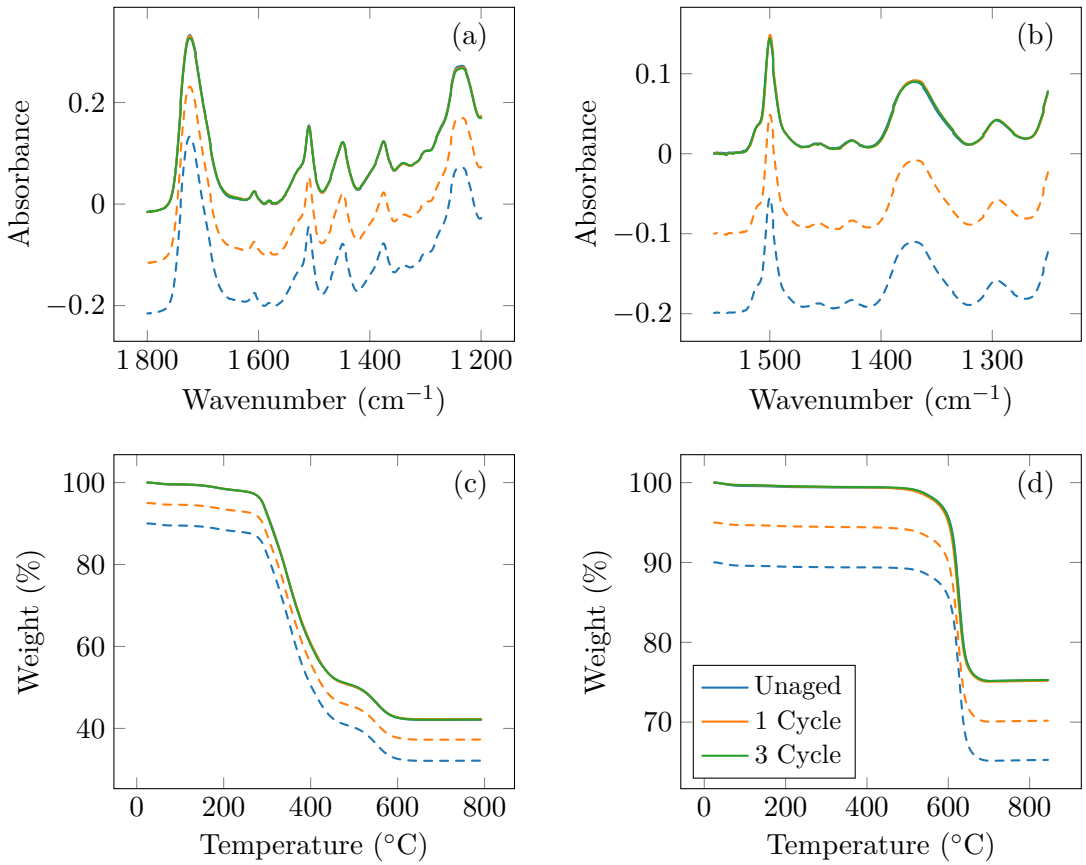

Figure 6.3: FTIR and TGA curves of unaged and cycled fibre coatings provided by OFS. Select regions of the FTIR spectra for the secondary acrylate (a) and polyimide (b) coatings are shown with a subset of wavenumbers. TGA curves are shown for acrylate (c) and polyimide (d) coatings. These measurements do not show evidence of fibre coating degradation after cycling. The legend in (d) applies to all four plots; for visibility, two dashed curves are added to each plot showing the *Unaged* and *1 Cycle* curves offset by 0.1 in (a) and (b) and 5 % in (c) and (d).

are proprietary and not disclosed, however, spectra for the primary coatings showed similar results.

Thermogravimetric analysis (TGA) was employed to analyze a potential loss in volatiles due to high vacuum exposure which may alter the coating chemistry. OFS provided the TGA curves shown in Figures 6.3c and 6.3d. obtained using TA Instruments TGA Q500 [259] thermogravimeter. Small fibre samples with masses in the 10 to 20 mg range were analyzed over temperatures from ambient to 800 °C. Samples were placed on a platinum pan in a chamber purged with dry air at a flow rate of 60 cm^3/min and heated to 650 °C at 10 °C/min then to 800 °C at 20 °C/min. A shift in the curves of Figures 6.3c and 6.3d denote a loss of volatiles, however, as the curves are nearly identical for each test condition, there is no evidence for a significant change in chemistry. A loss of volatiles would shift the mass-temperature curves, which are superposed in Figures 6.3c and 6.3d for acrylate and polyimide, respectively. The curves of Figures 6.3c and 6.3d are nearly identical, indicating that any loss of volatiles is insignificant.

Both the FTIR and TGA analyses show no evidence of coating degradation after one and three cryogenic temperature cycles. With respect to coating integrity, there is no evidence of degradation in either acrylate or polyimide, and both coating types are suitable for cryogenic range-resolved laser interferometry applications.

6.3 Optical Transmittance of Fibres

In addition to the mechanical properties of optical fibres explored in Sections 6.1 and 6.2, the optical performance of OFS single-mode fibres was characterized at cryogenic temperatures. Two 25 m lengths of ferrule-connector angled physical contact (FC/APC) terminated fibres were prepared by OFS for optical testing. One fibre sample was acrylate coated OFS AllWave ZWP BF07090 fibre [246] and the other was polyimide coated OFS ClearLite BF05717-01 fibre [247]. Both fibres conform

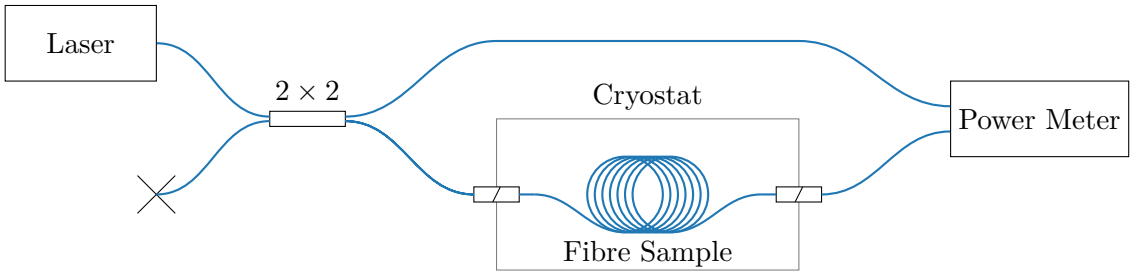

Figure 6.4: Schematic of the fibre transmittance experiment. The coil of fibre in the cryostat is wound around a bobbin that is cooled to ∼4 K.

to the ITU-T G.652 fibre design [231] and are single-mode at the test wavelength of 1550 nm.

A schematic of the experiment is shown in Figure 6.4, in which light from a 1550 nm Fitel FRL15DCWD laser diode (LD) [260] driven by a Koheron CTL200 LD controller [207] (respective specifications given in Tables C.6 and C.11) is passed through a cryostat. The signal is split by a Thorlabs TN1550R5A2 2 × 2 50:50 coupler [261]: the reference signal is directly measured, and the measurement signal passes through the fibre sample cycled in a cryostat. The fibre sample is secured to a custom aluminum bobbin, shown in Figures 6.1c and 6.1d. At each end of the fibre, 50(3) cm was not secured to the bobbin so that the connectors may reach a custom Kurt J. Lesker hermetic fibre feedthrough installed in the cryostat (specifications given in Table C.10); ∼24 m of fibre was secured to the bobbin. The reference and measurement signal were sampled using a Keysight N7744A optical power meter [219] at a rate of 1 Hz (specifications given in Table C.13). On average, the temperature of the bobbin followed profiles like those plotted in Figure 6.1e. Each fibre sample was cycled 3 times and monitored on every descent and ascent.

Power measurements of P_r and P_m, were recorded for the reference and measurement signals, respectively. Variations in laser power were corrected using the reference measurement, to obtain the corrected power ratio $p[n] = P_\mathrm{m}[n]/P_\mathrm{r}[n]$. The change in

transmittance from the initial value is given by

$$\Delta\mathcal{T} = 10\log_{10}\frac{p[n]}{p[0]}, \qquad \text{[dB]} \quad (6.1)$$

where $\Delta\mathcal{T}$ is the change in optical transmittance. The measured changes in transmittance are plotted in Figure 6.5, which are shown in solid and dashed lines for the temperature descent and ascent phases, respectively. It is common for optical loss to be reported as a positive value in decibels, however, since $\Delta\mathcal{T}$ is the change in optical transmittance, values where $\Delta\mathcal{T} < 0\,\text{dB}$ correspond to optical loss.

The acrylate coated fibre shows repeatable behaviour over all temperature cycles, while the polyimide coated fibre is less so. On the temperature descent, an increase in transmittance of the acrylate coated fibre is observed over the 220 to 120 K range, reaching a maximum of 0.014 dB near 180 K. At ∼4 K, a loss of −0.023 to −0.027 dB is measured relative to room temperature before cycling, but all curves consistently return to ±0.003 dB of their initial transmittance values after cycling. Attenuation within silica fibres over the 1300 to 1600 nm range is dominated by Rayleigh scattering caused by localized density variations in the glass [262]. Additionally, losses occur due to microbends in the fibre, which are microscopic deflections in the fibre axis. Microbends are lateral shifts in the fibre axis that are random in amplitude and randomly distributed along the fibre, resulting in a discontinuity that decreases the local overlap integral of the fibre core, and thus contributes to optical loss [262]. The nonlinear change in transmittance through the acrylate fibre is attributed to the combination of these two effects. When cooling, the frequency of thermally activated density variations is reduced, and differential contractions caused by different coefficients of thermal expansion (CTE) of the fibre and coating lead to a compressive stress on the fibre. The former decreases the effects of Rayleigh scattering while the latter increases the effects of microbending. These two effects counteract each other,

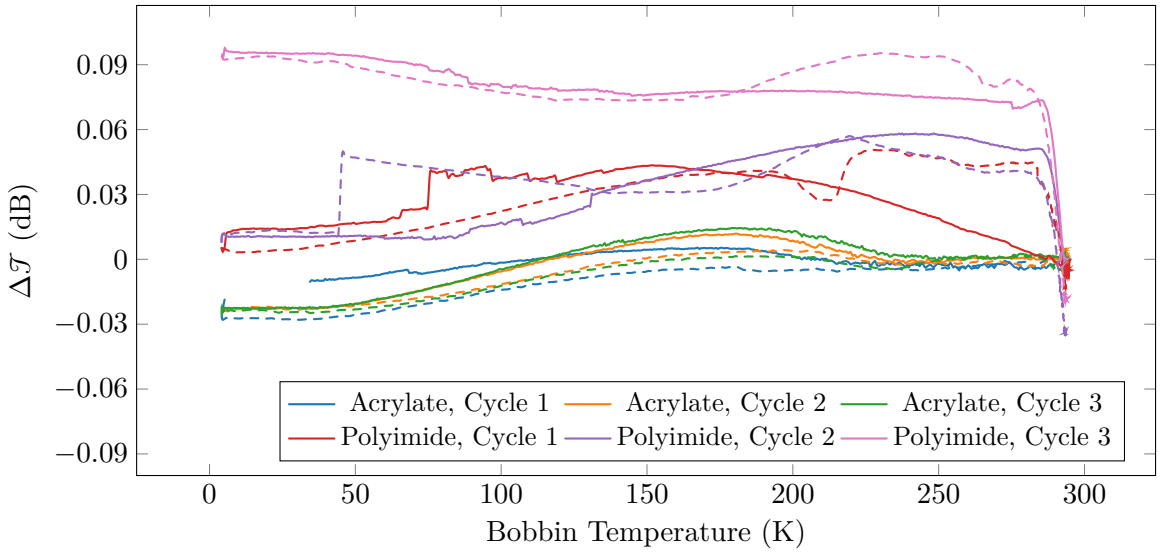

Figure 6.5: Changes in optical transmittance of cycled fibres. Negative values correspond to optical loss. The curves are found from Equation (6.1). Each cycle is split into descent and ascent phases, which are plotted in solid and dashed lines, respectively. The estimated measurement uncertainty is <0.001 dB. Curves for the acrylate sample are generally consistent and relatively smooth while the polyimide sample are generally inconsistent with sudden changes. *Acrylate, Cycle 1* is missing data over 5 to 30 K as the thermometer was briefly lost. For reference, a change of 0.1 dB is approximately 2.3 %.

leading to the nonlinear, yet consistent, transmittance profile for the acrylate coated fibre.

Unlike the acrylate coated fibre, the polyimide coated fibre did not exhibit consistency over all temperature cycles. Several random step changes in transmittance are observed in Figure 6.5, which generally occur at temperatures <130 K. For example, the cycle 1 descent shows a loss of 0.016 dB around 75 K, and cycle 2 ascent shows a gain of 0.035 dB around 45 K. The estimated measurement uncertainty is <0.001 dB, indicating that the small observed jumps are physical and not due to measurement errors. On the first temperature cycle, the greatest number of step changes are observed, and their frequency decreases on each subsequent cycle. It was found that after cycling to cryogenic temperatures, the transmission of the fibre does not return to its initial value, with typical hysteresis values of −0.036 to −0.013 dB. after the

temperature ascent. This behaviour indicates that irreversible changes to the fibre and coating occur when cooling the polyimide coated fibres. Like the acrylate coated fibre, the polyimide coated fibre is affected by Rayleigh scattering and microbends; however, polyimide is a more rigid material than acrylate, so the strain induced by the polyimide coating is greater which may lead to fractures responsible for the observed irreversible changes. Curves 1 and 2 for polyimide follow somewhat of a similar shape, with each settling in a small ∼0.01 dB near 4 K. Cycle 3, however, is inconsistent with cycles 1 and 2. If the fibre sustains damage, it appears that most is done to the fibre on the first two cycles, as step changes in transmittance are reduced in frequency and amplitude in the third cycle. Below 280 K, the cycle 3 curve is relatively flat and reaches a gain of ∼0.095 dB at 4.2 K.

When secured to the aluminum bobbin, ∼50 cm of the sample fibre was left unwound at each end and ∼24 m was in contact with the bobbin. The ends of the fibres are connected to the hermetic fibre feedthrough on the vacuum chamber wall, which is at room temperature. Since the bobbin is cooled to ∼4 K, there is a ∼290 K temperature gradient across the ∼50 cm lengths of fibre. In Figure 6.5, non-reproducible and irreversible effects are observed for the polyimide coated fibres, but not the acrylate coated fibres. These effects may be explained by localized coating defects, such as cracking and delaminations at the coating-glass interface. The induced stress, σ_{PI}, on the polyimide coating may be estimated as

$$\sigma_{\mathrm{PI}} = E_{\mathrm{PI}}(\alpha_{\mathrm{PI}} - \alpha_{\mathrm{silica}})\Delta T, \qquad \text{[Pa]} \quad (6.2)$$

where E_{PI} is Young's modulus of the polyimide coating, α_{PI} and α_{silica} are the linear CTEs of the coating and silica glass fibre, respectively, and ΔT is the change in temperature.

At room temperature, silica has a CTE of ∼0.65 ppm/K [263]; OFS has provided that their polyimide coating has a CTE of 40 ppm/K and Young's modulus of ap-

proximately 2 GPa. An induced tensile stress of ∼23 MPa on the polyimide coating is estimated by Equation (6.2). OFS provided that the ultimate tensile strength of the polyimide is ∼130 MPa at room temperature, or ∼6 times the induced stress on the coating. Assuming a similar or greater strength at cryogenic temperatures, systematic cracking in the coating due to temperature effects seems unlikely. Furthermore, the optical microscopy images in Figure 6.2a indirectly support the absence of cracking, as no cracks in either the acrylate or polyimide coatings were observed over lengths of several centimetres. These results illustrate that further characterization of polyimide coatings are required, and it is inconclusive whether polyimide offers benefits over acrylate at low temperatures as it does at high temperatures.

Optical intensity fluctuations are problematic for most range-resolved laser interferometers, as the change in intensity may be interpreted as a change of phase. The acrylate coated fibre shows minimal and repeatable changes in transmittance while the characterization of the polyimide coated fibre is inconclusive and shows irregular behaviour. An acrylate coating is recommended for cryogenic applications based on its consistent and relatively flat transmittance profile when temperature cycled.

6.4 Optical Transmittance of Fibre Mating Sleeves

Connectors on all fibres used in this work are ferrule-connector physical contact (FC/PC) and ferrule-connector angled physical contact (FC/APC). Fibre mating sleeves typically consist of a thin zirconia tube commonly housed in stainless steel or plated brass. The fibres key into the housing, which ensures properly alignment of angled polishes (and polarization, if employed), and the zirconia sleeve aligns the connector ferrules such that the fibre tips make contact over the core region. Since mating is achieved by carefully holding the fibre cores in axial alignment, differential contraction of the components involved may lead to a loss in transmittance through a mating junction when cryogenically cooled. To characterize these effects, several

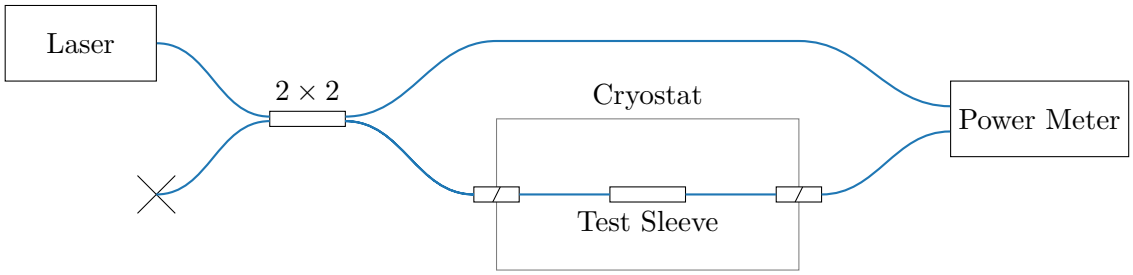

Figure 6.6: Schematic of the cryogenic mating transmittance experiment. In the control configuration without a mating sleeve, the fibre is mounted directly to the 4 K plate.

Thorlabs SMF-28-J9 [229] fibre samples were prepared Thorlabs 30126C9 ferrule-connector physical contact (FC/PC) [233] and Thorlabs 30126A9 FC/APC [230] connectors following the procedure in Section 4.6. A 150(3) cm control fibre was prepared as a control sample which was not mated when cooled. All other samples underwent mating, and were made to lengths of 100(3) cm. The tested configurations are summarized in Table 6.2, and from this point forward, are individually referred to by their assigned ID number.

Configuration 1 was the control test, in which no fibres were mated. In configurations 2 through 5, the fibres mated on the 4 K plate of a cryostat. The tested mating sleeves were standard two-piece Thorlabs ADAFC3 [264] and monolithic polarization maintaining Thorlabs ADAFCPM2 [265]. A Thorlabs ADABS1 aluminum L-bracket mating sleeve mount [266] was used to secure the mating sleeves to the plate. To ensure good thermal contact between the sleeves, L-bracket, and 4 K plate, the anodized paint was polished from the mounting surfaces of the L-bracket using fine sandpaper.

A schematic of the experiment is shown in Figure 6.6. The procedure is the same as the one used for the fibre transmittance monitoring in Section 6.3, with the exception that the fibre is mated at 4 K rather than wound around a bobbin. For the control configuration, there is no mating sleeve; a ∼1 cm length in the centre of the fibre was taped to the 4 K plate to produce similar thermal contact to the mating sleeve, and the slack was left dangling. In configurations 2 through 5, the fibres were mated in

Table 6.2: Cryogenic fibre mating transmittance configurations and results. Configuration 1 is a control test consisting of a single fibre without any mating junctions at 4 K. For reference, 0.1 dB ≈ 2.3 %.

ID	Termination	Mating Sleeve	$\Delta\mathcal{T}_{\text{cool}}$ (dB)	$\Delta\mathcal{T}_{\text{cyc}}$ (dB)
1	—	—	−0.002(1)	−0.002(1)
2	FC/APC	Two-piece	−0.093(1)	−0.019(1)
3	FC/APC	Monolithic	−0.028(1)	0.015(1)
4	FC/PC	Two-piece	−0.118(2)	−0.014(2)
5	FC/PC	Monolithic	−0.126(2)	0.009(3)

the sleeve and slack in the fibres was again left dangling. Inside the cryostat, the other ends of the fibres are mated to passes of a custom Kurt J. Lesker receptacle hermetic feedthrough [267] through which an Eblana NLW 1550 nm LD [186] in a Koheron CTL200 LD controller [207] provided 1550 nm laser light (refer to Tables C.5, C.6 and C.10 for respective specifications). Reference and measurement signals were sampled at 1 Hz by a Keysight N7744A optical power meter [219] and fluctuations in laser power were corrected using the procedure from Section 6.3 (specifications given in Table C.13).

Results are plotted in Figure 6.7, and key changes in transmittance are summarized in Table 6.2. Two changes in transmittance are tabulated: $\Delta\mathcal{T}_{\text{cool}}$ is the change in transmittance from room temperature to 4 K and $\Delta\mathcal{T}_{\text{cyc}}$ is the change in transmittance over the entire temperature cycle, which is the transmittance at room temperature after cooling compared to the transmittance at room temperature before cooling. Like Section 6.3, $\Delta\mathcal{T}$ is used, which is the change in transmittance, not loss, so $\Delta\mathcal{T} < 0\,\text{dB}$ values are optical loss.

From Figure 6.7 and Table 6.2, FC/APC terminations consistently, but not significantly, outperform FC/PC at 4 K, and there is not clear evidence to support that either two-piece or monolithic mating sleeves offer better cryogenic performance. On average, the transmittance at 4 K of the FC/APC configurations was ∼1.4 % better than the FC/PC configurations, and ∼0.7 % with the monolithic mating sleeve over

the two-piece mating sleeve. Overall, these results are not strong enough, especially over one trial per configuration, to recommend one termination-sleeve configuration over the others. Since the differences are small, a useful result is that one does not need to take any special considerations in fibre mating for a cryogenic deployment of the range-resolved interferometer. The sinusoidal frequency modulation (SFM) technique can tolerate a significant optical loss and has been successfully deployed in systems where losses exceed 90 %.

While $\Delta\mathcal{T}_{\text{cool}}$ is negative for every trial, indicating a loss when cooled, there is not agreement on the sign of $\Delta\mathcal{T}_{\text{cyc}}$. When cooling, there are discrete jumps in the transmittance curves in Figure 6.7, either up or down, visible in configurations 2 to 5. Jumps occur due to slippage of the fibre within the sleeve as the zirconia ferrules and sleeve inserts have different CTEs than the nickel-plated brass of the sleeve housings. On the ascent, there are no jumps, however, some configurations warmed into a position with a positive $\Delta\mathcal{T}_{\text{cyc}}$. These results show that cycling is not a reversible process, and the fibres may relax into a better alignment position in the mating sleeves when warmed.

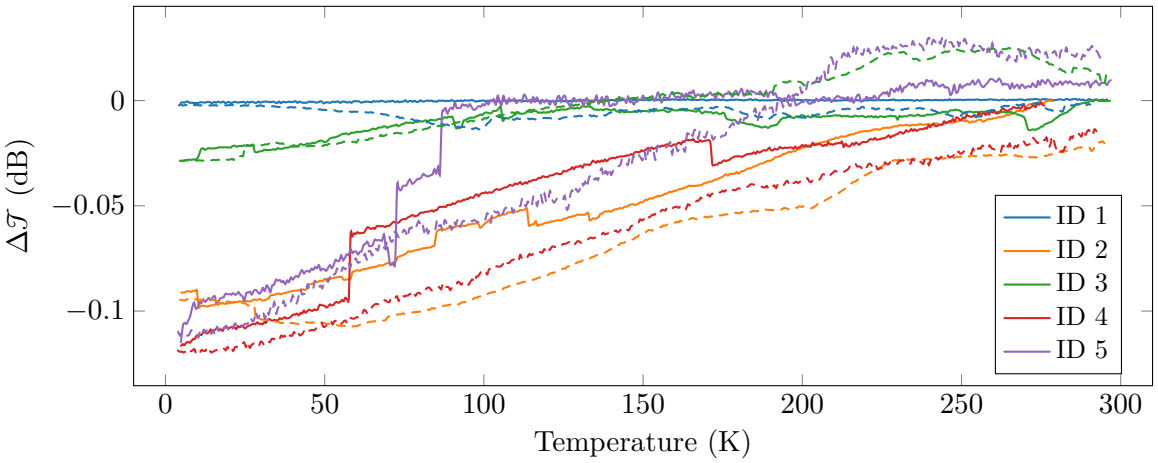

Figure 6.7: Cryogenic fibre mating transmittance curves. Negative values correspond to optical loss. The ID numbers in the legend correspond to the configuration IDs in Table 6.2. Temperature descent and ascent curves are shown by solid and dashed lines, respectively. The estimated measurement uncertainty is <0.001 dB.

The change in transmittance of the control fibre of configuration 1 is less than that observed in the fibre transmittance testing in Section 6.3. Samples cycled in fibre transmittance testing had ∼24 m segments secured to the bobbin and cooled to 4 K, while the control sample in the mating tests had a ∼1 cm segment near the middle of the fibre secured to the 4 K plate. Since mating configurations 2 through 5 in Table 6.2 show similar losses of ∼0.1 dB at ∼4 K compared to room temperature, there is no reason to prefer FC/PC termination, FC/APC termination, two-piece mating sleeves, or monolithic mating sleeves with respect to optical performance in a laboratory environment. The choice of mating configuration among the tested parameters should be selected based on other factors, such as cost, as monolithic mating sleeves are more expensive than two-piece mating sleeves, or other optical characteristics, for instance, if reflection from the surface of an FC/PC termination is desired. These recommendations assume a laboratory setting where low-cost and reconfigurability may be preferable over a slight performance improvement, however, one must appreciate that permanent solutions, such as splices, offer the lowest risk for space-based applications.

6.5 Optical Characteristics of Fibre Collimators

The cryogenic behaviour of discrete fibre collimators was characterized to compare the performance of off-the-shelf collimators against those designed specifically for cryogenic operation. Two collimators were selected: a commercial off-the-shelf Thorlabs F230APC-1550 stainless steel collimator with 4.61 mm focal length [268] and a custom OZ Optics 18.75 mm focal length Kovar collimator with cryogenic epoxy [269], which are referred to as stainless steel and Kovar, respectively. Kovar was selected as it was designed to have a CTE close to that of silicate glasses [270]. Each collimator is characterized individually. The collimator under test was mounted on the 4 K plate of a cryostat and aligned through a cryogenic iris and window on the vac-

uum chamber wall; a 1550 nm Fitel FRL15DCWD LD [260] in a Koheron CTL200 LD controller [207] at room temperature provided infrared light to the collimator via a custom Kurt J. Lesker hermetic fibre feedthrough [267] (respective specifications given in Tables C.6, C.10 and C.11). The iris was necessary to reduce radiant loading on the 4 K plate from the window and vacuum chamber which would have otherwise prevented the collimator from reaching 4 K. As the collimator was cooled, the beam passing through the cryostat window was recorded by a WiDy SenS 640 V-ST InGaAs camera [271] (640512 resolution, 9.6×7.68 mm array, 15 µm pixel pitch; further specifications given in Table C.15) placed ∼1 m from the collimator lens. A custom ∼27 dB fibre attenuator fabricated by intentionally misaligning a splice between two fibres was used to avoid saturating the camera. Figure 6.8a shows a collimator and iris in the cryostat, and Figure 6.8b shows the beam profile of the stainless steel collimator when it is at ∼4 K.

Fitted Gaussian parameters are shown in Figure 6.9 for the stainless steel and Kovar collimators on the temperature descent. Three parameters are plotted: the amplitude at the centre of the beam profile, the change in full width at half maximum (FWHM) in each direction (Δx_{FWHM} and Δy_{FWHM}), and the motion of the centre of the beam (Δx_{c} and Δy_{c}). These results can be summarized as:

1. The intensities of the stainless steel and Kovar collimators decrease by 21 % and increase by 16 %, respectively, from room temperature to 4 K.
2. For the stainless steel collimator, the Δx_{FWHM} and Δy_{FWHM} measurements increase by 42 µm and 61 µm, respectively, while the measurements for the Kovar collimator decrease by 144 µm and 108 µm, respectively. These changes fall in the range of 6 to 9 %.
3. The Δx_{c} measurements for the beam centre show changes of 143 µm and 20 µm for the stainless steel and Kovar collimators, respectively. The vertical change

is significantly larger, with corresponding measurements in Δy_c of 922 µm and 1012 µm.

The observed change in amplitude and FWHM are consistent. The Kovar collimator shows a narrowing of the beam profile, and thus the intensity at the beam centre increases; the stainless steel shows the opposite, as the beam profile widens leading to a reduction in intensity. This effect is likely due to the position of the fibre tip relative to the lens within the collimator housing. At room temperature, if the tip of the fibre is positioned at the focal length of the lens in the stainless steel collimator, then the launched beam is collimated. When cooled, the stainless steel housing contracts and pulls the fibre tip closer to the lens so that the beam diverges, leading to the observed widening of the beam and reduced intensity. Similarly, if the tip of the fibre in the Kovar collimator is farther from the lens than the focal length, then the launched

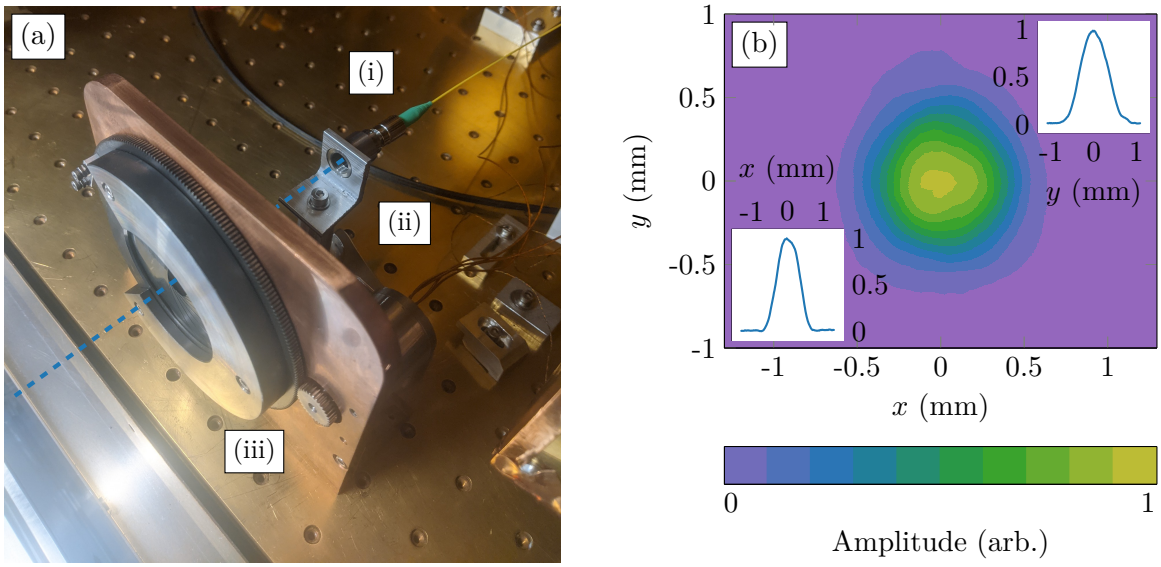

Figure 6.8: Experimental configuration and beam image obtained in cryogenic discrete collimator characterization. In (a), the stainless steel collimator (i) in a custom aluminum mount (ii) on the 4 K plate of a cryostat. The beam passes through a cryogenic iris (iii) to reduce light entering the cryostat. The beam profile from the stainless steel collimator at ∼4 K is shown in (b) with normalized units; respective x and y cross sections are shown in the lower left and upper right corners with position in mm on the horizontal axes and amplitude in arbitrary units on the vertical axes.

beam converges with the beam waist likely located before the camera 1 m away. As the Kovar housing contracts, the fibre tip is brought into focus, and the waist of the launched beam is pushed closer to the camera resulting in the observed narrowing of the beam and increased intensity.

It is expected that Δx_c is small, as there is little to no motion in the horizontal direction when cooling. Small changes in horizontal alignment are present due to vibrations introduced by the pulse tube coolers and differential contraction between

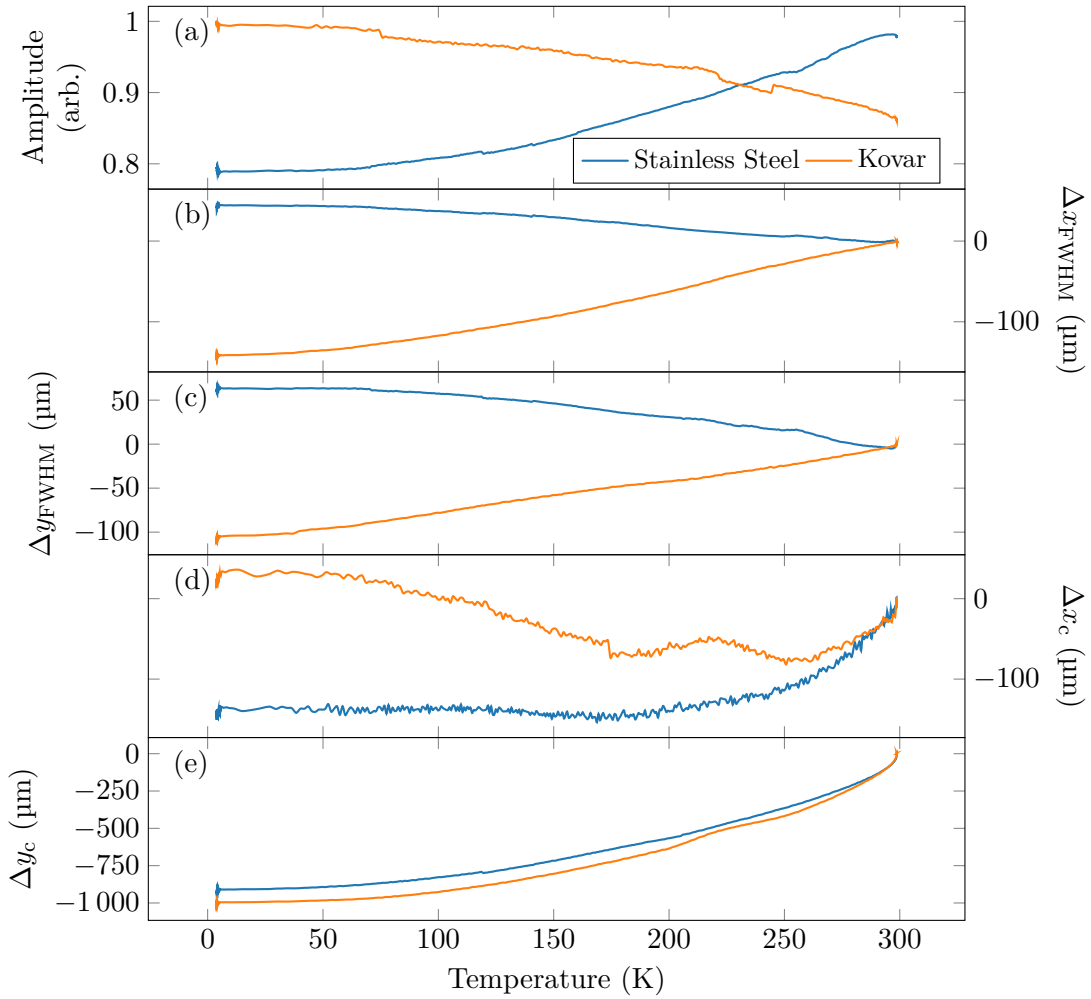

Figure 6.9: Beam parameters of stainless steel and Kovar collimators recorded on the temperature descent showing the beam amplitude (a); change in beam width Δx_{FWHM} (b) and Δy_{FWHM} (c); and change in beam centre location Δx_c (d) and Δy_c (e). A summary of the key results from these data are given in the enumerated list on page 156.

the optical components and housings. The most significant change is attributed to the epoxy that holds the lens in the collimation package, which can contract and relax the fit of the lens in the housing, allowing it to shift. A change in vertical position of the beam centre is expected, and a consistent change is observed for both collimators. The 4 K plate is suspended in the cryostat, and when cooled, the suspension contracts, pulling the 4 K plate upward with it. As the collimator is mounted on the 4 K, the collimator moves upward and "scans" the beam along the camera. The camera readout is inverted since it assumes a lens in place, but for this application, the beam was directly on the detector array, resulting in the negative Δy_c as the collimator is pulled upward.

Overall, the horizontal and vertical drift in the beam centre positions is negligible over the 1 m distance from the collimator to the camera, as these drifts correspond to a maximum $\sim$1 mrad change in pointing angle. The stainless steel collimator exhibited a reduction in beam size and increase in amplitude, while the Kovar collimator behaved oppositely — neither the stainless steel nor Kovar collimator showed a sufficiently significant difference to preclude either from adoption in a practical cryogenic range-resolved laser interferometer configuration.

Although the sample size is too small to establish meaningful statistics, it is encouraging that these results suggest commercial off-the-shelf collimators offer an inexpensive route to cryogenic range-resolved laser interferometer deployments. Where possible, Kovar may be preferred due to its better CTE match with glass than stainless steel, however, in some cryogenic applications, such as the cryogenic multiaxis measurements in Section 7.2, FC/APC stainless steel collimators are required due to limitations in the length of the free space beam path since part of the optical path difference (OPD) must be made up in fibre to ensure demodulatability of all axes — this is not possible with the available FC/PC Kovar collimators, which would introduce a $\sim$4 % Fresnel reflection [10] from the fibre tip. Altogether, the measured

characteristics show that both the commercial off-the-shelf stainless steel collimator and the custom Kovar collimator are acceptable for cryogenic range-resolved laser interferometry applications.

6.6 Conclusions

Key results from the cryogenic characterization experiments discussed in this chapter are summarized in Table 6.3. Acrylate coated fibres are recommended due to their repeatable transmittance behaviour. While polyimide coatings may offer benefits in longevity over many temperature cycles, their testing was inconclusive. Neither acrylate nor polyimide coatings showed evidence of degradation in mechanical strength and coating integrity over one and three temperature cycles. Another practical benefit is that acrylate coatings are cheaper and easier to work with than polyimide. Fibre mating tests do not suggest preference of one mating strategy over another, so

Table 6.3: Key results of cryogenic characterization of fibre and optical components in the context of a cryogenic deployment of a range-resolved laser interferometer. A ★ in the *Summary* denotes a recommendation based solely on the *Characterization* performed in that *Section*.

Section	Characterization	Summary
6.1	Fibre Mechanical Strength	Polyimide shows greater strength No strength degradation of acrylate or polyimide ★ Both acrylate and polyimide are acceptable
6.2	Fibre Coating Integrity	No coating degradation of acrylate or polyimide ★ Both acrylate and polyimide are acceptable
6.3	Fibre Transmittance	Acrylate shows minimal and repeatable transmittance changes Polyimide is inconclusive ★ Acrylate is preferred
6.4	Fibre Mating Transmittance	FC/APC and FC/PC performed similarly Two-piece and monolithic sleeves performed similarly ★ No special mating considerations are required
6.5	Fibre Collimators	Stainless steel and Kovar collimators performed similarly ★ May prefer Kovar due to CTE match with glass
6.6	Summary	★ Acrylate fibre coating is preferred over polyimide ★ No special mating considerations ★ Both stainless steel and Kovar collimators are acceptable

mating should be selected based on other considerations, such as cost and reduction of back reflections. This assumes a laboratory environment, and in space applications where hardware must survive launch forces, monolithic configurations including fibre splices, are preferred. There was insufficient evidence to favour expensive monolithic mating sleeves over cheaper two-piece sleeves. Discrete collimator testing showed similar performance between the commercial off-the-shelf stainless steel collimator and the custom Kovar collimator.

A significant outcome of these characterization results is that in general, standard commercial off-the-shelf components may be used in cryogenic applications without special consideration. Due to the harsh conditions in cryogenic environments, the component testing described in this chapter was necessary to establish the robustness of components used in the cryogenic SFM range-resolved laser interferometer applications explored in Chapter 7.

Chapter 7

Multiaxis Sinusoidal Frequency Modulation Interferometry Applications

Having implemented the sinusoidal frequency modulation (SFM) technique in the frequency-modulation-demodulation unit (FMDU), I designed several experiments which aimed at demonstrating cryogenic and multiaxis applications of the technique. In total, eight applications were explored:

Section 7.1 presents simultaneous multiaxis measurements in atmosphere.

Section 7.2 presents simultaneous multiaxis measurements at cryogenic temperatures.

Section 7.3 presents a strategy for determining the resolution of the SFM range-resolved laser interferometer.

Section 7.4 presents an investigation into the long-term stability of the technique.

Section 7.5 presents a novel wave division multiplexing HeNe interferometer used to verify the SFM technique.

Section 7.6 presents the integration of the FMDU with several components to implement a cryogenic force feedback accelerometer.

Section 7.7 presents the cryogenic characterization of a monolithic silica resonator.

Section 7.8 presents a novel technique that exploits the multiaxis nature of the SFM approach to extend the measurement range beyond the conventional single-axis limit.

At the end of the chapter, the experimental results are summarized into Table 7.5 to show that the SFM technique exceeds the SPICA Far-Infrared Instrument (SAFARI) Fourier transform spectrometer (FTS) metrology requirements introduced in Section 1.2.

7.1 Application #1: Multiaxis Interferometer

To demonstrate the simultaneous measurement of multiple axes, a three-axis interferometer was constructed at room temperature in atmosphere. Several measurements were recorded and are presented in this section as a realization of the theory presented in Chapter 3.

7.1.1 Experiment

The three-axis interferometer shown in Figure 7.1 was constructed under ambient conditions with the demodulatability configuration $M_\ell = \{0, 1, 3\} \implies M_\Delta = \{1, 2, 3\} \implies d_\star = 1$ from Section 3.4 to achieve total demodulatability (i.e., all axes are demodulatable). A laser modulation frequency of $f_\mathrm{m} = 100\,\mathrm{kHz}$ and modulation amplitude $\nu_\mathrm{A} = 1.51(12)\,\mathrm{GHz}$ to produce the sinusoidal optical frequency modulation in Equation (3.1). Recall from Section 4.5.2 that the modulation frequency is equal to the displacement sample rate, thus each axis is sampled at 100 kHz. A Thorlabs CM05-BS018 mounted cube beamsplitter [272] was used to split the probing beam from a custom OZ Optics 18.75 mm focal length Kovar collimator [269] to form three axes. The primary axes, $\alpha\beta$ and $\alpha\gamma$, probe the displacements of two Thorlabs PS974M-C prism retroreflectors [273] mounted to PI PIHera linear piezoelectric transducer (PZT) positioners [274]. The secondary axis, $\beta\gamma$, is redundant, and measures the difference in displacement between the two primary axes. Table 7.1 shows the selected optical path differences (OPD) and corresponding modulation amplitudes for each axis.

Table 7.1: Modulation parameters for the three-axis interferometer in Figure 7.1. The paremeters Λ_c and A are defined in Sections 3.1.1 and 3.2.3, f_b^+ in Section 3.2.4, and η in Section 3.2.6.

Axis	Λ_c (cm)	A (rad)	f_b^+ (MHz)	η
$\alpha\beta$	50(1)	15.8(13)	1.58(13)	0.40(1)
$\alpha\gamma$	162(1)	51.2(42)	5.12(42)	0.34(1)
$\beta\gamma$	112(1)	35.4(29)	3.54(29)	0.26(1)

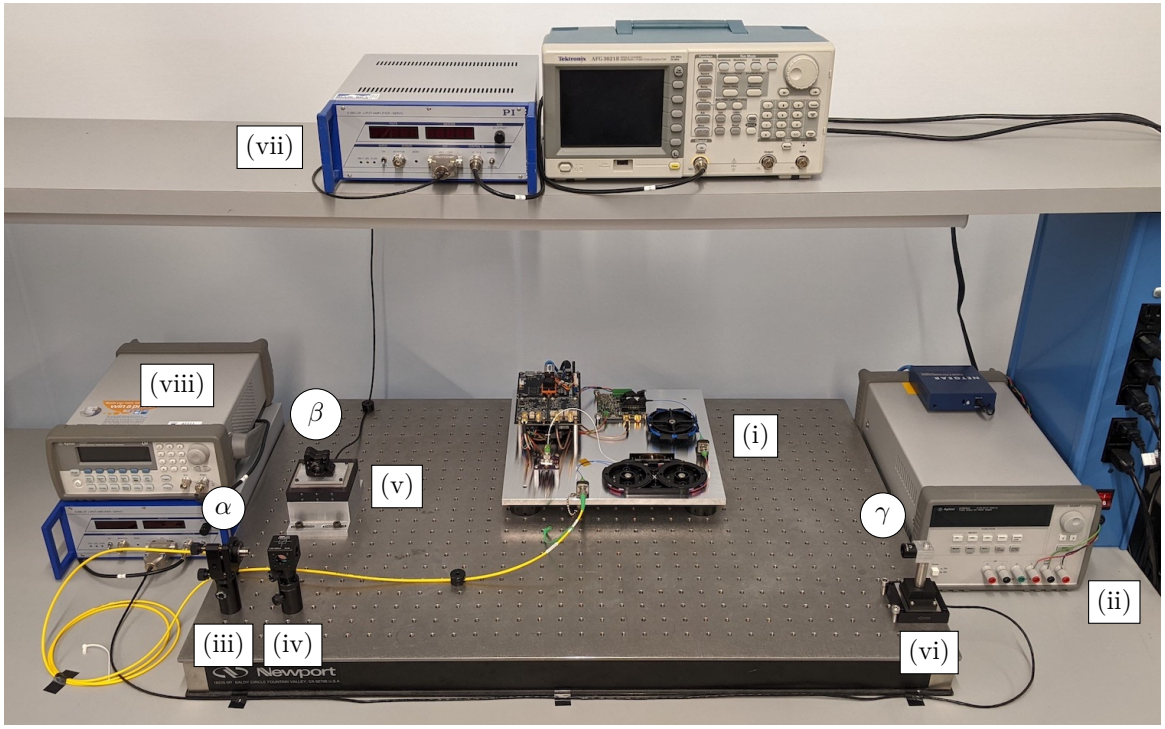

Figure 7.1: Room temperature three-axis interferometer configuration. The LD controller and detector of the FMDU (i) receive power from a low-noise power supply (ii). The FMDU delivers a probing signal to a collimator (iii) where the FC/PC termination provides a ∼4 % Fresnel reflection [10]. The remaining light is launched by the collimator where it is split by the cube beamsplitter (iv) and probes PZT-mounted retroreflectors (v) and (vi). The left and right PZT positions are modulated by waveform generators and amplifiers (vii) and (viii), respectively. This interferometer forms three axes with $S = \{\alpha, \beta, \gamma\}$.

The PZT positioners were driven with two different motion profiles. The positioner at β was driven with a 2 Hz sine wave, and the positioner at γ with a 0.2 Hz triangular wave. Assuming that the fibre tip at α is fixed, the $\alpha\beta$ and $\alpha\gamma$ axes depend on the positions of *one* reflector, while the $\beta\gamma$ axis depends on *both*. This interferometer has a folding factor of 2, so upon measurement of the optical displacement, $\Delta\Lambda$, the mechanical displacement, Δx, can be determined as $\Delta x = \Delta\Lambda/2$.

Several simulations in Chapter 5 required an estimate of the signal-to-noise ratio (SNR) in a multiaxis interferometer. The SNR was estimated over ten modulation periods where the detector signal was sampled at $f_s = 100\,\text{MHz}$ using a Tektronix DPO4034 oscilloscope [275], which is the same rate as the analog-to-digital converter (ADC) on the FMDU. Determining the SNR of a frequency modulated signal is challenging, however, by inspection, the SNR is large, so it was estimated by low-pass filtering the detector voltage using a three-point moving average to obtain the signal and subtracting the signal from the detector voltage to obtain the noise. The signal

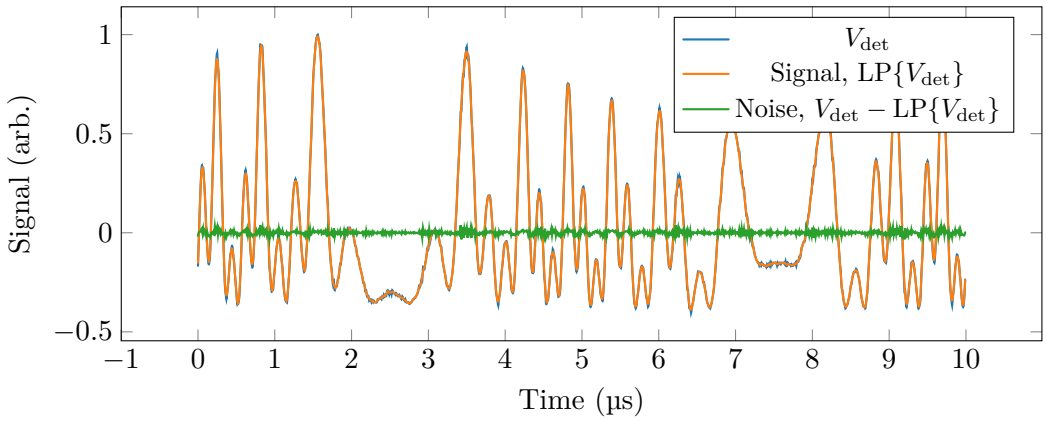

Figure 7.2: SNR measurement of a three-axis interferometer over one modulation period. The signal is sampled at $f_s = 100\,\text{MHz}$. Determination of SNR for a frequency modulated signal is challenging but was estimated using a basic procedure. By inspection, the SNR is large, so low-pass filtering of the detector voltage was used to obtain estimates of the signal (LP$\{V_{\text{det}}\}$) and the noise ($V_{\text{det}} - \text{LP}\{V_{\text{det}}\}$) to determine the SNR by Equation (5.1); the low-pass filter is a moving average with a width of three. An SNR of ∼960 was estimated.

and noise are shown in Figure 7.2 and correspond to SNR $\approx$ 960, thus, even in this three-axis interferometer with several reflections, the SNR is $\sim 10^3$.

The displacement measurement of $\Delta x_{\beta\gamma}$ is redundant, as it can be calculated from the displacements $\Delta x_{\alpha\beta}$ and $\Delta x_{\alpha\gamma}$. When the OPD of the $\alpha\beta$ axis increases to motion of the β positioner, the OPD of the $\beta\gamma$ axis decreases by the same amount, however, the $\alpha\gamma$ and $\beta\gamma$ OPDs both increase and decrease together by the same amount due to the motion of the γ positioner. One may calculate the displacement of the $\beta\gamma$ axis as $\Delta x_{\beta\gamma} = \Delta x_{\alpha\gamma} - \Delta x_{\alpha\beta}$, which is plotted over the directly measured displacements in Figure 7.3a. This property can be leveraged to assess the internal consistency of the technique, since ideally, $(\Delta x_{\alpha\gamma} - \Delta x_{\alpha\beta}) - \Delta x_{\beta\gamma} = 0$. The calculated and measured displacements for the $\beta\gamma$ axis are nearly identical and agree to 13 nm rms in a 50 kHz bandwidth over the entire 5 s measurement period. It must be noted that this measurement is not the resolution of the interferometer; this is simply a measurement of $(\Delta x_{\alpha\gamma} - \Delta x_{\alpha\beta}) - \Delta x_{\beta\gamma}$ to show the consistency among all three axes. The resolution is determined experimentally in Section 7.3.

A longer acquisition with the exact same interferometer configuration was recorded over 48 h with the displacement sampling reduced from 100 kHz to 1 kHz, which in turn reduces the data volume from $\sim$140 GB to $\sim$1.4 GB. Figure 7.3b shows the difference $(\Delta x_{\alpha\gamma} - \Delta x_{\alpha\beta}) - \Delta x_{\beta\gamma}$. Over the entire interval, the measurements again agree to 13 nm rms but in a 500 Hz bandwidth. For additional context, in this time, the $\alpha\beta$, $\alpha\gamma$, and $\beta\gamma$ axes traveled total distances of approximately 8.3, 65.7, and 66.0 km, respectively. These results show that the demodulation has excellent phase stability over extended measurement periods, however, the results cannot be interpreted as a lack of drift in the measurement. One must appreciate that these results demonstrate internal consistency amongst redundant measurements, but not effects due to long-term drift in the laser frequency. Frequency drifting effects are canceled in the

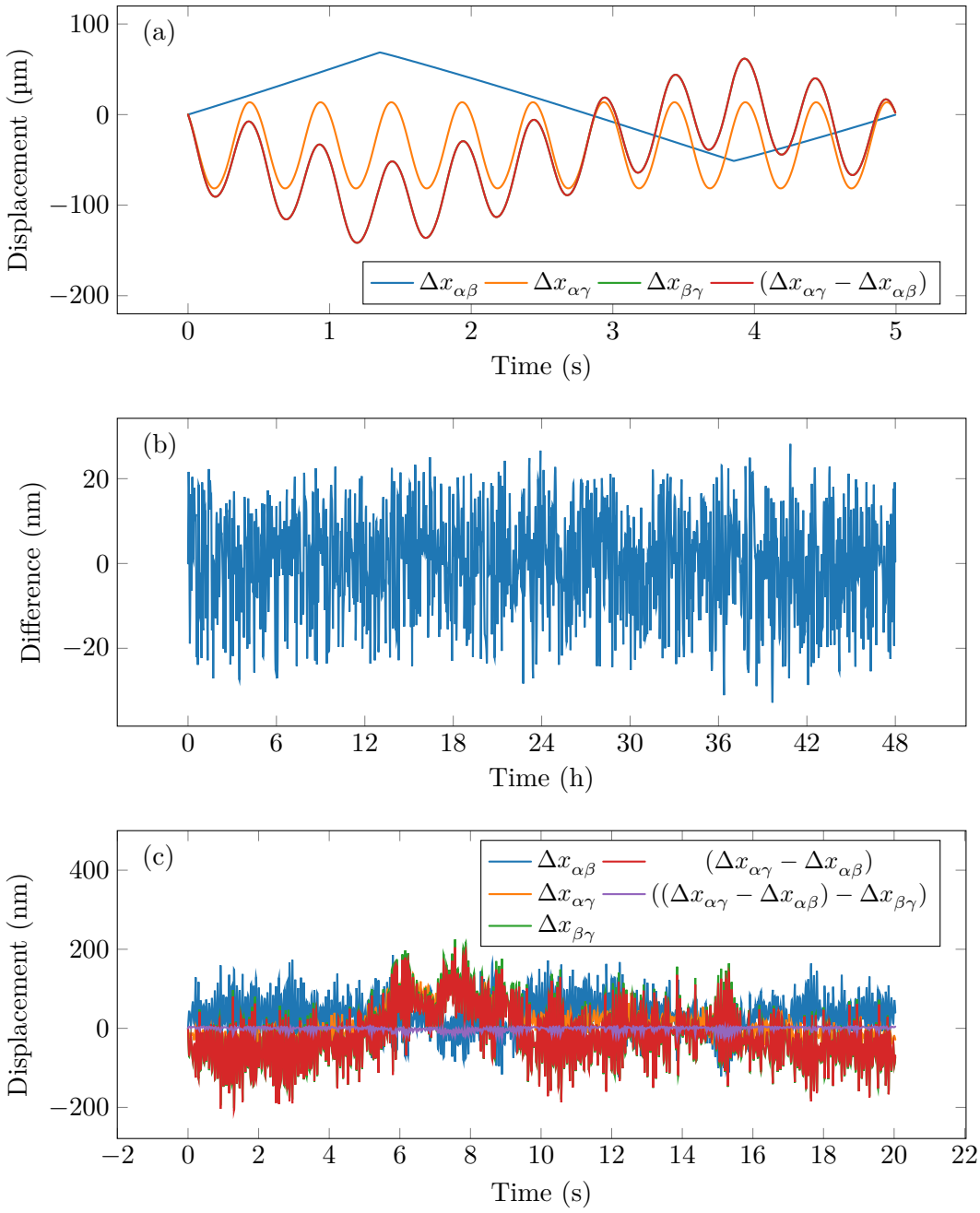

Figure 7.3: Measured mechanical displacements for the three-axis interferometer in Figure 7.1. Simultaneously measured displacements are plotted in (a) include the calculated displacement of the $\beta\gamma$ axis as the $\Delta x_{\alpha\gamma} - \Delta x_{\alpha\beta}$ curve; $\Delta x_{\beta\gamma}$ is not visibile because it is covered by $\Delta x_{\alpha\gamma} - \Delta x_{\alpha\beta}$. The calculated and measured displacements of the $\beta\gamma$ axis agree to 13 nm rms in a 50 kHz bandwidth. Residual (downsampled for plotting purposes) of a 48 h acquisition is shown in (b) for $(\Delta x_{\alpha\gamma} - \Delta x_{\alpha\beta}) - \Delta x_{\beta\gamma}$ with 13 nm rms in a 500 Hz bandwidth. PZTs were not driven for the measurements in (c), and the residual, $(\Delta x_{\alpha\gamma} - \Delta x_{\alpha\beta}) - \Delta x_{\beta\gamma}$, shows 6 nm rms in a 50 kHz bandwidth.

calculation of $(\Delta x_{\alpha\gamma} - \Delta x_{\alpha\beta}) - \Delta x_{\beta\gamma}$ since the same drift is experienced by every axis of the interferometer.

A similar set of measurements were collected for the interferometer, but this time, the PZT positioners at β and γ were not driven. Figure 7.3c shows the direct displacement measurements along with the redundant $\Delta x_{\beta\gamma}$ computed from $\Delta x_{\alpha\gamma} - \Delta x_{\alpha\beta}$ and the residual $(\Delta x_{\alpha\gamma} - \Delta x_{\alpha\beta}) - \Delta x_{\beta\gamma}$; the resisdual shows 6 nm rms in a 50 kHz bandwidth. This result further demonstrates the internal consistency of the FMDU implementation of the SFM technique. The relatively large observed displacement in the direct measurements of $\Delta x_{\alpha\beta}$, $\Delta x_{\alpha\gamma}$, and $\Delta x_{\beta\gamma}$ are due to stray charge in the PZTs — a similar measurement in atmosphere presented in Section 7.4 with the retroreflector secured directly to a breadboard rather than a PZT shows ∼0.4 nm rms stability over the 20 Hz bandwidth called for by the SAFARI FTS [33] outlined in Table 1.1.

7.1.2 Windowed Spectrum

A theoretical windowed spectrum can be found via Equation (3.38). To achieve correct scaling of the peaks in the spectrum, the normalized signal contributions, η, defined in Equation (3.29), must be determined for each axis. A procedure for finding η is presented, which requires measurement of I_a (or the equivalent power, P_a) for each a in S.

For the three-axis interferometer, the powers were measured using a Keysight N7744A optical power meter [219] in two steps (specifications given in Table C.13). The fibre from the third arm of the circulator that is mated to the detector was transferred to a port on the power meter and the laser was enabled but not modulated. The power from the Fresnel reflection [10] at the ferrule-connector physical contact (FC/PC) fibre tip, P_α, was measured by inserting a card in front of the collimator

to block the beam from the rest of the interferometer optics and found to be $P_\alpha = 71.3(2)\,\mu\text{W}$.

To measure P_β and P_γ, the same procedure as P_α was repeated, but the retroreflector other than the one that is part of the axis to be measured was blocked, so the $\alpha\beta$ axis was active for the P_β measurement and $\alpha\gamma$ for the P_γ measurement. The retroreflectors were displaced so that fringes were detected, and the maximum and minimum power, P_{max} and P_{min}, respectively, were recorded. Let P_x be the measurement for either P_β or P_γ. From Equation (3.27), the maximum power occurs at $P_0 + 2\sqrt{P_\alpha P_x}$ and the minimum at $P_0 - 2\sqrt{P_\alpha P_x}$, where P_0 is the offset power. From these relationships, P_x may be determined by solving $P_{\text{max}} - P_{\text{min}}$ as

$$P_x = \frac{(P_{\text{max}} - P_{\text{min}})^2}{16 P_\alpha}. \qquad \text{[W]} \quad (7.1)$$

Using Equation (7.1), $P_\beta = 42(3)\,\mu\text{W}$ and $P_\gamma = 29.8(9)\,\mu\text{W}$ were found. The η for each axis was determined with Equation (3.29) and shown in Table 7.1.

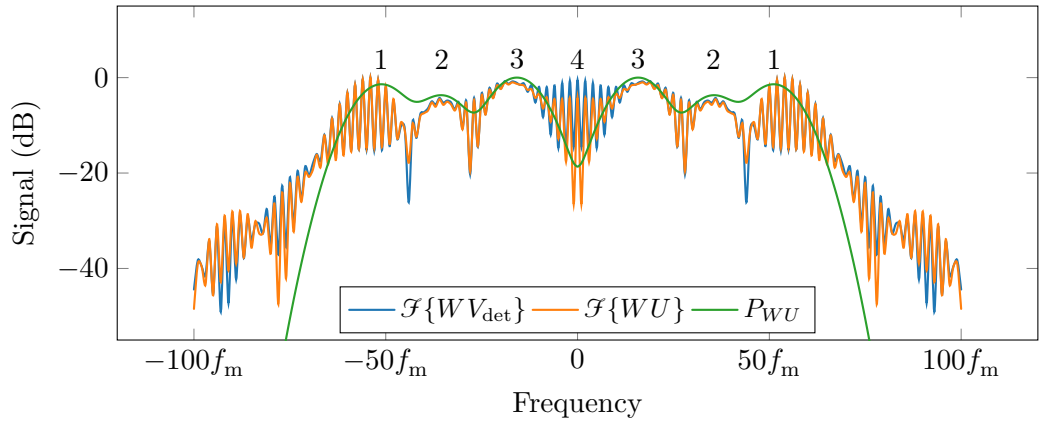

Figure 7.4: Power spectra of the detector, V_{det}, and high-pass filtered, U, interference signals. An approximated theoretical power spectrum, P_{WU}, from Equation (3.38), is shown. Lobes (ordered by increasing frequency) are: 4 is due to the signal offset voltage, 3 is the $\alpha\beta$ axis, 2 is the $\beta\gamma$ axis, and 1 is the $\alpha\gamma$ axis. Close agreement is seen between the measured and theoretical power spectrum using the calibrated normalized power contributions, η, and this result can be compared to the theoretical spectra plotted in Figure 3.8.

Measured power spectra for the windowed V_{det} and U are shown in Figure 7.4; U was obtained by high-pass filtering V_{det} having filter widths of $K_{\text{HP1}} = 250$ and $K_{\text{HP2}} = 500$ with low-pass filtering and amplitude normalization disabled. Additionally, a theoretical power spectrum, P_{WU}, computed using Equation (3.38) and the efficiency parameters in Table 7.1 are plotted, and can be compared to the theoretical spectra plotted in Figure 3.8. The theoretical spectrum shows close agreement with $\mathcal{F}\{WV_{\text{det}}\}$ for lobes 1, 2, and 3. The power spectrum using the unfiltered V_{det} shows a strong baseband component in lobe 4 due to the signal offset that carries approximately equal power to the signal lobes 1, 2, and 3. With the high-passed filtered U, the power in the 4^{th} lobe is reduced, but not completely, as total removal of the lobe would be observed as the upper envelope of $\mathcal{F}\{WU\}$ following a curve like P_{WU} in the $\pm 10 f_{\text{m}}$ region. This indicates that the implementation can benefit from improvements to offset removal in the front-end filtering.

7.2 Application #2: Cryogenic Multiaxis Interferometer

Section 7.1 demonstrated simultaneous multiaxis measurements at room temperature, and this section explores similar multiaxis measurements at cryogenic temperatures. As the PZTs in Section 7.1 would not work when cooled, thermal expansion of an aluminum 6061 sample and the displacement of a custom cryogenic linear stage designed for the SAFARI FTS, the Fourier transform spectrometer mechanism (FTSM) [73, 276], was provided by ABB [277] and measured.

It must be appreciated that this experiment was challenging. Several single-axis interferometers have been tested at cryogenic temperatures in the past, but this was the first successful multiaxis configuration. A 2×2 fibre coupler was used to split the probing beam so that both the aluminum sample and the FTSM could be measured. On the first attempt, the 2×2 coupler was installed inside the cryostat on the 45 K shielding. When cooled, the signal was completely lost around 200 K and was believed

to have been due to cooling of the coupler. On the second attempt, the coupler was again installed in the cryostat but held at room temperature as it was suspended from the upper vacuum chamber using a custom bracket. This improved matters, but the signal was lost before reaching the target temperature. The first two attempts used a ∼1 mm thick aluminum sample compared to the ∼3 mm thick sample in later tests, and it was speculated that alignment was lost due to bowing of the sample as it was cooled. On the third attempt, a thicker ∼3 mm aluminum sample was used. This initially worked and expansion of the aluminum sample was measured at around 10 K. While waiting for the FTSM to reach its target temperature, the signal was again lost entirely. Since measurements initially worked at ∼10 K, it was speculated that parasitic cooling of the coupler through the fibres was responsible for this failure. On the fourth and final attempt that yielded the results presented in this section, anything that could have gone wrong was eliminated. Cooling of the 2×2 coupler was a failure point (and has been in previous work [278]) so it was moved to the outside of the cryostat and held at room temperature. Custom purpose-built fibres were prepared to deliver the probing signal from the hermetic feedthrough directly to the 4 K plate. The custom fibres also eliminated three mating sleeves that were required in the 4 K workspace for the previous configurations that used several readily available fibres to achieve appropriate OPD offsets.

The interferometer was constructed using the design in Figure 7.5a. The probing signal from the FMDU was split by a Thorlabs TW1550R5A2 2×2 fibre coupler [279] external to the cryostat. To measure the aluminum sample installed in a custom aluminum measurement jig (Figure 7.5b) and the FTSM (Figure 7.5c), the split signals are passed through the custom Kurt J. Lesker hermetic fibre feedthrough [267] in Figure 7.5d (specifications given in Table C.10). Three custom purpose-built SMF-28-J9 [229] fibres were prepared for installation inside the cryostat: one 150(1) cm with ferrule-connector angled physical contact (FC/APC) and FC/PC terminations,

one 25.0(5) cm with both ends FC/APC terminated, and one 250(1) cm with both ends FC/APC terminated. These lengths lead to the total demodulatability configuration described below so that both the aluminum sample and the FTSM may be simultaneously measured.

The 150 cm fibre guided one probing beam from the 2×2 coupler to the aluminum sample, and the FC/PC terminated end produced the reference reflection, α. The 25 cm fibre introduced an OPD offset required for the aluminum measurement since the optical frequency of the laser diode (LD) cannot be swept far enough to measure the ∼8 cm aluminum sample directly. Two custom aluminum clamps were fixed on either end of the 76.50(5) mm aluminum sample and hold a Thorlabs F260APC-1550 collimator [280] and a Thorlabs PS974M-C prism retroreflector [273] in alignment. A reflection, β, was produced by the retroreflector. A Lake Shore Cryotronics Cernox CO thermometer [249] installed on the aluminum sample measured its temperature and a $25\,\Omega \pm 1\,\%$ power resistor bolted to the sample was used to heat it so that its expansion could be measured. The aluminum measurement jig was placed on the 4 K plate but not bolted down to avoid introduction of a mounting force that may hold the collimator and retroreflector mounts in place. The 250 cm fibre delivers the other probing beam from the 2×2 coupler to the FTSM with the same collimator model to probe an aligned-by-design integrated prism retroreflector on the mechanism that produced the γ reflection. The aluminum sample and FTSM are shown in the cryostat side-by-side in Figure 7.5e before cooling.

The configuration depicted in Figure 7.5a shows that the aluminum sample in the $\alpha\beta$ axis has an OPD of $\Lambda_{\alpha\beta} \approx 90$ cm. The arm with the FTSM does not have an integrated reference reflection, just γ from the retroreflector on the mechanism, however, it can be measured with respect to α in the arm with the aluminum sample. Since the fibre to the FTSM is ∼100 cm longer than the FC/PC terminated fibre from the hermetic feedthrough, the OPD of the $\alpha\gamma$ axis is comprised of this length

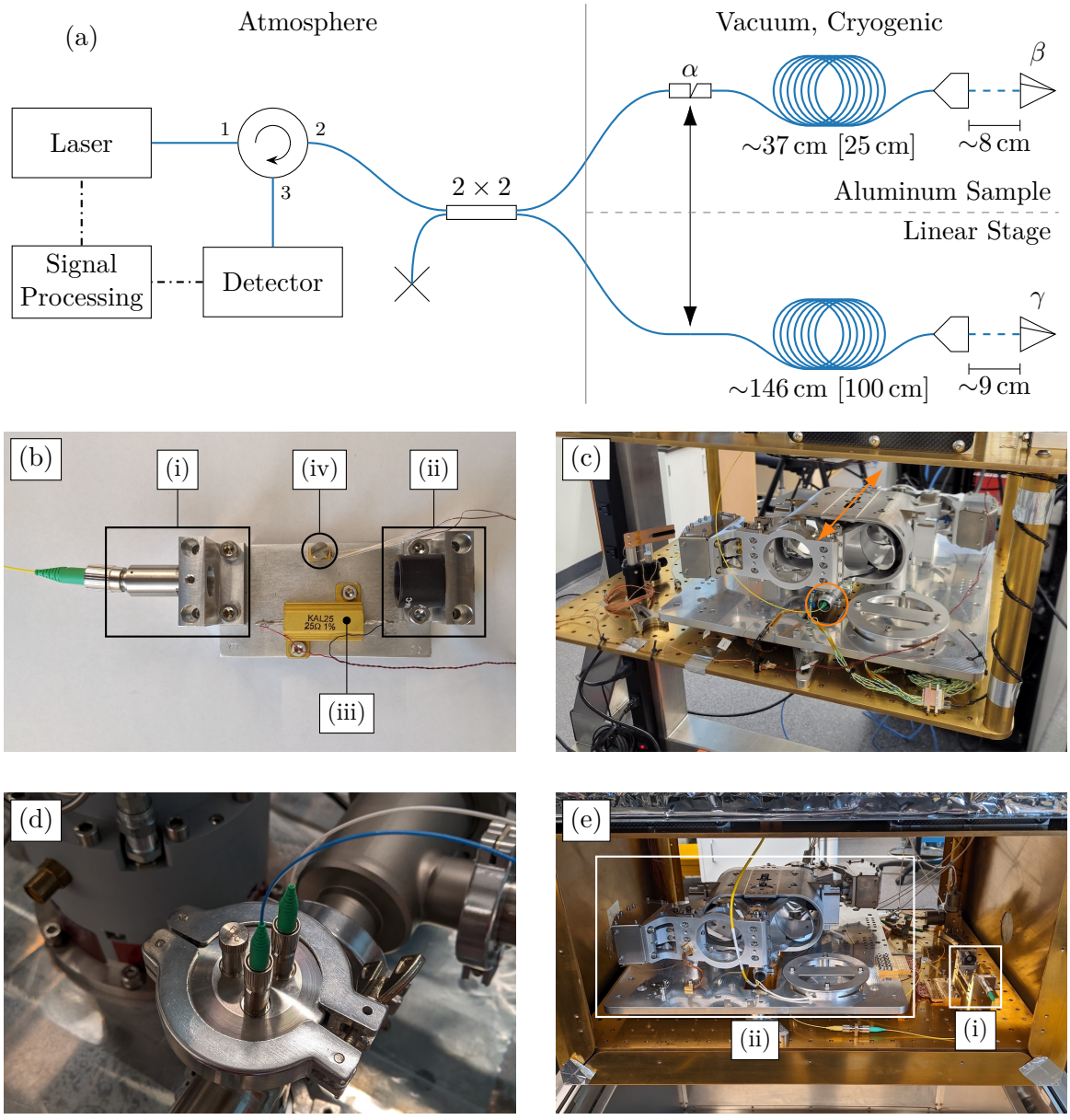

Figure 7.5: Configuration for a cryogenic multiaxis measurement of an aluminum sample and linear translation stage. The schematic (a) shows a three-axis interferometer formed by $S = \{\alpha, \beta, \gamma\}$. The vertical arrow points to locations in each fibre that are the same length from the 2×2 coupler. Provided fibre lengths are measured from the vertical arrow to the respective collimator in each path; lengths are optical with mechanical lengths of fibres shown in brackets. The aluminum sample is shown in (b) with collimator (i), retroreflector (ii), heating resistor (iii), and thermometer (iv). The cryogenic linear translation stage is shown in (c); the arrow shows the direction of travel and the circle indicates the fibre delivering the probing beam. The 2×2 fibre coupler was outside the vacuum chamber and connected to the hermetic fibre feedthrough in (d). In (e), both the aluminum sample (i) and linear translation stage (ii) can be seen installed in the cryostat. I would like to thank Alain Cournoyer at ABB [277] for permission to use the photos of the FTSM in (c) and (e).

and the ∼9 cm collimator to retroreflector distance in the FTSM, giving an OPD of $\Lambda_{\alpha\gamma} = \sim 310\,\text{cm}$. The remaining $\beta\gamma$ axis then has an OPD of $\Lambda_{\beta\gamma} = \sim 220\,\text{cm}$. This configuration has the $M_\ell = \{0, 1, 3\} \implies M_\Delta = \{1, 2, 3\} \implies d_\star = 1$ demodulatability condition from the model in Section 3.4. Although the $\beta\gamma$ axis can be measured as in Section 7.1, it is not presented in these results.

One drawback of this configuration is that the $\alpha\gamma$ axis is sensitive not just to the ∼310 cm OPD described above, but also the two ∼100 cm fibre pigtails from the 2×2 coupler outside the cryostat to the hermetic feedthrough and the two ∼150 cm lengths of fibre in the cryostat from the hermetic feedthrough to α and the equivalent point in the FTSM arm marked by the vertical arrow in Figure 7.5a. However, these fibres are differential, and were taped together along their lengths to better common-mode the temperature fluctuations and vibrations experienced along their lengths. The pigtailed fibres from the 2×2 coupler were also wound around a capstan near the feedthrough. As both the $\alpha\beta$ and $\alpha\gamma$ OPDs are sensitive to length fluctuations in the fibres, the aluminum sample was installed in the shorter $\alpha\beta$ axis since the expansion of the aluminum sample is three orders of magnitude less than the displacement of the driven FTSM.

The FMDU was configured to modulate the LD at a rate of $f_\text{m} = 100\,\text{kHz}$ with a modulation amplitude of $\nu_\text{A} = 1.00(8)\,\text{GHz}$ from the modulation equations in Sections 3.1 and 3.2. When the FTSM settled at an average temperature of <6 K, it was driven in an open-loop control mode with a 0.01 Hz sine wave and the FMDU measured both the aluminum sample and FTSM for 30 min while ∼3 mW was dissipated through the resistor for the first 6 minutes. The measured displacements of the $\alpha\beta$ and $\alpha\gamma$ axes, which from now on are referred to as Δx_Al and Δx_FTSM, respectively, are plotted in Figure 7.6a. The measured change in length of the aluminum sample and its temperature, T_Al, are shown in Figure 7.6b. The FTSM temperature did not change significantly over the measurement period and was <6 K the entire time.

The FTSM shows a consistent motion profile with a ∼7.2 mm stroke. A sinusoid was fitted to Δx_{FTSM}, and the difference between the measured and fitted displacements gives the residual, $\Delta x_{\text{FTSM,res}}$, plotted in Figure 7.6a. The residual is ∼130 µmpp but is scaled up by a factor of ten in the plot for visualization. The periodic residual displacement results from the nonlinearity of the mechanism and was expected when operating in open loop mode.

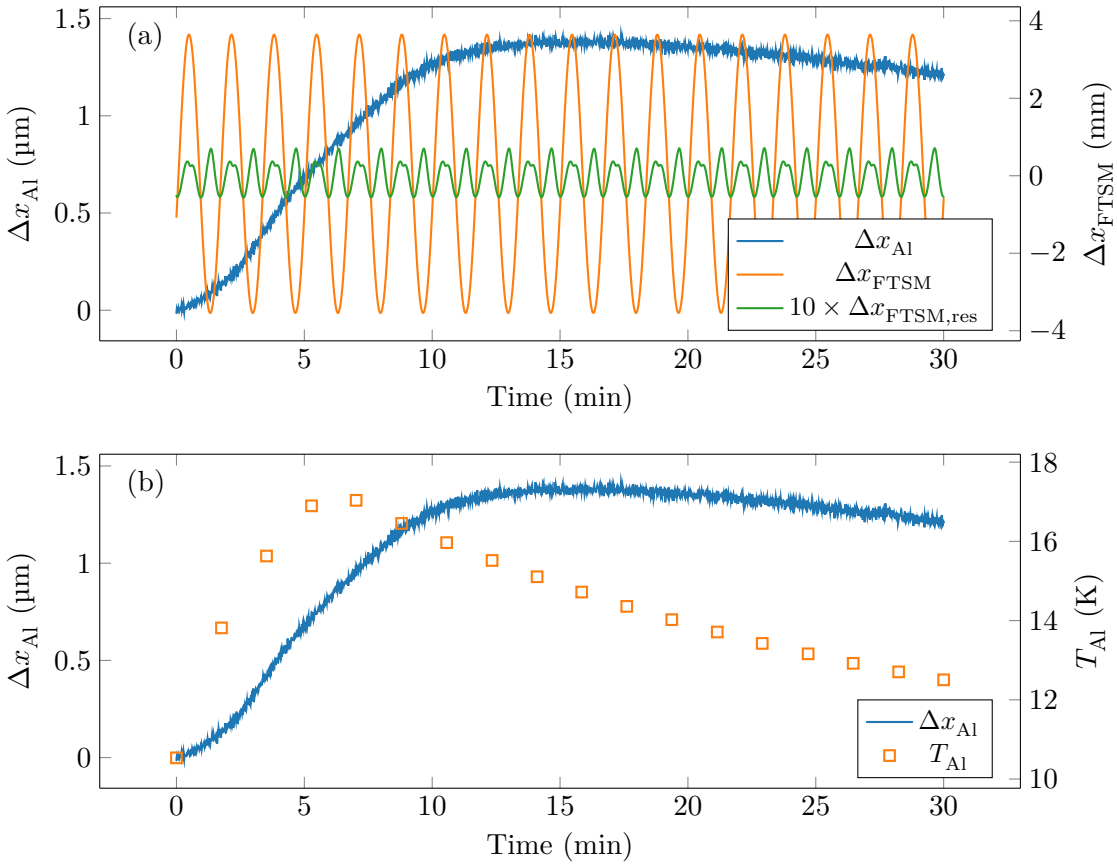

Figure 7.6: Simultaneous measurements of the aluminum sample and FTSM. The measured displacements are plotted in (a) on separate vertical scales due to the three orders of magnitude difference in displacement; $\Delta x_{\text{FTSM,res}}$ shows the residual between the FTSM displacement and a sinusoidal fit. The residual amplitude is scaled up by a factor of ten for visualization purposes. The expansion of the aluminum sample is plotted in (b) along with the temperature reading from the thermometer attached to the sample. The temperature in (b) is plotted as discrete points because it is sampled as part of a cycle once every ∼1.7 min.

The maximum change in length of the aluminum sample was ∼1.4 µm. There is a noticeable lag between the temperature read by the thermometer and the expansion of the aluminum sample. Since the thermometer was near the resistor as shown in Figure 7.5b, the point measurement is near the warmest region of the sample. The aluminum continued to expand after power to the resistor was disabled. The heat was transferred away from the centre of the sample where the thermometer was located, resulting in the drop in measured temperature, but the resistor was still warm and continued to heat the sample. As mentioned above, the measurement jig was placed on the 4 K plate but not bolted down, so heat transferred to the 4 K plate through conduction is inefficient. The displacement of the aluminum sample shows a plateau around 15 min in Figure 7.6b before slowly contracting as energy is lost via radiation and conduction through the collimator and retroreflector mounts at the ends of the sample.

The purpose of this experiment was to demonstrate simultaneous multiaxis measurements at cryogenic temperatures. It would not be appropriate to assess the performance of the FTSM or determine the coefficient of thermal expansion (CTE) of aluminum from these data. The measured displacement of the FTSM was undoubtedly impacted by the extra ∼5 m of fibre required for the configuration of the multiaxis interferometer in cryostat. Although small, the extra 25 cm fibre inserted into the aluminum axis to provide the OPD offset required for demodulation is highly sensitive to temperature induced changes in length — especially when tracking a ∼1 µm change in displacement over a period of 30 min. Simultaneous multiaxis measurements of the slowly varying ∼1.4 µm length of the aluminum sample and the higher velocity ∼7.2 mm travel of the FTSM using the SFM technique were demonstrated at cryogenic temperatures.

7.3 Application #3: FSI Resolution Investigation

A key performance metric of any sensor is its resolution, which for a displacement metrology system, is the smallest change in displacement that can be detected. A challenge arising in the determination of the resolution is that one must be able to impart a small displacement and have confidence that the generated displacement is not influenced by environmental factors such as temperature or vibration — this is difficult at the subnanometre level. To address these challenges, a novel fibre segment interferometry (FSI) resolution characterization strategy is presented, in which the OPD is modulated at a frequency much greater than the length changes that can occur due to temperature or vibration.

All other applications presented in this chapter are Fizeau interferometers with free space probing beams, however, to achieve very small displacements, an entirely fibre-coupled single-axis Mach-Zehnder [10] FSI was constructed as shown in Figure 7.7. The schematic in Figure 7.7a shows the two paths that the signal follows after splitting at a 2×2 coupler. The upper path, α, contains an Optiphase PZ1 PZT fibre stretcher [281] that is used to modulate the length of the fibre (specifications given in Table C.12). The lower path, β, contains a custom made 4.98(1) m compensating fibre that closely matches the length of the PZT fibre (4.984 m) and a 50.1(3) cm fibre to add a delay to the β path, resulting in an OPD of $\sim$73 cm (assuming a refractive index of 1.46 for the fibre core). The constructed interferometer is shown in Figure 7.7b. A small modification to the FMDU connectivity was required for the Mach-Zehnder design. The interferometer is transmissive, not reflective, so no signal returns to the bidirectional port on the FMDU. The third arm of the circulator on the FMDU was bypassed as the output from the second 2×2 coupler was directly connected to the photodetector and can be seen in Figure 7.7b.

Figure 7.8 illustrates the measurement procedure and shows the computed results. The PZT was sinusoidally modulated to introduce a periodic change in OPD of the

interferometer, and the optical displacement, $\Delta\Lambda$, is measured. The displacement amplitude is gradually reduced by decreasing the PZT modulation voltage until the change in displacement could no longer be resolved. All measurements are recorded with the LD modulated at a frequency $f_{\mathrm{m}} = 100\,\mathrm{kHz}$ and an optical frequency modulation amplitude of $\nu_{\mathrm{A}} = 1.51(12)\,\mathrm{GHz}$. A sample displacement measurement for 100 mVpp PZT modulation at 1 kHz is shown in the time and frequency domains in Figures 7.8a and 7.8b, respectively, having a 6.4 nmpp displacement change at 1 kHz. As this experiment determined smallest resolvable point-to-point change through peak-to-peak displacement measurements, the units of displacement spectra are cho-

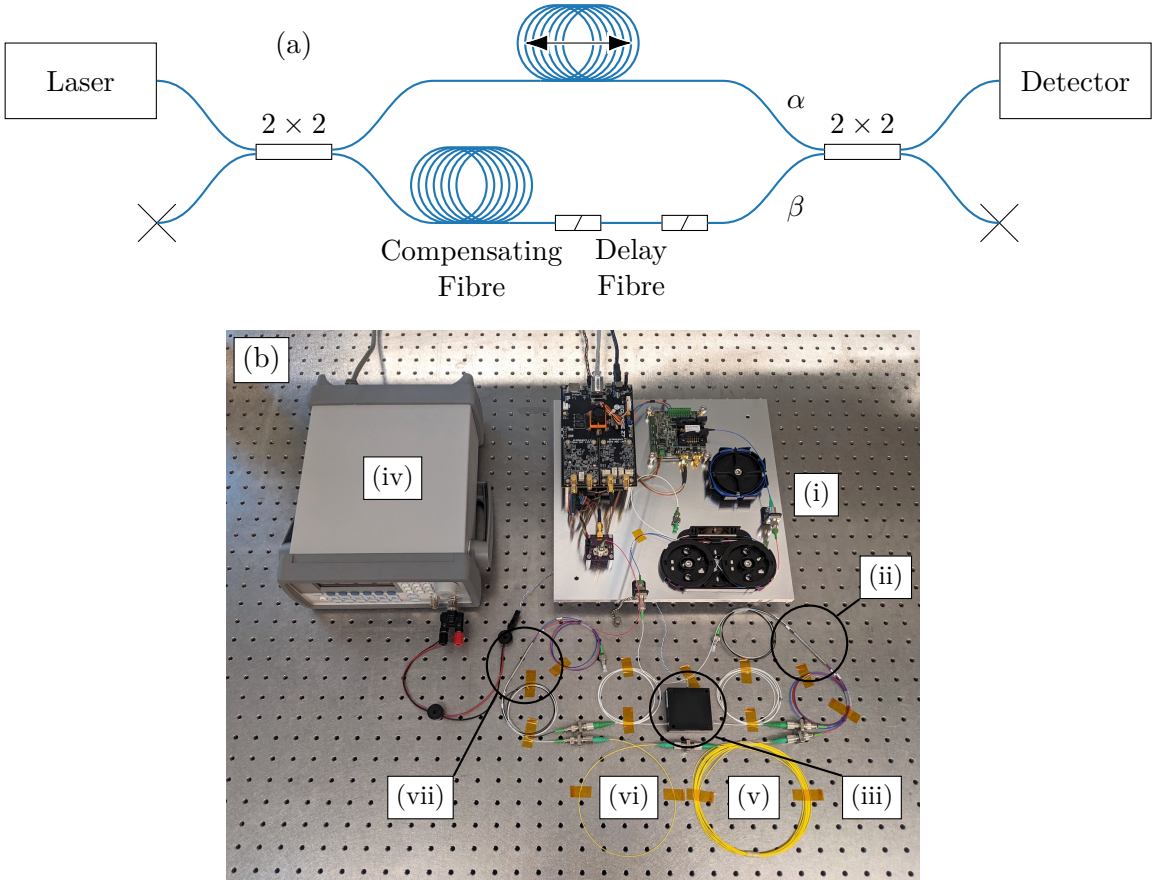

Figure 7.7: Mach-Zehnder FSI schematic (a) and realized interferometer (b). The experimental configuration in (b) shows: the FMDU (i), the first 2×2 coupler (ii), the PZT (iii) driven by a waveform generator (iv), the compensating fibre (v), the delay fibre (vi), and the second 2×2 coupler (vii).

sen to reflect this (e.g., nmpp in Figures 7.8b to 7.8d). Peak-to-peak units are used in the resolution characterization since the minimum resolvable displacement is not the amplitude of the displacement oscillation, but the total stroke of the sinusoidal OPD modulation for point-to-point motion. The measurement procedure was repeated for several PZT modulation amplitudes to obtain the line in Figure 7.8c showing the displacements that were resolved and unresolved. In this context, *resolved* was defined such that the displacement at the 1 kHz frequency carries at least twice the

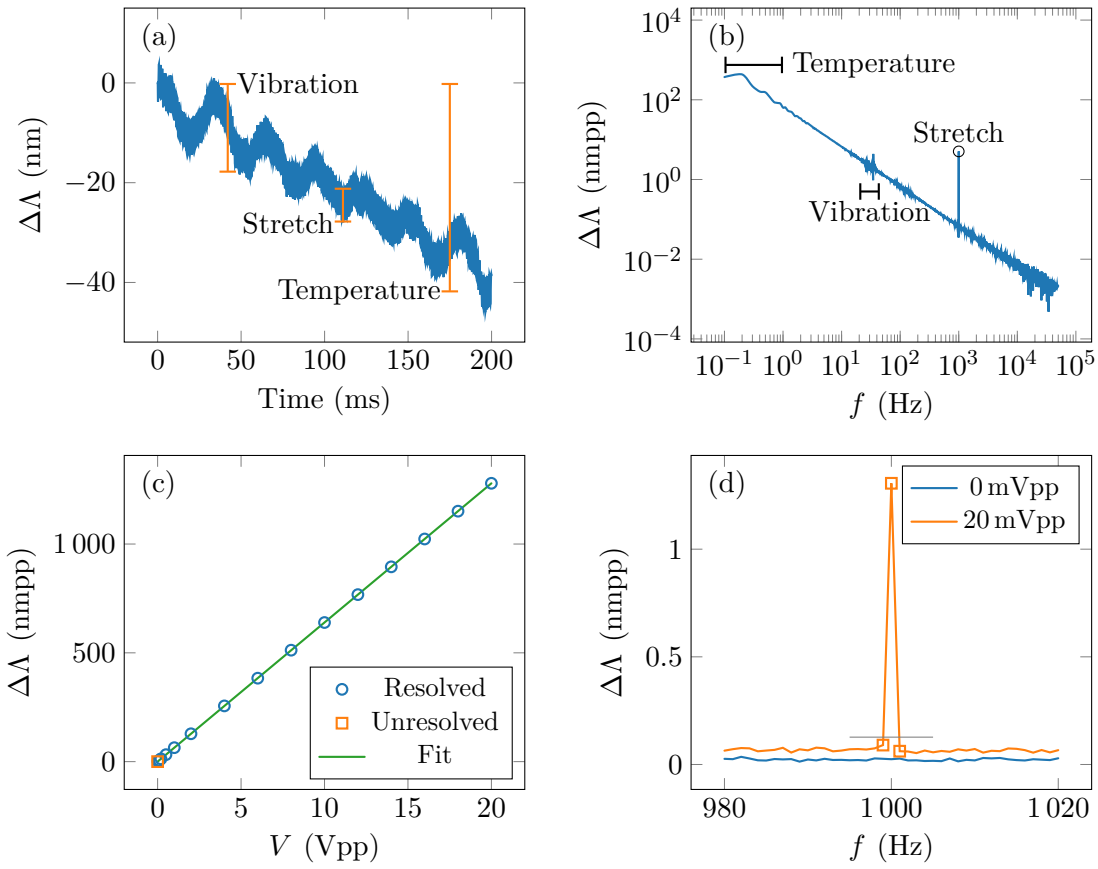

Figure 7.8: A 100 mVpp PZT modulation at 1 kHz is shown in time (a) and frequency (b) domains to illustrate the different frequency components present in the displacement. Stretch voltages of 0 to 20 Vpp at 1 kHz were applied and the displacement amplitudes extracted to obtain sets of resolved and unresolved points in (c); all voltages were resolved except for the case where the stretch voltage was 0 Vpp. Displacement spectra for the 0 and 20 mVpp cases are plotted in (d); the three points used to determine if the displacement was resolved are shown. The horizontal gray line at 0.13 nmpp indicates the minimum height of the 20 mVpp peak for it to be resolved based on the factor of $\sqrt{2}$ criterion.

power of the displacements in adjacent frequency bins of the displacement spectrum obtained by a discrete Fourier transform (DFT). Figure 7.8d shows spectra for the 0 and 20 mVpp PZT modulation cases. The displacement was sampled at 100 kHz for 1 s, giving a frequency bin width of 1 Hz. The 0 mVpp case is unresolved, and the 20 mVpp is well resolved showing a displacement of 1.3 nmpp. Since the displacement is plotted on the vertical axis in Figure 7.8d, the peak at 1 kHz must be at least a factor of $\sqrt{2}$ greater than the adjacent points. These three points are highlighted and a gray horizontal line is drawn at the level that the displacement at the 20 mVpp must exceed to be classified as resolved. The only case that was not resolved was the 0 mVpp case where the PZT was not driven; all other cases from 20 mVpp to 20 Vpp were resolved.

Highlighted in Figures 7.8a and 7.8b are the main displacement contributions. Low frequency temperature induced fluctuations are observed mostly due to changes in air temperature around the fibres. All data collected show a consistent overall decrease in OPD. As I approached the interferometer to adjust the modulation voltage of the waveform generator, heat transferred from my body led to expansion of the fibres. The β path is longer than the α path so the temperature induced change in length is generally greater in β than α, and as the fibres contract after I walk away, thermal contraction is observed as a decrease in OPD. Since the fibres are highly temperature sensitive, they were taped directly to the optical breadboard as shown in Figure 7.7b, in which the breadboard serves as a thermal sink, rather than winding the fibres around plastic capstans as seen in other applications. Also shown are ambient vibrations in the laboratory that occur in the 25 to 40 Hz frequency range. The prominent peak at 1 kHz is due to the PZT modulation. A least squares fit to the resolved points in Figure 7.8c gives

$$\Delta\Lambda(V) = \big(63.948(7)\,\text{nmpp/V}\big)V + 0.057(72)\,\text{nmpp}. \qquad \text{[nmpp]} \quad (7.2)$$

The fitted slope of 63.948(7) nmpp/V, which closely matches the stretch coefficient of 64.9 nm/V at $\lambda = 1550$ nm provided by the manufacturer (see Table C.12 for specifications). The small 0.057(72) nmpp offset is negligible at the observed displacement amplitude levels and implies that the experimental setup is clean.

The lower limit of the waveform generator is 20 mVpp, which corresponds to a stretch of ∼1.3 nmpp. Since Figure 7.8d shows that this case is resolved, a resistor network was used to reduce the driving voltage to the PZT by a factor of ∼100 using 1 and 100 kΩ resistors. The measurements in Figure 7.9 were obtained using the same procedure but with reduced displacement amplitude due to the resistor network. A least squares fit to the resolved points in Figure 7.9a yields

$$\Delta\Lambda(V) = \big(0.619(1)\,\text{nmpp/V}\big)V + 0.032(12)\,\text{nmpp}. \qquad \text{[nmpp]} \quad (7.3)$$

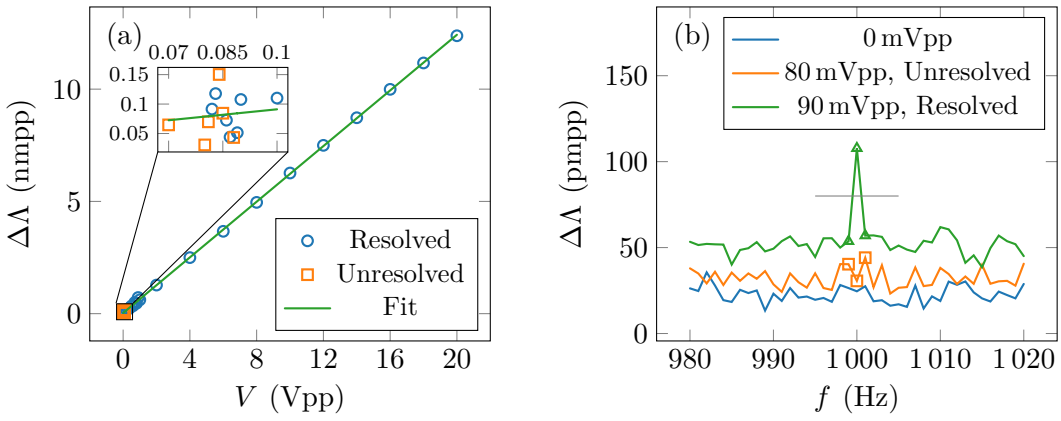

Figure 7.9: Repetition of the measurements presented in Figure 7.8 with a resistor network inserted to reduce the stretch coefficient by a factor of ∼100. Stretch voltages of 0 to 20 Vpp at 1 kHz were applied to produce (a); a zoom on the 70 to 100 mVpp region is shown. All measurements truncated to the left of the 70 mVpp in the zoom are unresolved and all truncated to the right of 100 mVpp are resolved. Spectra for several cases are plotted in (b); the three points used to determine if the displacement was resolved are shown. The horizontal gray line at 80 pmpp indicates the minimum height of the 90 mVpp peak for it to be resolved based on factor of $\sqrt{2}$ criterion. These data demonstrate ∼100 pm resolution.

The fitted 0.619(1) nmpp/V stretch coefficient is ∼103 times less than the stretch coefficient before the resistors were introduced. The zoomed region in Figure 7.9a shows the failure to resolve over the 80 to 90 mVpp PZT modulation range. Although difficult to pinpoint an exact value for the resolution, as the points generally alternate between resolved and unresolved in this range, all displacements greater than ∼100 pmpp are resolved (which is well above the 0.032(12) nmpp fitted offset). Figure 7.9b shows the displacement spectra at 80 and 90 mVpp modulation that bound the ambiguous range shown in the zoom of Figure 7.9a and that the background displacement decreases as the modulation voltage is lowered, suggesting that either the waveform generator or the PZT leak into nearby frequencies.

Figure 7.8b suggest that increasing the PZT frequency from 1 kHz to 10 kHz would allow for an improved measurement at a lower background vibration level. The measurements were repeated with the only change being the increase in PZT modulation frequency to 10 kHz, and results are plotted in Figure 7.10. The line in Figure 7.10a at 10 kHz PZT modulation looks like the 1 kHz case in Figure 7.9a, with the exception that the displacement is reduced by ∼25 %, which is reflected in least squares the fit

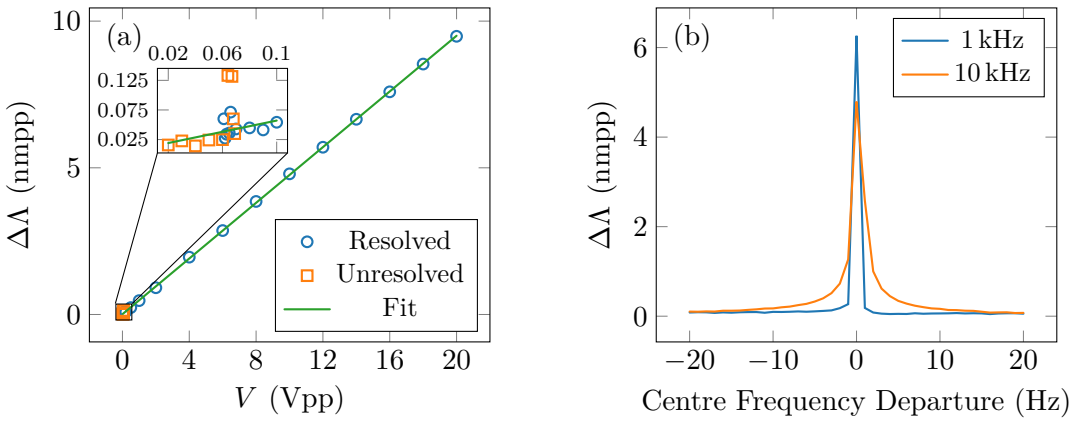

Figure 7.10: Repetition of the measurements presented in Figure 7.9 with a 10 kHz PZT modulation frequency. Stretch voltages of 0 to 20 Vpp were applied to produce (a); a zoom on the 20 to 100 mVpp region is shown. All measurements truncated to the right of 100 mVpp are resolved. Spectra for several 1 and 10 kHz cases are plotted in (b) centred about their respective PZT modulation frequency. These data demonstrate ∼50 pm resolution.

of

$$\Delta\Lambda(V) = \big(0.475(6)\,\text{nmpp/V}\big)V + 0.009(5)\,\text{nmpp}. \qquad \text{[nmpp]} \quad (7.4)$$

This can be better observed in Figure 7.10b, which shows the central displacement reduces as the profile is broadened at the 10 kHz PZT modulation frequency. It should be noted that the time domain measurements show similar peak-to-peak displacements for both the 1 and 10 kHz PZT modulation frequencies, suggesting that the reduced amplitude for the 10 kHz case in Figure 7.10b is due to the broadening of the spectrum, not some frequency dependence of the stretch coefficient. Although the displacement magnitude cannot be accurately recovered with the DFT, the overall trend is consistent with the 1 kHz PZT modulation measurements. By adjusting for the ∼25 % reduction in displacement amplitude where the displacement can no longer be resolved in the zoomed region of Figure 7.10a, the measurements at 10 kHz PZT modulation suggest a resolution of ∼50 pmpp, which is well above the fitted 9(5) pmpp offset. Furthermore, at $\lambda = 1550$ nm, one least significant bit (LSB) of the displacement readout from the FMDU has a resolution of 24 pm, which suggests that the resolution of the implemented SFM is bit width limited and matches the theory presented in Section 5.1.2.

All other interferometers presented in this chapter are two-pass Fizeau configurations. The determined ∼50 to ∼100 pm resolution in *optical* path from the single-pass Mach-Zehnder design then corresponds to a ∼25 to ∼50 pm *mechanical* resolution in the free space Fizeau configurations.

7.4 Application #4: Long-Term Stability Investigation

To reduce sources of low amplitude noise in a long period displacement measurement in atmosphere, a single-axis interferometer in Figure 7.11 was configured on an air-damped breadboard in a clean room environment. Furthermore, an enclosure was placed over the collimator, retroreflector, and beam path to reduce air currents in the

beam. Unlike the three-axis interferometer in Figure 7.1 where optical components were mounted on posts for convenience of alignment, the collimator and retroreflector were secured to thin aluminum slabs that allowed them to be bolted to a damped breadboard. This strategy reduces potential vibrations by eliminating the posts that may act like pendula. Furthermore, an enclosure was installed over the collimator and retroreflector and this experiment was performed in a clean room with the fans powered off over a weekend where the laboratory was empty.

The constructed interferometer has an OPD of $\Lambda = 100(1)\,\mathrm{cm}$, and the laser was modulated at $f_\mathrm{m} = 100\,\mathrm{kHz}$ with an amplitude of $\nu_\mathrm{A} = 1.51(12)\,\mathrm{GHz}$. The OPD separates the FC/PC terminated end of a fibre patch cord connected to a Thorlabs F280APC-1550 collimator [282] and a Thorlabs PS974M-C collimator [273]. The detector signal is shown in Figure 7.12a, for which the SNR was estimated as ∼1200 using the same procedure as for the three-axis interferometer in Figure 7.2. Since the

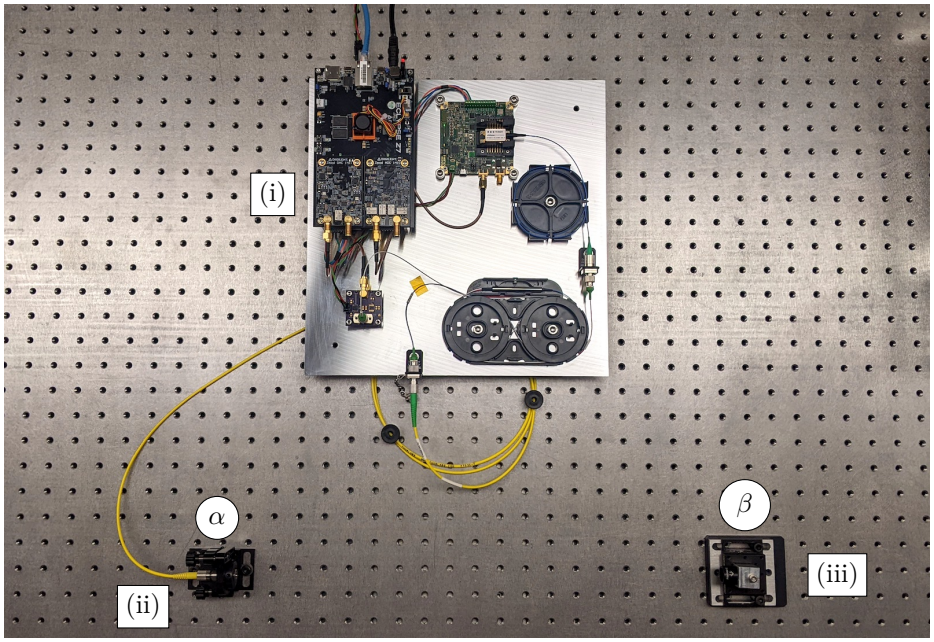

Figure 7.11: Single-axis interferometer for fixed measurements. The probing signal generated by the FMDU (i) is partially reflected at the tip of the FC/PC terminated fibre mated to the collimator (ii) giving reflection α. The beam probes the retroreflector at (iii) giving rise to β, forming an $S = \{\alpha, \beta\}$ interferometer. An enclosure (not pictured) is placed over the collimator and retroreflector during acquisition.

detector voltage has high SNR and moderate amplitude modulation, only high-pass filtering was employed to remove the signal offset.

A 48 h measurement was recorded at a 1 kHz sampling rate, the results are plotted in Figure 7.12b showing fluctuations over a range of 3.2 µm. The measurements show no evidence of errors in phase unwrapping, which would manifest as discontinuities with jumps of $\lambda/4 \approx 388$ nm — the largest point-to-point jump was 4 nm. Assuming that the measured fluctuations in OPD are entirely caused by temperature fluctuations in the stainless steel breadboard having a CTE of ∼9 ppm/K (the type of stainless steel is not specified by the manufacturer, but it is assumed to have a CTE typical of most stainless steels) [283], the temperature fluctuates over a range of ∼0.7 K. For a small enclosed volume in a clean room environment, a temperature stability of ∼1 K is reasonable over the measurement period. Furthermore, the combined effects of a 1 K temperature change, 1 kPa pressure change, and 10 % RH change from standard conditions results in a maximum of ∼4 ppm wavelength change in air at 1550 nm [284], leading to a perceived ∼2 µm change in mechanical displacement that is consistent with the measured fluctuations. There is evidence to suggest diurnal behaviour, as the first and second 24 h periods exhibit similar "cup" shapes. The linear region spanning 23 to 28 h is likely due to the HVAC infrastructure that is outside of laboratory control.

Overall, there are several factors that contribute to the observed displacement drift, such as temperature fluctuations in the breadboard and optics, drifting in laser frequency, and fluctuations in refractive index due to air temperature, humidity, and currents. With a temperature stabilized laser in an atmospheric environment, the SFM measurements do not exhibit significant drift, with only ∼3 µm fluctuations over a 48 h measurement period. It should be appreciated that this stability is not guaranteed for all interferometers, and in prior work with a three-phase interferometer based on an unmodulated laser (see Sections 2.3.1 and 2.3.2) drifts of several metres were observed with the same experimental configuration. Figure 7.12b also shows a

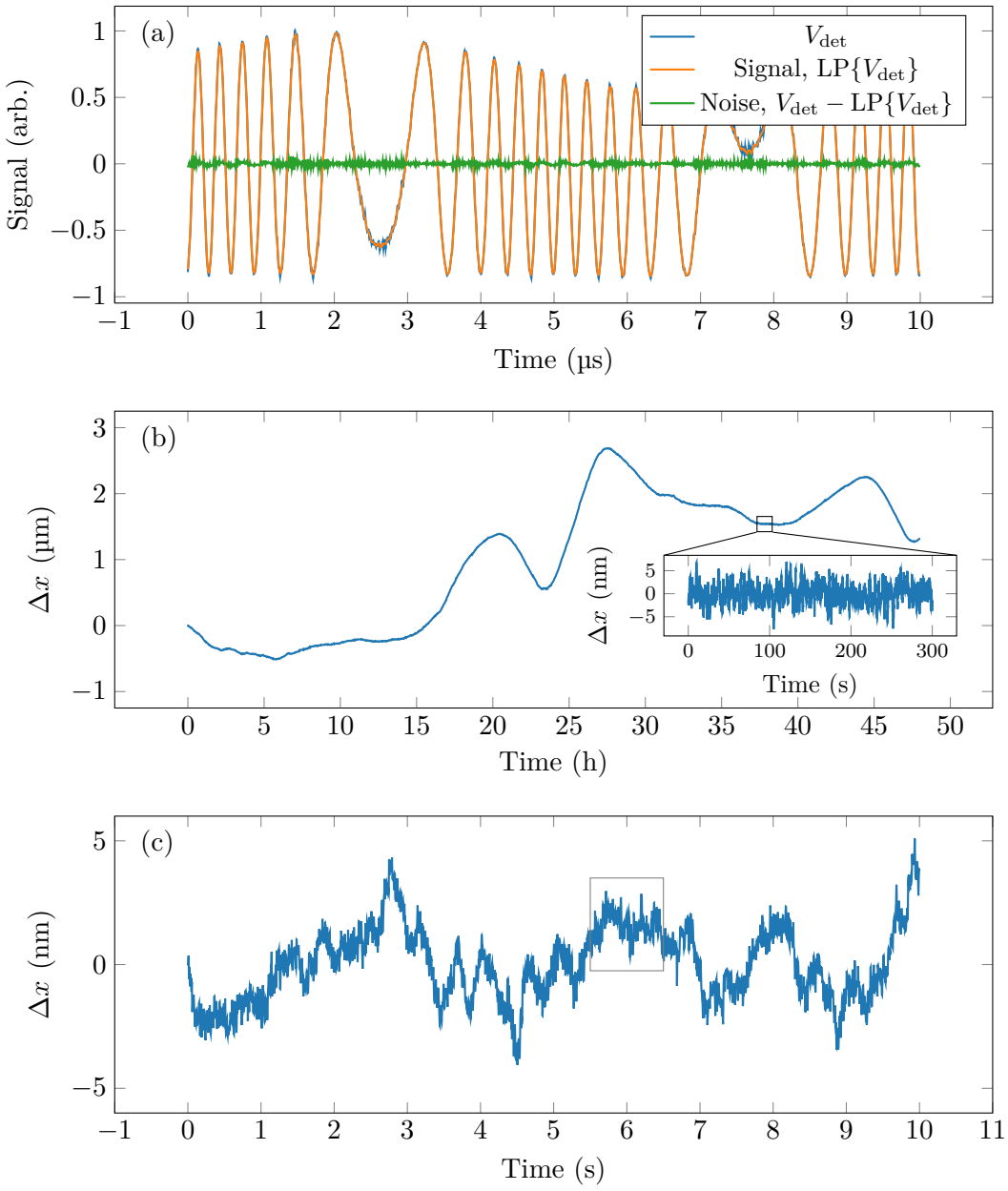

Figure 7.12: Long-term single-axis measurement of a fixed target. The detector signal collected over one modulation period in (a) was to estimate the SNR at ∼1200 using the procedure outlined in Figure 7.2. A 48 h acquisition with 1 kHz sampling is shown in (b) beginning at midnight over a period where no one was in the laboratory. A zoom on an arbitrary 5 min region is shown where the stability over the entire interval is 2.2 nm rms in a 500 Hz bandwidth; the vertical axis of the zoom is adjusted so that 0 nm is centred on the average displacement over the 300 s interval. A measurement with the full 100 kHz sample rate in (c) shows a stability of 0.5 nm rms in a 50 kHz bandwidth over the relatively flat 1 s boxed interval spanning 5.5 to 6.5 s.

zoom on an arbitrary 5 min region of the displacement with an 8 nm maximum absolute departure from the mean and an amplitude of 2.2 nm rms in a 500 Hz bandwidth over the entire 5 min period.

Since the 48 h acquisition was prohibitively long for the full 100 kHz sample rate, a shorter acquisition with the same interferometer was obtained over a 10 s interval and plotted in Figure 7.12c. The relatively flat region from 5.5 to 6.5 s shows 0.5 nm rms in a 50 kHz bandwidth. Recall the requirements for the SAFARI FTS outlined in Table 1.1 call for an uncertainty of 10 nm rms in a 20 Hz measurement bandwidth. By applying a 5^{th} order Butterworth low-pass filter [285] with a cutoff frequency of 20 Hz to the measurement over the 5.5 to 6.5 s region, a stability of 0.4 nm rms in a 20 Hz bandwidth was obtained. These results should be compared to the theoretical uncertainty simulations in Section 5.2.4 that predict a 0.3 nm rms displacement uncertainty. Furthermore, this value exceeds the Space Infrared telescope for Cosmology and Astrophysics (SPICA) FTS requirement by over an order of magnitude *and* was obtained in laboratory environment; an improvement is expected in spaceborne platforms which provide a more stable environment in terms of vacuum and temperature.

7.5 Application #5: HeNe Laser Metrology Verification

The HeNe laser is the *gold standard* in displacement metrology. To evaluate the SFM implementation, a novel technique was employed to obtain simultaneous measurements from SFM and HeNe interferometers of the same target so that the SFM approach may be tested against a measurement using the well-known HeNe vacuum wavelength of 632.991 nm [44] (or 632.816 nm in air).

7.5.1 Theory

One challenge with comparing two independent range-resolved interferometers is the cosine error [286] that occurs when the probing beams are not parallel to each other or the measurement vectors deviate during travel. An advantage of the fibre coupling in the FMDU is that one may exploit commercially available wavelength division multiplexers (WDM) to enable coaxial propagation of the probing beams. Figure 7.13a shows a wavelength division interferometer with WDM combining and splitting at wavelengths of 1550 and 633 nm. Light from the two laser sources is combined into the same fibre by the WDM and launched to probe the same target using a coaligned beam. The reflected beam returns to the fibre and is split by the WDM so that the SFM and HeNe signals can be processed independently. The SFM interferometer generates sufficient phase information to track displacement, however, this HeNe interferometer is not capable of producing a quadrature signal and thus cannot measure displacement. To compare measurements between interferometers, one must take care to ensure that the change in OPD is either increasing or decreasing *monotonically* over the measurement period, since the simple fringe counting technique employed by the HeNe interferometer does not have directional sensitivity.

Measurements of the SFM displacement and HeNe fringes were collected over several scans of the OPD. The SFM displacement was used to determine regions of travel over which the change in OPD is monotonic. These regions were extracted for analysis, and segments near the turnaround points of the motion were discarded. Figure 7.13b shows a simulation of the procedure, in which regions are identified based on SFM displacement. Approximately 10 % of the data were discarded at the limits of travel to limit the artefacts from the acceleration and deceleration phases of the mechanism. In this example, two regions, labeled #1 and #2 and outlined with green and red, respectively, are identified. Within each region, the number of HeNe fringes are counted and multiplied by the HeNe wavelength to determine the

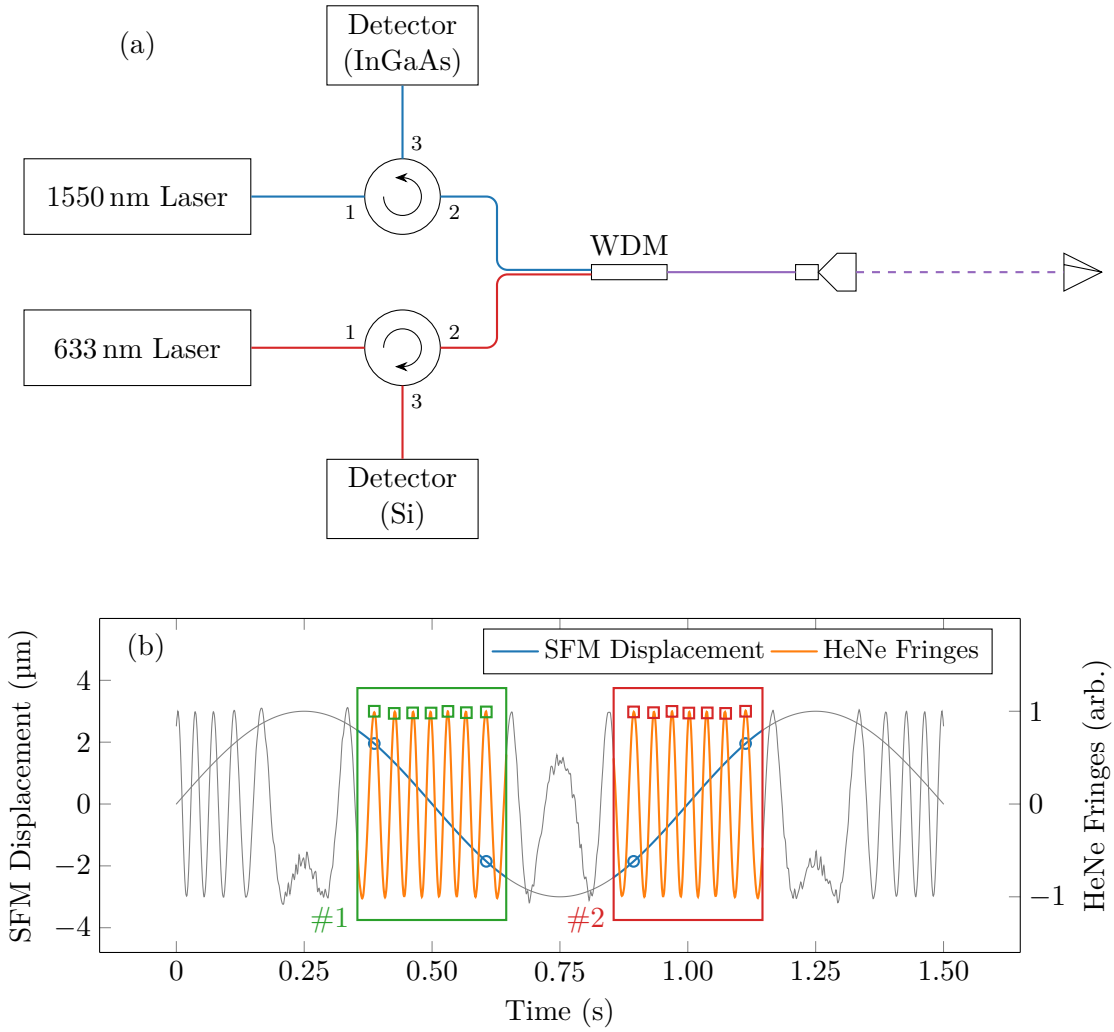

Figure 7.13: Principle of a wavelength division 633 nm and 1550 nm interferometer. The schematic in (a) shows infrared light (1550 nm) is in blue, visible HeNe light (633 nm) in red, and combined light in purple. A ∼4 % Fresnel reflection [10] from the FC/PC fibre tip is used for the interferometer reference. Commercially available HeNe lasers are generally free space, and an optomechanical adapter is used to achieve fibre coupling. The simulated waveforms in (b) illustrate the HeNe laser interferometer verification processing procedure. Regions of monotonic travel are detected (#1, #2) and the HeNe fringes within each region are counted. The distance measured by the HeNe is proportional to the number of fringes, and the SFM displacement is found as the difference between the displacement measurements (blue circles) at the times of the first and last HeNe fringes (green squares and red triangles) within a monotonic displacement region. Parts of each signal outside of an identified monotonic region are plotted in gray; the green and red outlined areas show the two identified regions for fringe counting.

change in OPD as measured by the HeNe interferometer. The change in OPD from the SFM interferometer is determined by the difference in displacement at the time when the first HeNe fringe occurs with the displacement at the time of the final HeNe fringe. Using the secondary ADC channel on the FMDU, the HeNe fringes can be sampled simultaneously with the SFM interference signal. Samples from the secondary ADC are delay-compensated in the field-programmable gate array (FPGA) for the demodulation pipeline, and the SFM displacement measurements are kept in phase with the sampled HeNe fringes. This procedure is entirely automated and enables the acquisition of very long measurements so that a statistically significant number of measurements may be easily recorded. In this section, all measurements are discussed in terms of optical, not mechanical, path. The SFM displacement measurement, $\Delta\Lambda_{1550}$, is recorded and the HeNe distance measurement, $\Delta\Lambda_{633}$, is computed from the delayed HeNe interference signal.

7.5.2 Timing Characterization

Since the displacement at the end of the demodulation pipeline is compared to the HeNe fringes from the secondary ADC channel, the timing of these two signals must be examined. The recovered optical displacement, $\Delta\Lambda_{1550}$, is plotted against the

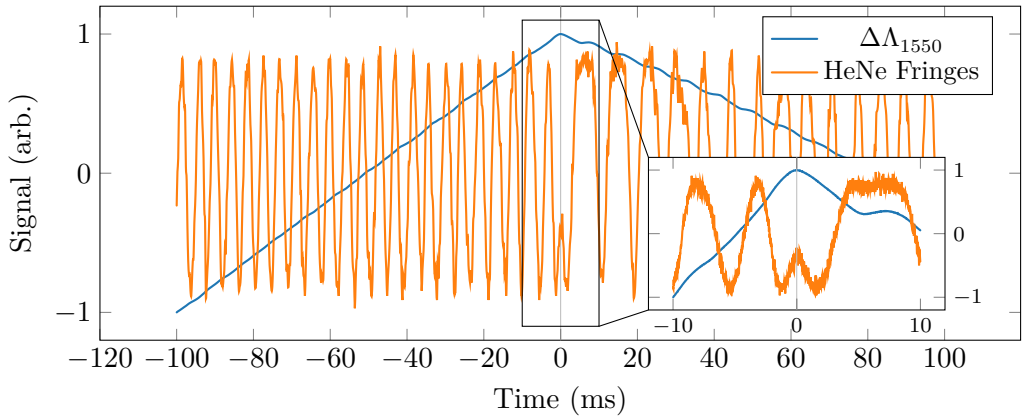

Figure 7.14: Displacement and secondary ADC timing. The stage was driven with a 200 mHz triangular motion profile to produce a sharp turnaround point centred at 0 ms. The peak of $\Delta\Lambda_{1550}$ is centred at 0 ms.

HeNe fringes in Figure 7.14, showing a region near a turnaround point of a 200 mHz triangular motion profile.

When approaching the turnaround point, the HeNe fringes carry a frequency of ∼230 Hz. The amplifier uses the design shown in Figure 4.2, and has $R_f = 10\,M\Omega$ and $C = 10\,pF$, and thus a cutoff frequency of ∼1.6 kHz. The velocity of the PZT positioner was limited so that the HeNe fringe rate is kept well below the cutoff. From Equation (4.2), the phase shift of the amplifier is ∼172° at 230 Hz. At low frequencies the phase shift of the inverting amplifier is 180°. The inverting nature of the amplifier does not matter for the HeNe laser interferometer verification analysis, so the phase shift can be treated as ∼8° for determining the delay. The expected delay of the amplifier is ∼100 µs and agrees with Figure 7.14 showing that the HeNe fringes lag $\Delta\Lambda_{1550}$ by 50 to 140 µs. This ∼100 µs is not considered by the secondary ADC delay, as the delay lines only account for the time taken by the demodulation pipeline in digital signal processing (DSP).

7.5.3 Metrology Verification in Atmosphere

A HeNe laser interferometer verification module was assembled on a small optical breadboard so that it can be easily moved and deployed in different configurations. Figure 7.15 shows the verification module. A Spectra-Physics 117A stabilized HeNe laser is coupled into a custom prepared fibre using a Thorlabs PAF2-A4B FiberPort coupler [287]. The HeNe beam is coupled into a Thorlabs SMF-28-J9 fibre [229] that is custom spliced to a length of Thorlabs 630HP fibre [288]. The SMF-28-J9 fibre is single-mode at 1550 nm, but multimode at 633 nm [11]. Coupling directly into the small 3.5 µm diameter core of the 630HP fibre is difficult, so instead, the beam is coupled into the larger 8.2 µm diameter core of the SMF-28-J9. A splice between the fibres gives a short tapered region that acts as a mode field adapter for the beam to gradually adjust to the smaller diameter of circulator input fibre; the

splice is shown in the lower left corner of Figure 7.15. As part of this research, the collection of photonics equipment listed in Appendix C.4 was built-up to enable in-house production of custom optical fibre systems and components, including an arc fusion splicer with selected specifications given in Table C.17. The visible Ascenta VCIR 635 nm circulator [289] uses 630HP equivalent fibres, but the Lfiber Optic Limited 650/1550nm WDM [290] uses SMF-28-J9 equivalent fibres. A second SMF-

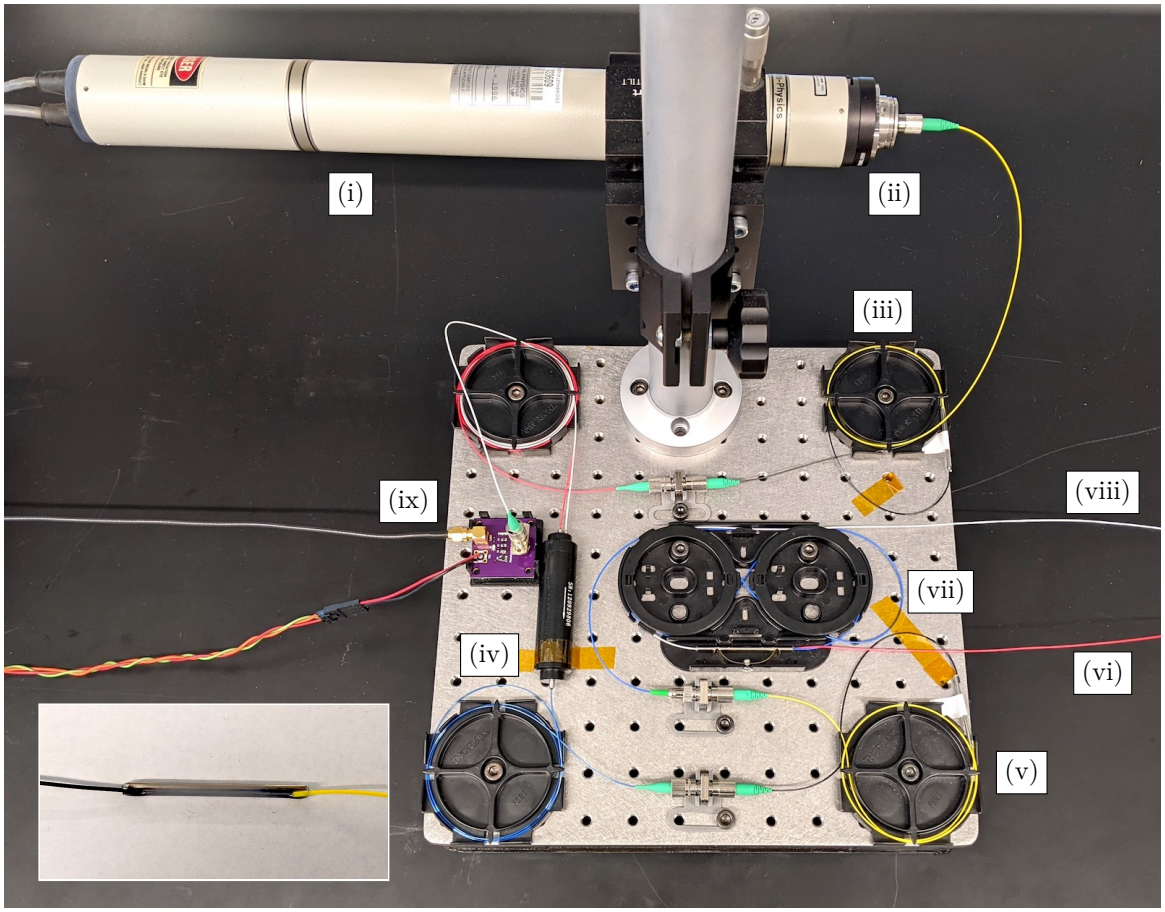

Figure 7.15: HeNe laser interferometer verification module. Light from the HeNe (i) passes through the FiberPort (ii) and couples into a custom SMF-28-J9/630HP fibre (iii). The signal passes through the visible circulator (iv) and another custom SMF-28-J9/630HP fibre (v) where it is mixed with the SFM signal (vi) at the WDM (vii). The combined 1550 nm and 633 nm are sent to the interferometer optics (viii). The return signal is split so that the 1550 nm signal returns to the SFM system and 633 nm signal to the custom photodetector and amplifier (ix). A custom SMF-28-J9/630HP splice is shown in the lower left corner with the 8.2 µm core SMF-28-J9 fibre on the right side to the 3.5 µm core 630HP fibre on the left side.

Table 7.2: Refractive index of dry air at 15 °C and 101.325 kPa for HeNe and SFM wavelengths.

Book	n at 633 nm	n at 1549.7 nm
Ciddor [292]	1.000 276 53	1.000 273 26
Peck and Reeder [293]	1.000 276 52	1.000 273 25
Mean	1.000 276 53	1.000 273 26

28-J9 to 630HP fibre is employed to couple the light between these components, since there is a large loss when coupling from a larger core to a smaller core. These custom fibre adapters offer a ∼3× reduction in loss over coupling the HeNe directly into the 630HP and mating directly between SMF-28-J9 and 630HP fibres. The amplifier circuitry is the same as Figure 4.2, but with $R_f = 10\,M\Omega$ and a Thorlabs FDS02 silicon photodiode [291] selected to provide better responsivity at 633 nm than the InGaAs photodiode used for the detection of the infrared SFM signal.

The interferometer in Figure 7.13a was constructed by connecting the FMDU to the HeNe laser interferometer verification module in Figure 7.15 and launching the combined beam from a custom OZ Optics 18.75 mm focal length Kovar collimator [269] to probe a Thorlabs PS974M-C prism retroreflector [273] mounted on a PI PIHera linear PZT positioner [274]. The positioner was driven with a 1 Hz sinusoidal motion profile with an optical stroke of ∼275 µm. Coupling the HeNe laser into the 3.5 µm core fibre was challenging. The alignment process began with a large core fibre in that was adjusted until the DC signal from a photodetector was maximized. This required the introduction of several attenuators as improvements to the alignment led to saturation of the detector. Furthermore, the 3.5 µm core is difficult to couple into directly, so the HeNe light was first coupled into an 8.2 µm core fibre that was spliced to the smaller 3.5 µm core as shown in the lower left of Figure 7.15. The splicing strategy yielded a greater optical power in the small core fibre than by direct coupling.

Since these measurements are taken in air, it is important to account for the refractive index of air to be considered at test wavelengths of 1550 and 633 nm. The refractive index, $n(\lambda)$, of air is computed as the average from values from Table 7.2. The values from the literature are reported for dry air at 15 °C and 101.325 kPa [292, 293], and are assumed similar enough to the laboratory atmospheric conditions so that the refractive index values remain reasonable estimates.

SFM and HeNe measurements are compared in two ways: the relative and absolute errors, with the former being a scaling error between the measurements. In total, 2000 scans were recorded to compute the scaling and absolute errors, $\Delta\Lambda_{1550}/\Delta\Lambda_{633} - 1$ and $\Delta\Lambda_{1550} - \Delta\Lambda_{633}$, respectively. In both cases, the HeNe measurement serves as the reference, so a positive error means that the SFM measurement is greater than the HeNe measurement. From the fits in Figure 7.16, the mean scaling error is 3.5 ppm and the mean absolute error is 0.95 nm, indicating that on average, the SFM measurement is *greater* than the HeNe measurement.

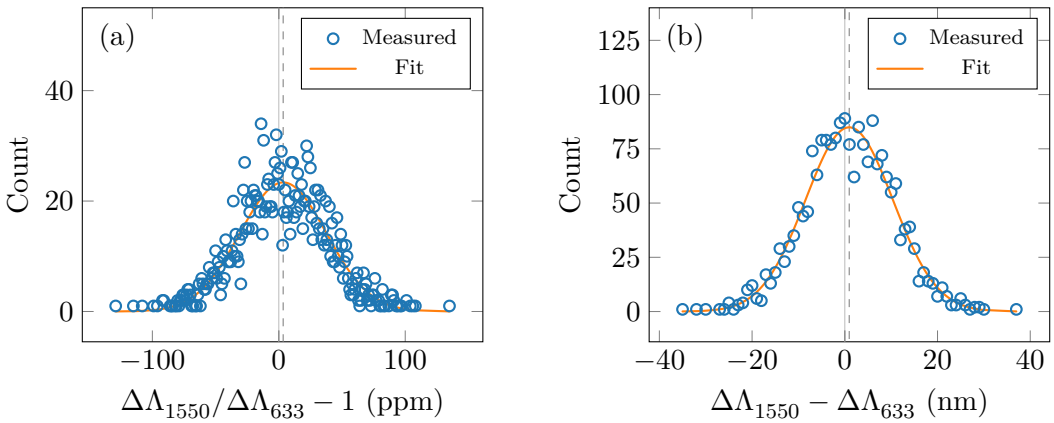

Figure 7.16: Room temperature HeNe laser interferometer verification in atmosphere. A total of 2000 scans were recorded over optical displacements of ∼275 µm. Distributions and Gaussian fits to the relative (a) and absolute (b) errors were produced with bin widths of 1 ppm and 1 nm, respectively; bins having a count of zero are omitted for visualization purposes. Fitting determined that the scaling error distribution had mean and standard deviation of 3.5 ppm and 34 ppm, and the absolute error had a mean and standard deviation of 0.95 nm and 9.4 nm, respectively. The solid vertical lines pass through zero and the dashed lines pass through the location of the fitted peak.

Assuming that the HeNe measurement is the true measurement of displacement, these results can be used to estimate the calibration error in the wavelength of the SFM laser. Recall from Equation (3.35), that in the SFM measurement, the displacement is recovered by scaling the unwrapped phase with λ_c, which is the centre wavelength about which the laser is modulated. The scaling error found above is then equal to the relative error in λ_c. From the LD calibration curves in Section 4.3, the FMDU used $\lambda_c = 1549.7400(42)\,\text{nm}$ for these tests. Given the scaling error of 3.5 ppm, the calibrated λ_c is 5.4 pm too large, which is in close agreement to the 4.2 pm uncertainty in λ_c from the calibrated LD curves in Section 4.3.1. Some amount of error is expected in the wavelength calibration, as the LD calibration curves were determined for a non-modulated input. All things considered, a calibration error on the order of ppm is exceptional. Furthermore, this small error can easily be corrected by subtracting 5.4 pm from the calibrated wavelength curve in Equation (4.4c).

7.6 Application #6: Cryogenic Force Feedback Accelerometer

Mechanical accelerometers can be classified as either passive or active designs [294–297]. In a passive design, the displacement of a proof mass is measured and converted to an acceleration based on a transfer function. While in a force feedback design, the position of the proof mass is actively servo controlled to keep it stationary relative to some point, such as the sensor chassis, and the acceleration may be determined from the applied force. In this section, a basic cryogenic force feedback accelerometer is presented to demonstrate how the FMDU may be integrated into a cryogenic system and showcases all its features. Following this, Section 7.7 introduces a technique for the cryogenic characterization of a monolithic silica resonator for a passive accelerometer design.

A force feedback accelerometer was constructed using several components developed during the course of previous projects, and is based upon a scanning pendulum from a cryogenic Fabry-Pérot interferometer [278,298]. Since the pendulum is a rotary mechanism, one may correctly call it a *torque* feedback accelerometer, however, for consistency with the literature, the term "force feedback" is used. Figure 7.17 shows the accelerometer configuration at room temperature. At the time this experiment was performed, the FMDU was not assembled as a singular unit, but rather the several discrete components: (i), (ii), (iii), and (vi) in Figure 7.17. For consistency, the set of these components is referred to as the FMDU in this section.

Before assembling the accelerometer, the pendulum was investigated to establish its key mechanical properties. The moment of inertia was determined as $I_{\mathrm{M}} = 3.05(1) \times 10^{-3}\,\mathrm{kg\,m^2}$, which was estimated using the CAD model for the pendulum, the datasheet for the BEI Kimco rotary voice coil actuators [299], and manual measurements of the Thorlabs PS974M-C prism retroreflector [273] attached to the underside of the mechanism.

The pendulum was set up in the laboratory with an OPD of 55.0(5) cm and probed using an interferometer formed between the FC/PC 50:50 beamsplitter coated end of a Thorlabs P5-SMF28ER-50-1 fibre patch cord [300] mated to a custom OZ Optics 18.75 mm focal length Kovar collimator [269] and the Thorlabs PS974M-C prism retroreflector [273] mounted to the underside of the pendulum. Unlike the other experiments in this chapter that use the $\sim$4 % Fresnel reflection [10] from a plane polished FC/PC fibre tip, a 50:50 beamsplitter coated fibre was used since this experiment was performed early on before it was found that the Fresnel reflection generally results in larger amplitude interference signals for the interferometer configurations discussed in this thesis. The two voice coil actuators are stacked vertically about the axis of rotation. The top coil was reserved for the motion controller, and an excitation signal of a square impulse from 0 V to 2 V for 100 ms produced by a waveform generator was

applied to the bottom coil. Using this configuration, the response was measured at room temperature. The coil connections and excitation parameters are kept the same in all tests.

The quality factor (refer to Appendix B and Section 7.7) of the pendulum is large due to its large moment of inertia and small torsion constant of the flexure bearings. From the non-damped plot Figure 7.18a, the quality factor was found to be $Q \approx 180$ from the ringdown method as described later in Section 7.7. Eddy current damping was employed by fitting an aluminum fin on the pendulum that passes near 12 mm

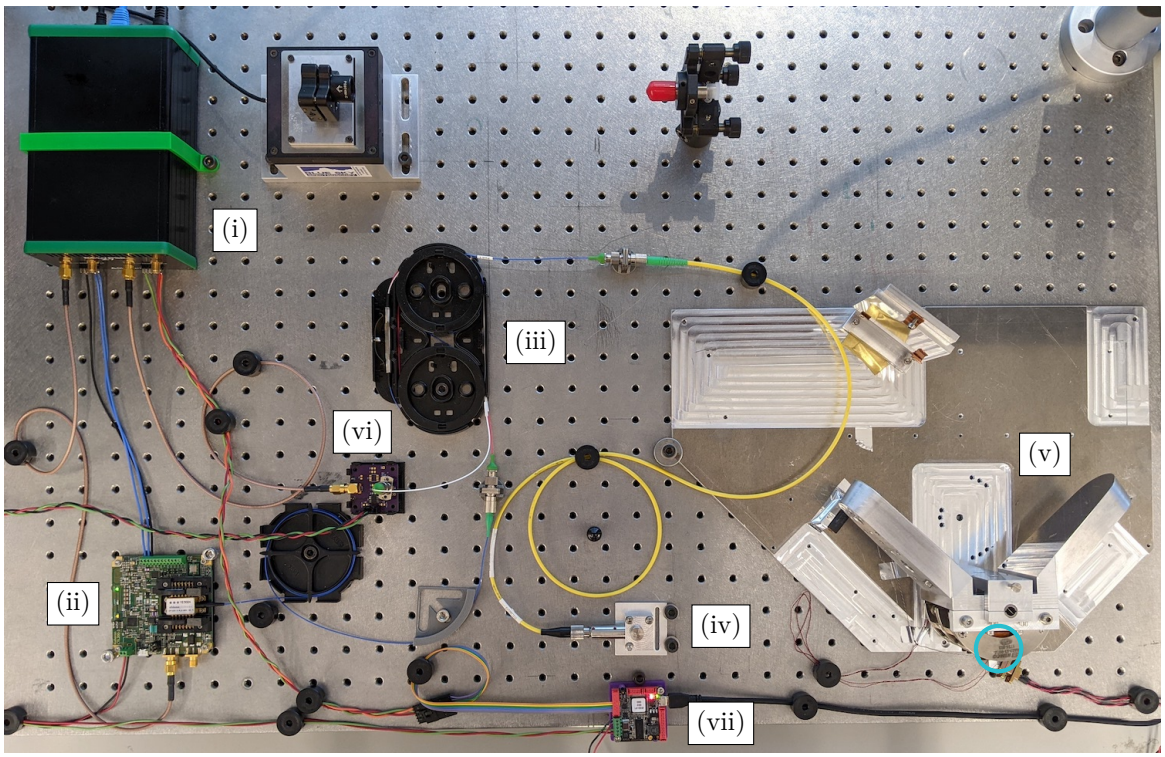

Figure 7.17: Room temperature force feedback accelerometer configuration. The FMDU was not yet constructed as shown in Figure 4.1, and its components are instead secured to the optical breadboard. The FPGA (i) modulates the laser (ii), which sends an optical frequency modulated signal to the circulator (iii). From the circulator, the light travels to a collimator (iv) where it probes a prism retroreflector on the pendulum (v); the retroreflector is not visible as it is mounted to the underside of the pendulum at the location of the cyan circle. A prism retroreflector mounted on the underside of the pendulum reflects light toward the collimator, where it is collected and routed back through the circulator to the detector and amplifier (vi). The detected signal is demodulated by the FPGA, which provides a quadrature signal to the motion controller (vii) that servos to keep the pendulum stationary.

rare earth magnets. The tested configurations used zero (non-damped), one, or two magnets. With one and two magnets, Q drops to $\sim$16 and $\sim$3, respectively. The dynamics of the pendulum, and thus the optimal control parameters, change with pressure and temperature, as observed later in Figure 7.20. To minimize the risk of the servo losing control of the pendulum and driving it into the end stops (which may damage the mechanism), damping with two magnets was used to add contingency in the control parameters.

In the initial accelerometer configuration, an Ingenia Neptune servo controller [301] was used to keep the system at zero, as seen in Figure 7.18. The curves in Figure 7.18b demonstrate the effectiveness of the control loop, as the mechanism is deflected $\sim$20 µm by the impulse due to the servo working to keep the pendulum positioned at zero; without the servo, Figure 7.18a) shows the pendulum deflect 107 to 137 µm from most to least damping. Although successful in servoing the position to zero, the Ingenia Neptune controller was abandoned for this application since it uses a pulse-width modulation (PWM) drive signal that cannot easily be measured and converted to an equivalent torque by which one obtains the acceleration. Instead, an Aerotech Soloist ML linear current driver [302] was selected, and the current was measured via the voltage across a 8.3586(10) Ω resistor placed in series with the drive output. The second ADC channel on the FMDU was used to measure the resistor voltage.

Configuration of the motion controller requires measurements of the winding resistance, R, and inductance, L. In Table 7.3, these measurements are shown for both coils under several environmental conditions and include any additional wiring, the most notable being the long 37 AWG wires in the cryostat. Measurements for the top coil include the inserted resistor. These parameters are updated in the control loop when tested under each condition. The control loop parameters were tuned at room

Table 7.3: Measurements of the pendulum winding resistance, R, and inductance, L, at room temperature, including the wires that feed to the servo. An 8.3586(10) Ω was placed in series with the top coil. The measurements were recorded using a B&K Precision LCR/ESR Meter Model 885 [303] with a 1 kHz excitation frequency.

Condition	295 K (Laboratory)		295 K (Cryostat)		9 K (Cryostat)	
Coil	R (Ω)	L (mH)	R (Ω)	L (mH)	R (Ω)	L (mH)
Top	22.36(4)	12.03(2)	27.80(6)	12.00(2)	11.24(2)	13.59(3)
Bottom	13.94(3)	12.22(2)	19.22(4)	12.20(3)	2.780(6)	12.09(2)

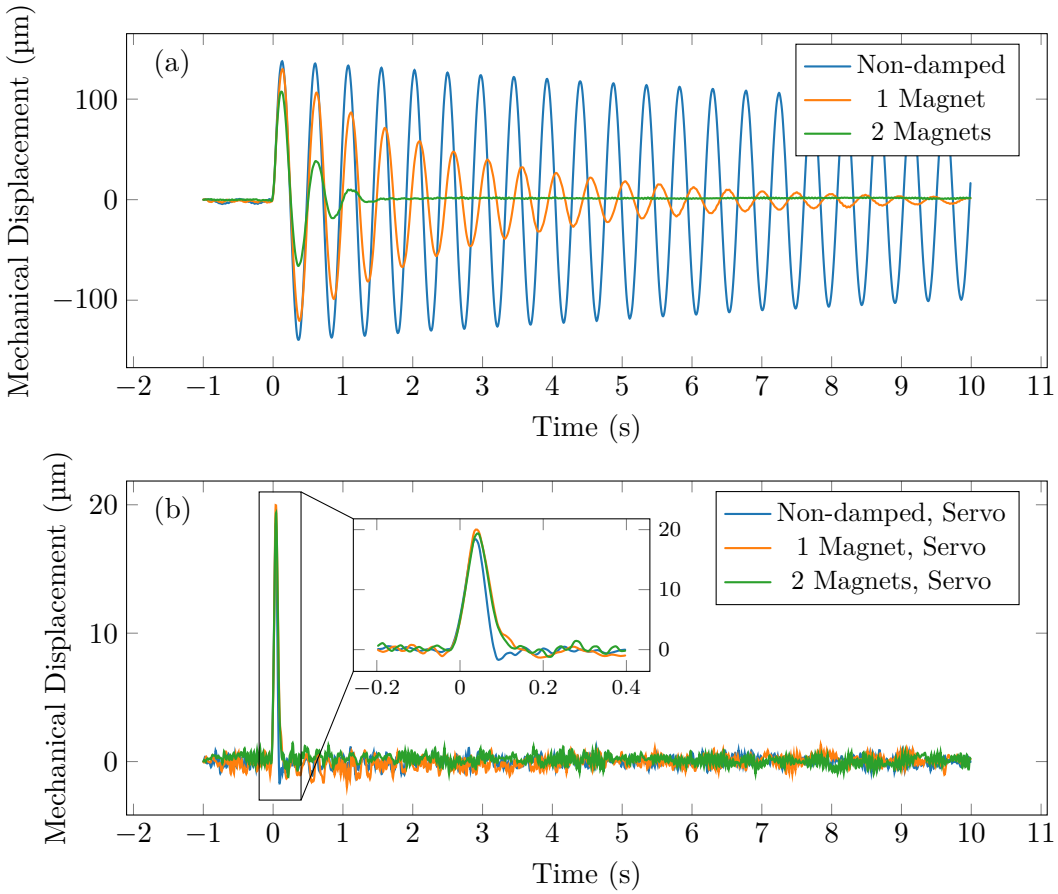

Figure 7.18: Pendulum response to an impulse as damping is varied. Each series is aligned so that the impulse is applied at 0 s. An impulse of 2 V was applied to one of the voice coils for 100 ms. Eddy current damping was applied by a metal fin on the pendulum passing near one or two 12 mm diameter rare earth magnets. The configurations were tested with the servo disabled (a) and with the servo enabled (b). Damping with two magnets was selected to to add contingency in the control parameters that minimize the risk of the servo losing control of the pendulum and driving it into the end stops (which may damage the mechanism).

temperature in atmosphere and at cryogenic temperatures, but not room temperature under vacuum.

The FMDU was configured to provide a quadrature feedback signal to the motion controller with 4× quadrature multiplication for increased resolution, as discussed in Section 4.2. This experiment was performed at a point in the development of the FMDU when the maximum allowed modulation frequency was 25 kHz. As quadrature multiplication trades velocity for resolution, Quadrature multiplication above 4× was not possible due to this limit on the displacement sampling rate and the FMDU would skip quadrature steps due to the velocity of the pendulum. To tune the control loop, quadrature multiplication was required. Without the increased resolution, the digital quadrature step size given to the motion controller was too large and the pendulum would move too far before the FMDU would output the next quadrature step, and the control loop would drive the pendulum into oscillation. Using quadrature multiplication allowed the control loop to make finer adjustments to keep departures from the zero position minimal.

The pendulum was installed in the cryostat as shown in Figure 7.19 with the same 55.0(5) cm OPD as the room temperature tests. When cooled, the cryostat temperature plateaued just below 9 K, and did not reach the target of <4 K. A hole in the 4 and 45 K shielding from a previous cooldown was not blocked, and radiant loading from the outer vacuum chamber prevented the pendulum from reaching <4 K. Since all components in this experiment have been previously validated at <4 K, performance differences are expected to be negligible.

The acceleration can be recovered from the pendulum (to first order) via measurement of the drive current to the voice coil. Since the voltage across the resistor is the measured quantity, the acceleration can instead be expressed in terms of voltage as

$$a = r\alpha = \frac{\tau r}{I_{\mathrm{M}}} = \frac{K_{\mathrm{T}} r}{I_{\mathrm{M}}} I = \frac{K_{\mathrm{T}} r}{I_{\mathrm{M}} R} V, \qquad [\mathrm{m/s^2}] \quad (7.5)$$

where a is the acceleration, $r = 0.027(1)\,\mathrm{m}$ is the radius of the voice coil assembly, α is the angular acceleration, τ is torque, $K_\mathrm{T} = 0.113(11)\,\mathrm{N\,m/A}$ is the torque sensitivity of the voice coil actuator [299], I is electrical current, $R = 8.3586(10)\,\Omega$ is the resistance of the series resistor, V is the voltage across the resistor. The acceleration sensitivity is $K_\mathrm{T} r / I_\mathrm{M} R = 12(1)\,\mathrm{m}g/\mathrm{V}$. The uncertainty in V is estimated as $\pm 0.52\,\mathrm{mV}$, which is equals to 4 LSBs of the ADC.

Figure 7.20 shows the force feedback accelerometer results in atmosphere at room temperature, vacuum at room temperature, and at cryogenic temperatures. There are two cryogenic conditions: one with the pulse tube cryocoolers (PTC) on and the other with them off. The PTCs introduce a $\sim$1 Hz vibration into the cryostat and disabling them gives the best possible test environment. Ring-downs of the pendulum are shown in Figure 7.20a where the impulse was given with the servo disabled. The curves are similar in atmosphere and vacuum at room temperature, however, under vacuum the natural frequency increases in the absence of drag. Both cryogenic cases exhibit a

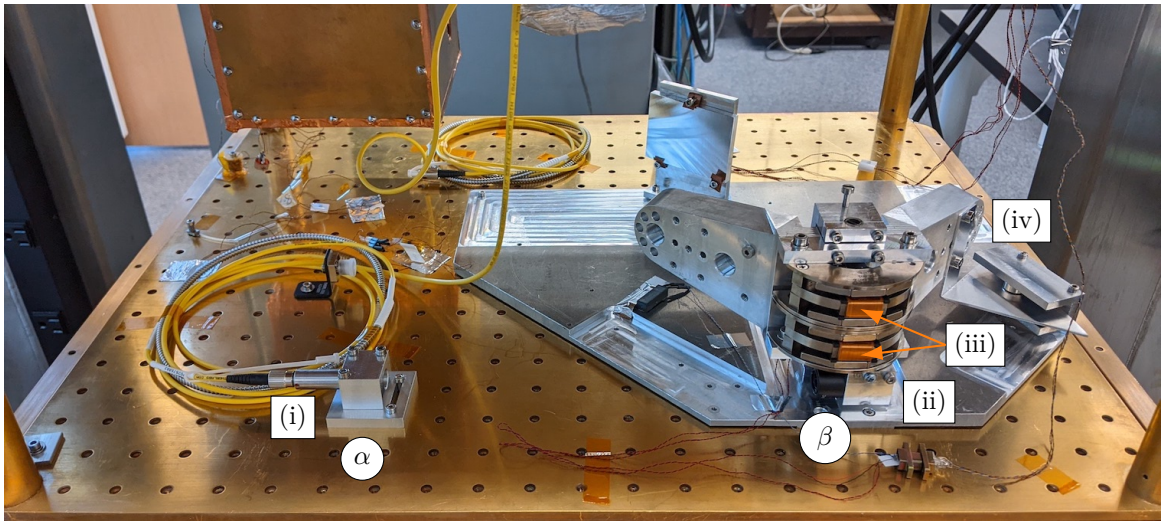

Figure 7.19: Pendulum force feedback accelerometer installed on the 4 K plate of a cryostat. A fibre patch cord with its FC/PC 50:50 beamsplitter coated end was mated to a custom Kovar collimator (i). A prism retroreflector (ii) mounted on the underside of the pendulum is probed by the beam and forms the single interferometer axis, $\alpha\beta$, with an OPD is $\sim$55 cm. The top and bottom voice coil actuators (iii) are used for the servo and impulse, respectively. An aluminum fin (iv) fixed to the pendulum passes near rare earth metal magnets for damping.

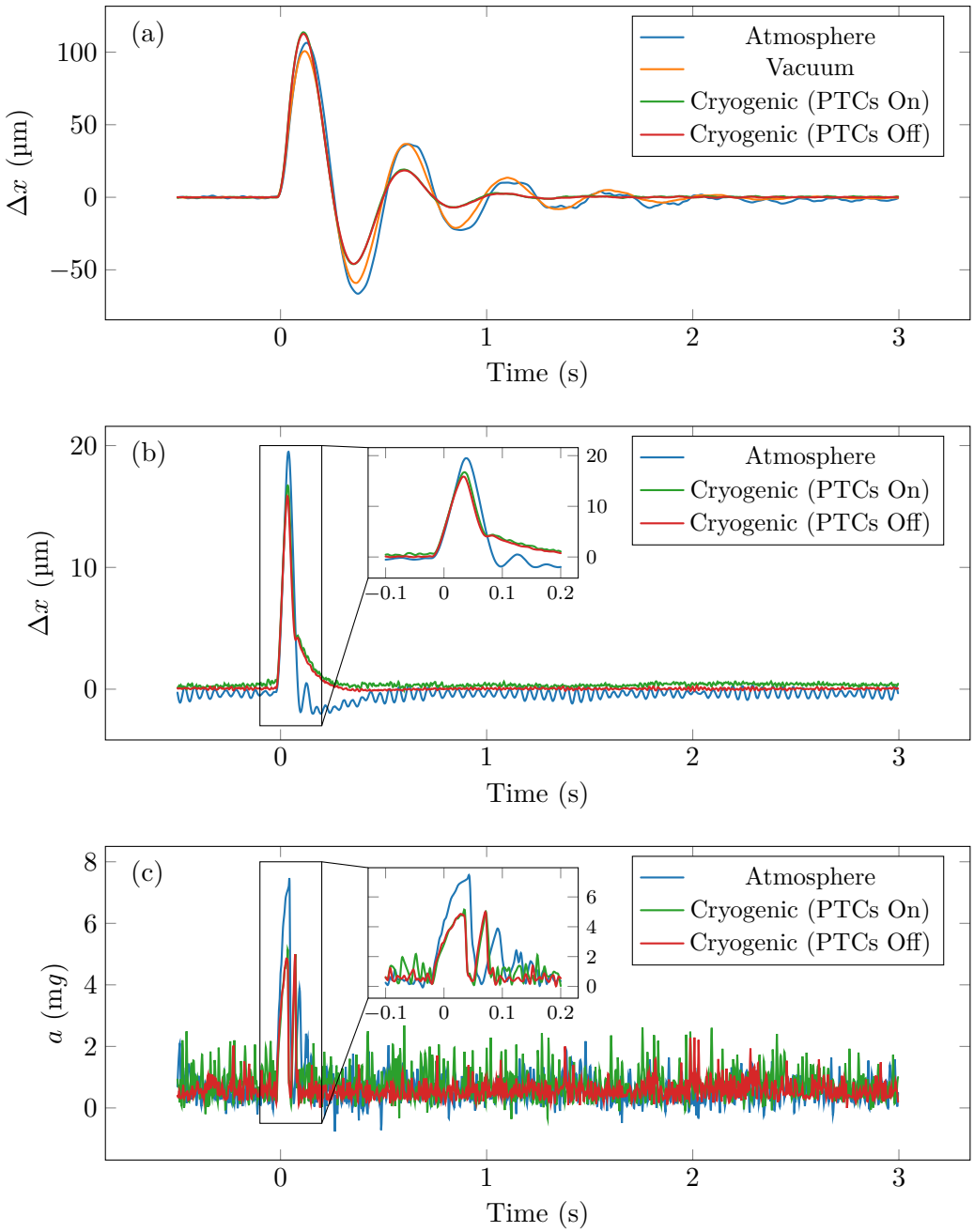

Figure 7.20: Displacement without the servo (a), with the servo (b), and the measured acceleration (c) of the cryogenic force feedback accelerometer. The pendulum was excited with a square pulse for 2 V for 100 ms applied at 0 s. Vacuum curves are not shown in (b) and (c) as the servo was not tuned for vacuum at ambient temperature. Accerlations in (c) are 7.2(8) mg in atmosphere, 5.0(5) mg at cryogenic temperatures with the PTC on, and 4.9(5) mg with the PTC off.

similar natural frequency to the system under vacuum at room temperature, but with reduced amplitude, as the damping magnets increase in strength when cooled [304].

With the servo enabled in Figure 7.20b, the atmospheric and cryogenic cases show consistent behaviour with the displacements in Figure 7.20a, where the peak displacement is reduced at cryogenic temperatures. Figures 7.20b and 7.20c do not show curves for the vacuum case as the servo was not tuned for this condition. The purpose of the experiment was to evaluate whether the force feedback technique was viable at cryogenic temperatures, so the control loop was not tuned for vacuum conditions. Nonetheless, Figure 7.20a does highlight the importance of the control parameters, as the only difference between the atmospheric and vacuum cases is drag due to air. It is also observed in Figure 7.20b that the servo is more effective at holding the pendulum in the zero position at cryogenic temperatures than at room temperature, and even more so with the PTCs off. Over the 1 to 2 s of Figure 7.20b, the atmospheric, cryogenic with PTCs on, and cryogenic with PTCs off show respective displacement fluctuations of 481, 341, and 73 nm rms (vacuum fluctuations in the servo position are not included since the loop was not tuned for this case).

Figure 7.20c shows the accelerations computed to first order via Equation (7.5) using measured voltage across the inserted resistor. Accelerations are computed for the atmospheric and cryogenic cases for which the control loop was tuned. Both cryogenic cases show similar accelerations of $5.0(5)\,\mathrm{m}g$ and $4.9(5)\,\mathrm{m}g$ with and without the PTCs on, respectively, while the atmospheric case is $\sim$45 % greater at $7.2(8)\,\mathrm{m}g$, indicating that calibration of the magnetic damping at cryogenic temperatures is required for a real application of this force feedback technique. Nonetheless, Figure 7.20c shows that the impulse imparts an equivalent acceleration of $4.9(5)\,\mathrm{m}g$ with a noise floor of $0.7\,\mathrm{m}g$ rms at 9 K when the PTCs are off.

The intent of this application is not to develop a sensitive accelerometer, but instead demonstrate how the FMDU may be integrated into more complex systems.

A cryogenic force feedback accelerometer was constructed upon the (non-optimal) remnants of another experiment using all features of the FMDU. The probing beam from the FMDU was used to measure the displacement of the pendulum, the digital quadrature output with multiplication was used to provide position feedback to the servo controller, and the secondary ADC sampled a voltage to determine the acceleration. Having explored a cryogenic force feedback accelerometer, a practical cryogenic accelerometer developed for ground-based gravity wave detectors [305–309] is next investigated in Section 7.7.

7.7 Application #7: Cryogenic Silica Resonator

I gave two presentations at SPIE Photonics West 2023 on the SFM technique [278] and cryogenic characterizations of optical fibres in Sections 6.1 to 6.3 [243]. One goal in attending the conference was to develop a collaboration through which the SFM range-resolved laser interferometer could be applied. Following discussions with researchers from Texas A&M University (TAMU) who were reporting accelerometers for ground-based gravity wave detectors [305–309] such as the Laser Interferometer Gravitational-Wave Observatory (LIGO) [310], a collaboration was struck in which Texas A&M University (TAMU) would provide a monolithic silica resonator and I would investigate its resonant frequency and quality factor at cryogenic temperatures using my SFM range-resolved laser interferometer.

7.7.1 Theory

The quality factor, Q, of an oscillator can be measured in several ways, for instance, the full width at half maximum (FWHM) and ring-down approaches. As seen in Appendix B, the average energy of a high Q driven harmonic oscillator is Lorentzian in frequency. By measuring the displacement of the oscillator while sweeping the driving frequency, a measurement proportional to the average energy may be obtained from

the square of the displacement, which can be seen from Equation (B.4). A Lorentzian function, given by

$$L(f) = h\frac{1}{1+4\left(\frac{f_\mathrm{r}-f}{\Gamma}\right)^2}, \qquad \text{[m]} \quad (7.6)$$

where h is the height, f_r is the resonant frequency, f is the driving frequency, and Γ is the FWHM, may be fitted to the displacement power spectrum to determine Q. As outlined in Appendix B, the resonant frequency, f_r — not the natural frequency — is fitted, as f_r is the location of the peak in the displacement power spectrum. The height of the peak is irrelevant for the determination of Q, as Equation (B.11) shows that the quality factor may be found using

$$Q \approx \frac{f_\mathrm{r}}{\Gamma} \quad \text{when} \quad f_\mathrm{r} \gg \Gamma. \qquad (7.7)$$

An alternative strategy to determine Q is the ring-down method in which the decay of a damped harmonic oscillator is analyzed. As the oscillator *rings down*, the exponential envelope, $\exp(-\omega_0/2Q)$, where ω_0 is the natural angular frequency of the resonator [189], is examined to obtain Q. Although simple, this technique was not used in cryogenic testing, as TAMU predicted that the resonant frequency will increase by $\sim$15 Hz when cooled from room to cryogenic temperature. It is challenging to follow and excite the narrow peak of the high Q resonator, and for this reason, the FWHM approach using Equations (7.6) and (7.7) was adopted since the frequency sweep can be selected to cover the range of expected resonant frequencies.

7.7.2 Room Temperature Measurements

The alignment of the resonator with the probing SFM signal was initially achieved and verified at room temperature in atmosphere. Figure 7.21 shows several images of the resonator and mounting strategy. The resonator itself is shown in Figure 7.21a. As the entire resonator is fused silica, it can be probed via Fresnel reflection [10],

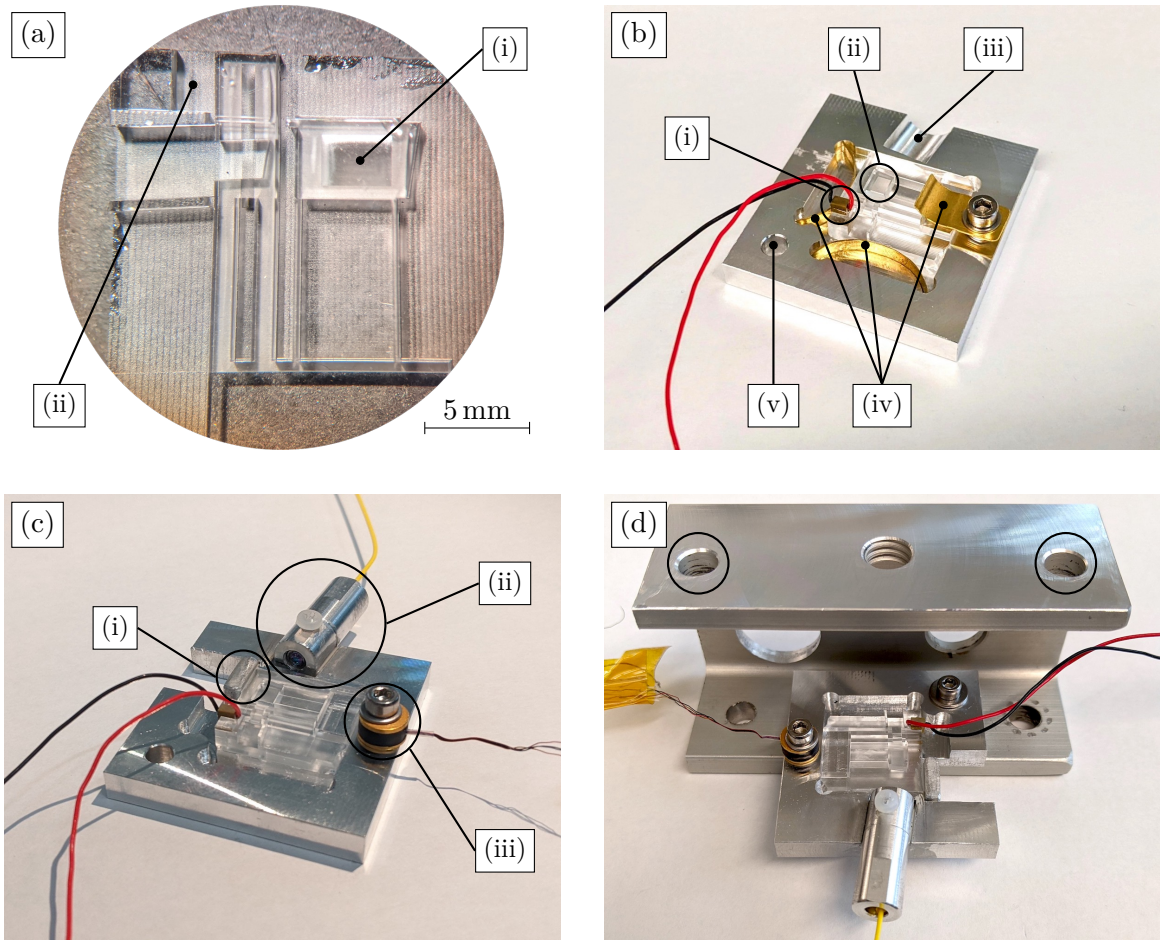

Figure 7.21: The fused silica resonator (a) with a proof mass (i) and channel for a PZT (ii). The initial design (b) shows the resonator in the pocket of the aluminum mount. The PZT (i) excites the resonator so that the proof mass (ii) is displaced. A collimator installed in the uper channel (iii) directs the probing beam from the FMDU toward the back surface of the proof mass. The resonator is secured in the mount by brass leaf springs (iv) and the entire mount can be fastened using a mounting hole (v). Leaf spring are removed in the modified design (c) and replaced by an aluminum tab epoxied to the mount and side of the resonator. The collimator (ii) is held in a collar mount and epoxied into the upper channel after alignment. A thermometer (iii) is installed near the resonator using the tapped hole left over from a leaf spring. The entire mount was installed in channel aluminum (d) for vacuum cryogenic testing discussed in Section 7.7.3; the circled through holes were used to secure the channel aluminum to the 4 K plate. As the cryostat is inverted, the channel aluminum is required to hold the resonator mount with the pocket facing upward in the cryostat. This is a safety measure in case the epoxy fails so that the resonator cannot fall out and be damaged.

and once mounted, the right face of the proof mass is probed. The initial mounting strategy is shown in Figure 7.21a in which the resonator is seated in the pocket of a custom aluminum mount. Three brass leaf springs hold the resonator in place so that a collimator may be aligned with the proof mass. Upon testing this initial design, the mounting was abandoned as the losses were too great. Since the resonator was held tightly to the mount, its energy was rapidly lost through the mount and small Q values ($\sim$100) were measured. The collimator was removed and the aluminum mount was modified by cutting a channel into the pocket as shown in Figure 7.21c. A small aluminum tab was roughened with diamond film and epoxied to the side of the resonator and newly cut channel in the aluminum mount. The epoxy holds the resonator in place with minimal mounting force. Subsequently, the collimator was aligned and epoxied into place. Low outgassing and low temperature EPO-TEK 920 epoxy [311] was used in both cases. Figure 7.21c also shows the location of a Lake Shore Cryotronics Cernox CU thermometer [249] near the resonator, which is used when cooled in the configuration shown in Figure 7.21d. Selection of the channel aluminum in Figure 7.21d are discussed in Section 7.7.3.

A Thorlabs PA2JEW PZT [312] was installed by TAMU for testing. The PZT was glued in the indicated channel in Figure 7.21a using Norland Optical Adhesive 61 ultraviolet curing glue [313]. The PZT is used to excite the resonator so that a response can be measured as the mechanical displacement, Δx. A waveform generator and audio amplifier were used to produce a sufficient voltage to drive the PZT. The average resonator energy, $\langle E \rangle$, is required for determination of Q, as f_{r} and Γ are obtained by a least squares fit to the Lorentzian energy distribution for use in Equation (7.7). A scaled measure of energy may be estimated from the displacement since $\langle E \rangle \propto \Delta x^2$ by Equation (B.5).

Several measurements were recorded at room temperature in atmosphere with different collimator and mounting configurations, and are plotted in Figure 7.22. Before

Table 7.4: Summary of experimentally determined parameters for the configurations plotted in Figure 7.22b.

Collimator	f_r (Hz)	Γ (Hz)	Q
External	677.193(1)	1.193(4)	566(2)
Epoxy	676.941(5)	2.067(16)	327(3)
Mass	678.541(4)	2.005(11)	338(2)
Channel	677.300(5)	0.252(1)	2688(15)

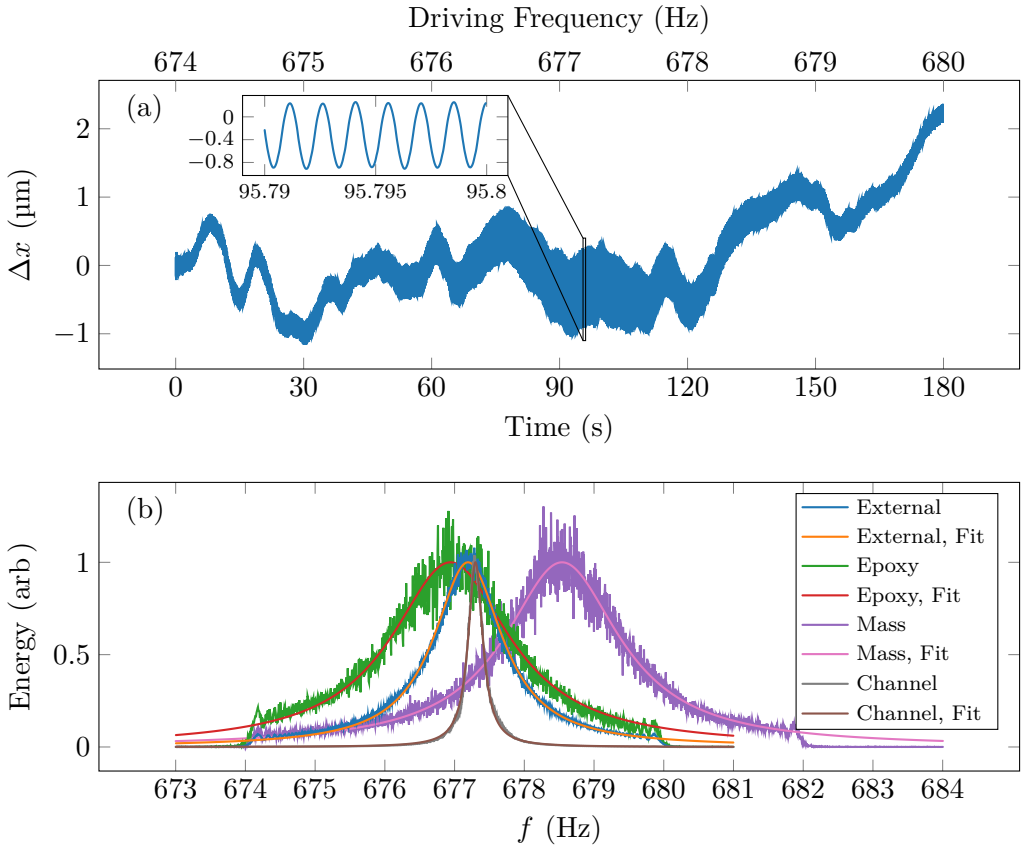

Figure 7.22: Procedure for obtaining Q and f_r from resonator displacement. The displacement of the resonator in atmosphere for the *external* case is plotted as a function of time in (a) with a zoom when the driving frequency is near resonance; the instantaneous driving frequency is drawn on the upper horizontal axis. Temperature fluctuations along the fibre resulted in the low frequency displacement changes. Normalized displacement power spectra are plotted in (b) along with associated least squares fits to the Lorentzian profile in Equation (7.6). These results highlight the sensitivity of the resonator to the mounting; and the greatest quality factor is achieved with the *channel* configuration.

the photo in Figure 7.21c was taken, a custom OZ Optics titanium 0.4 mm beam diameter 2 mm focal length titanium pigtailed collimator [269] was shortened so that its fibre was 70(1) cm. The collimator was placed in a custom aluminum collar and held in alignment with the resonator using a kinematic mount. After the resonator was epoxied in place but before the collimator was epoxied into the mount, the displacement of the resonator was recorded while the driving signal to the PZT was swept over the frequency range from 674 to 680 Hz at a rate of 0.33 Hz/s. This configuration, prior to applying epoxy to the collimator, is known as the *external* configuration in Figure 7.22 and the fitted parameters in Table 7.4. The displacement in Figure 7.22a is plotted for this case. The signal amplitude is maximum over 677 to 677.5 Hz, which includes the fitted resonant frequency. Drifting in Figure 7.22a is due to temperature fluctuations in the ∼70 cm pigtailed fibre from the collimator, which is the largest component of the OPD, and the lens to resonator distance is ∼1 cm.

As discussed above, the collimator was epoxied in place to arrive at the configuration referred to as the *epoxy* case shown in Figure 7.21c. A slight reduction in resonant frequency was observed along with a broadening of the energy distribution, resulting in a reduced Q from the *external* case. To test the sensitivity of the mounting scheme, a ∼14 g mass was attached to the end of the collimator to obtain the *mass* configuration, and the resonant frequency was observed to increase significantly with little change in Q. Finally, the mounted resonator was installed in the channel aluminum as shown in Figure 7.21d to arrive at the *channel* configuration. In the *external*, *epoxy*, and *mass* configurations, the resonator mount was bolted flat to an optical breadboard using the bolt hole highlighted in Figure 7.21b, however, in the *channel* configuration of Figure 7.21d it can be seen that the resonator mount is secured only at one end. Since the mount is free to wag, less energy is lost through the channel aluminum and the quality factor is observed to greatly increase. These results show that the resonator is extremely sensitive to mounting, and the point was

well known to TAMU whose mount evolved to suspend the resonator upon 13 ball bearings to minimize losses [306].

7.7.3 Cryogenic Characterization

For cryogenic testing, the mounted resonator and aluminum channel were secured to the 4 K plate of a cryostat as shown in Figure 7.23. When installed, the resonator mount is initially inverted due to its position on the aluminum channel. After the cryostat is rotated 180° into its normal operating orientation, the channel ensures that the pocket faces upward so that if the epoxy fails the resonator will not fall out and be damaged. The probing beam enters the cryostat through a custom Kurt J. Lesker hermetic fibre feedthrough [267] (specifications given in Table C.9).

Before cooling, an appropriate frequency sweep rate for the PZT excitation signal was determined under vacuum (<1 mTorr). Previously, in Section 7.7.2, the PZT signal was swept at a rate of 0.033 Hz/s for atmospheric testing. TAMU models predict that the resonant frequency increases by ∼15 Hz when cooled, thus, a sweep range

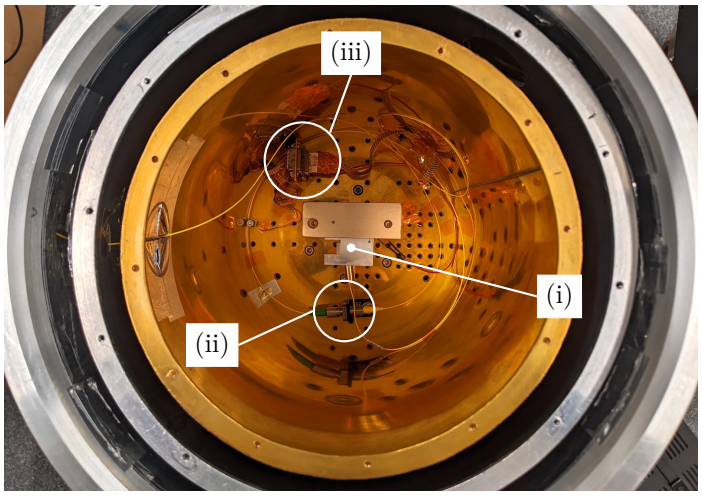

Figure 7.23: Top down view of the resonator installed in a cryostat. The aluminum channel holding the resonator mount (i) is secured to the 4 K plate and the FC/APC end of the fibre collimator is mated to an FC/PC fibre (ii) that is connected to a hermetic fibre feedthrough on the outer vacuum chamber wall. The cryostat electrical harness (iii) has connections to the thermometer on the resonator mount and the PZT.

of 20 Hz was selected. A single sweep would take 600 s at a rate of 0.033 Hz/s, over which time the temperature of the resonator would change by ∼20 K. To reduce the temperature variation in the resonator, the sweep rate was increased to 0.1 Hz/s so that the temperature change falls to ∼7 K over the sweep period. Figure 7.24 shows the measurements obtained in vacuum before cooling with the vacuum pump off. The displacement in Figure 7.24a shows two differences between the atmospheric measurements in Figure 7.22a. First, the displacement is much smoother in vacuum, as temperature induced length fluctuations of the collimator fibre are largely eliminated by the removal of air currents. Second, since air drag was removed, the displacement amplitude at resonance showed a marked increase from 0.6 µm in atmosphere to 2.8 µm in vacuum. Along with the increase in displacement amplitude, the fit in Figure 7.24b shows an increase in Q from ∼2700 in atmosphere to ∼6600 in vacuum was observed as the energy distribution narrowed.

Sampling of the resonator displacement was automated for the temperature descent. The waveform generator was used to produce two outputs: a frequency swept

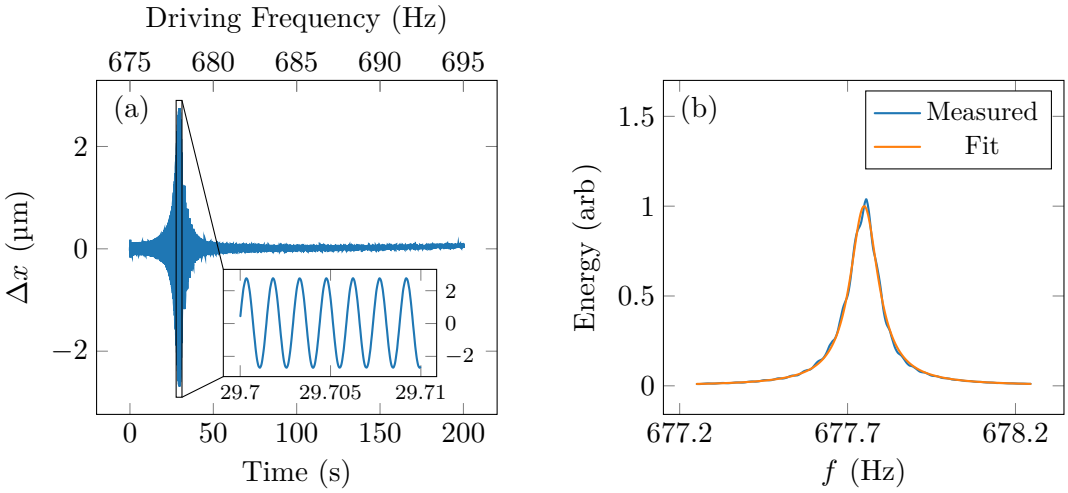

Figure 7.24: Resonator measurements under vacuum at room temperature with a 0.1 Hz/s sweep rate over 675 to 695 Hz. The displacement in (a) does not show the same amplitude displacement fluctuations at low frequencies as Figure 7.22a since fibre temperature stability is greater in the absence of air. The fitted resonant frequency and quality factor in (b) are $f_r = 677.749(2)$ Hz and $Q = 6603(37)$.

sinusoid over a 20 Hz range at 0.1 Hz/s and a 3.3 V synchronization pulse whose rising edge occurs every time a new sweep is started. The secondary ADC of the FMDU was used to sample the synchronization pulse and record every second sweep. A total of 20 measurements were taken and are shown in Figure 7.25. The vacuum measurement in Figure 7.24 is the same as Figure 7.25a with the PTC off; measurements in Figure 7.25b through Figure 7.25t were recorded during cooling with the PTC on. Comparing Figure 7.25a and Figure 7.25b, it is clear that the vibration from the PTC disrupts the near ideal nature of the resonator under vacuum.

From the 20 measurements in Figure 7.25a through Figure 7.25t, f_r and Γ were fitted to obtain Q from Equation (7.7); the fitted f_r is plotted Figure 7.25u. The resonant frequency shows a linear relationship with temperature given by

$$f_\mathrm{r}(T) = \big(0.0685(8)\,\mathrm{Hz/K}\big)T + 658.23(16)\,\mathrm{Hz}, \qquad [\mathrm{Hz}]\ (7.8)$$

where T is absolute temperature. The resonant frequency was expected to increase when cooled due to two effects: Young's modulus of fused silica is known to increase as the temperature is reduced to 70 K [314] and fused silica contracts until ∼100 K [315]. Both the increase in stiffness and decrease in length should lead to increased natural and resonant frequencies. The observed decrease in resonant frequency is not understood currently and is under investigation by our collaborators at TAMU, but the robustness of the measurement is beyond doubt.

The measurement at 63 K in Figure 7.25t was the final measurement that showed any evidence of motion — the next measurement at 49(4) K and all following are not shown since the epoxy had completely failed and alignment with the proof mass was lost. At 197 K, similar disturbances are observed, which may have been cracking in the epoxy holding the PZT, resonator, or collimator in place. Upon inspection of the resonator after cryogenic cycling, the PZT was easily removed by applying little force to the leads, indicating that the glue had failed at some point during the cycle.

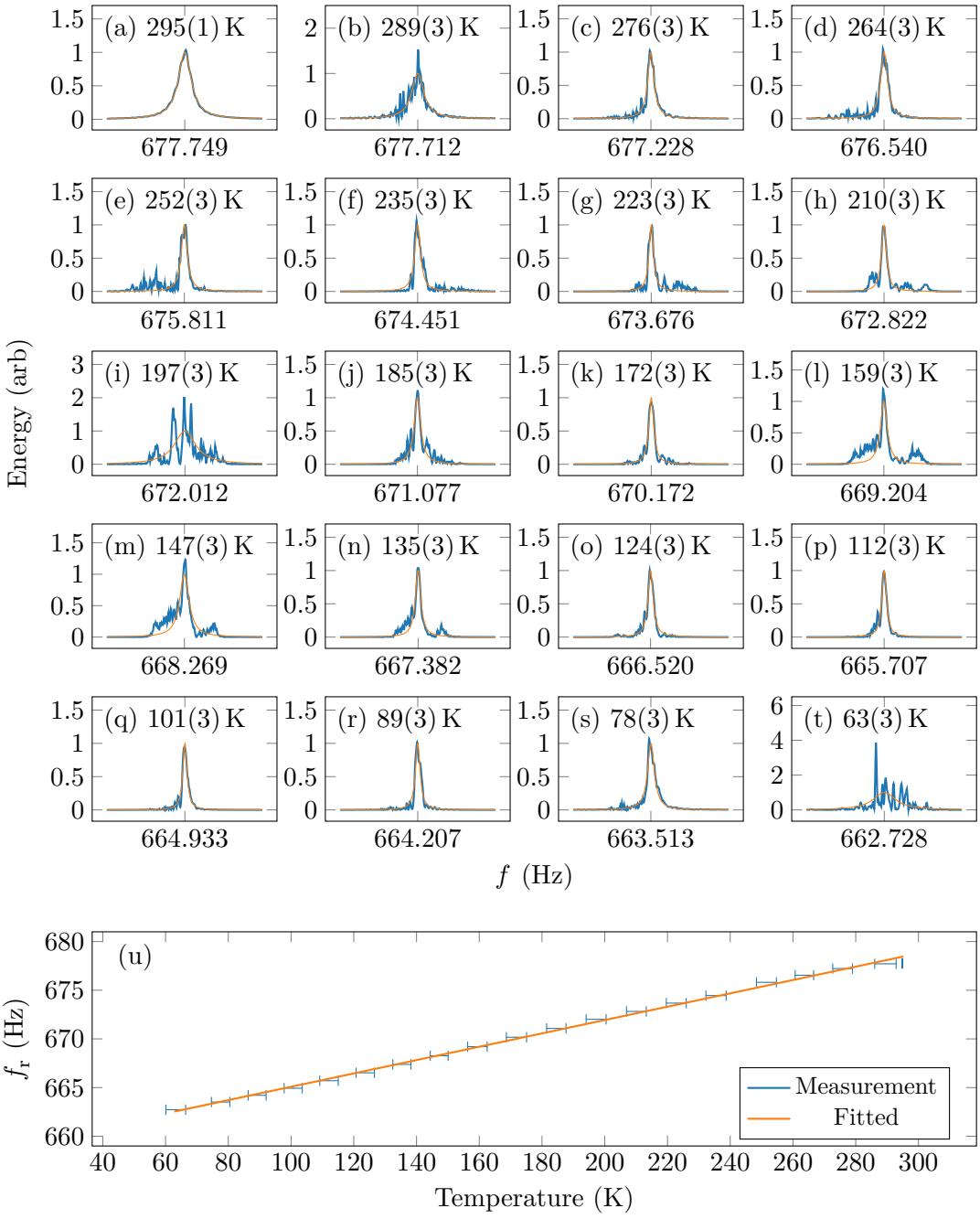

Figure 7.25: Results from resonator characterization during cryogenic cycling. Plots (a) through (t) show the measurements (blue) and fitted curve (orange) centred at the fitted resonant frequency and showing a span of ±0.5 Hz. Measurements in (a) were recorded under vacuum with the PTC off; the PTC was on for measurements in (b) to (t). Uncertainty in temperature is reported as the maximum departure from the mean over the measurement period. Fitted resonant frequencies are shown in (u); vertical error bars are not drawn as the maximum uncertainty of 0.005 Hz in the fitted f_r is too small to visualize.

The quality factor was challenging to calculate based on the difficulty of fitting Γ with the vibration introduced by the PTC when cooling. Determination of Q via Equation (7.7) is sensitive to small fluctuations in Γ, since the numerator is large ($f_\mathrm{r} \approx 700\,\mathrm{Hz}$) and the denominator is small ($\Gamma \approx 0.1\,\mathrm{Hz}$). Calculated Q values were distributed over a range of 4×10^3 to 20×10^3 with no discernable pattern. Without overinterpreting Figures 7.25a to 7.25t, the optimal environment to collect these data is on the smoother temperature ascent where the PTC is off (i.e., not introducing vibrations) and the temperature rate of change is $\sim$25 times less than the descent.

Although alignment was completely lost on the descent somewhere between 63 to 49 K, cycling continued until the thermometer on the resonator mount read $<8\,\mathrm{K}$. After warming, the resonator was inspected under a microscope for possible damage. There was no evidence of damage to the pendulum or gluing sites where the PZT and aluminum tab were secured. Although the mounting strategy of the resonator can be improved, for example, by using a mount made of fused silica to better match the CTE of the resonator, the resonator itself survived its excursion to $<8\,\mathrm{K}$ without damage. As mentioned above, the temperature ascent from $\sim 4\,\mathrm{K}$ is expected to yield better results. Failure of the resonator or the mounting was a concern so data was collected on the temperature descent. Because the mounting *did* fail and no further data could be obtained, the data collected on the temperature descent were presented. Nonetheless, this first attempt at the cryogenic characterization of a fused silica resonator yielded reliable resonant frequency measurements and showed that future attempts should invest more effort into the mounting strategy to exploit the reduced vibration environment during the slower temperature ascent.

7.8 Application #8: Range Fragmentation

7.8.1 Theory

One limitation of the SFM technique is the OPD range that may be demodulated. A novel technique, which is referred to as *fragmentation*, is used to measure changes in OPD exceeding the conventional range of a single-axis configuration. A conceptually simpler adaptive modulation scheme was also considered for extension of the measurement range but is difficult to implement in practice because it requires real-time tuning of the modulation or demodulation. The adaptive and fragmentation approaches may be respectively summarized as:

1. An adaptive demodulation scheme employs real-time tuning to keep demodulation in-band. Either the laser modulation can be adjusted to hold the beat frequency at the detector in-band with a carrier or the carrier adjusted to follow the changing beat frequency.
2. A fragmented measurement scheme employs several overlapping carriers that cover the desired measurement range. Only one carrier need be in-band at a time, and the demodulation is transferred between adjacent carriers as the OPD changes. As the range is divided into several smaller segments called *fragments*, one must hold knowledge of every fragment to reconstruct — or *defragment* — the total measurement.

Fragmentation was chosen over an adaptive scheme due to the simplicity in implementation. Without any modification to the FMDU software, a fragmented measurement can be defragmented in post-processing.

Figure 7.26 illustrates an example fragmentation for a single-axis interferometer. The maximum optical range of any individual fragment is given by $\Delta\Lambda_{\max}$ from Equation (5.3). By employing k fragments, the range may be extended to $\sim k\Delta\Lambda_{\max}$. It is not possible to achieve exactly $k\Delta\Lambda_{\max}$, since each fragment must have a small overlap with its neighbour so that the measurement may follow the OPD as it traverses across

fragment boundaries. For stability, one may use hysteresis when defining the fragment boundaries, which are visualized as the overlaps in the hand off regions of Figure 7.26. The principle of fragmentation is rooted in the ability for two carriers to demodulate in-band simultaneously within the hand off regions, allowing the range to be extended by transferring the measurement from one fragmentation to the next. While it is required that fragments exhibit some amount of overlap, fragmentation does not impose any additional constraints on demodulatability discussed in Section 3.4.

7.8.2 Experiment

Demonstration of a fragmented measurement not only provides confirmation that the technique may be applied to extend the measurement range beyond that of a conventional single-axis configuration, but also gives a characterization of the maximum range that can be measured using a single carrier. In this section, all lengths and displacements are reported in mechanical path (unless stated otherwise), which is 1/2 of the optical path for this interferometer configuration.

The interferometer and fragmentation configuration is shown in Figure 7.27. A Thorlabs PS974M-C prism retroreflector [273], was mounted to an Aerotech ATS20030-

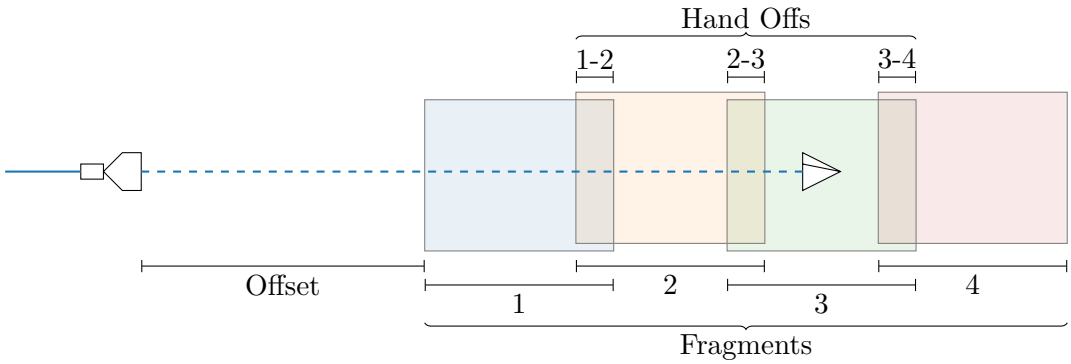

Figure 7.26: Fragmentation of a single-axis interferometer. Each shaded region represents a fragment over which the range is demodulated with a single carrier. By employing four fragments, the motion of the retroreflector can be tracked over a range ∼4× greater than that of a single fragment. There are three hand off regions between fragments where the measurement must be passed from one fragment to the next.

M linear translation stage [316] having a stroke of 300 mm. The probing signal was delivered by a FC/PC terminated fibre mated to a custom OZ Optics 18.75 mm focal length Kovar collimator [269]. The range was broken into six fragments of 50 mm each. To avoid spurious switches, 1 mm of hysteresis was used before switching fragments.

The stage used in these tests has a 300 mm stroke, which unfortunately, is less than the range that can be measured using a single carrier with the modulation capabilities of the LD. Nonetheless, to demonstrate the technique, the 300 mm stroke was split into six fragments of 50 mm, each demodulated by a carrier having Λ_c in the centre of

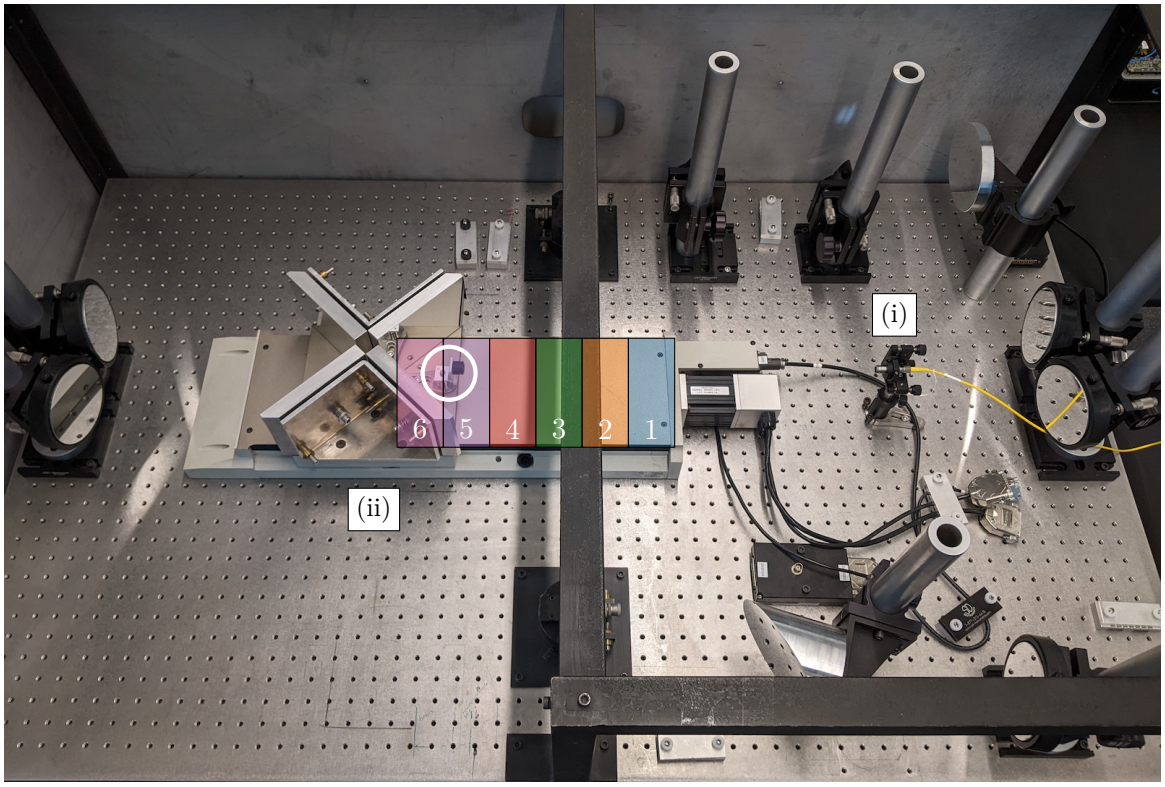

Figure 7.27: Interferometer configuration for a fragmented measurement. The FC/PC tip of the delivery fibre from the FMDU is connected to a collimator (i) and the beam probes a retroreflector (white circle) on a linear stage (ii). The range is split into six fragments shown by the shaded areas. Fragments do not cover the entire length of the stage since the retroreflector is offset; when the stage is positioned all the way to the left, the retroreflector (currently in the 5^{th} fragment) will lie in fragment 6. The stage is part of a Mach-Zehnder interferometer, and the other optics, including the rooftop mirrors on the stage and parabolic mirrors on posts, are not used in the fragmentation experiment.

its individual range. A seventh carrier was generated in the centre of the range of the stage that provides uninterrupted measurement of the full stage motion. The distance from the FC/PC fibre tip secured in the collimator to the retroreflector when the stage is in the zero position is 310(5) mm. Since each fragment is 50 mm, six carriers were generated using OPDs of $\Lambda_{c,k} = 2([310(5)\,\text{mm}] + [50\,\text{mm}]k)$ where $k = 1, \ldots, 6$ to obtain $\Lambda_{c,1}$ through $\Lambda_{c,6}$ of 670(10) mm, 770(10) mm, 870(10) mm, 970(10) mm, 1070(10) mm, and 1170(10) mm, respectively. The seventh carrier was generated at $\Lambda_{c,\text{direct}} = 920(10)\,\text{mm}$, which is the central OPD between the six fragmented carriers.

The LD was modulated at $f_m = 100\,\text{kHz}$ with an optical frequency modulation amplitude $\nu_A = 1.51(12)\,\text{GHz}$. Since there were seven axes, the signal was downsampled to 10 kHz to keep the rate below the 500 kHz combined throughput capacity. Figure 7.28a shows the seven direct displacement measurements, for which the fragments are denoted by Δx_k where k is the fragment number from Figure 7.27, and Δx_{direct} is the measurement by a single carrier that covers the full range of travel in-band. Fragments near the centre of the travel range can be demodulated over the whole stroke, however, those at either end lose track of the displacement as their demodulation goes out-of-band at the opposite end. Estimated from Figure 7.28a, the measurement range in mechanical path is ∼400 mm, based on the points where Δx_1, Δx_2, and Δx_6 go out-of-band around 5, 45, 80, and 120 s. The range predicated from theory using Equation (5.3) with the recommended $w = 2.5$ (established in Section 5.3) is 395 mm in mechanical path, which agrees with the observed behaviour.

Measurements of the individual fragments in Figure 7.27 are plotted in Figure 7.28a along with their defragmentation in Figure 7.28b with 1 mm hysteresis. The defragmented measurement, Δx_{defrag}, direct measurement, Δx_{direct}, and their difference are plotted in Figure 7.28c. The absolute maximum difference is 14 nm, and over the entire series the difference is 5 nm rms in a 5 kHz bandwidth. The dif-

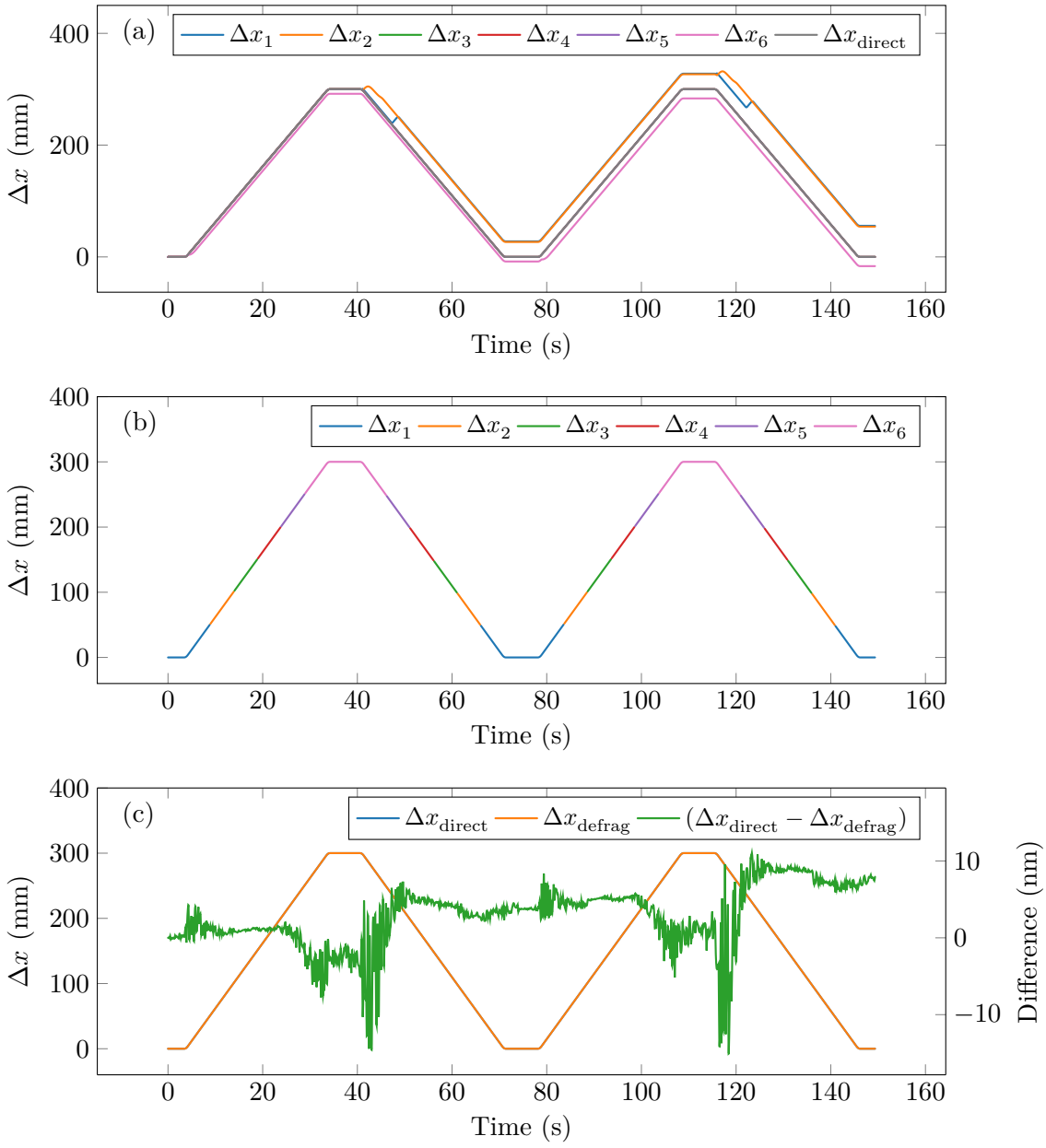

Figure 7.28: Fragmented measurements using $\nu_{\text{A}} = 1.51(12)\,\text{GHz}$ and $\sigma = 0.0225$. The measurements are distributed over six fragments in (a); some are observed to go in and out-of-band. The direct measurement using the central OPD of the entire travel is collected and plotted for reference. Using the fragmented measurements, full travel is defragmented in (b). The difference between the direct and defragmented measurements are shown in (c) with Δx_{direct} and Δx_{defrag} plotted on the left vertical axis scale and $\Delta x_{\text{direct}} - \Delta x_{\text{defrag}}$ on the right scale. The difference between the fragments and direct measurements is 5 nm rms in a 5 kHz bandwidth. Fragments are colour-coded to match the stage illustration in Figure 7.27.

ference does not show any sudden jumps, which indicates that the defragmentation procedure does not leave artefacts when transitioning between fragments.

The fragmented measurement is expected to provide better accuracy at the limits of travel than the full measurement as fragment carrier is better matched to the true phase modulation amplitude of the signal in those regions. As the displacements and difference are overplotted in Figure 7.28c, it is obvious that the largest discrepancy occurs when the stage starts or stops. These points are where the acceleration is greatest ($\sim$10 mm/s^2) and the stage control loop rings while trying to stabilize. The results show that even when the stage is 150 mm from the position about which the carrier is referenced, errors due to the demodulation transitioning out-of-band are on the order of 5 nm rms in 5 kHz measurement bandwidth.

7.8.3 Modified Modulation and Demodulation Parameters

A limitation of the Section 7.8.2 fragmentation results is that they are not illustrative for the potential for fragmentation to be of use in long range applications as the stroke of the stage is within the range that can be demodulated by a single carrier. Since a longer stage was not available, the demodulatable range can be reduced by using non-optimal modulation and demodulation parameters, and is done so purely to demonstrate the technique in a configuration where the fragments have minimal overlap.

Recall from Equation (5.3) that the measurement range is inversely proportional to ν_A and σ, and the measurement range may be dropped by increasing these parameters. The optical frequency modulation amplitude was increased to its maximum, $\nu_\mathrm{A} = 2.40(20)$ GHz, which is limited by the current modulation that the LD controller can provide, and the window width was increased from 0.0225 to $\sigma = 0.135$. Although the reduced range is useful for demonstrating how fragmentation enables the measurement

of greater ranges, the results are not explored in-depth, since the range reduction by modified parameters comes at a performance cost.

Measurements with the reduced range are shown in Figure 7.29. Individual fragment measurements are plotted in Figure 7.29a, and each fragment can be observed to go out-of-band during the motion at the points where the displacement suddenly changes direction as the demodulation is aliased. From the individual fragments, the defragmented displacement is shown in Figure 7.29b. While the individual fragments are nearly senseless on their own, when interpreted as a whole, they can be

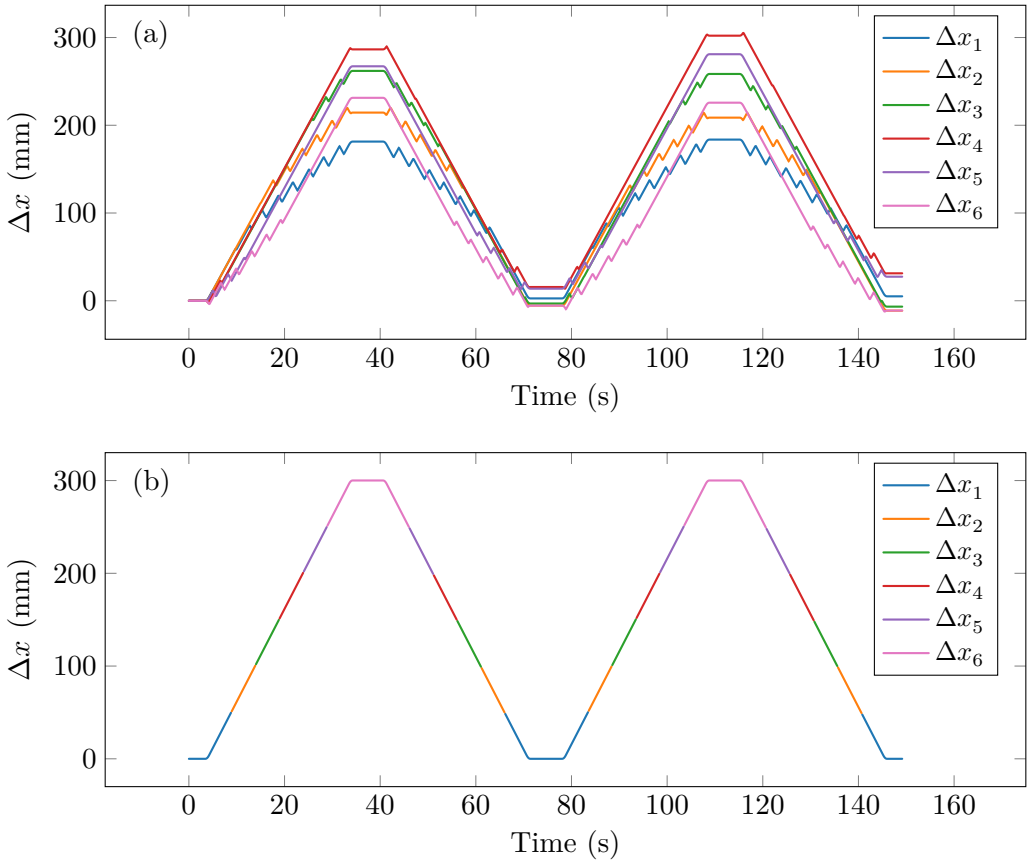

Figure 7.29: Fragmented measurement results with a reduced single-axis measurement range achieved by setting $\nu_\mathrm{A} = 2.40(20)\,\mathrm{GHz}$ and $\sigma = 0.135$. The measurements are distributed over six fragments in (a); all are observed to go in and out-of-band. Using the fragmented measurements, full 300 mm travel is defragmented in (b). Fragments are colour-coded to match the stage illustration in Figure 7.27.

defragmented to obtain a measurement of a range exceeding the conventional limit of single-axis interferometer.

7.9 Conclusions

Eight applications of the SFM technique were explored in this chapter, of which two have demonstrated simultaneous multiaxis measurements. First, in Section 7.1, a three-axis interferometer was constructed at room temperature in atmosphere using two PZT positioners and all three axes were simultaneously measured. The measurements showed 13 nm rms agreement in a 50 kHz bandwidth over short and long period measurements of up to 48 h; in the latter, the combined distance traveled by each axis was ∼140 km. An investigation of the SNR found it to be $\sim 10^3$, which is the nominal SNR level used in the simulations presented in Chapter 5. A comparison against theory showed close agreement between the measured and predicted power spectrum for an SFM interferometer with three axes. Second, in Section 7.2, a cryogenic multiaxis interferometer was constructed to measure the position of a linear translation stage and the thermal expansion of an aluminum sample, which confirmed operation under vacuum at <6 K.

The single-axis performance of the SFM technique was investigated in three experiments. First, in Section 7.3, a novel FSI technique was employed to characterize the resolution of the interferometer. The resolution was determined to be ∼50 pm, which is bit width limited as predicted by theory in Section 5.1.2. To establish the practical noise limits for applications in the laboratory, measurements of a fixed optical distance were obtained at room temperature over a period of two days in a clean room environment subject only to background vibration, temperature, and atmospheric variations. The measurements showed a 3.2 µm mechanical range fluctuation over a 50 cm length using a temperature stabilized laser and an uncertainty of 0.4 nm rms in a 20 Hz bandwidth was obtained. This is promising for long period measurements such as those

which may be recorded during the several day temperature ascent in a cryostat. Furthermore, this offers a significant improvement over the performance observed by the three-phase technique outlined in Sections 2.3.1 and 2.3.2 which would drift several metres (or more) over such a measurement period. Lastly, in Section 7.5, a novel HeNe laser interferometer verification strategy was presented that shows 3.5 ppm agreement between the SFM and HeNe measurements. This difference is comparable to the uncertainty in the calibrated central wavelength of the SFM laser. Together, these single-axis characterization results show that the SFM technique exceeds the minimum requirement of 10 nm rms in a 20 Hz bandwidth outlined in Table 1.1 for the SAFARI FTS.

Realizing the versatility of the SFM technique, three other applications were explored. First, in Section 7.6, a cryogenic force feedback accelerometer was implemented that integrated all functionality offer by the FMDU, showing the ease with which the FMDU can be integrated into larger systems for real-time position measurement and feedback. Second, the cryogenic characterization of a silica resonator for a passive accelerometer was explored in Section 7.7. The resonant frequency was accurately followed as a function of temperature, however, measurement of the quality factor was difficult with noise introduced by the PTC when cooling before the epoxy that secured the pendulum failed and prevented high quality data from being obtained on the temperature ascent. Nonetheless, the strategy was promising, and improvements to the resonator mounting configuration would allow for the quality factor to be better characterized on the temperature ascent when the PTC is powered off. Finally, a novel technique, referred to as *range fragmentation*, was presented in Section 7.8 that enables measurements of ranges beyond the conventional limit of a single SFM axis by exploiting the inherent multiaxis nature of the technique. A maximum measurement range of $\sim$400 mm was estimated, with a demonstrated measurement range of 300 mm limited by the size of the translation stage available. With

Table 7.5: Summary of SPICA SAFARI FTS displacement metrology requirements [33] and demonstrated SFM performance.

Metrology Parameter	SAFARI FTS Requirement	SFM Performance
Resolution[1]	—	∼50 pm
Uncertainty[2]	10 nm rms	0.4 nm rms
Range[3]	33.5 mm	300 mm
Environment[4]	Vacuum, <4 K	Vacuum, <6 K
Thermal Power[5]	<1 mW	TBC

[1] Not specified by SPICA SAFARI; found in Section 7.3.
[2] 20 Hz measurement bandwidth; found in Section 7.4.
[3] Extendable by range fragmentation (Section 7.8); found in Section 7.8.
[4] Conditions in Sections 7.2, 7.6 and 7.7.
[5] Total power dissipated in the cryogenic workspace; to be confirmed.

measurement of up to eight axes provided by the FMDU implementation, ranges of up to ∼3 m may be measured.

Table 7.5 repeats the SAFARI FTS metrology requirements listed in Table 1.1 and provides a third column with the achieved SFM performance. The SFM technique exceeds the uncertainty and range requirements and has been verified in vacuum at <6 K. The thermal power dissipation at cryogenic temperatures was not confirmed, however, it is straightforward to limit by reducing the laser optical power since the primary source of cryogenic power dissipation by the SFM interferometer is through the photons that enter the cryogenic workspace but do not exit. Anecdotally, heating resulting in a temperature increase of ∼1 K has been observed when the laser is powered on, but parasitic heating through the fibre and radiant loading of the fibre, collimator, and retroreflector appears to be negligible. These results have not only demonstrated the versatility of a multiaxis SFM interferometer, but also that the SFM technique is a strong candidate for a displacement metrology solution in future cryogenic space applications.

Chapter 8

Summary and Outlook

This thesis has been concerned with the implementation of the sinusoidal frequency modulation (SFM) technique to meet the challenging displacement metrology requirements of the next generation of cryogenic space-based instrumentation being developed to explore the far-infrared universe. The concept of range-resolved interferometry was introduced in Chapter 1 and its application at cryogenic temperatures was motivated by the requirements of cryogenic far-infrared space astronomy missions, namely the Space Infrared telescope for Cosmology and Astrophysics (SPICA) [15] and the PRobe far-Infrared Mission for Astrophysics (PRIMA) [35]. Chapter 2 reviewed the landscape of displacement metrology techniques including those that have already been employed in space-based applications at cryogenic temperatures and those which might be. My master's thesis studied the three-phase interferometer concept (Sections 2.3.1 and 2.3.2), which had the advantage of simple signal processing, but its poor performance at low velocities could not be overcome. It was realized that the signal of interest must be moved away from DC. The shortcoming of the three-phase system pointed the way forward to the adoption of the SFM technique, the development and cryogenic validation of which has been the central theme of this thesis. Chapter 4 discusses the real-time SFM implementation in the frequency-modulation-demodulation unit (FMDU). I was responsible for the design, procurement, and integration of hardware and software along with the required calibration of the hardware components to realize the SFM equations presented in Chapter 3.

These efforts represent over half the work completed in this thesis. Theoretical performance characteristics were investigated in Chapter 5 to allow comparison with the experimental results that are presented in Chapter 7. Since an important aspect of this thesis is the implementation of the SFM technique at cryogenic temperatures, Chapter 6 focused on measuring the performance of subcomponents to arrive at a robust SFM implementation that can survive and operate at cryogenic temperatures. Chapter 7 concludes the thesis with eight applications of the SFM technique. This chapter provides a summary of the SFM technique and outlook for future work.

8.1 Results

A cryogenic multiaxis range-resolved laser interferometer based on sinusoidal frequency modulation (SFM) was developed and characterized. The optical frequency of a laser diode (LD) was bias current modulated to produce an optical frequency modulated signal resulting in different beat frequencies at the detector due the differing optical path differences (OPD) between all axes. Interferometers can be constructed such that the OPDs, and thus beat frequencies, are unique, enabling simultaneous multiaxis displacement measurements using a single LD and photodetector.

In Chapter 7 I presented results from eight different applications of the SFM technique using the FMDU that I constructed. The thesis represents the first fully cryogenic implementation of the SFM technique for displacement metrology measurements, and the results show that the technique exceeds the stringent requirements (Table 8.1) for the Fourier transform spectrometers (FTS) that have been proposed for both SPICA and PRIMA missions. The lowest demonstrated operating temperature is $<6\,\mathrm{K}$ and there are not any additional difficulties expected at $<4\,\mathrm{K}$. Thermal power dissipation in the cryogenic workspace is yet to be confirmed but is expected to be minimal since the only heating contribution of the SFM interferometer is the photons which are absorbed by the workspace. These results demonstrate that the SFM

Table 8.1: Summary of SPICA SAFARI FTS displacement metrology requirements [33] and demonstrated SFM performance.

Metrology Parameter	SAFARI FTS Requirement	SFM Performance
Resolution[1]	—	∼50 pm
Uncertainty[2]	10 nm rms	0.4 nm rms
Range[3]	33.5 mm	300 mm
Environment[4]	Vacuum, <4 K	Vacuum, <6 K
Thermal Power[5]	<1 mW	TBC

[1] Not specified by SPICA SAFARI; found in Section 7.3.
[2] 20 Hz measurement bandwidth; found in Section 7.4.
[3] Extendable by range fragmentation (Section 7.8); found in Section 7.8.
[4] Conditions in Sections 7.2, 7.6 and 7.7.
[5] Total power dissipated in the cryogenic workspace; to be confirmed.

technique is a strong candidate for robust, precise, cryogenic displacement metrology in future cryogenic far-infrared space astronomy missions.

The range of applications investigated demonstrates the versatility of the SFM approach and includes Simultaneous multiaxis measurements were performed under ambient and cryogenic conditions. Applications in fibre segment interferometry (FSI), long period low-velocity measurements, and a novel wavelength division HeNe laser interferometer verification strategy were used to characterize the performance of the SFM technique with respect to the SPICA Far-Infrared Instrument (SAFARI) FTS requirements and assess the quality of the LD calibration. The SFM technique was subsequently applied to cryogenic accelerometry. First, a low sensitivity cryogenic force feedback accelerometer was constructed using a cryogenic scanning mechanism. The accelerometer demonstrated simultaneous displacement measurement, analog voltage measurement, and digital quadrature feedback capabilities, while also providing an of example of the integration of a range-resolved laser interferometer with other cryogenic hardware. Second, SFM interferometry was used to investigate the cryogenic behaviour of a monolithic silica resonator designed for vibration measurement in ground-based gravity wave detectors [305–309]. In the final application, a novel

technique was proposed and implemented to extend the measurement range of the SFM interferometer beyond its conventional single-axis limit.

8.2 Outlook

The FMDU is a complete system that provides real-time simultaneous demodulation of up to eight interferometer axes with the current hardware. The number of supported axes can be increased by either raising the minimum supported modulation frequency or using a larger field-programmable gate array (FPGA), but a greater number of axes has implications in splitting of the optical power that must be considered. There are several enhancements that can be made to improve performance, eliminate signal processing steps and calibration products, and simplify the operation of the FMDU.

An automatic amplitude normalization strategy was investigated to address the sinusoidal signal envelope introduced through the power modulation of the LD associated with injection of a laser bias current. Due to the optical frequency modulation of the laser, the interference signal at the photodetector is always greater than the modulation frequency — even for fixed OPDs. This property may be leveraged to automatically extract the interference signal envelope and provide real-time amplitude normalization, thereby eliminating the need for extensive calibration of the laser optical power modulation characteristics. A Hilbert transform approach was investigated but did not provide significant improvements over the non-corrected interference signal. It was shown by simulation that optimal normalization of the interference signal produced by a typical modulation configuration with the selected hardware results in a small ($\sim$4 %) reduction in phase uncertainty. Since the performance improvement is minimal, the corrected carrier approach proposed by Kissinger et al. [166] was concluded to be a better choice (even at the cost of an additional calibration product) due to its straightforward implementation that does not require any additional signal

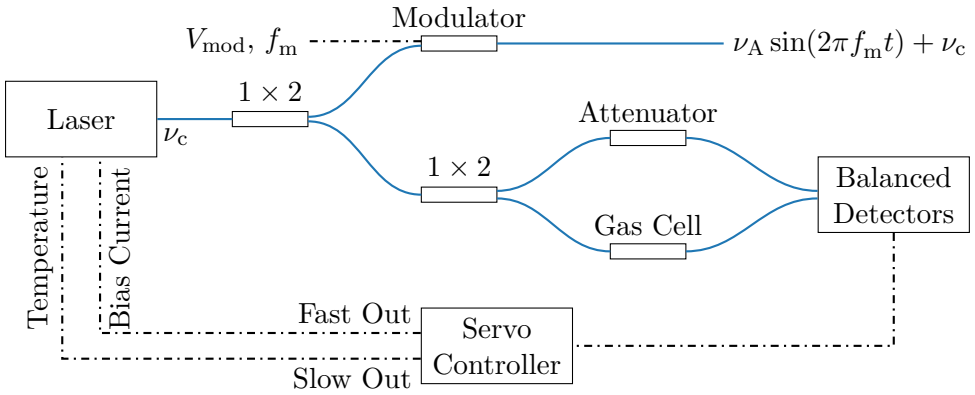

Figure 8.1: A proposed laser frequency stabilization scheme with external modulation of the optical frequency. The laser frequency is locked to the absorption line of a gas cell with an arbitrary frequency modulation applied through an external modulator such as an EOM or PZT.

processing stages such as the filters and Hilbert transform used in the automatic amplitude normalization. Furthermore, since the improvement is small, corrections can be foregone entirely with a negligible impact on performance.

The laser frequency stability can in principle be improved by locking to the absorption line of a gas cell. A $H^{13}C^{14}N$ gas cell was procured for this purpose, but not implemented due to the imposed restrictions on the optical frequency modulation amplitude by the small linear regions of the absorption profile. One way that locking and optical frequency modulation can be achieved is through external modulation of the laser rather than direct modulation of the LD bias current used in this thesis. Figure 8.1 shows an external modulation scheme with laser frequency stabilization using a gas cell. Light from the non-modulated LD at the optical frequency ν_{c} is split so that some fraction of the light passes through a gas cell for locking to an absorption line and the rest goes to an external modulator, such as an electro-optic modulator (EOM) [317] or piezoelectric transducer (PZT) [165,318]. In one arm, the servo loop locks the laser frequency to an absorption line at ν_{c}, while the other arm responds to a modulation voltage, V_{mod}, at a modulation frequency, f_{m}, to add an external optical frequency modulation of $\nu_{\mathrm{A}} \sin(2\pi f_{\mathrm{m}} t)$ to produce the desired optical

frequency of $\nu_{\mathrm{A}} \sin(2\pi f_{\mathrm{m}} t) + \nu_{\mathrm{c}}$ from Equation (3.1), where ν_{c} is the stabilized frequency corresponding to a point on the side of an absorption line. With this strategy, the frequency modulation range is no longer restricted by the linear region of the absorption line, which was the reason that laser frequency stabilization was not adopted in the SFM implementation.

The versatility of the cryogenic multiaxis SFM technique enabled the investigation of several applications in Chapter 7. In all applications, the optical frequency modulation amplitude and central OPDs of each axis was manually configured, however, in principle, these parameters can be automatically discovered for a given interferometer configuration by using a different modulation scheme. For example, with only modification to the software, the sawtooth frequency modulation scheme from Section 3.5.1 may be exploited to find the OPDs of each axis. The optical frequency modulation amplitude may then be automatically selected from the shortest OPD based upon the minimum modulation amplitude dictated by Equation (3.41). Due to the automatic determination of the critical modulation and demodulation parameters, such a feature would make the FMDU plug-and-play — an appealing aspect for the end user.

8.3 Conclusions

In this thesis I have described the theory, implementation, and validation of a cryogenic multiaxis range-resolved laser interferometer using a sinusoidal frequency modulation (SFM) technique. Leveraging the versatility of the multiaxis and cryogenic nature of the SFM interferometer, a broad range of single-axis and multiaxis applications were investigated, including the validation of the technique using a novel HeNe wavelength division multiplexer (WDM) interferometer technique, determination of the resolution using a novel fibre segment interferometry (FSI) approach, and a novel strategy to extend the range of the SFM technique beyond the conventional single-axis limit. The original goal of this research was to demonstrate that the

SFM interferometer can meet the requirements of a cryogenic space-based application. I have shown that the measured performance of the SFM technique satisfies the stringent requirements for the next generation of cryogenic far-infrared astronomical instrumentation and represents an improvement of several orders of magnitude over the cryogenic metrology systems flown on previous missions.

Bibliography

[1] B. Teodosio, P. L. P. Wasantha, E. Yaghoubi, M. Guerrieri, S. Fragomeni, and R. C. van Staden. Monitoring of geohazards using differential interferometric satellite aperture radar in Australia. *International Journal of Remote Sensing*, 43(10):3769–3802, 2022.

[2] J. Wasowski and F. Bovenga. Remote sensing of landslide motion with emphasis on satellite multi-temporal interferometry applications: an overview. *Landslide Hazards, Risks, and Disasters*, pages 365–438, 2022.

[3] L. Solari, M. Del Soldato, F. Raspini, A. Barra, S. Bianchini, P. Confuorto, N. Casagli, and M. Crosetto. Review of satellite interferometry for landslide detection in Italy. *Remote Sensing*, 12(8):1351, 2020.

[4] P. Mastro, C. Serio, G. Masiello, and A. Pepe. The multiple aperture SAR interferometry (MAI) technique for the detection of large ground displacement dynamics: an overview. *Remote Sensing*, 12(7):1189, 2020.

[5] Z. Djinovic, M. Tomic, R. Pavelka, G. Sprinzl, and H. Traxler. Measurement of the human cadaver ossicle vibration amplitude by fiber-optic interferometry. In *2020 43rd International Convention on Information, Communication and Electronic Technology (MIPRO)*, pages 1894–1898. IEEE, 2020.

[6] J. A. N. Buytaert, J. E. F. Aernouts, and J. J. J. Dirckx. Indentation measurements on the eardrum with automated projection moiré profilometry. *Optics and Lasers in Engineering*, 47(3-4):301–309, 2009.

[7] O. N. Budagovskaya and A. V. Budagovsky. Nondestructive laser testing of fruit. *Russian Journal of Nondestructive Testing*, 51(4):236–244, 2015.

[8] S. Terasaki, N. Wada, N. Sakurai, N. Muramatsu, R. Yamamoto, and D. J. Nevins. Nondestructive measurement of kiwifruit ripeness using a laser doppler vibrometer. *Transactions of the ASAE*, 44(1):81–87, 2001.

[9] G. H. Banwell, J. R. Roberts, B. J. Halkon, S. J. Rothberg, and S. Mohr. Understanding the dynamic behaviour of a tennis racket under play conditions. *Experimental Mechanics*, 54:527–537, 2014.

[10] E. Hecht. *Optics*. Addison-Wesley, 4th edition, 2002.

[11] B. E. A. Saleh and M. C. Teich. *Fundamentals of Photonics*. John Wiley & Sons, Inc., 3 edition, 2019.

[12] F. L. Pedrotti and L. S. Pedrotti. *Introduction to Optics*. Prentice Hall, 2 edition, 1993.

[13] A. A. Michelson and E. W. Morley. On the relative motion of the Earth and the luminiferous ether. *American Journal of Science*, 34(203):333–345, 1887.

[14] J. D. C. Jones. Interferometry and polarimetry for optical sensing. *Handbook of Optical Fibre Sensing Technology*, pages 227–245, 2002.

[15] P. R. Roelfsema, H. Shibai, L. Armus, D. Arrazola, M. Audard, M. D. Audley, C. M. Bradford, I. Charles, P. Dieleman, Y. Doi, et al. SPICA – a large cryogenic infrared space telescope: unveiling the obscured universe. *Publications of the Astronomical Society of Australia*, 35, 2018.

[16] B. D. Jackson, P. A. J. De Korte, J. Van der Kuur, P. D. Mauskopf, J. Beyer, M. P. Bruijn, A. Cros, J.-R. Gao, D. Griffin, R. Den Hartog, et al. The SPICA-SAFARI detector system: TES detector arrays with frequency-division multiplexed SQUID readout. *IEEE Transactions on Terahertz Science and Technology*, 2(1):12–21, 2011.

[17] M. F. Kessler, J. A. Steinz, M. E. Anderegg, J. Clavel, G. Drechsel, P. Estaria, J. Faelker, J. R. Riedinger, A. Robson, B. G. Taylor, et al. The Infrared Space Observatory (ISO) mission. *Astronomy and Astrophysics*, 315:L27–L31, 1996.

[18] G. R. Davis, I. Furniss, W. A. Towlson, P. A. R. Ade, R. J. Emery, W. M. Glencross, D. A. Naylor, T. J. Patrick, R. C. Sidey, and B. M. Swinyard. Design and performance of cryogenic, scanning Fabry-Perot interferometers for the Long-Wavelength Spectrometer on the Infrared Space Observatory. *Applied Optics*, 34(1):92–107, 1995.

[19] P. E. Clegg, P. A. R. Ade, C. Armand, J.-P. Baluteau, M. J. Barlow, M. A. Buckley, J.-C. Berges, M. Burgdorf, E. Caux, C. Ceccarelli, et al. The ISO long-wavelength spectrometer. *Astronomy & Astrophysics*, 315(2):L38–L42, 1996.

[20] S. Calcutt, F. Taylor, P. Ade, V. Kunde, and D. Jennings. The Composite Infrared Spectrometer. *Journal of the British Interplanetary Society*, 45:381–386, 1992.

[21] C. F. Hakun and K. A. Blumenstock. A cryogenic scan mechanism for use in Fourier transform spectrometers. In *NASA Johnson Space Center, The 29th Aerospace Mechanisms Symposium*, 1995.

[22] K. J. King and S. J. Leeks. *SPIRE Instrument User Manual*, 2009. Issue 1.5. Available: `https://www.cosmos.esa.int/documents/12133/1035800/SPIRE+Instrument+User+Manual`. Accessed: 14$^{\text{th}}$ July, 2023.

[23] G. L. Pilbratt et al. Herschel Space Observatory – an ESA facility for far-infrared and submillimetre astronomy. *Astronomy & Astrophysics*, 518:L1, 2010.

[24] M. J. Griffin et al. The Herschel-SPIRE instrument and its in-flight performance. *Astronomy & Astrophysics*, 518:L3, 2010.

[25] M. W. Werner, T. L. Roellig, F. J. Low, G. H. Rieke, M. Rieke, W. F. Hoffmann, E. Young, J. R. Houck, B. Brandl, G. G. Fazio, et al. The Spitzer space telescope mission. *The Astrophysical Journal Supplement Series*, 154(1):1, 2004.

[26] R. D. Gehrz, T. L. Roellig, M. W. Werner, G. G. Fazio, J. R. Houck, F. J. Low, G. H. Rieke, B. T. Soifer, D. A. Levine, and E. A. Romana. The NASA Spitzer space telescope. *Review of Scientific Instruments*, 78(1):011302, 2007.

[27] G. H. Rieke, E. T. Young, J. Cadien, C. W. Engelbracht, K. D. Gordon, D. M. Kelly, F. J. Low, K. A. Misselt, J. E. Morrison, J. Muzerolle, et al. On-orbit performance of the MIPS instrument. In *Optical, Infrared, and Millimeter Space Telescopes*, volume 5487, pages 50–61. SPIE, 2004.

[28] R. M. Warden and G. B. Heim. Cryogenic scan mirror mechanism for SIRT-F/MIPS. In *32nd Aerospace Mechanisms Symposium*, page 45, 1998.

[29] H. Murakami et al. The infrared astronomical mission AKARI. *Publications of the Astronomical Society of Japan*, 59(sp2):S369–S376, 2007.

[30] M. Kawada et al. Performance of an imaging Fourier transform spectrometer with photoconductive detector arrays: an application for the AKARI far-infrared instrument. *Publications of the Astronomical Society of Japan*, 60(sp2):S389–S397, 2008.

[31] D. B. Leviton. Image processing for new optical pattern recognition encoders. In *Algorithms and Systems for Optical Information Processing IV*, volume 4113, pages 32–40. SPIE, 2000.

[32] D. B. Leviton, T. Anderjaska, J. Badger, T. Capon, C. Davis, B. Dicks, W. Eichhorn, M. Garza, C. Guishard, S. Haghani, et al. Cryogenic optical position encoders for mechanisms in the JWST optical telescope element simulator (OSIM). In *Cryogenic Optical Systems and Instruments 2013*, volume 8863, page 886306. SPIE, 2013.

[33] D. van Loon, A. Cournoyer, and D. Naylor. SAFARI FTS development plan. Technical Report SRON-SAF-PL-2020-003, Netherlands Institute for Space Research, 2020.

[34] D. L. Clements, S. Serjeant, and J. Shoko. Explain ESA's last-minute ditching of new space telescope. *Nature*, 587(7835):548–549, 2020.

[35] C. Bradford, J. Glenn, L. Armus, C. Battersby, A. Bolatto, B. Hensley, M. Meixner, E. Mills, K. Pontoppidan, A. Pope, et al. The PRIMA Far-Infrared Probe: observatory and instrumentation. In *American Astronomical Society Meeting Abstracts*, volume 54, pages 304–07, 2022.

[36] A. Christiansen. Cryogenic fibre-fed laser metrology. Master's thesis, University of Lethbridge, 2020.

[37] A. J. Fleming. A review of nanometer resolution position sensors: operation and performance. *Sensors and Actuators A: Physical*, 190:106–126, 2013.

[38] D. S. Nyce. *Linear Position Sensors*. John Wiley & Sons, Inc., 2004.

[39] H. Haitjema. The calibration of displacement sensors. *Sensors*, 20(3):584, 2020.

[40] J. Shieh, J. E. Huber, N. A. Fleck, and M. F. Ashby. The selection of sensors. *Progress in Materials Science*, 46(3-4):461–504, 2001.

[41] T. R. Hicks, P. D. Atherton, Y. Xu, and M. McConnell. *The NanoPositioning Book*. Queensgate Instruments, 1997.

[42] M. R. Nabavi and S. N. Nihtianov. Design strategies for eddy-current displacement sensor systems: Review and recommendations. *IEEE Sensors Journal*, 12(12):3346–3355, 2012.

[43] H. Yu, X. Chen, C. Liu, G. Cai, and W. Wang. A survey on the grating based optical position encoder. *Optics & Laser Technology*, 143:107352, 2021.

[44] J. D. Ellis. *Field Guide to Displacement Measuring Interferometry*. SPIE, 2014.

[45] H. D. Young and R. A. Freedman. *University physics with modern physics*. Pearson, 14 edition, 2014.

[46] Queensgate Instruments. *NanoSensors – NX Series*, 2019. Ver. 1. Available: `https://www.nanopositioning.com/product/nanosensors-nx-series`. Accessed: 14th July, 2023.

[47] M. R. Nabavi and S. Nihtianov. A survey of eddy current displacement sensors: imperfections and signal conditioning methods. In *Proc. Int. Sci. Appl. Sci. Conf*, pages 116–122, 2007.

[48] Micro-Epsilon. *eddyNCDT Catalog*. Available: `https://www.micro-epsilon.com/download/products/cat--eddyNCDT--en-us.pdf`. Accessed: 14th July, 2023.

[49] Lion Precision. *ECL202 High-Resolution*, 2019. Available: `https://www.lionprecision.com/wp-content/uploads/2019/04/EddyCurrent-ECL202.pdf`. Accessed: 20th October, 2023.

[50] M. R. Nabavi and S. Nihtianov. Eddy-current sensor interface for advanced industrial applications. *IEEE Transactions on Industrial Electronics*, 58(9):4414–4423, 2010.

[51] M. Pimenta, Ç. Gürleyük, P. Walsh, D. O'Keeffe, M. Babaie, and K. A. A. Makinwa. A 200 µw interface for high-resolution eddy-current displacement sensors. *IEEE Journal of Solid-State Circuits*, 56(4):1036–1045, 2021.

[52] F. Fiorillo. *Characterization and Measurement of Magnetic Materials*. Academic Press, 2004.

[53] H. Wang and Z. Feng. Ultrastable and highly sensitive eddy current displacement sensor using self-temperature compensation. *Sensors and Actuators A: Physical*, 203:362–368, 2013.

[54] P. Sagar, A. S. Gour, and R. Karunanithi. A multilayer planar inductor based proximity sensor operating at 4.2 k. *Sensors and Actuators A: Physical*, 264:151–156, 2017.

[55] M. Martino, A. Danisi, R. Losito, A. Masi, and G. Spiezia. Design of a linear variable differential transformer with high rejection to external interfering magnetic field. *IEEE Transactions on Magnetics*, 46(2):674–677, 2010.

[56] Heidenhain. *Exposed Linear Encoders*, 2014. Available: `https://www.heidenhain.us/lp/encoders/ExposedLinearEncoders.pdf`. Accessed: 14th July, 2023.

[57] K. Miyashita, T. Takahashi, and M. Yamanaka. Features of a magnetic rotary encoder. *IEEE Transactions on Magnetics*, 23(5):2182–2184, 1987.

[58] Y. Kikuchi, F. Nakamura, H. Wakiwaka, H. Yamada, and Y. Yamamoto. Consideration for a high resolution of magnetic rotary encoder. *IEEE Transactions on Magnetics*, 32(5):4959–4961, 1996.

[59] F. Kimura, M. Gondo, N. Yamashita, A. Yamamoto, and T. Higuchi. Capacitive-type flexible linear encoder with untethered slider using electrostatic induction. *IEEE Sensors Journal*, 10(5):972–978, 2010.

[60] M. Kim, W. Moon, E. Yoon, and K.-R. Lee. A new capacitive displacement sensor with high accuracy and long-range. *Sensors and Actuators A: Physical*, 130:135–141, 2006.

[61] F. Paredes, C. Herrojo, and F. Martín. Position sensors for industrial applications based on electromagnetic encoders. *Sensors*, 21(8):2738, 2021.

[62] W. Gao, S.-W. Kim, H. Bosse, H. Haitjema, Y. L. Chen, X. D. Lu, W. Knapp, A. Weckenmann, W. T. Estler, and H. Kunzmann. Measurement technologies for precision positioning. *CIRP annals*, 64(2):773–796, 2015.

[63] T. Oiwa, M. Katsuki, M. Karita, W. Gao, S. Makinouchi, K. Sato, and Y. Oohashi. Questionnaire survey on ultra-precision positioning. *Int. J. Autom. Technol.*, 5(6):766–772, 2011.

[64] J. P. Gardner et al. The James Webb Space Telescope. *Space Science Reviews*, 123:485–606, 2006.

[65] D. A. Naylor, J.-P. Baluteau, M. J. Barlow, D. Benielli, M. Ferlet, T. R. Fulton, M. J. Griffin, T. Grundy, P. Imhof, S. Jones, et al. In-orbit performance of the Herschel/SPIRE imaging Fourier transform spectrometer. In *Space Telescopes and Instrumentation 2010: Optical, Infrared, and Millimeter Wave*, volume 7731, page 773116. SPIE, 2010.

[66] B. M. Swinyard et al. Imaging FTS for Herschel SPIRE. In *IR Space Telescopes and Instruments*, volume 4850, pages 698–709. SPIE, 2003.

[67] Renishaw plc. *L-8003-3193-02 B Data Sheet: HS20 laser head*, 2015. Available: `https://www.renishaw.com/resourcecentre/download?data=78548`. Accessed: 10th August, 2023.

[68] SmarAct. *PICOSCALE Interferometer V2*, 2022. Available: `https://www.smaract.com/files/media/categories/Optical%20Metrology/Spec-Sheets/PS-SS00020_PSV2-SpecSheet.pdf`, Accessed: 10th August, 2023.

[69] Renishaw plc. *L-9904-2352-06-B Data Sheet: RPI20 parallel interface*, 2014. Available: `https://www.renishaw.com/resourcecentre/download?data=64090`. Accessed: 10th August, 2023.

[70] T. Kissinger, T. O. H. Charrett, S. W. James, A. Adams, A. Twin, and R. P. Tatam. Simultaneous laser vibrometry on multiple surfaces with a single beam system using range-resolved interferometry. In *Optical Measurement Systems for Industrial Inspection IX*, volume 9525, pages 470–476. SPIE, 2015.

[71] I. Veenendaal, D. Naylor, B. Gom, T. Fulton, A. Christiansen, W. Jellema, M. Eggens, and P. Ade. A novel design for a cryogenic angle-scanned Fabry-Pérot interferometer. In *Advances in Optical and Mechanical Technologies for Telescopes and Instrumentation III*, volume 10706, page 107061C. SPIE, 2018.

[72] D. Naylor, I. Veenendaal, T. Fulton, B. Gom, A. Christiansen, W. Jellema, C. Feenstra, M. Eggens, and P. Ade. First light results from a novel cryogenic Fabry-Pérot interferometer. In *2019 44th International Conference on Infrared, Millimeter, and Terahertz Waves (IRMMW-THz)*, pages 1–2. IEEE, 2019.

[73] A. Cournoyer, H. Bourque, É. Carbonneau, P. Gilbert, S. Houle, J.-A. Boulet, I. Silversides, F. Grandmont, D. Naylor, B. Gom, A. Christiansen, and M. Buchan. Cryogenic testing and performance characterization of a novel stiffness-compensated, reactionless scan mechanism for a far-infrared post-dispersed polarizing Fourier transform spectrometer. In *Fourier Transform Spectroscopy*, pages FM4B–5. Optica Publishing Group, 2023.

[74] L. D. Spencer, I. T. Veenendaal, D. A. Naylor, B. G. Gom, G. R. H. Sitwell, A. I. Huber, A. Christiansen, et al. Composite material evaluation at cryogenic

temperatures for applications in space-based far-infrared astronomical instrumentation. In *Advances in Optical and Mechanical Technologies for Telescopes and Instrumentation III*, volume 10706, page 107063R. SPIE, 2018.

[75] L. D. Spencer, A. Christiansen, I. T. Veenendaal, S. Gunuganti, D. A. Naylor, B. G. Gom, G. R. H. Sitwell, N. Zobeiry, and A. Poursartip. Evaluation of composite materials at cryogenic temperatures. In *Canadian International Conference on Composite Materials – CANCOM 2019*, 2019.

[76] C. Wang, K. Liu, Z. Ding, J. Jiang, Z. Chen, Y. Feng, Y. Zheng, Q. Liu, and T. Liu. High sensitivity distributed static strain sensing based on differential relative phase in optical frequency domain reflectometry. *Journal of Lightwave Technology*, 38(20):5825–5836, 2020.

[77] D.-P. Zhou, L. Chen, and X. Bao. Distributed dynamic strain measurement using optical frequency-domain reflectometry. *Applied optics*, 55(24):6735–6739, 2016.

[78] J. Peng, Y. Lu, Y. Zhang, and Z. Zhang. Distributed strain and temperature fast measurement in Brillouin optical time-domain reflectometry based on double-sideband modulation. *Optics Express*, 30(2):1511–1520, 2022.

[79] S. Qu, Y. Xu, S. Huang, M. Sun, C. Wang, and Y. Shang. Recent advancements in optical frequency domain reflectometry: a review. *IEEE Sensors Journal*, 2022.

[80] B. Lee. Review of the present status of optical fiber sensors. *Optical Fiber Technology*, 9(2):57–79, 2003.

[81] H. Li, Q. Liu, D. Chen, and Z. He. Centimeter spatial resolution distributed temperature sensor based on polarization-sensitive optical frequency domain reflectometry. *Journal of Lightwave Technology*, 39(8):2594–2602, 2021.

[82] T. F. B. Marie, Y. Bin, H. Dezhi, and A. Bowen. Principle and application state of fully distributed fiber optic vibration detection technology based on Φ-OTDR: a review. *IEEE Sensors Journal*, 21(15):16428–16442, 2021.

[83] C. Ibarra-Castanedo, S. Sfarra, D. Ambrosini, D. Paoletti, A. Bendada, and X. Maldague. Subsurface defect characterization in artworks by quantitative pulsed phase thermography and holographic interferometry. *Quantitative InfraRed Thermography Journal*, 5(2):131–149, 2008.

[84] D. Paoletti, G. S. Spagnolo, M. Facchini, and P. Zanetta. Artwork diagnostics with fiber-optic digital speckle pattern interferometry. *Applied Optics*, 32(31):6236–6241, 1993.

[85] N. Li, C. P. Ho, J. Xue, L. W. Lim, G. Chen, Y. H. Fu, and L. Y. T. Lee. A progress review on solid-state LiDAR and nanophotonics-based LiDAR sensors. *Laser & Photonics Reviews*, 16(11):2100511, 2022.

[86] F. Piron, D. Morrison, M. R. Yuce, and J.-M. Redouté. A review of single-photon avalanche diode time-of-flight imaging sensor arrays. *IEEE Sensors Journal*, 21(11):12654–12666, 2020.

[87] Y. He and S. Chen. Recent advances in 3D data acquisition and processing by time-of-flight camera. *IEEE Access*, 7:12495–12510, 2019.

[88] C. Bamji, J. Godbaz, M. Oh, S. Mehta, A. Payne, S. Ortiz, S. Nagaraja, T. Perry, and B. Thompson. A review of indirect time-of-flight technologies. *IEEE Transactions on Electron Devices*, 69(6):2779–2793, 2022.

[89] I. Gyongy, N. A. W. Dutton, and R. K. Henderson. Direct time-of-flight single-photon imaging. *IEEE Transactions on Electron Devices*, 69(6):2794–2805, 2021.

[90] L. Li. Time-of-flight camera - an introduction. Technical white paper SLOA190B, 2014.

[91] H. Sarbolandi, M. Plack, and A. Kolb. Pulse based time-of-flight range sensing. *Sensors*, 18(6):1679, 2018.

[92] K. Yasutomi and S. Kawahito. Lock-in pixel based time-of-flight range imagers: an overview. *IEICE Transactions on Electronics*, 105(7):301–315, 2022.

[93] A. Kilpelä, R. Pennala, and J. Kostamovaara. Precise pulsed time-of-flight laser range finder for industrial distance measurements. *Review of Scientific Instruments*, 72(4):2197–2202, 2001.

[94] Y. Liang, J. Huang, M. Ren, B. Feng, X. Chen, E. Wu, G. Wu, and H. Zeng. 1550-nm time-of-flight ranging system employing laser with multiple repetition rates for reducing the range ambiguity. *Optics Express*, 22(4):4662–4670, 2014.

[95] R. E. Warburton, A. McCarthy, A. M. Wallace, S. Hernandez-Marin, R. H. Hadfield, S. W. Nam, and G. S. Buller. Subcentimeter depth resolution using a single-photon counting time-of-flight laser ranging system at 1550 nm wavelength. *Optics letters*, 32(15):2266–2268, 2007.

[96] P. A. Hiskett, C. S. Parry, A. McCarthy, and G. S. Buller. A photon-counting time-of-flight ranging technique developed for the avoidance of range ambiguity at gigahertz clock rates. *Optics Express*, 16(18):13685–13698, 2008.

[97] S. Cova, A. Longoni, and A. Andreoni. Towards picosecond resolution with single-photon avalanche diodes. *Review of Scientific Instruments*, 52(3):408–412, 1981.

[98] J. Lee, Y.-J. Kim, K. Lee, S. Lee, and S.-W. Kim. Time-of-flight measurement with femtosecond light pulses. *Nature Photonics*, 4(10):716–720, 2010.

[99] J. Lee, K. Lee, S. Lee, S.-W. Kim, and Y.-J. Kim. High precision laser ranging by time-of-flight measurement of femtosecond pulses. *Measurement Science and Technology*, 23(6):065203, 2012.

[100] D. Bastos, P. P. Monteiro, A. S. R. Oliveira, and M. V. Drummond. An overview of LiDAR requirements and techniques for autonomous driving. In *2021 Telecoms Conference (ConfTELE)*, pages 1–6. IEEE, 2021.

[101] M. Khader and S. Cherian. An introduction to automotive LiDAR. Technical report, Texas Instruments, 2020.

[102] S. Lee, K. Yasutomi, M. Morita, H. Kawanishi, and S. Kawahito. A time-of-flight range sensor using four-tap lock-in pixels with high near infrared sensitivity for LiDAR applications. *Sensors*, 20(1):116, 2019.

[103] A. R. Ximenes, P. Padmanabhan, M.-J. Lee, Y. Yamashita, D.-N. Yaung, and E. Charbon. A modular, direct time-of-flight depth sensor in 45/65-nm 3-d-stacked CMOS technology. *IEEE Journal of Solid-State Circuits*, 54(11):3203–3214, 2019.

[104] M. Perenzoni, D. Perenzoni, D. Stoppa, A. Pollini, J. Haesler, and C. Pache. 3D imaging with CMOS single-photon detector arrays for space applications: ground-based measurements and irradiation tests. In *Proc. Int. Image Sensor Workshop*, pages 262–265, 2017.

[105] M. Perenzoni, D. Perenzoni, and D. Stoppa. A 64×64-pixels digital silicon photomultiplier direct TOF sensor with 100-Mphotons/s/pixel background rejection and imaging/altimeter mode with 0.14% precision up to 6 km for spacecraft navigation and landing. *IEEE Journal of Solid-State Circuits*, 52(1):151–160, 2016.

[106] J. Brooks and D. Faccio. A single-shot non-line-of-sight range-finder. *Sensors*, 19(21):4820, 2019.

[107] J. H. Nam, E. Brandt, S. Bauer, X. Liu, M. Renna, A. Tosi, E. Sifakis, and A. Velten. Low-latency time-of-flight non-line-of-sight imaging at 5 frames per second. *Nature Communications*, 12(1):6526, 2021.

[108] M. Horio, Y. Feng, T. Kokado, T. Takasawa, K. Yasutomi, S. Kawahito, T. Komuro, H. Nagahara, and K. Kagawa. Resolving multi-path interference in compressive time-of-flight depth imaging with a multi-tap macro-pixel computational CMOS image sensor. *Sensors*, 22(7):2442, 2022.

[109] N. A. W. Dutton, L. Parmesan, S. Gnecchi, I. Gyongy, N. Calder, B. R. Rae, L. A. Grant, and R. K. Henderson. Oversampled ITOF imaging techniques using SPAD-based quanta image sensors. In *Proc. Int. Image Sensor Workshop*, pages 170–173, 2015.

[110] D. Stoppa, L. Viarani, A. Simoni, L. Gonzo, and M. Malfatti. A new architecture for TOF-based range-finding sensor. In *IEEE Sensors Journal*, pages 481–484. IEEE, 2004.

[111] V. S. Damian, M. Bojan, P. Schiopu, I. Iordache, B. Ionita, and D. Apostol. White light interferometry applications in nanometrology. In *Advanced Topics in Optoelectronics, Microelectronics, and Nanotechnologies IV*, volume 7297, pages 275–278. SPIE, 2009.

[112] G. Zhang, S. Yang, J. Fluegge, and H. Bosse. Fiber optic white light interferometer for areal surface measurement. *Measurement Science and Technology*, 31(2):025005, 2019.

[113] J. C. Wyant. White light interferometry. In *Holography: A Tribute to Yuri Denisyuk and Emmett Leith*, volume 4737, pages 98–107. SPIE, 2002.

[114] J. M. Schmitt. Optical coherence tomography (OCT): a review. *IEEE Journal of Selected Topics in Quantum Electronics*, 5(4):1205–1215, 1999.

[115] Y.-J. Rao and D. A. Jackson. Recent progress in fibre optic low-coherence interferometry. *Measurement Science and Technology*, 7(7):981, 1996.

[116] E. A. Swanson, D. Huang, M. R. Hee, J. G. Fujimoto, C. P. Lin, and C. A. Puliafito. High-speed optical coherence domain reflectometry. *Optics letters*, 17(2):151–153, 1992.

[117] R. C. Youngquist, S. Carr, and D. E. N. Davies. Optical coherence-domain reflectometry: a new optical evaluation technique. *Optics Letters*, 12(3):158–160, 1987.

[118] J. F. Bille. *High resolution imaging in microscopy and ophthalmology: new frontiers in biomedical optics*. Springer, 2019.

[119] X. Shu, L. Beckmann, and H. F. Zhang. Visible-light optical coherence tomography: a review. *Journal of Biomedical Optics*, 22(12):121707–121707, 2017.

[120] A. M. Zysk, F. T. Nguyen, A. L. Oldenburg, D. L. Marks, and S. A. Boppart. Optical coherence tomography: a review of clinical development from bench to bedside. *Journal of Biomedical Optics*, 12(5):051403–051403, 2007.

[121] A. F. Fercher. Optical coherence tomography. *Journal of Biomedical Optics*, 1(2):157–173, 1996.

[122] J. Scholler, D. Mandache, M. C. Mathieu, A. B. Lakhdar, M. Darche, T. Monfort, C. Boccara, et al. Automatic diagnosis and classification of breast surgical samples with dynamic full-field OCT and machine learning. *Journal of Medical Imaging*, 10(3):034504–034504, 2023.

[123] F. Liu, G. Liu, Q. Zhao, and L. Shen. Robust and high-security fingerprint recognition system using optical coherence tomography. *Neurocomputing*, 402:14–28, 2020.

[124] F. Liu, G. Liu, and X. Wang. High-accurate and robust fingerprint anti-spoofing system using optical coherence tomography. *Expert Systems with Applications*, 130:31–44, 2019.

[125] A. Dubois, O. Levecq, H. Azimani, A. Davis, J. Ogien, D. Siret, and A. Barut. Line-field confocal time-domain optical coherence tomography with dynamic focusing. *Optics Express*, 26(26):33534–33542, 2018.

[126] K. Li, Z. Yang, W. Liang, J. Shang, Y. Liang, and S. Wan. Low-cost, ultracompact handheld optical coherence tomography probe for in vivo oral maxillofacial tissue imaging. *Journal of Biomedical Optics*, 25(4):046003–046003, 2020.

[127] H. Kakuma, K. Ohbayashi, and Y. Arakawa. Optical imaging of hard and soft dental tissues using discretely swept optical frequency domain reflectometry optical coherence tomography at wavelengths from 1560 to 1600 nm. *Journal of Biomedical Optics*, 13(1):014012–014012, 2008.

[128] K. Hotate and O. Kamatani. Optical coherence domain reflectometry by synthesis of coherence function. *Journal of Lightwave Technology*, 11(10):1701–1710, 1993.

[129] Y. Xue, Y. Niu, and S. Gong. External modulation optical coherent domain reflectometry with long measurement range. *Sensors*, 21(16):5510, 2021.

[130] M. Kashiwagi and K. Hotate. Long range and high resolution reflectometry by synthesis of optical coherence function at region beyond the coherence length. *IEICE Electronics Express*, 6(8):497–503, 2009.

[131] Y. Mizuno, Z. He, and K. Hotate. Enlargement of measurement range of Brillouin optical correlation-domain reflectometry based on temporal gating scheme. In *2008 34th European Conference on Optical Communication*, pages 1–2. IEEE, 2008.

[132] Y. Mizuno, Z. He, and K. Hotate. Measurement range enlargement in Brillouin optical correlation-domain reflectometry based on double-modulation scheme. *Optics Express*, 18(6):5926–5933, 2010.

[133] Z. He, T. Tomizawa, and K. Hotate. High-speed high-reflectance-resolution reflectometry by synthesis of optical coherence function. *IEICE Electronics Express*, 3(7):122–128, 2006.

[134] T. Saida and K. Hotate. High-spatial resolution reflectometry by synthesis of optical coherence function for measuring reflectivity distribution at a long distance. *IEEE Photonics Technology Letters*, 10(4):573–575, 1998.

[135] S. Liu, F. Yu, R. Hong, W. Xu, L. Shao, and F. Wang. Advances in phase-sensitive optical time-domain reflectometry. *Opto-Electronic Advances*, 5(3):200078–1, 2022.

[136] X. Bao and Y. Wang. Recent advancements in Rayleigh scattering-based distributed fiber sensors. *Advanced Devices & Instrumentation*, 2021, 2021.

[137] R. Davis. A short story on length. *Nature Physics*, 14(8):868–868, 2018.

[138] W. B. Penzes. Time line for the definition of the meter. Retrieved 16th October, 2002 from the National Institute of Standards and Technology. Available: `http://www.mel.nist.gov/div821/museum/timeline.htm`. Accessed: 14th August, 2023.

[139] P. Giacomo. The Michelson interferometer. *Microchimica Acta*, 93:19–31, 1987.

[140] K. Burns and K. B. Adams. Energy levels and wavelengths of natural cadmium and of cadmium-114. *JOSA*, 46(2):94–99, 1956.

[141] P. Gregorčič, T. Požar, and J. Možina. Quadrature phase-shift error analysis using a homodyne laser interferometer. *Optics express*, 17(18):16322–16331, 2009.

[142] T. Požar and J. Možina. Enhanced ellipse fitting in a two-detector homodyne quadrature laser interferometer. *Measurement Science and Technology*, 22(8):085301, 2011.

[143] T. Požar, P. Gregorčič, and J. Možina. Optical measurements of the laser-induced ultrasonic waves on moving objects. *Optics Express*, 17(25):22906–22911, 2009.

[144] T. Požar, P. Gregorčič, and J. Možina. A precise and wide-dynamic-range displacement-measuring homodyne quadrature laser interferometer. *Applied Physics B*, 105:575–582, 2011.

[145] M. Pisani. A homodyne michelson interferometer with sub-picometer resolution. *Measurement Science and Technology*, 20(8):084008, 2009.

[146] R. Fuest, N. Fabricius, U. Hollenbach, and B. Wolf. Interferometric displacement sensor realized with a planar 3×3 directional coupler in glass. In *Integrated Optical Circuits II*, volume 1794, pages 352–365. SPIE, 1993.

[147] D. Stowe and T.-Y. Hsu. Demodulation of interferometric sensors using a fiber-optic passive quadrature demodulator. *Journal of Lightwave Technology*, 1(3):519–523, 1983.

[148] A. J. Christiansen, D. A. Naylor, I. T. Veenendaal, and B. G. Gom. A frequency-modulated laser interferometer for nanometer-scale position sensing at cryogenic temperatures. In *Photonic Instrumentation Engineering VI*, volume 10925, page 1092514. SPIE, 2019.

[149] D. T. Smith, J. R. Pratt, and L. P. Howard. A fiber-optic interferometer with subpicometer resolution for dc and low-frequency displacement measurement. *Review of Scientific Instruments*, 80(3), 2009.

[150] A. J. Sutton, O. Gerberding, G. Heinzel, and D. A. Shaddock. Digitally enhanced homodyne interferometry. *Optics express*, 20(20):22195–22207, 2012.

[151] P. Z. Peebles Jr. *Digital Communication Systems*. Prentice Hall, 1987.

[152] C. Polhemus. Two-wavelength interferometry. *Applied Optics*, 12(9):2071–2074, 1973.

[153] T. Lagadec, M. Ireland, J. Hansen, J. Mathew, T. Travouillon, and S. Madden. Compact unambiguous differential path-length metrology with dispersed Fabry-Perot laser diodes for a space interferometer array. In *Optical and Infrared Interferometry and Imaging VII*, volume 11446, pages 549–556. SPIE, 2020.

[154] K. Thurner, P.-F. Braun, and K. Karrai. Absolute distance sensing by two laser optical interferometry. *Review of Scientific Instruments*, 84(11), 2013.

[155] D. Lin, X. Jiang, F. Xie, W. Zhang, L. Zhang, and I. Bennion. High stability multiplexed fibre interferometer and its application on absolute displacement measurement and on-line surface metrology. *Optics Express*, 12(23):5729–5734, 2004.

[156] Y. Zhang and F. Guzman. Fiber-based two-wavelength heterodyne laser interferometer. *Optics Express*, 30(21):37993–38008, 2022.

[157] Y. Zhang, K.-N. Joo, and F. Guzman. Fiber-based two-wavelength heterodyne displacement interferometer. In *Photonic Instrumentation Engineering IX*, volume 12008, pages 179–184. SPIE, 2022.

[158] G. de Vine, D. S. Rabeling, B. J. J. Slagmolen, T. T.-Y. Lam, S. Chua, D. M. Wuchenich, D. E. McClelland, and D. A. Shaddock. Picometer level displacement metrology with digitally enhanced heterodyne interferometry. *Optics Express*, 17(2):828–837, 2009.

[159] T. Kissinger, T. O. H. Charrett, and R. P. Tatam. Fibre segment interferometry using code-division multiplexed optical signal processing for strain sensing applications. *Measurement Science and Technology*, 24(9):094011, 2013.

[160] G. Shi, K. Hei, W. Wang, and N. Bhattacharya. Frequency-modulated continuous-wave laser distance measurement system using Fabry-Perot cavity as measuring reference, arXiv:1901.01131 [physics.ins-det], 2019.

[161] I. Kim, R. J. Martins, J. Jang, T. Badloe, S. Khadir, H.-Y. Jung, H. Kim, J. Kim, P. Genevet, and J. Rho. Nanophotonics for light detection and ranging technology. *Nature Nanotechnology*, 16(5):508–524, 2021.

[162] J. Zheng. Analysis of optical frequency-modulated continuous-wave interference. *Applied Optics*, 43(21):4189–4198, 2004.

[163] G. Shi, F. Zhang, X. Qu, and X. Meng. High-resolution frequency-modulated continuous-wave laser ranging for precision distance metrology applications. *Optical Engineering*, 53(12):122402–122402, 2014.

[164] H. Jang, J. W. Kim, G. H. Kim, C. H. Park, S. W. Jun, M. Jo, H. Lee, and C.-S. Kim. Simultaneous distance and vibration mapping of FMCW-LiDAR with akinetic external cavity diode laser. *Optics and Lasers in Engineering*, 160:107283, 2023.

[165] I. Sakai, R. Youngquist, and G. Parry. Multiplexing of optical fiber sensors using a frequency-modulated source and gated output. *Journal of Lightwave Technology*, 5(7):932–940, 1987.

[166] T. Kissinger, T. O. H. Charrett, and R. P. Tatam. Range-resolved interferometric signal processing using sinusoidal optical frequency modulation. *Optics Express*, 23(7):9415–9431, 2015.

[167] attocube - Your partner in nanoscale applications. `https://www.attocube.com`. Accessed: 10th August, 2023.

[168] Attocube. *Displacement Measuring Interferometer*. Available: `https://www.attocube.com/downloads/displacement-measuring-interferometer.pdf`, Accessed: 10th August, 2023.

[169] M. Mathéus, K. v. Grafenstein, , and C. Schäfermeier. Metrology aspects of the IDS3010. Technical Report Technical Note 19, Attocube, 2018. Available: `https://marketing.attocube.com/acton/attachment/4434/f-b921924c-962e-4df9-9fa5-bdad73dd813d/0/-/-/-/-/TN19%20MetrologyAspectsIDS.pdf`, Accessed: 9th October, 2023.

[170] High Precision Positioning, Automation and Metrology Solutions - SmarAct. `https://www.smaract.com`. Accessed: 10th August, 2023.

[171] Key Features of the PICOSCALE Interferometer - SmarAct. `https://www.smaract.com/picoscale-interferometer`. Accessed: 10th August, 2023.

[172] Advantages of Michelson interferometers - SmarAct. `https://www.smaract.com/en/advantages-of-michelson-interferometers`. Accessed: 10th August, 2023.

[173] ZYGO | Precision Optical Metrology | Optical Components. `https://www.zygo.com`. Accessed: 10th August, 2023.

[174] Zygo. *ZMI Differential Plane Interferometer (DPMI)*, 2022. Available: `https://www.zygo.com/products/nano-position-sensors/displacement-measuring-interferometers/4462ed6f-2f25-464b-84de-e15ee88b876c`, Accessed: 10th August, 2023.

[175] Zygo. *ZMI Compact 3-Axis HSPMI*, 2022. Available: https://www.zygo.com/products/nano-position-sensors/displacement-measuring-interferometers/89212f5f-8e43-4b99-ada6-639e815d8960, Accessed: 10th August, 2023.

[176] Zygo. *ZMI 4104 Measurement Board*, 2022. Available: https://www.zygo.com/products/nano-position-sensors/displacement-measuring-interferometers/f5dd393a-0c24-41dd-aca8-e3a596aeee16, Accessed: 10th August, 2023.

[177] Renishaw: enhancing efficiency in manufacturing and healthcare. https://www.renishaw.com. Accessed: 10th August, 23.

[178] Renishaw plc. *L-9904-2348-05-A Data Sheet: RLD10 0° laser unit*, 2017. Available: https://resources.renishaw.com/download.aspx?data=93260. Accessed: 10th August, 2023.

[179] Renishaw plc. *L-9904-2346-05-B Data Sheet: RLU10 laser unit*, 2014. Available: https://resources.renishaw.com/download.aspx?data=64093. Accessed: 10th August, 2023.

[180] D. Naylor, I. Veenendaal, B. Gom, and A. Christiansen. A fiber-fed laser interferometer for optical metrology at cryogenic temperatures. In *Photonic Instrumentation Engineering V*, volume 10539, page 105390T. SPIE, 2018.

[181] E. Clarke. *Circuit analysis of A-C power systems: symmetrical and related components*, volume 1. Wiley, 1943.

[182] Maryland State Archives. Edith Clarke, MSA SC 3520-14065. https://msa.maryland.gov/megafile/msa/speccol/sc3500/sc3520/014000/014065/html/14065bio.html, 2006. Accessed: 7th June, 2023.

[183] National Inventors Hall of Fame. Edith Clarke. https://www.invent.org/inductees/edith-clarke. Accessed: 7th June, 2023.

[184] Newport. *Photonics Technical Note #25: Fiber Optics: How Fused Fiber Optic Couplers Work*, 2013. Available: https://www.newport.com/medias/sys_master/images/images/h86/hb2/8797287088158/Tech-Note-26-How-Fused-Fiber-Optic-Couplers-Work.pdf. Accessed: 7th June, 2023.

[185] T. Kissinger. *Range-Resolved Optical Interferometric Signal Processing*. PhD thesis, Cranfield University, 2015.

[186] Eblana Photonics Ltd. *EP1550-NLW-B-100 Datasheet*, 2020. Rev. 2.3. Available: https://eblanaphotonics.com/products/1550-nlw. Accessed: 5th April, 2023.

[187] Klaus Petermann. *Laser Diode Modulation and Noise*, volume 3. Kluwer Academic Publishers, 1988.

[188] A. Nuttall. Some windows with very good sidelobe behavior. *IEEE Transactions on Acoustics, Speech, and Signal Processing*, 29(1):84–91, 1981.

[189] G. Woan. *The Cambridge Handbook of Physics Formulas*. Cambridge University Press, 2003 edition, 2000.

[190] R. Lyons. Windowing functions improve FFT results, Part 1. *Test and Measurement World*, 18(7):37–46, 1998.

[191] N. Guo, C. Gao, M. Xue, L. Niu, S. Zhu, L. Feng, H. He, and Z. Cao. Ranging method based on linear frequency modulated laser. *Laser Physics*, 27(6):065108, 2017.

[192] K. Kou, C. Wang, and Y. Liu. All-phase FFT based distance measurement in laser self-mixing interferometry. *Optics and Lasers in Engineering*, 142:106611, 2021.

[193] F. Cavedo, P. Esmaili, and M. Norgia. Self-mixing laser distance-sensor enhanced by multiple modulation waveforms. *Sensors*, 22(21):8456, 2022.

[194] Y.-S. Huang and K.-H. Lu. Formulation of the classical and the relativistic Doppler effect by a systematic method. *Canadian Journal of Physics*, 82(11):957–964, 2004.

[195] F. Zhang, L. Yi, and X. Qu. Simultaneous measurements of velocity and distance via a dual-path FMCW lidar system. *Optics Communications*, 474:126066, 2020.

[196] Y. Li and J. Ibanez-Guzman. LiDAR for autonomous driving: the principles, challenges, and trends for automotive LiDAR and perception systems. *IEEE Signal Processing Magazine*, 37(4):50–61, 2020.

[197] H. Holzhüter, J. Bödewadt, S. Bayesteh, A. Aschinger, and H. Blume. Technical concepts of automotive LiDAR sensors: a review. *Optical Engineering*, 62(3):031213, 2023.

[198] T. Raj, F. H. Hashim, A. H. Baseri, M. F. Ibrahim, and A. Hussain. A survey on LiDAR scanning mechanisms. *Electronics*, 9(5):741, 2020.

[199] D. Wang, C. Watkins, and H. Xie. MEMS mirrors for LiDAR: a review. *Micromachines*, 11(5):456, 2020.

[200] G. Economou, R. Youngquist, and D. Davies. Limitations and noise in interferometric systems using frequency ramped single-mode diode lasers. *Journal of Lightwave Technology*, 4(11):1601–1608, 1986.

[201] Xilinx, Inc. *Zynq-7000 SoC Data Sheet: Overview*, 2018. Ver. 1.11.1. Available: `https://www.xilinx.com/content/dam/xilinx/support/documents/data_sheets/ds190-Zynq-7000-Overview.pdf`. Accessed: 10$^{\text{th}}$ May, 2023.

[202] Digilent Inc. *Eclypse Z7 Hardware Reference Manual*. Available: `https://digilent.com/reference/programmable-logic/eclypse-z7/reference-manual`. Accessed: 6th March, 2023.

[203] Opal Kelly Incorporated. *SYZYGY Specification*, 2019. Ver. 1.1. Available: `https://syzygyfpga.io/specification`. Accessed: 10th May, 2023.

[204] Digilent Inc. *Zmod AWG Reference Manual*. Available: `https://digilent.com/reference/zmod/awg/reference-manual`. Accessed: 6th March, 2023.

[205] Digilent Inc. *Zmod Scope Reference Manual*. Available: `https://digilent.com/reference/zmod/scope/reference-manual`. Accessed: 6th March, 2023.

[206] R. Phelan, B. Kelly, D. Jones, C. Herbert, J. O'Carroll, M. Rensing, B. Cai, A. Kaszubowska-Anandarajah, P. Perry, J. Stopford, P. Anandarajah, L. P. Barry, and J. O'Gorman. Discrete mode laser diodes with ultra narrow linewidth emission <3 kHz. In *Optical Fiber Communication Conference*, page OThK5. Optical Society of America, 2008.

[207] Koheron. *Digital butterfly laser diode controller*. Available: `https://www.koheron.com/photonics/ctl200-digital-laser-controller`. Accessed: 6th March, 2023.

[208] Thorlabs, Inc. *6015-3-APC Fiber Optic Circulator,* 1525–1610 nm*, SMF, FC/APC*, 2023. Rev. D. Available: `https://www.thorlabs.com/thorproduct.cfm?partnumber=6015-3-APC`. Accessed: 6th March, 2023.

[209] Thorlabs, Inc. *FGA01FC InGaAs Photodiode,* 300 ps *Rise Time,* 800–1700 nm*,* ⌀0.12 mm *Active Area, FC/PC Bulkhead*, 2016. Rev. D. Available: `https://www.thorlabs.com/thorproduct.cfm?partnumber=FGA01FC`. Accessed: 6th March, 2023.

[210] Analog Devices, Inc. *AD8009 Datasheet*, 2004. Rev. F. Available: `https://www.analog.com/en/products/ad8009.html`. Accessed: 27th March, 2023.

[211] Analog Devices, Inc. *LTSpice*. Available: `https://www.analog.com/en/design-center/design-tools-and-calculators/ltspice-simulator.html`. Accessed: 5th April, 2023.

[212] Real Time Engineers Ltd. *The FreeRTOS Reference Manual*, 2017. Ver. 10.0.0. Available: `https://freertos.org/Documentation/RTOS_book.html`. Accessed: 10th May, 2023.

[213] N. D. Matsakis and F. S. Klock II. The Rust language. *ACM SIGAda Ada Letters*, 34(3):103–104, 2014.

[214] G. van Rossum and F. L. Drake. *Python 3 Reference Manual*. CreateSpace, Scotts Valley, CA, 2009.

[215] PyO3 Project and Contributors. PyO3. Available: https://github.com/PyO3/pyo3. Accessed: 1st August, 2023.

[216] C. R. Harris et al. Array programming with NumPy. *Nature*, 585(7825):357–362, 2020.

[217] J. S. Steinhart and S. R. Hart. Calibration curves for thermistors. In *Deep Sea Research and Oceanographic Abstracts*, volume 15, pages 497–503. Elsevier, 1968.

[218] ILX Lightwave. *Application Note #4: Thermistor Calibration and the Steinhart-Hart Equation*, 2006. Rev. 03.071709. Available: https://www.newport.com/medias/sys_master/images/images/h67/hc1/8797049487390/AN04-Thermistor-Calibration-and-Steinhart-Hart.pdf. Accessed: 10th May, 2023.

[219] Keysight Technologies. *Keysight Technologies N7744A 4-Channel Optical Multiport Power Meter Datasheet*, 2017. Available: https://www.keysight.com/us/en/support/N7744A/optical-multiport-power-meter-4-sensor-ports.html. Accessed: 10th May, 2023.

[220] EXFO Electro-Optical Engineering Inc. *EXFO WA-1000/WA-1500 Wavemeter*, 2006. Available: https://www.exfo.com/en/discontinued-products/wa-1500-and-wa-1000-wavemeter. Accessed: 1st April, 2023.

[221] J. R. Minch, F. G. Walther, S. J. Savage, A. Plante, and V. Scalesse. Frequency stabilization of laser diodes in an aggressive thermal environment. In *Free-Space Laser Communication and Atmospheric Propagation XXVII*, volume 9354, page 93540T. SPIE, SPIE, 2015.

[222] F. Benabid, F. Couny, J. C. Knight, T. A. Birks, and P. St. J. Russell. Compact, stable and efficient all-fibre gas cells using hollow-core photonic crystal fibres. *Nature*, 434(7032):488–491, 2005.

[223] P. Meras Jr., I. Y. Poberezhskiy, D. H. Chang, J. Levin, and G. D. Spiers. Laser frequency stabilization for coherent LiDAR applications using novel all-fiber gas reference cell fabrication technique. 2008.

[224] A. Dandridge and L. Goldberg. Current-induced frequency modulation in diode lasers. *Electronics Letters*, 18(7):302–304, 1982.

[225] Xilinx, Inc. *CORDIC v6.0 LogiCORE IP Product Guide*, 2021. Ver. 6.0. Available: https://docs.xilinx.com/v/u/en-US/pg105-cordic. Accessed: 20th October, 2023.

[226] J. E. Volder. The CORDIC trigonometric computing technique. *IRE Transactions on Electronic Computers*, (3):330–334, 1959.

[227] C.-C. Tseng and S.-C. Pei. Design of discrete-time fractional Hilbert transformer. In *2000 IEEE International Symposium on Circuits and Systems (ISCAS)*, volume 5, pages 525–528. IEEE, 2000.

[228] S. C. Kak. The discrete Hilbert transform. *Proceedings of the IEEE*, 58(4):585–586, 1970.

[229] Thorlabs, Inc. *SMF-28-J9 SMF-28 Ultra with ⌀900 µm Jacket, ⌀125 µm Cladding*, 2015. Rev. H. Available: `https://www.thorlabs.com/thorproduct.cfm?partnumber=SMF-28-J9`. Accessed: 23rd March, 2023.

[230] Thorlabs, Inc. *30126A9 FC/APC Single Mode Connector, ⌀126 µm Bore, Ceramic Ferrule, ⌀900 µm Boot*, 2012. Rev. A. Available: `https://www.thorlabs.com/thorproduct.cfm?partnumber=30126A9`. Accessed: 23rd March, 2023.

[231] International Telecommunication Union. *G.652: Characteristics of a single-mode optical fibre and cable*, 2016. Rev. G.652 (11/16). Available: `https://www.itu.int/rec/T-REC-G.652/en`. Accessed: 10th May, 2023.

[232] Thorlabs, Inc. *NRS913A Polishing Pad for PC Finishes, 8.75 × 13", 50 Durometer*, 2016. Rev. B. Available: `https://www.thorlabs.com/thorproduct.cfm?partnumber=NRS913A`. Accessed: 23rd March, 2023.

[233] Thorlabs, Inc. *30126C9 FC/PC Single Mode Connector, ⌀126 µm Bore, Ceramic Ferrule, ⌀900 µm Boot*, 2012. Rev. A. Available: `https://www.thorlabs.com/thorproduct.cfm?partnumber=30126C9`. Accessed: 23rd March, 2023.

[234] Thorlabs, Inc. *FS201 Fiber Inspection Scope with FS201-FC and FS201-SMA Adapters*, 2018. Rev. B. Available: `https://www.thorlabs.com/thorproduct.cfm?partnumber=FS201`. Accessed: 23rd March, 2023.

[235] Inno Instrument Inc. *INNO View 7 User Manual*, 2016. Rev. 1.11. Available: `https://www.innoinstrument.eu/en/fusion-splicer/devices/VIEW7`. Accessed: 1st August, 2023.

[236] G. Vasilescu. *Electronic Noise and Interfering Signals: Principles and Applications*. Springer Science & Business Media, 2005.

[237] Wavelength References. *Hydrogen cyanide fiber coupled gas cell for remote optical gas sensor and calibration C-band*, 2020. Available: `https://www.wavelengthreferences.com/wp-content/uploads/Data-HCN.pdf`. Accessed: 22nd October, 2023.

[238] Koheron. 100 MHz *balanced photodetector*. Available: `https://www.koheron.com/photonics/pd100b-photodetection`. Accessed: 22nd October, 2023.

[239] Koheron. 100 MHz *balanced photodetector*. Available: `https://www.koheron.com/photonics/pi200-laser-servo-controller`. Accessed: 22nd October, 2023.

[240] S. L. Gilbert, W. C. Swann, and C.-M. Wang. Hydrogen cyanide $H^{13}C^{14}N$ absorption reference for 1530 nm to 1565 nm wavelength calibration – SRM 2519a. *NIST Special Publication*, 260:137, 2005.

[241] Optical Fiber Cable and Connectivity Solutions - OFS. https://www.ofsoptics.com. Accessed: 22nd September, 2023.

[242] Blue Sky Spectroscopy Inc. https://blueskyspectroscopy.com. Accessed: 3rd October, 2023.

[243] A. J. Christiansen, M. Popelka, B. G. Gom, D. A. Naylor, and A. A. Stolov. Characterization of optical fiber at cryogenic temperatures. In *Optical Components and Materials XX*, volume 12417, pages 158–166. SPIE, 2023.

[244] S. R. Schmid, A. F. Toussaint, A. Mendez, and T. F. Morse. Optical fiber coatings. *Specialty Optical Fibers Handbook*, pages 95–122, 2007.

[245] M. Popelka, A. A. Stolov, A. S. Hokansson, J. Li, and M. J. Hines. A new polyimide coating for optical fibers: demonstration of advantageous characteristics in harsh environments. In Shibin Jiang and Michel J. F. Digonnet, editors, *Optical Components and Materials XIX*, volume 11997, page 119970J. SPIE, SPIE, 2022.

[246] OFS Fitel, LLC. *AllWave Optical Fiber - Zero Water Peak Datasheet*, 2017. Available: https://fiber-optic-catalog.ofsoptics.com/documents/pdf/AllWave-117-web.pdf. Accessed: 31st March, 2023.

[247] OFS Fitel, LLC. *ClearLite POLY P2 1310 11 NA Optical Fiber Datasheet*, 2020. Available: https://fiber-optic-catalog.ofsoptics.com/documents/pdf/BF05717-01-ClearLite-POLY-P2-1310-11-NA-Optical-Fiber-web.pdf. Accessed: 31st March, 2023.

[248] L. G. Baikova, T. I. Pesina, M. F. Kireenko, L. V. Tikhonova, and C. R. Kurkjian. Strength of optical silica fibers measured in liquid nitrogen. *Technical Physics*, 60:869–872, 2015.

[249] Lake Shore Cryotronics, Inc. *Cernox*. Available: https://www.lakeshore.com/products/categories/overview/temperature-products/cryogenic-temperature-sensors/cernox. Accessed: 4th April, 2023.

[250] Two-Point Bend. https://www.fibersigma.com/two-point_bend.htm. Accessed: 22nd September, 2023.

[251] M. J. Matthewson, C. R. Kurkjian, and S. T. Gulati. Strength measurement of optical fibers by bending. *Journal of the American Ceramic Society*, 69(11):815–821, 1986.

[252] C. R. Kurkjian and M. J. Matthewson. Mechanical strength and reliability of glass fibers. *Specialty Optical Fibers Handbook*, pages 735–781, 2007.

[253] F. C. Allard. *Fiber Optics Handbook for Engineers and Scientists*. McGraw-Hill Companies, 1990.

[254] A. A. Stolov, B. E. Slyman, D. A. Simoff, A. S. Hokansson, R. S. Allen, and J. P. Earnhardt. Optical fibers with polyimide coatings for medical applications. In *Design and Quality for Biomedical Technologies V*, volume 8215, pages 55–64. SPIE, 2012.

[255] Y.-S. Shiue and M. J. Matthewson. Mechanical reliability of silica optical fiber: a case study for a biomedical application. In *Optical Fiber Reliability and Testing*, volume 3848, pages 115–123. SPIE, 1999.

[256] G. Ramer and B. Lendl. Attenuated total reflection Fourier transform infrared spectroscopy. *Encyclopedia of Analytical Chemistry*, 2006.

[257] F. M. Mirabella. Principles, theory, and practice of internal reflection spectroscopy. *Internal Reflection Spectroscopy: Theory and Applications*, pages 17–52, 1993.

[258] Thermo Fisher Scientific Inc. *Nicolet iS50 FTIR Spectrometer*, 2001. Available: `https://www.thermofisher.com/order/catalog/product/912A0760`. Accessed: 3rd April, 2023.

[259] TA Instruments. *TA Instruments Thermogravimetric Analyzers*, 2001. Rev. F. Available: `https://www.tainstruments.com/pdf/literature/OLD_tgabrochure.pdf`. Accessed: 3rd April, 2023.

[260] Furukawa Electric Co., Ltd. *Data Sheet FRL15DCWx-A8x-xxxxx-x*, 2016. Available: `https://www.furukawa.co.jp/fitel/english/active/signal.htm`. Accessed: 23rd September, 2023.

[261] Thorlabs, Inc. *TN1550R5A2* 2×2 *Narrowband Fiber Optic Coupler,* (1550 ± 15) nm*, 50:50 Split, FC/APC Connectors*, 2018. Rev. B. Available: `https://www.thorlabs.com/thorproduct.cfm?partnumber=TN1550R5A2`. Accessed: 28th September, 2023.

[262] R. Lingle, D. Peckham, A.H. McCurdy, and J. Kim. Light-guiding fundamentals and fiber design. *Specialty Optical Fibers Handbook*, pages 19–68, 2007.

[263] AZoM. *Silica – Fused Silica (Silicon Dioxide)*. Available: `https://www.azom.com/properties.aspx?ArticleID=1387`. Accessed: 8th September, 2023.

[264] Thorlabs, Inc. *ADAFC3 FC/APC to FC/APC Mating Sleeve, Narrow Key (*2.0 mm*), Square Flange*, 2022. Rev. E. Available: `https://www.thorlabs.com/thorproduct.cfm?partnumber=ADAFC3`. Accessed: 27th March, 2023.

[265] Thorlabs, Inc. *ADAFCPM2 FC/PC to FC/PC or FC/APC to FC/APC Mating Sleeve, Narrow Precision Key (*2.0 mm*), Square Flange*, 2016. Rev. D. Available: `https://www.thorlabs.com/thorproduct.cfm?partnumber=ADAFCPM2`. Accessed: 27th March, 2023.

[266] Thorlabs, Inc. *ADABS1 Single L-Bracket for Square Flange FC Mating Sleeves*, 2019. Rev. C. Available: https://www.thorlabs.com/thorproduct.cfm?partnumber=ADABS1. Accessed: 27th March, 2023.

[267] Kurt J. Lesker Company. https://www.lesker.com/. Accessed: 18th October, 2023.

[268] Thorlabs, Inc. *F230APC-1550* 1550 nm, $f = 4.61$ mm, NA $= 0.54$ *FC/APC Fiber Collimation Pkg.*, 2015. Rev. A. Available: https://www.thorlabs.com/thorproduct.cfm?partnumber=F230APC-1550 Accessed: 4th April, 2023.

[269] Oz optics ltd. https://ozoptics.com. Accessed: 3rd October, 2023.

[270] R. L. Bertolotti. Thermal expansion of Kovar, Ceramvar and seals of these materials to alumina. *Sandia Laboratories, Livermore*, 1974.

[271] New Imaging Technologies. *WiDy SenS 640*. Available: https://new-imaging-technologies.com/product/widy-sens-640. Accessed: 4th October, 2023.

[272] Thorlabs, Inc. *CM05-BS018* 16 mm *Cage Cube-Mounted Non-Polarizing Beamsplitter,* 1100–1600 nm*, 8-32 and M4 Adapters*, 2013. Rev. A. Available: https://www.thorlabs.com/thorproduct.cfm?partnumber=CM05-BS018. Accessed: 17th July, 2023.

[273] Thorlabs, Inc. *PS974M-C TIR Retroreflector, SM05-Threaded Mount, AR Coating:* 1050–1700 nm, 2021. Rev. A. Available: https://www.thorlabs.com/thorproduct.cfm?partnumber=PS974M-C. Accessed: 17th May, 2023.

[274] PI. *PIHera Piezo Linear Precision Positioner Datasheet*, 2022. Rev. 2022-02-14. Available: https://www.pi-usa.us/en/products/piezo-flexure-nanopositioners/x-linear-piezo-flexure-nanopositioning-stages/p-6201-p-6291-pihera-piezo-linear-stage-202300. Accessed: 9th May, 2023.

[275] Tektronix, Inc. *Digital Phosphor Oscilloscopes MSO4000 Series, DPO4000 Series Data Sheet*, 2016. Available: https://www.tek.com/datasheet/dpo4000-series-digital-phosphor-oscilloscopes-datasheet Accessed: 18th September, 2023.

[276] A. Cournoyer, É. Carbonneau, P. Gilbert, I. Silversides, S. Houle, M. Larouche, H. Bourque, G. Delisle, F. Grandmont, D. Naylor, B. Gom, and B. Louwerse. Cryogenic testing towards TRL-5 demonstration of a novel stiffness-compensated, reactionless scan mechanism for the Fourier transform spectrometer of SPICA SAFARI instrument. In *Millimeter, Submillimeter, and Far-Infrared Detectors and Instrumentation for Astronomy XI*, volume 12190, pages 1015–1030. SPIE, 2022.

[277] ABB Canada - Leading digital technologies for industry. https://abb.com/ca. Accessed: 28th September, 2023.

[278] A. J. Christiansen, D. A. Naylor, and B. G. Gom. Multiaxis applications of a cryogenic range-resolved laser interferometer. In *Photonic Instrumentation Engineering X*, volume 12428, page 124280Z. SPIE, 2023.

[279] Thorlabs, Inc. *TW1550R5A2* 2×2 *Wideband Fiber Optic Coupler,* (1550 ± 100) nm*, 50:50 Split, FC/APC Connectors*, 2015. Rev. C. Available: `https://www.thorlabs.com/thorproduct.cfm?partnumber=TW1550R5A2`. Accessed: 16th October, 2023.

[280] Thorlabs, Inc. *F260APC-1550* 1550 nm*,* $f = 15.58$ mm*,* NA $= 0.16$ *FC/APC Fiber Collimation Pkg.*, 2010. Rev. B. Available: `https://www.thorlabs.com/thorproduct.cfm?partnumber=F260APC-1550` Accessed: 26th September, 2023.

[281] Optiphase. *PZ1 High-speed Fibre Stretcher Datasheet*, 2015. Rev. G. Available: `https://www.optiphase2.com/product/pz1-high-speed-fiber-stretcher`. Accessed: 19th September, 2023.

[282] Thorlabs, Inc. *F280APC-1550* 1550 nm*,* $f = 18.75$ mm*,* NA $= 0.15$ *FC/APC Fiber Collimation Pkg.*, 2010. Rev. B. Available: `https://www.thorlabs.com/thorproduct.cfm?partnumber=F280APC-1550` Accessed: 19th September, 2023.

[283] The Engineering ToolBox. *Metals – Temperature Expansion Coefficients*, 2005. Rev. A. Available: `https://www.engineeringtoolbox.com/thermal-expansion-metals-d_859.html`. Accessed: 23rd October, 2023.

[284] J. Stone and J. Zimmerman. Index of refraction of air, 2001. Available: `http://emtoolbox.nist.gov/Wavelength/Documentation.asp`. Accessed: 17th October, 2023.

[285] I. W. Selesnick and C. S. Burrus. Generalized digital Butterworth filter design. *IEEE Transactions on Signal Processing*, 46(6):1688–1694, 1998.

[286] N. Bobroff. Recent advances in displacement measuring interferometry. *Measurement Science and Technology*, 4(9):907, 1993.

[287] Thorlabs, Inc. *PAF2-A4B Achromatic FiberPort, FC/PC & FC/APC,* $f =$ 4.0 mm*,* 600–1050 nm*,* ⌀0.87 mm *Waist*, 2017. Rev. C. Available: `https://www.thorlabs.com/thorproduct.cfm?partnumber=PAF2-A4B`. Accessed: 8th May, 2023.

[288] Thorlabs, Inc. *630HP Single Mode Optical Fiber,* 600–770 nm*,* ⌀125 µm *Cladding*, 2017. Rev. F. Available: `https://www.thorlabs.com/thorproduct.cfm?partnumber=630HP`. Accessed: 8th May, 2023.

[289] Ascentta, Inc. *3-Port Optical (TGG Type) Circulator: Single-mode Datasheet*, 2018. Rev. V.D1. Available: `https://ascentta.com/circulator.html`. Accessed: 8th May, 2023.

[290] Lfiber Optic Limited. *650/1310 and 650/1550 nm Fused WDM Coupler Datasheet*, 2017. Available: `https://www.lfiber.com/650-1310-1550-wdm-coupler`. Accessed: 8th May, 2023.

[291] Thorlabs, Inc. *FDS02 Si Photodiode,* 47 ps *Rise Time,* 400–1100 nm*,* ⌀0.25 mm *Active Area, FC/PC Bulkhead*, 2016. Rev. D. Available: `https://www.thorlabs.com/thorproduct.cfm?partnumber=FDS02`. Accessed: 18th July, 2023.

[292] P. E. Ciddor. Refractive index of air: new equations for the visible and near infrared. *Applied Optics*, 35(9):1566–1573, 1996.

[293] E. R. Peck and K. Reeder. Dispersion of air. *JOSA*, 62(8):958–962, 1972.

[294] N. Ackerley. Principles of broadband seismometry. *Encyclopedia of Earthquake Engineering*, 2014.

[295] H. Eren. Acceleration, vibration, and shock measurement. *The Measurement, Instrumentation, and Sensors Handbook*, pages 1–30, 1999.

[296] D. Titterton and J. L. Weston. *Strapdown Inertial Navigation Technology*, volume 17. IET, 2004.

[297] S. Desrochers, D. Pasini, and J. Angeles. Optimum design of a compliant uniaxial accelerometer. *Journal of Mechanical Design*, 132(4):041011, 2010.

[298] I. Veenendaal, D. Naylor, B. Gom, A. Christiansen, W. Jellema, C. Feenstra, M. Ridder, M. Eggens, and P. Ade. An angle-scanned cryogenic Fabry-Pérot interferometer for far-infrared astronomy. *Review of Scientific Instruments*, 91(8):083108, 2020.

[299] Sensata Technologies, Inc. *Rotary Voice Coil Actuators (VCA)*, 2023. Rev. 04/12/23. Available: `https://www.sensata.com/products/motors-actuators/rotary-voice-coil-actuators-ra29-11-002a`. Accessed: 12th May, 2023.

[300] Thorlabs, Inc. *P5-SMF28ER-50-1 SM 50:50 Partial Reflector Patch Cable,* 1260–1620 nm*, FC/APC*, 2019. Rev. F. Available: `https://www.thorlabs.com/thorproduct.cfm?partnumber=P5-SMF28ER-50-1`. Accessed: 22nd July, 2023.

[301] Ingenia Cat S.L.U. *Neptune 2/48: Panel Mount, CANopen Servo Drive* 2.5 A 48 V. Available: `https://www.ingeniamc.com/servo-drives/dc/canopen/neptune-2a-48v-panel-mount`. Accessed: 12th May, 2023.

[302] Aerotech. *Motion Controllers Soloist Linear*, 2021. Available: `https://www.aerotech.com/wp-content/uploads/2021/01/soloist-hle-7.pdf`. Accessed: 12th May, 2023.

[303] B&K Precision Corporation. *Synthesized In-Circuit LCR/ESR Meters Models 885 & 886*, 2018. Ver. 082218. Available: `https://www.bkprecision.com/products/component-testers/885`. Accessed: 12th May, 2023.

[304] Arnold Magnetic Technologies. *Using Permanent Magnets at Low Temperature*, 2015. Rev. 2015a. Available: `https://www.arnoldmagnetics.com/wp-content/uploads/2017/10/TN_0302_rev_150715.pdf`. Accessed: 19th September, 2023.

[305] A. Nelson and F. Guzman. Compact optomechanical inertial sensors with fused silicia and si-based resonators. In *Optical and Quantum Sensing and Precision Metrology II*, volume 12016, pages 91–96. SPIE, 2022.

[306] A. Hines, L. Richardson, H. Wisniewski, and F. Guzman. Optomechanical inertial sensors. *Applied Optics*, 59(22):G167–G174, 2020.

[307] B. B. Martinez, A. Nelson, A. Hines, J. P. Mock, G. Valdés, J. Sanjuan, and F. Guzmán. Modeling, fabrication, and readout of compact optomechanical accelerometers. In *MOEMS and Miniaturized Systems XXII*, volume 12434, pages 9–17. SPIE, 2023.

[308] F. Guzmán Cervantes, L. Kumanchik, J. Pratt, and J. M. Taylor. High sensitivity optomechanical reference accelerometer over 10 khz. *Applied Physics Letters*, 104(22), 2014.

[309] O. Gerberding, F. Guzmán Cervantes, J. Melcher, J. R. Pratt, and J. M. Taylor. Optomechanical reference accelerometer. *Metrologia*, 52(5):654, 2015.

[310] B. P. Abbott et al. LIGO: the Laser Interferometer Gravitational-Wave Observatory. *Reports on Progress in Physics*, 72(7):076901, 2009.

[311] Epoxy Technology, Inc. *EPO-TEK 920 Product Information Sheet*, 2019. Rev. V. Available: `https://www.epotek.com/docs/en/Datasheet/920.pdf`. Accessed: 19th September, 2023.

[312] Thorlabs, Inc. *PA2JEW Piezo Chip,* 75 V*,* 2.0 µm *Displacement,* 3.0 × 3.0 × 2.0 mm*, Pre-Attached Wires*, 2015. Rev. A. Available: `https://www.thorlabs.com/thorproduct.cfm?partnumber=PA2JEW`. Accessed: 19th September, 2023.

[313] Norland Products. *Norland Optical Adhesive 61.* Available: `https://norlandprod.com/adhesives/NOA%2061.html`. Accessed: 19th September, 2023.

[314] R. Munro. Elastic moduli data for polycrystalline oxide ceramics. NIST Interagency/Internal Report (NISTIR), National Institute of Standards and Technology, 2002.

[315] J. W. Ekin. Appendix data tables from experimental techniques for low-temperature measurements. Oxford University Press, 2007.

[316] Aerotech. *Screw-Driven Linear Stages ATS100*, 2021. Available: https://www.aerotech.com/wp-content/uploads/2020/10/ATS100-New-Datasheet-9.2021-Revised.pdf. Accessed: 19th September, 2023.

[317] H. Lu, M. Wang, X. Dai, and W. Guo. All-fiber self-mixing interferometer based on DFB laser and phase modulating technique. *IEEE Photonics Technology Letters*, 23(4):221–223, 2011.

[318] B. En, D. Fa-jie, L. Chang-rong, Z. Fu-kai, and F. Fan. Sinusoidal phase modulating interferometry system for 3D profile measurement. *Optics & Laser Technology*, 59:137–142, 2014.

[319] M. Abramowitz and I. A. Stegun. *Handbook of Mathematical Functions with Formulas, Graphs, and Mathematical Tables*. Dover Publications, Inc., 9 edition, 1972.

[320] A. V. Oppenheim, A. S. Willsky, and S. H. Nawab. *Signals and Systems*. Prentice Hall, 2 edition, 1996.

[321] P. A. Tipler. *Physics*. Worth Pulishers, Inc., 1976.

[322] D. C. Giancoli. *Physics for Scientists & Engineers with Modern Physics*. Addison-Wesley, 4 edition, 2008.

[323] S. S. Rao. *Mechanical Vibrations*. Prentice Hall, 5 edition, 2011.

[324] E. W. Weisstein. Lorentzian Function. From MathWorld – A Wolfram Web Resource. https://mathworld.wolfram.com/LorentzianFunction.html. Accessed: 8th September, 2023.

[325] Thorlabs, Inc. *BFCT Passive Component Fiber Tray*, 2015. Rev. A. Available: https://www.thorlabs.com/thorproduct.cfm?partnumber=BFCT. Accessed: 6th June, 2023.

[326] Thorlabs, Inc. *FSR1 Storage Reel for Patch Cables with ⌀900 µm Jackets*, 2015. Rev. A. Available: https://www.thorlabs.com/thorproduct.cfm?partnumber=FSR1. Accessed: 6th June, 2023.

[327] Thorlabs, Inc. *AV6/M ⌀45.0 mm Sorbothane Feet, Internal M6 Mounting Thread, 4 Pieces*, 2015. Rev. A. Available: https://www.thorlabs.com/thorproduct.cfm?partnumber=AV6/M. Accessed: 6th June, 2023.

[328] Digilent Inc. *Digilent Pmod Interface Specification*, 2020. Ver. 1.3.1. Available: https://digilent.com/reference/pmod/start. Accessed: 23rd October, 2023.

[329] Analog Devices, Inc. *AD9717 Datasheet*, 2022. Rev. C. Available: https://www.analog.com/en/products/ad9717.html. Accessed: 5th June, 2023.

[330] Analog Devices, Inc. *AD9648 Datasheet*, 2015. Rev. C. Available: https://www.analog.com/en/products/ad9648.html. Accessed: 5th June, 2023.

[331] Thorlabs, Inc. *FTS4 Three-Hole Stripping Tool for Fiber Buffers and Jackets*. Available: https://www.thorlabs.com/thorproduct.cfm?partnumber=FTS4. Accessed: 1st August, 2023.

[332] Thorlabs, Inc. *F112 Epoxy for Fiber Optic Connectors, Long Pot Life, 10 Packets*, 2012. Available: https://www.thorlabs.com/thorproduct.cfm?partnumber=F112. Accessed: 1st August, 2023.

[333] Thorlabs, Inc. *MS403-10* 3 cc *Empty Epoxy Syringe, Package of 10, Disposable*. Available: https://www.thorlabs.com/thorproduct.cfm?partnumber=MS403-10. Accessed: 1st August, 2023.

[334] Thorlabs, Inc. *S90R Ruby DualScribe Fiber Optic Scribe*, 2015. Rev. B. Available: https://www.thorlabs.com/thorproduct.cfm?partnumber=S90R. Accessed: 23rd March, 2023.

[335] Thorlabs, Inc. *D50-FC/APC FC/APC Connector Polishing Disc*, 2014. Rev. E. Available: https://www.thorlabs.com/thorproduct.cfm?partnumber=D50-FC/APC. Accessed: 23rd March, 2023.

[336] Thorlabs, Inc. *D50-FC FC/PC and SC/PC Connector Polishing Disk*, 2014. Rev. C. Available: https://www.thorlabs.com/thorproduct.cfm?partnumber=D50-FC. Accessed: 23rd March, 2023.

[337] Thorlabs, Inc. *LF30D* 6 × 6" *Diamond Lapping (Polishing) Sheets,* 30 µm *Grit (5 Sheets)*. Available: https://www.thorlabs.com/thorproduct.cfm?partnumber=LF30D. Accessed: 1st April, 2023.

[338] Thorlabs, Inc. *LF6D* 6 × 6" *Diamond Lapping (Polishing) Sheets,* 6 µm *Grit (5 Sheets)*. Available: https://www.thorlabs.com/thorproduct.cfm?partnumber=LF6D. Accessed: 1st April, 2023.

[339] Thorlabs, Inc. *LF3D* 6 × 6" *Diamond Lapping (Polishing) Sheets,* 3 µm *Grit (5 Sheets)*. Available: https://www.thorlabs.com/thorproduct.cfm?partnumber=LF3D. Accessed: 1st April, 2023.

[340] Thorlabs, Inc. *LF1D* 6 × 6" *Diamond Lapping (Polishing) Sheets,* 1 µm *Grit (5 Sheets)*. Available: https://www.thorlabs.com/thorproduct.cfm?partnumber=LF1D. Accessed: 1st April, 2023.

[341] Thorlabs, Inc. *LCFC* 6 × 6" *Final Lapping (Polishing) Sheets,* 0.02 µm *Grit (5 Sheets)*. Available: https://www.thorlabs.com/thorproduct.cfm?partnumber=LCFC. Accessed: 1st April, 2023.

Appendix A

Derivations of Sinusoidal Frequency Modulation Equations

A.1 Modulation

At a time, t, the signal processing system of a sinusoidal frequency modulation (SFM) laser interferometer sinusoidally modulates the optical frequency of a laser at a modulation frequency, f_{m}, about a centre optical frequency, ν_{c}, with an optical frequency amplitude ν_{A}. After the signal has traversed a path through the interferometer with time-of-flight delay τ_{f}, the optical frequency, ν, at the detector at time t' is given by

$$\nu(t' - \tau_{\mathrm{f}}(t')) = \nu_{\mathrm{A}} \sin\Big(2\pi f_{\mathrm{m}}\big[t' - \tau_{\mathrm{f}}(t')\big]\Big) + \nu_{\mathrm{c}}. \qquad \text{[Hz]} \quad \text{(A.1)}$$

Each path through the interferometer an interfering signal at the detector carrying a phase due to the modulation of the laser and time-of-flight along the path. The phase, ϕ, of an optical signal is dictated by its angular frequency, $\omega = 2\pi\nu$, and wavevector, $\vec{k}$, such that

$$\phi(t, \vec{r}) = \phi_0 + \int \omega \ \mathrm{d}t - \int \vec{k} \cdot \mathrm{d}\vec{r}\,, \qquad \text{(A.2)}$$

where $\vec{r}$ is the position vector and ϕ_0 is the initial phase. For all interferometers discussed in this thesis, $\vec{k}$ and $\vec{r}$ are parallel, allowing $\vec{k} \cdot \vec{r}$ to be expressed as $k\ell$, where $k = 2\pi\nu/\mathrm{c}$ is the angular wave number and $\ell = \mathrm{c}[\tau_{\mathrm{del,out}} + \tau_{\mathrm{del,in}} + \tau_{\mathrm{f}}]$ is the optical path length (OPL) from the laser to the detector. The frequency $\nu(t' - \tau_{\mathrm{f}}(t'))$ from Equation (A.1) reaching the detector is emitted by the laser at $t - \tau_{\mathrm{da}} - \tau_{\mathrm{mod}}$,

and the phase of the signal written in the form of Equation (A.2) is

$$\begin{aligned}\phi(t'-\tau_{\mathrm{f}}(t')) &= \phi_0 + \int \omega \ \mathrm{d}t' - \int k \ \mathrm{d}\ell \\ &= \phi_0 + \int 2\pi\nu\big(t'-\tau_{\mathrm{f}}(t')\big) \ \mathrm{d}\big(t-\tau_{\mathrm{da}}-\tau_{\mathrm{mod}}\big) \\ &\quad - \int 2\pi\nu\big(t'-\tau_{\mathrm{f}}(t)\big) \ \mathrm{d}\big(\tau_{\mathrm{del,out}}+\tau_{\mathrm{del,bound}}+\tau_{\mathrm{del,in}}+\tau_{\mathrm{f}}(t')\big)\,. \end{aligned} \qquad \text{[rad] (A.3)}$$

The OPL includes the fixed delays in the interferometer and the time-of-flight delay arising due to the axis optical path difference (OPD). Since $\mathrm{d}\ell$ is in terms of time and delay in Equation (A.3), the two integrals may be combined into one with the infinitesimal in terms of t' as

$$\phi(t'-\tau_{\mathrm{f}}(t')) = \phi_0 + 2\pi \int_0^{t'-\tau_{\mathrm{f}}(t')} \nu\big(t'-\tau_{\mathrm{f}}(t')\big) \ \mathrm{d}\big(t'-\tau_{\mathrm{f}}(t')\big)\,. \qquad \text{[rad] (A.4)}$$

Equation (A.4) shows that Equation (A.2) devolves into the form $\phi = \int \omega \ \mathrm{d}t$, which is the canonical representation of the phase for a time varying signal and is commonly used in the analysis of frequency-modulated continuous-wave (FMCW) systems [162, 163]. Formally, Equation (A.4) is integrated over $-\infty$ to $t'-\tau_{\mathrm{f}}(t')$, however, the phase for $t<0$ is coalesced into ϕ_0, yielding

$$\phi(t'-\tau_{\mathrm{f}}(t')) = \phi_0 + \frac{\nu_{\mathrm{A}}}{f_{\mathrm{m}}}\Big[1-\cos\Big(2\pi f_{\mathrm{m}}\big[t'-\tau_{\mathrm{f}}(t')\big]\Big)\Big] + 2\pi\nu_{\mathrm{c}}\big[t'-\tau_{\mathrm{f}}(t')\big]. \quad \text{[rad] (A.5)}$$

In a multiaxis interferometer, an arbitrary number of signals interfere. These signals are given by members of S from Section 3.2, and are considered in pairwise combinations, a and b. All signals in S experience the same common-mode delays, but different time-of-flight delays, $\tau_{\mathrm{f},a}$ and $\tau_{\mathrm{f},b}$, incurred during traversal of the OPLs. The time-of-flight varies and is thus defined as the delay due to OPD traversal at the time at which the photons that have traversed it reach the detector. With time-of-flight delays, pairs of interfering frequencies, ν_a and ν_b, are given by

$$\nu_a(t') = \nu\big(t'-\tau_{\mathrm{f},a}(t')\big), \qquad \text{[Hz] (A.6a)}$$

$$\nu_b(t') = \nu\big(t'-\tau_{\mathrm{f},b}(t')\big). \qquad \text{[Hz] (A.6b)}$$

Combining the signal frequencies from Equation (A.6) with the general phase solution from Equation (A.5), the phases, ϕ_a and ϕ_b, are given by

$$\phi_a(t') = \phi_0 + \frac{\nu_\mathrm{A}}{f_\mathrm{m}}\left[1 - \cos\Big(2\pi f_\mathrm{m}\big[t' - \tau_{\mathrm{f},a}(t')\big]\Big)\right] + 2\pi\nu_\mathrm{c}\big[t' - \tau_{\mathrm{f},a}(t')\big], \quad \text{[rad]} \text{ (A.7a)}$$

$$\phi_b(t') = \phi_0 + \frac{\nu_\mathrm{A}}{f_\mathrm{m}}\left[1 - \cos\Big(2\pi f_\mathrm{m}\big[t' - \tau_{\mathrm{f},b}(t')\big]\Big)\right] + 2\pi\nu_\mathrm{c}\big[t' - \tau_{\mathrm{f},b}(t')\big]. \quad \text{[rad]} \text{ (A.7b)}$$

The phase difference for each pair a and b in S contributes a component $\Delta\phi_{ab} = \phi_a - \phi_b$ to the interference signal. The choice to express the phase difference as $\phi_a - \phi_b$ or $\phi_b - \phi_a$ is arbitrary, however, the former was selected so that the phase difference may be expressed in terms of $\tau_{\mathrm{f},b} - \tau_{\mathrm{f},a}$ without an extraneous negative sign. The difference between the phases of Equation (A.7) is

$$\begin{aligned}\Delta\phi_{ab}(t') = \frac{\nu_\mathrm{A}}{f_\mathrm{m}}&\left[\cos\Big(2\pi f_\mathrm{m}\big[t' - \tau_{\mathrm{f},b}(t')\big]\Big) - \cos\Big(2\pi f_\mathrm{m}\big[t' - \tau_{\mathrm{f},a}(t')\big]\Big)\right] \\ &+ 2\pi\nu_\mathrm{c}\big[\tau_{\mathrm{f},b}(t') - \tau_{\mathrm{f},a}(t')\big].\end{aligned} \quad \text{[rad]} \text{ (A.8)}$$

The difference of cosines in Equation (A.8) may be reduced by applying the trigonometric identity $\cos(\gamma - \beta) - \cos(\gamma - \alpha) = 2\sin(\frac{\beta-\alpha}{2})\sin(\gamma - \frac{\beta+\alpha}{2})$ found in Equation (A.10), yielding

$$\begin{aligned}\Delta\phi_{ab}(t') = &\underbrace{\underbrace{\frac{2\nu_\mathrm{A}}{f_\mathrm{m}}\sin\Big(\pi f_\mathrm{m}\big[\tau_{\mathrm{f},b}(t') - \tau_{\mathrm{f},a}(t')\big]\Big)}_{A_{ab}(t')}\sin\left(2\pi f_\mathrm{m}\left[t' - \frac{1}{2}\big[\tau_{\mathrm{f},b}(t') + \tau_{\mathrm{f},a}(t')\big]\right]\right)}_{\theta_{ab}(t')} \\ &+ \underbrace{2\pi\nu_\mathrm{c}\big[\tau_{\mathrm{f},b}(t') - \tau_{\mathrm{f},a}(t')\big]}_{\varphi_{ab}(t')}.\end{aligned} \quad \text{[rad]} \text{ (A.9)}$$

The required trigonometric identity is found by manipulating the more common $\cos(A - B) - \cos(A + B) = 2\sin B \sin A$ [189] to obtain

$$\begin{aligned}\cos(\gamma - \beta) - \cos(\gamma - \alpha) &= \cos\left(\gamma - \beta - \frac{\alpha}{2} + \frac{\alpha}{2}\right) - \cos\left(\gamma - \alpha - \frac{\beta}{2} + \frac{\beta}{2}\right) \\ &= \cos\left(\underbrace{\gamma - \frac{\beta+\alpha}{2}}_{A} - \underbrace{\frac{\beta-\alpha}{2}}_{B}\right) - \cos\left(\underbrace{\gamma - \frac{\beta+\alpha}{2}}_{A} + \underbrace{\frac{\beta-\alpha}{2}}_{B}\right) \\ &= 2\sin\left(\frac{\beta-\alpha}{2}\right)\sin\left(\gamma - \frac{\beta+\alpha}{2}\right)\end{aligned} \quad \text{(A.10)}$$

The phase modulation amplitude, $A_{ab}(t')$, is the angular disturbance of the ab axis due to modulation of the laser. Although expressed in terms of $\tau_{\mathrm{f},a}$ and $\tau_{\mathrm{f},b}$ in Equation (A.9), A_{ab} can also be written as a function of the OPD,

$$A_{ab}(t') = \frac{2\nu_{\mathrm{A}}}{f_{\mathrm{m}}} \sin\Big(\pi f_{\mathrm{m}}\big[\tau_{\mathrm{f},b}(t') - \tau_{\mathrm{f},a}(t')\big]\Big) = \frac{2\nu_{\mathrm{A}}}{f_{\mathrm{m}}} \sin\left(\frac{\pi f_{\mathrm{m}} \Lambda_{ab}(t')}{\mathrm{c}}\right), \quad \text{[rad]} \text{ (A.11)}$$

where $\Lambda_{ab}(t') = \mathrm{c}[\tau_{\mathrm{f},b}(t') - \tau_{\mathrm{f},a}(t')]$ is the OPD of the ab axis and c is the vacuum speed of light.

While A_{ab} gives the phase modulation amplitude, the overall phase modulation due to the frequency modulation of the laser is given by

$$\theta_{ab}(t') = A_{ab}(t') \sin\left(2\pi f_{\mathrm{m}}\left[t' - \frac{1}{2}\big[\tau_{\mathrm{f},b}(t') + \tau_{\mathrm{f},a}(t')\big]\right]\right). \quad \text{[rad]} \text{ (A.12)}$$

The OPD of the interferometer contributes a phase component proportional to the displacement in optical path, which is ultimately the phase component recovered in the demodulation step. The OPD dependent phase is given by

$$\varphi_{ab}(t') = 2\pi\nu_{\mathrm{c}}\big[\tau_{\mathrm{f},b}(t') - \tau_{\mathrm{f},a}(t')\big] = \frac{2\pi\nu_{\mathrm{c}}\Lambda_{ab}(t')}{\mathrm{c}}. \quad \text{[rad]} \text{ (A.13)}$$

Equation (A.9) can be expressed in terms of Equations (A.12) and (A.13) to obtain a short form of the phase difference,

$$\Delta\phi_{ab}(t') = \theta_{ab}(t') + \varphi_{ab}(t'). \quad \text{[rad]} \text{ (A.14)}$$

Equation (A.14) shows that there are two components to the resulting phase difference: one that is controlled by laser modulation (θ_{ab}) and one that is dictated solely by the OPD (φ_{ab}).

A.2 Beat Frequency

The derivation of the beat frequency, $f_{\mathrm{b},ab}$, follows a similar procedure $\Delta\phi_{ab}$ in Equation (A.9), but with a difference of sines rather than cosines as in Equation (A.10). Using $\sin(A+B) - \sin(A-B) = 2\cos A \sin B$ [189], alternatively written

as $\sin(A-B)-\sin(A+B) = -2\sin B\cos A$ to match the form of the equations, gives

$$\begin{aligned}\sin(\gamma-\alpha)-\sin(\gamma-\beta) &= \sin\left(\gamma-\alpha-\frac{\beta}{2}+\frac{\beta}{2}\right)-\sin\left(\gamma-\beta-\frac{\alpha}{2}+\frac{\alpha}{2}\right)\\ &= \sin\left(\underbrace{\gamma-\frac{\alpha+\beta}{2}}_{A}-\underbrace{\frac{\alpha-\beta}{2}}_{B}\right)-\sin\left(\underbrace{\gamma-\frac{\alpha+\beta}{2}}_{A}+\underbrace{\frac{\alpha-\beta}{2}}_{B}\right)\\ &= -2\sin\left(\frac{\alpha-\beta}{2}\right)\cos\left(\gamma-\frac{\alpha+\beta}{2}\right).\end{aligned} \tag{A.15}$$

The beat frequency, $f_{\mathrm{b},ab}(t') = \nu_a(t') - \nu_b(t')$, is the difference of optical frequencies from Equation (A.6) With the identity from Equation (A.15), $f_{\mathrm{b},ab}$ may be written as

$$\begin{aligned}f_{\mathrm{b},ab}(t') = 2\nu_{\mathrm{A}}\sin&\Big(\pi f_{\mathrm{m}}\big[\tau_{\mathrm{f},b}(t')-\tau_{\mathrm{f},a}(t')\big]\Big)\\ &\cos\left[2\pi f_{\mathrm{m}}\left(t'-\frac{1}{2}\big[\tau_{\mathrm{f},b}(t')+\tau_{\mathrm{f},a}(t')\big]\right)\right].\end{aligned} \qquad [\mathrm{Hz}] \tag{A.16}$$

The maximum positive beat frequency is observed during the modulation ramp up of ν_a and ν_b, and the maximum negative frequency on the ramp down. The positive and negative beat frequency envelopes, $f^{+}_{\mathrm{b},ab}(t')$ and $f^{-}_{\mathrm{b},ab}(t')$, respectively, are dictated by the time-of-flight delay between the two axes. From Equation (A.16), these frequencies are

$$\begin{aligned}f^{+}_{\mathrm{b},ab}(t') = -f^{-}_{\mathrm{b},ab}(t') &= 2\nu_{\mathrm{A}}\sin\Big(\pi f_{\mathrm{m}}\big[\tau_{\mathrm{f},b}(t')-\tau_{\mathrm{f},a}(t')\big]\Big)\\ &= 2\nu_{\mathrm{A}}\sin\left(\frac{\pi f_{\mathrm{m}}\Lambda_{ab}(t')}{\mathrm{c}}\right).\end{aligned} \qquad [\mathrm{Hz}] \tag{A.17}$$

A.3 Intensity

Interference equations in this section are derived upon the assumption that the interfering light is quasi-monochromatic. The intensity of an optical wave proportional to the time average of its electric field squared, thus, the intensity measured at the detector at time t' is [10]

$$I(t') = \frac{1}{2}\epsilon v\left\langle \vec{E}(t')\cdot\vec{E}^{*}(t')\right\rangle, \qquad [\mathrm{W/m^2}] \tag{A.18}$$

where ϵ is the permittivity of the medium, v is the speed of the wave in the medium, $\vec{E}(t') = \vec{E}_0(t')\exp[\mathrm{j}\phi(t')]$, $\vec{E}_0$ is the real electric field amplitude, $\mathrm{j}^2 = -1$, ϕ is the phase of the electric field, $\langle\ldots\rangle$ is a time average, and * is complex conjugation. The factor of $1/2$ must be explicitly inserted into Equation (A.18) since the definition of $\vec{E}$ uses $\exp[\mathrm{j}\phi(t')]$ rather than $\cos[\phi(t')]$; the complex exponential carries twice the energy

than the cosine, but only the real part of the signal is measurable. Conventionally, the leading constant of $\epsilon v/2$ is omitted, and this notation is adopted for the rest of this section. Considering all electric fields from S, the total electric field is

$$\vec{E}(t') = \sum_{a\in S} \vec{E}_a\big(t' - \tau_{\mathrm{f},a}(t')\big) = \sum_{a\in S} \vec{E}_{0a}(t') \exp\Big[\mathrm{j}\phi_a\big(t' - \tau_{\mathrm{f},a}(t')\big)\Big]. \quad [\mathrm{V/m}] \text{ (A.19)}$$

The intensity is expressed as the time average of all interfering fields in S. Combining Equations (A.18) and (A.19) yields

$$\begin{aligned} I(t') &= \left\langle \left(\sum_{a\in S} \vec{E}_a(t')\right) \cdot \left(\sum_{b\in S} \vec{E}^*_b(t')\right) \right\rangle \\ &= \left\langle \sum_{(a,b)\subseteq S} \vec{E}_a(t') \cdot \vec{E}^*_b(t') \right\rangle, \end{aligned} \qquad [\mathrm{W/m^2}] \text{ (A.20)}$$

where $(a, b) \subseteq S$ denotes an ordered pair from S, thus the sum is taken over all pairwise *permutations* of the elements in S. Expanding the electric field terms in Equation (A.20) yields

$$I(t') = \left\langle \sum_{(a,b)\subseteq S} \vec{E}_{0a}(t') \cdot \vec{E}_{0b}(t') \exp\Big[\mathrm{j}\Delta\phi_{ab}(t')\Big] \right\rangle, \qquad [\mathrm{W/m^2}] \text{ (A.21)}$$

where $\Delta\phi_{ab}$ is the phase difference from Equation (3.22) that arises from the difference $\phi_a - \phi_b$ due to the complex conjugate. Note that the conjugates were dropped since it was stated that $\vec{E}_{0a}$ and $\vec{E}_{0b}$ are real. The sum can be split into two cases: $a = b$ and $a \neq b$. For all a and b in the $a \neq b$ case, there are two ordered pairs, (a, b) and (b, a). These are combined into a single unordered pair, $\{a, b\}$, thus the sum is taken over all pairwise *combinations* of S, allowing Equation (A.21) to be expressed as

$$\begin{aligned} I(t') = &\left\langle \sum_{a\in S} \vec{E}_{0a}(t') \cdot \vec{E}_{0a}(t') \right\rangle \\ &+ \left\langle \sum_{\{a,b\}\subseteq S} \Big[\vec{E}_{0a}(t') \cdot \vec{E}_{0b}(t') \exp\big[\mathrm{j}\Delta\phi_{ab}(t')\big] + \vec{E}_{0b}(t') \cdot \vec{E}_{0a}(t') \exp\big[\mathrm{j}\Delta\phi_{ba}(t')\big]\Big] \right\rangle. \end{aligned} \qquad [\mathrm{W/m^2}] \text{ (A.22)}$$

By recognizing that $\Delta\phi_{ab} = -\Delta\phi_{ba}$, the exponentials of the second sum in Equation (A.22) may be simplified to a single cosine. Furthermore, it is assumed that $\vec{E}_{0a}$ and $\vec{E}_{0b}$ are parallel for all $a, b \in S$. Applying these remarks and assumptions reduces

Equation (A.22) to

$$I(t') = \left\langle \sum_{a\in S} E_{0a}(t')^2 \right\rangle + \left\langle \sum_{\{a,b\}\subseteq S} 2E_{0a}(t')E_{0b}(t')\cos\Delta\phi_{ab}(t') \right\rangle. \quad [\mathrm{W/m^2}] \text{ (A.23)}$$

The first term is the sum of each intensity, I_a, for each a in S. From Equations (A.18) and (A.19), $E_{0\alpha} = \sqrt{2I_\alpha/\epsilon v}$ in full, or more simply with the modified notation, $E_{0\alpha} = \sqrt{I_\alpha}$. Making this substitution into Equation (A.23) gives

$$I(t') = \sum_{a\in S} I_a(t') + \sum_{\{a,b\}\subseteq S} 2\sqrt{I_a(t')I_b(t')}\cos\Delta\phi_{ab}(t'). \quad [\mathrm{W/m^2}] \text{ (A.24)}$$

To simplify further, the first term of Equation (A.24) is replaced by I_0, which is the offset intensity. The substitution $I_{ab} = 2\sqrt{I_a I_b}$ is also made for the interference term, yielding

$$I(t') = I_0(t') + \sum_{\{a,b\}\subseteq S} I_{ab}(t')\cos\Delta\phi_{ab}(t'). \quad [\mathrm{W/m^2}] \text{ (A.25)}$$

A.4 Windowed Power Spectrum

A.4.1 Exact Power Spectrum

The normalized interference signal from Equation (3.28) may be expanded, yielding

$$U(t'') = \sum_{\{a,b\}\subseteq S} \eta_{ab}\cos\left(A_{ab}\sin\Big(2\pi f_{\mathrm{m}}\Big[t'' - \frac{1}{2}\big[\tau_{\mathrm{f},b}(t'') + \tau_{\mathrm{f},a}(t'')\big]\Big]\Big) + \varphi_{ab}(t'')\right). \quad \text{(A.26)}$$

To ease the notation in this section, some simplifications are made: $\tau_{\mathrm{f},a}$, $\tau_{\mathrm{f},b}$, and φ_{ab}, are functions of time, however, the power spectrum is considered for the interferometer at a snap shot in time so these variables are held constant; $\frac{1}{2}[\tau_{\mathrm{f},b}(t'') + \tau_{\mathrm{f},b}(t'')]$ is substituted for the single term $\tau_{\mathrm{f},ab}$. Equation (A.26) may then be rewritten as

$$U(t'') = \sum_{\{a,b\}\subseteq S} \eta_{ab}\cos\Big(A_{ab}\sin\big(2\pi f_{\mathrm{m}}[t'' - \tau_{\mathrm{f},ab}]\big) + \varphi_{ab}\Big). \quad \text{(A.27)}$$

To find the Fourier transform of Equation (A.27), it is first expressed as a Fourier series by making use of the expansion [319],

$$\exp(\pm \mathrm{j}\alpha\sin\beta) = J_0(\alpha) + 2\sum_{n=1}^{\infty} J_{2n}(\alpha)\cos(2n\beta) \pm 2\mathrm{j}\sum_{n=0}^{\infty} J_{2n+1}(\alpha)\cos\big([2n+1]\beta\big), \quad \text{(A.28)}$$

where J_n is the order n Bessel function of the first kind [319]. Rewriting Equation (A.27) in terms of complex exponentials gives

$$U(t'') = \frac{1}{2}\sum_{\{a,b\}\subseteq S}\eta_{ab}\Bigg[\exp\Big(\mathrm{j}A_{ab}\sin\big(2\pi f_{\mathrm{m}}[t''-\tau_{\mathrm{f},ab}]\big)\Big)\exp(\mathrm{j}\varphi_{ab}) + \exp\Big(-\mathrm{j}A_{ab}\sin\big(2\pi f_{\mathrm{m}}[t''-\tau_{\mathrm{f},ab}]\big)\Big)\exp(-\mathrm{j}\varphi_{ab})\Bigg], \tag{A.29}$$

which when expanded using Equation (A.28), gives the Fourier series

$$U(t'') = \sum_{\{a,b\}\subseteq S}\eta_{ab}\Bigg[\cos(\varphi_{ab})\Bigg[J_0(A_{ab}) + 2\sum_{n=1}^{\infty}J_{2n}(A_{ab})\cos\big(4n\pi f_{\mathrm{m}}[t''-\tau_{\mathrm{f},ab}]\big)\Bigg] - 2\sin(\varphi_{ab})\sum_{n=0}^{\infty}J_{2n+1}(A_{ab})\sin\big([4n+2]\pi f_{\mathrm{m}}[t''-\tau_{\mathrm{f},ab}]\big)\Bigg]. \tag{A.30}$$

With the introduction of the window function from Equation (3.31), the windowed signal is the product of the window and Equation (A.30), however, the window in its purest form, W_{ab}, is delay-compensated for the time-of-flight of the ab axis. With negligible effect on the outcome, the $t''-\tau_{\mathrm{f},ab}$ can be substituted for t''_{c} from Equation (3.32), giving

$$\begin{aligned} W(t''_{\mathrm{c}},\sigma)U(t''_{\mathrm{c}}) = {} & \sum_{\{a,b\}\subseteq S}\sum_{m\in\mathbb{Z}}\alpha_{ab,0}\exp\left[-\frac{1}{2\sigma^2}\left(\frac{t''_{\mathrm{c}}}{T_{\mathrm{m}}}-\frac{m}{2}\right)^2\right] \\ & +2\sum_{\{a,b\}\subseteq S}\sum_{m\in\mathbb{Z}}\sum_{n=1}^{\infty}\alpha_{ab,2n}\exp\left[-\frac{1}{2\sigma^2}\left(\frac{t''_{\mathrm{c}}}{T_{\mathrm{m}}}-\frac{m}{2}\right)^2\right]\cos(4n\pi f_{\mathrm{m}}t''_{\mathrm{c}}) \\ & -2\sum_{\{a,b\}\subseteq S}\sum_{m\in\mathbb{Z}}\sum_{n=0}^{\infty}\beta_{ab,2n+1}\exp\left[-\frac{1}{2\sigma^2}\left(\frac{t''_{\mathrm{c}}}{T_{\mathrm{m}}}-\frac{m}{2}\right)^2\right]\sin\big([4n+2]\pi f_{\mathrm{m}}t''_{\mathrm{c}}\big). \end{aligned} \tag{A.31}$$

where $\alpha_{ab,n} = \eta_{ab}\cos(\varphi_{ab})J_n(A_{ab})$ and $\beta_{ab,n} = \eta_{ab}\sin(\varphi_{ab})J_n(A_{ab})$. In the form of Equation (A.31), the Fourier transform of WU can easily be obtained by noting that $\alpha_{ab,n}$ and $\beta_{ab,n}$ are constant and that the cosine and sine in the second and third terms can be expanded into complex exponentials so that the frequency shifting property of the Fourier transform may be used on the Gaussian function [320].

The Fourier transform of a Gaussian is also Gaussian, and in the general form is given by [319, 320]

$$\mathcal{F}\Big\{\exp\big(-a(t''_{\mathrm{c}}-b)^2\big)\Big\}(f) = \sqrt{\frac{\pi}{a}}\exp\left(-\frac{\pi^2}{a}f^2\right)\exp(-\mathrm{j}2\pi bf). \tag{A.32}$$

The Fourier transform of the window function given by the Gaussian exponential in Equation (A.31) may then be written as

$$\begin{aligned} G(f,\sigma,m) &= \mathcal{F}\left\{\exp\left[-\frac{1}{2\sigma^2}\left(\frac{t_{\mathrm{c}}''}{T_{\mathrm{m}}}-\frac{m}{2}\right)^2\right]\right\}(f) \\ &= \frac{\sqrt{2\pi}\sigma}{f_{\mathrm{m}}}\exp\left(-\frac{2\pi^2\sigma^2}{f_{\mathrm{m}}^2}f^2\right)\exp\left(-\frac{\mathrm{j}m\pi}{f_{\mathrm{m}}}f\right). \end{aligned} \tag{A.33}$$

The Fourier transform $F_{WU}(f) = \mathcal{F}\{W(t_{\mathrm{c}}'',\sigma)U(t_{\mathrm{c}}'')\}(f)$ then follows as

$$\begin{aligned} F_{WU}(f) = &\sum_{\{a,b\}\subseteq S}\sum_{m\in\mathbb{Z}}\alpha_{ab,0}G(f,\sigma,m) \\ &+\sum_{\{a,b\}\subseteq S}\sum_{m\in\mathbb{Z}}\sum_{n=1}^{\infty}\alpha_{ab,2n}G(f+2nf_{\mathrm{m}},\sigma,m) \\ &+\sum_{\{a,b\}\subseteq S}\sum_{m\in\mathbb{Z}}\sum_{n=1}^{\infty}\alpha_{ab,2n}G(f-2nf_{\mathrm{m}},\sigma,m) \\ &-\mathrm{j}\sum_{\{a,b\}\subseteq S}\sum_{m\in\mathbb{Z}}\sum_{n=0}^{\infty}\beta_{ab,2n+1}G(f+[2n+1]f_{\mathrm{m}},\sigma,m) \\ &+\mathrm{j}\sum_{\{a,b\}\subseteq S}\sum_{m\in\mathbb{Z}}\sum_{n=0}^{\infty}\beta_{ab,2n+1}G(f-[2n+1]f_{\mathrm{m}},\sigma,m). \end{aligned} \tag{A.34}$$

The first three sums can be combined by noticing that Equation (A.34) the first sum is the $n = 0$ case, the second is the $n > 0$ case, and the third is the $n < 0$ case. Likewise, the fourth and fifth sums each represent positive and negative cases and may combined into one using the signum function, sgn. Furthermore, the first three sums can be made to use even n and the final two sums to use odd n, giving the form

$$\begin{aligned} F_{WU}(f) = \sum_{\{a,b\}\subseteq S}\sum_{m\in\mathbb{Z}}\Bigg[&\sum_{\substack{n\in\mathbb{Z}\\ \text{even}}}\alpha_{ab,|n|}G(f-nf_{\mathrm{m}},\sigma,m) \\ &+\mathrm{j}\sum_{\substack{n\in\mathbb{Z}\\ \text{odd}}}\mathrm{sgn}(n)\beta_{ab,|n|}G(f-nf_{\mathrm{m}},\sigma,m)\Bigg]. \end{aligned} \tag{A.35}$$

Expanding $\alpha_{ab,n}$, $\beta_{ab,n}$, and $G(f + nf_\mathrm{m}, \sigma, m)$ in Equation (A.35) yields the result

$$F_{WU}(f) = \frac{\sqrt{2\pi}\sigma}{f_\mathrm{m}} \sum_{\{a,b\}\subseteq S} \sum_{m\in\mathbb{Z}} \eta_{ab} \Bigg[\sum_{\substack{n\in\mathbb{Z} \\ \text{even}}} \cos(\varphi_{ab}) J_{|n|}(A_{ab}) \exp\left(-\frac{2\pi^2\sigma^2}{f_\mathrm{m}^2}[f - nf_\mathrm{m}]^2\right) \exp\left(-\frac{\mathrm{j}m\pi}{f_\mathrm{m}}[f - nf_\mathrm{m}]\right) + \mathrm{j} \sum_{\substack{n\in\mathbb{Z} \\ \text{odd}}} \mathrm{sgn}(n) \sin(\varphi_{ab}) J_{|n|}(A_{ab}) \exp\left(-\frac{2\pi^2\sigma^2}{f_\mathrm{m}^2}[f - nf_\mathrm{m}]^2\right) \exp\left(-\frac{\mathrm{j}m\pi}{f_\mathrm{m}}[f - nf_\mathrm{m}]\right) \Bigg]. \tag{A.36}$$

The power spectrum is found from Equation (A.36) as

$$P_{WU}(f) = |F_{WU}(f)|^2. \tag{A.37}$$

A.4.2 Approximate Power Spectrum

The exact windowed power spectrum computed from the Fourier transform of Equation (A.36) derived in Appendix A.4.1 is not often useful in practice, as the main use for the power spectrum is estimation of the band locations and relative peak powers. Using the result for the Fourier transform of a Gaussian function in Equation (A.33) and the observation that the beat frequency under the window is approximately constant when the window width is small, a simple approximation can be developed.

As W is composed of infinitely many repeated Gaussian functions, its Fourier transform is the sum of infinitely many time-shifted Gaussian functions. Rather than considering all individual windows, a single window is used under the assumption that its width is small enough ($\sigma \ll 1$) so that neighbouring Gaussian functions have little effect on the Gaussian kernel. Using $m = 0$ in Equation (3.31), a single window, W_1, is given by

$$W_1(t_\mathrm{c}'', \sigma) = \exp\left[-\frac{1}{2\sigma^2}\frac{t_\mathrm{c}''^2}{T_\mathrm{m}^2}\right] = \exp\left[-\frac{f_\mathrm{m}^2}{2\sigma^2}t_\mathrm{c}''^2\right], \tag{A.38}$$

where t_c'' from Equation (3.32) is used as the time-of-flight delays are assumed to have negligible effects on the timing. From Equation (A.33), the Fourier transform of Equation (A.38) is another Gaussian function, and thus

$$\mathcal{F}\left\{W_1(t_\mathrm{c}'')\right\}(f) = \frac{\sqrt{2\pi}\sigma}{f_\mathrm{m}} \exp\left[-\frac{2\pi^2\sigma^2}{f_\mathrm{m}^2}f^2\right]. \tag{A.39}$$

When σ is small, the window function selects the region of U where $A\sin(2\pi f_\mathrm{m} t_\mathrm{c}'') \approx 2A\pi f_\mathrm{m} t_\mathrm{c}''$ by the small angle sine approximation. With this approximation applied to

Equation (3.31), the Fourier transform of WU is approximated by

$$\begin{aligned} F_{WU}(f) &= \left|\mathcal{F}\left\{W(t_{\mathrm{c}}'', \sigma)U(t_{\mathrm{c}}'')\right\}(f)\right| \\ &\approx \left|\mathcal{F}\left\{W_1(t_{\mathrm{c}}'', \sigma)\sum_{\{a,b\}\subseteq S}\eta_{ab}\cos\left(\Delta\phi_{ab}(t_{\mathrm{c}}'')\right)\right\}(f)\right|. \end{aligned} \tag{A.40}$$

With the small angle approximation over the windowed region, $\Delta\phi_{ab} \approx 2\pi A_{ab} f_{\mathrm{m}} t_{\mathrm{c}}'' + \varphi_{ab}$. The frequency shifting property of the Fourier transform [320] is applied through $\cos\Delta\phi_{ab}$ in Equation (A.40). Since F_{WU} is the absolute Fourier transform, the φ_{ab} term can be elided as this phase is lost in the power spectrum. The approximate Fourier transform of WU is given by

$$\begin{aligned} F_{WU}(f) \approx \frac{\sqrt{2\pi}\sigma}{f_{\mathrm{m}}}\sum_{\{a,b\}\subseteq S}\eta_{ab}\Bigg[&\exp\left(-\frac{2\pi^2\sigma^2}{f_{\mathrm{m}}^2}[f - A_{ab}f_{\mathrm{m}}]^2\right) \\ &+ \exp\left(-\frac{2\pi^2\sigma^2}{f_{\mathrm{m}}^2}[f + A_{ab}f_{\mathrm{m}}]^2\right)\Bigg]. \end{aligned} \tag{A.41}$$

The power spectrum is the square of the Fourier transform in Equation (A.41). In the general case, the power spectrum cannot be simplified further. If there exist some a, b, c, and d such that A_{ab} and A_{cd} are similar, then the exponentials of Equation (A.41) overlap and the product of $\exp(-2\pi^2\sigma^2(f + A_{ab}f_{\mathrm{m}})^2/f_{\mathrm{m}}^2)$ and $\exp(-2\pi^2\sigma^2(f + A_{cd}f_{\mathrm{m}})^2/f_{\mathrm{m}}^2)$ is no longer negligible. However, when there is adequate OPD separation, and thus adequate modulation amplitude separation, the product is nearly zero everywhere. Under the condition that there is adequate OPD separation, the product of all pairs of unlike exponential terms in Equation (A.41) are negligible, allowing the equation to be written as

$$\begin{aligned} P_{WU}(f) \approx \frac{2\pi\sigma^2}{f_{\mathrm{m}}^2}\sum_{\{a,b\}\subseteq S}\eta_{ab}^2\Bigg[&\exp\left(-\frac{4\pi^2\sigma^2}{f_{\mathrm{m}}^2}[f - A_{ab}f_{\mathrm{m}}]^2\right) \\ &+ \exp\left(-\frac{4\pi^2\sigma^2}{f_{\mathrm{m}}^2}[f + A_{ab}f_{\mathrm{m}}]^2\right)\Bigg]. \end{aligned} \tag{A.42}$$

A.5 Demodulation Power Spectrum

An exact demodulation power spectrum is not required for the analysis conducted in this work, however, one could be obtained following the derivation of the exact power spectrum for windowed interference signal in Appendix A.4.1. To analyze the demodulated signal, $D_{ab}(t_{\mathrm{c}}'', \sigma, A_{\mathrm{d}})$, an approximation of its Fourier transform and power spectrum are established in a similar fashion to the windowed power spectrum

in Equations (A.41) to (A.42). Instead of the carrier defined in Equation (3.30), an approximated carrier of $\exp[-\mathrm{j}2\pi A_\mathrm{d} f_\mathrm{m} t''_\mathrm{c}]$ is used, which uses the small angle approximation under the window discussed Appendix A.4, and thus the same assumption that $\sigma \ll 1$. The demodulated signal may be approximated as

$$\begin{aligned} D(t''_\mathrm{c}, \sigma, A_\mathrm{d}) \approx & W_1(t''_\mathrm{c}, \sigma) \exp\Big[-\mathrm{j}2\pi A_\mathrm{d} f_\mathrm{m} t''_\mathrm{c}\Big] \sum_{\{a,b\}\subseteq S} \eta_{ab} \cos(2\pi A_{ab} f_\mathrm{m} t''_\mathrm{c} + \varphi_{ab}) \\ & + W_1\left(t''_\mathrm{c} - \frac{1}{2}T_\mathrm{m}, \sigma\right) \exp\Big[\mathrm{j}2\pi A_\mathrm{d} f_\mathrm{m} t''_\mathrm{c}\Big] \sum_{\{a,b\}\subseteq S} \eta_{ab} \cos(-2\pi A_{ab} f_\mathrm{m} t''_\mathrm{c} + \varphi_{ab}), \end{aligned} \tag{A.43}$$

where U is written as a sum with θ_{ab} terms replaced using the same small angle approximation as the carrier and t''_c from Equation (3.32) is used as the time-of-flight delays are assumed to have negligible effects on the timing. Since the small angle approximation of the frequency (and thereby, θ_{ab} of Equation (A.12)) under the window is used, the first term in the second cosine of Equation (A.43) must have a negative sign to account for the implicit phase modulation. At this later time, the signs of the carrier phase and the phase modulation function are swapped, giving rise to the negative phase. In general, the signs of these two phases change every half modulation period due to the sinusoidal frequency modulation. By writing the cosines in terms of complex exponentials, the window and carrier can be moved into the sum to establish the components of each axis in the demodulated signal, giving

$$\begin{aligned} D(t''_\mathrm{c}, \sigma, A_\mathrm{d}) \approx & \frac{1}{2} W_1(t''_\mathrm{c}, \sigma) \sum_{\{a,b\}\subseteq S} \eta_{ab} \exp\Big[\mathrm{j}2\pi(A_{ab} - A_\mathrm{d}) f_\mathrm{m} t''_\mathrm{c} + \mathrm{j}\varphi_{ab}\Big] \\ & + \frac{1}{2} W_1(t''_\mathrm{c}, \sigma) \sum_{\{a,b\}\subseteq S} \eta_{ab} \exp\Big[-\mathrm{j}2\pi(A_{ab} + A_\mathrm{d}) f_\mathrm{m} t''_\mathrm{c} - \mathrm{j}\varphi_{ab}\Big] \\ & + \frac{1}{2} W_1\left(t''_\mathrm{c} - \frac{1}{2}T_\mathrm{m}, \sigma\right) \sum_{\{a,b\}\subseteq S} \eta_{ab} \exp\Big[-\mathrm{j}2\pi(A_{ab} - A_\mathrm{d}) f_\mathrm{m} t''_\mathrm{c} + \mathrm{j}\varphi_{ab}\Big] \\ & + \frac{1}{2} W_1\left(t''_\mathrm{c} - \frac{1}{2}T_\mathrm{m}, \sigma\right) \sum_{\{a,b\}\subseteq S} \eta_{ab} \exp\Big[\mathrm{j}2\pi(A_{ab} + A_\mathrm{d}) f_\mathrm{m} t''_\mathrm{c} - \mathrm{j}\varphi_{ab}\Big]. \end{aligned} \tag{A.44}$$

The absolute Fourier transform of the demodulated signal is $F_D = |\mathcal{F}\{D\}|$. Consequently, the phase terms of $\mathrm{j}\varphi$ and time shifting [320] by $\frac{1}{2}T_\mathrm{m}$ in Equation (A.44) do not affect the magnitude of the power spectrum, as both result in unity magnitude

scaling in the frequency domain. The absolute Fourier transform of D is

$$\begin{aligned} F_D(f, A_\mathrm{d}) \approx{}& \frac{\sqrt{2\pi}\sigma}{f_\mathrm{m}} \sum_{\{a,b\}\subseteq S} \eta_{ab} \exp\left[-\frac{2\pi^2\sigma^2}{f_\mathrm{m}^2}\big(f - [A_{ab} + A_\mathrm{d}]f_\mathrm{m}\big)^2\right] \\ &+ \frac{\sqrt{2\pi}\sigma}{f_\mathrm{m}} \sum_{\{a,b\}\subseteq S} \eta_{ab} \exp\left[-\frac{2\pi^2\sigma^2}{f_\mathrm{m}^2}\big(f - [A_{ab} - A_\mathrm{d}]f_\mathrm{m}\big)^2\right] \\ &+ \frac{\sqrt{2\pi}\sigma}{f_\mathrm{m}} \sum_{\{a,b\}\subseteq S} \eta_{ab} \exp\left[-\frac{2\pi^2\sigma^2}{f_\mathrm{m}^2}\big(f + [A_{ab} - A_\mathrm{d}]f_\mathrm{m}\big)^2\right] \\ &+ \frac{\sqrt{2\pi}\sigma}{f_\mathrm{m}} \sum_{\{a,b\}\subseteq S} \eta_{ab} \exp\left[-\frac{2\pi^2\sigma^2}{f_\mathrm{m}^2}\big(f + [A_{ab} + A_\mathrm{d}]f_\mathrm{m}\big)^2\right]. \end{aligned} \tag{A.45}$$

Like the approximation of P_{WU} in Appendix A.4.2, the individual terms of Equation (A.45) may be squared to obtain the power spectrum, provided that for all a and b in S, $A_{ab} - A_\mathrm{d}$ and $A_{ab} + A_\mathrm{d}$ are unique and the Gaussian peaks in the demodulated signal are sufficiently spaced. The resulting power spectrum is given by

$$\begin{aligned} P_D(f, A_\mathrm{d}) \approx{}& \frac{2\pi\sigma^2}{f_\mathrm{m}^2} \sum_{\{a,b\}\subseteq S} \eta_{ab}^2 \exp\left[-\frac{4\pi^2\sigma^2}{f_\mathrm{m}^2}\big(f - [A_{ab} + A_\mathrm{d}]f_\mathrm{m}\big)^2\right] \\ &+ \frac{2\pi\sigma^2}{f_\mathrm{m}^2} \sum_{\{a,b\}\subseteq S} \eta_{ab}^2 \exp\left[-\frac{4\pi^2\sigma^2}{f_\mathrm{m}^2}\big(f - [A_{ab} - A_\mathrm{d}]f_\mathrm{m}\big)^2\right] \\ &+ \frac{2\pi\sigma^2}{f_\mathrm{m}^2} \sum_{\{a,b\}\subseteq S} \eta_{ab}^2 \exp\left[-\frac{4\pi^2\sigma^2}{f_\mathrm{m}^2}\big(f + [A_{ab} - A_\mathrm{d}]f_\mathrm{m}\big)^2\right] \\ &+ \frac{2\pi\sigma^2}{f_\mathrm{m}^2} \sum_{\{a,b\}\subseteq S} \eta_{ab}^2 \exp\left[-\frac{4\pi^2\sigma^2}{f_\mathrm{m}^2}\big(f + [A_{ab} + A_\mathrm{d}]f_\mathrm{m}\big)^2\right]. \end{aligned} \tag{A.46}$$

This approximated power spectrum fails to capture one feature. When demodulation is in-band for the ab axis, $A_{ab} - A_\mathrm{d} \approx A_\mathrm{d} - A_{ab} \approx 0$, producing a Gaussian centred at $f = 0$ with four times the power of the lobes considered individually, and twice the power than that described by the approximation in Equation (A.46). Although this discrepancy is generally tolerable as the purpose of Equation (A.46) is to show the approximate locations of the Gaussian peaks, it can be corrected for in-band demodulation. Equation (A.46) may be rewritten to highlight this feature when $A_{ab} \approx A_\mathrm{d}$ in the second and third sums. Filtering the difference phase modulation

terms and introducing a new sum for in-band demodulation yields

$$\begin{aligned}
P_D(f, A_\mathrm{d}) \approx\ & \frac{2\pi\sigma^2}{f_\mathrm{m}^2} \sum_{\{a,b\}\subseteq S} \eta_{ab}^2 \exp\left[-\frac{4\pi^2\sigma^2}{f_\mathrm{m}^2}\big(f - [A_{ab} + A_\mathrm{d}]f_\mathrm{m}\big)^2\right] \\
& + \frac{2\pi\sigma^2}{f_\mathrm{m}^2} \sum_{\substack{\{a,b\}\subseteq S \\ A_{ab}\not\approx A_\mathrm{d}}} \eta_{ab}^2 \exp\left[-\frac{4\pi^2\sigma^2}{f_\mathrm{m}^2}\big(f - [A_{ab} - A_\mathrm{d}]f_\mathrm{m}\big)^2\right] \\
& + \frac{2\pi\sigma^2}{f_\mathrm{m}^2} \sum_{\substack{\{a,b\}\subseteq S \\ A_{ab}\not\approx A_\mathrm{d}}} \eta_{ab}^2 \exp\left[-\frac{4\pi^2\sigma^2}{f_\mathrm{m}^2}\big(f + [A_{ab} - A_\mathrm{d}]f_\mathrm{m}\big)^2\right] \\
& + \frac{2\pi\sigma^2}{f_\mathrm{m}^2} \sum_{\{a,b\}\subseteq S} \eta_{ab}^2 \exp\left[-\frac{4\pi^2\sigma^2}{f_\mathrm{m}^2}\big(f + [A_{ab} + A_\mathrm{d}]f_\mathrm{m}\big)^2\right] \\
& + \frac{8\pi\sigma^2}{f_\mathrm{m}^2} \sum_{\substack{\{a,b\}\subseteq S \\ A_{ab}\approx A_\mathrm{d}}} \eta_{ab}^2 \exp\left[-\frac{4\pi^2\sigma^2}{f_\mathrm{m}^2} f^2\right].
\end{aligned} \tag{A.47}$$

In Equation (A.47), the ranges of the second and third sums filter out the cases where $A_{ab} \approx A_\mathrm{d}$, and these cases are deferred to the fifth sum that represents the signal baseband for in-band demodulation.

Power spectra computed by Equation (A.47) for a three-axis interferometer are shown in Figure 3.9. Each axis contributes components at two frequencies, $A_{ab} - A_\mathrm{d}$ and $A_{ab} + A_\mathrm{d}$, outlined in Table 3.3. For interferometers with adequate OPD and modulation amplitude separation, there is exactly one $\{a, b\}$ in S for which in-band demodulation produces a baseband component at $A_{ab} - A_\mathrm{d} \approx 0$.

In Figures 3.9b and 3.9h there is a comb structure under the power spectrum in the baseband due to the $2f_\mathrm{m}$ frequency of the window function. In general, if g and G are time and frequency domain representations of a signal, respectively, then the time shifting property of the Fourier transform [320] gives

$$\begin{aligned}
&\mathcal{F}\left\{g(t - t_0) + g\left(t - t_0 - \frac{T_\mathrm{m}}{2}\right)\right\}(f) \\
&\qquad = G(f)\exp\left[-\mathrm{j}2\pi\frac{T_\mathrm{m}}{2}f\right] + G(f)\exp\left[-\mathrm{j}2\pi\left(t_0 + \frac{T_\mathrm{m}}{2}\right)f\right],
\end{aligned} \tag{A.48}$$

where t_0 is an arbitrary constant time shift. Shifting g by $T_\mathrm{m}/2$ within a modulation period is equivalent to repeating g at a frequency of $2f_\mathrm{m}$. For the discrete Fourier transform over one modulation period, such as the simulated spectra in Figures 3.9b, 3.9d, 3.9f and 3.9h, the frequency resolution is equal f_m. The spectrum is sampled at

the points mf_m where m is an integer, allowing Equation (A.48) to be written as

$$\mathcal{F}\left\{g(t-t_0)+g\left(t-t_0-\frac{T_\mathrm{m}}{2}\right)\right\}(f) \\ = G(f)\exp\Big[-\mathrm{j}2m\pi f_\mathrm{m}t_0\Big]\Big(1+\exp\big[-\mathrm{j}m\pi\big]\Big), \quad \text{(A.49)}$$

which leverages that $f_\mathrm{m}T_\mathrm{m}=1$. There are two simplifications that can be made to demonstrate the comb in the power spectrum. First, the $\exp[-\mathrm{j}m\pi]$ term reduces to $(-1)^m$, and all components for odd m disappear. Second, since the power spectrum is of interest, $|\exp[-\mathrm{j}2m\pi f_\mathrm{m}t_0]|^2 = |\exp[-\mathrm{j}2m\pi]^{f_\mathrm{m}t_0}|^2 = 1$, m, f_m, and t_0 are real. The square of Equation (A.49) may then be written as

$$\left|\mathcal{F}\left\{g(t)+g\left(t-\frac{T_\mathrm{m}}{2}\right)\right\}(f)\right|^2 = \begin{cases} 4\Big|G(f)\Big|^2 & m \text{ even} \\ 0 & m \text{ odd}, \end{cases} \quad \text{(A.50)}$$

which shows that every odd multiple of f_m is zero.

A.6 Sawtooth Frequency Modulation

Sawtooth frequency modulation is based on the periodic sawtooth function. Using the floor function, $\lfloor x \rfloor$, the saw function may be written as

$$\mathrm{saw}(x) = 2(x-\lfloor x \rfloor)-1, \quad \text{(A.51)}$$

which oscillates between -1 to 1 with an oscillatory factor of 1 (compared to 2π for trigonometric functions). Using the sawtooth function from Equation (A.51), the modulated optical frequency of a laser is given by

$$\nu(t) = \nu_\mathrm{A}\mathrm{saw}(f_\mathrm{m}t)+\nu_\mathrm{c}. \quad \text{[Hz] (A.52)}$$

From Equation (A.52), the time-of-flight delays for the ab axis of an interferometer result in the interference of two frequencies at the detector given by

$$\nu_a(t') = \nu_\mathrm{A}\mathrm{saw}\big(f_\mathrm{m}[t'-\tau_{\mathrm{f},a}]\big)+\nu_\mathrm{c}, \quad \text{[Hz] (A.53a)}$$

$$\nu_b(t') = \nu_\mathrm{A}\mathrm{saw}\big(f_\mathrm{m}[t'-\tau_{\mathrm{f},b}]\big)+\nu_\mathrm{c}. \quad \text{[Hz] (A.53b)}$$

The beat frequency is expressed as the difference $\nu_a-\nu_b$, however, there are two frequencies of particular interest, f_b^+ and f_b^-, on which occur on the positive and

negative modulation slopes. Using Equation (A.53), f_{b}^{+} and f_{b}^{-} are given by

$$\begin{aligned} f_{\mathrm{b},ab}^{+}(t') &= \left[\nu_{\mathrm{A}}\mathrm{saw}\Big(f_{\mathrm{m}}\big[t'-\tau_{\mathrm{f},a}(t')\big]\Big)+\nu_{\mathrm{c}}\right]-\left[\nu_{\mathrm{A}}\mathrm{saw}\Big(f_{\mathrm{m}}\big[t'-\tau_{\mathrm{f},b}(t')\big]\Big)+\nu_{\mathrm{c}}\right] \\ &= 2\nu_{\mathrm{A}}\Bigg(f_{\mathrm{m}}\big[\tau_{\mathrm{f},b}(t')-\tau_{\mathrm{f},a}(t')\big]-\underbrace{\Big[\Big\lfloor f_{\mathrm{m}}\big[t'-\tau_{\mathrm{f},b}(t')\big]\Big\rfloor-\Big\lfloor f_{\mathrm{m}}\big[t'-\tau_{\mathrm{f},a}(t')\big]\Big\rfloor\Big]}_{=0}\Bigg) \\ &= 2\nu_{\mathrm{A}}f_{\mathrm{m}}\big[\tau_{\mathrm{f},b}(t')-\tau_{\mathrm{f},a}(t')\big] \end{aligned} \quad \text{[Hz]} \tag{A.54}$$

and

$$\begin{aligned} f_{\mathrm{b},ab}^{-}(t') &= \left[\nu_{\mathrm{A}}\mathrm{saw}\Big(f_{\mathrm{m}}\big[t'-\tau_{\mathrm{f},a}(t')-T_{\mathrm{m}}\big]\Big)+\nu_{\mathrm{c}}\right]-\left[\nu_{\mathrm{A}}\mathrm{saw}\Big(f_{\mathrm{m}}\big[t'-\tau_{\mathrm{f},b}(t')\big]\Big)+\nu_{\mathrm{c}}\right] \\ &= 2\nu_{\mathrm{A}}f_{\mathrm{m}}\big[\tau_{\mathrm{f},b}(t')-\tau_{\mathrm{f},a}(t')-T_{\mathrm{m}}\big] \\ &\quad -2\nu_{\mathrm{A}}\underbrace{\Big[\Big\lfloor f_{\mathrm{m}}\big[t'-\tau_{\mathrm{f},b}(t')\big]\Big\rfloor-\Big\lfloor f_{\mathrm{m}}\big[t'-\tau_{\mathrm{f},a}(t')-T_{\mathrm{m}}\big]\Big\rfloor\Big]}_{=0} \\ &= 2\nu_{\mathrm{A}}f_{\mathrm{m}}\big[\tau_{\mathrm{f},b}(t')-\tau_{\mathrm{f},a}(t')-T_{\mathrm{m}}\big] \\ &= 2\nu_{\mathrm{A}}f_{\mathrm{m}}\big[\tau_{\mathrm{f},b}(t')-\tau_{\mathrm{f},a}(t')\big]-2\nu_{\mathrm{A}}. \end{aligned} \quad \text{[Hz]} \tag{A.55}$$

Note that in Equation (A.55), T_{m} is subtracted in the first saw function to account for a change in period. Over this region, ν_a is on its next period while ν_b is still on its current period, which is observed in Figure 3.11a. In Equation (A.55), the difference of floors is 0 as both interfering signals are on the same period, however, in Equation (A.55), the signals are on separate periods, but the difference of floors is still zero since $\tau_{\mathrm{f},a} < \tau_{\mathrm{f},b}$ and $\lfloor f_{\mathrm{m}}(t'-\tau_{\mathrm{f},a})\rfloor - \lfloor f_{\mathrm{m}}(t'-\tau_{\mathrm{f},b})\rfloor = 1$. From a measurement of f_{b}^{+}, Equation (A.54) may be used to determine the OPD as

$$\Lambda_{ab}(t'') = \frac{\mathrm{c}}{2\nu_{\mathrm{A}}}\frac{f_{\mathrm{b},ab}^{+}(t'')}{f_{\mathrm{m}}}. \quad \text{[m]} \tag{A.56}$$

A.7 Triangular Frequency Modulation

Triangular modulation is similar to the sawtooth modulation scheme discussed in Appendix A.6, but there is a negative modulation slope rather than a discontinuity. Like the saw function, a triangular periodic function is defined in terms of the floor function,

$$\mathrm{tri}(x) = \begin{cases} 4(x-\lfloor x\rfloor)-1 & x-\lfloor x\rfloor \le \frac{1}{2} \\ 4(\lfloor x\rfloor - x)+3 & x-\lfloor x\rfloor > \frac{1}{2} \end{cases}, \tag{A.57}$$

which oscillates between -1 to 1 with an oscillatory factor of 1 (compared to 2π for trigonometric functions). Using Equation (A.57), the optical frequency of a triangularly modulated signal is

$$\nu(t) = \nu_{\mathrm{A}}\mathrm{tri}(f_{\mathrm{m}}t) + \nu_{\mathrm{c}}. \qquad \text{[Hz] (A.58)}$$

After accounting for time-of-flight delays in the interferometer, the frequencies of the interfering signals at the detector are found as differences in ν from Equation (A.58), given by

$$\nu_a(t') = \nu_{\mathrm{A}}\mathrm{tri}\big(f_{\mathrm{m}}[t' - \tau_{\mathrm{f},a}]\big) + \nu_{\mathrm{c}}, \qquad \text{[Hz] (A.59a)}$$

$$\nu_b(t') = \nu_{\mathrm{A}}\mathrm{tri}\big(f_{\mathrm{m}}[t' - \tau_{\mathrm{f},b}]\big) + \nu_{\mathrm{c}}. \qquad \text{[Hz] (A.59b)}$$

The beat frequencies, f_{b}^{+} and f_{b}^{-}, are found when both frequencies in Equation (A.59) show positive or negative slope, respectively. These beat frequencies are given by

$$\begin{aligned} f_{\mathrm{b},ab}^{+}(t') &= \left[\nu_{\mathrm{A}}\mathrm{tri}\Big(f_{\mathrm{m}}\big[t' - \tau_{\mathrm{f},a}(t')\big]\Big) + \nu_{\mathrm{c}}\right] - \left[\nu_{\mathrm{A}}\mathrm{tri}\Big(f_{\mathrm{m}}\big[t' - \tau_{\mathrm{f},b}(t')\big]\Big) + \nu_{\mathrm{c}}\right] \\ &= 4\nu_{\mathrm{A}}\Bigg(f_{\mathrm{m}}\big[\tau_{\mathrm{f},b}(t') - \tau_{\mathrm{f},a}(t')\big] - \underbrace{\Big[\Big\lfloor f_{\mathrm{m}}\big[t' - \tau_{\mathrm{f},b}(t')\big]\Big\rfloor - \Big\lfloor f_{\mathrm{m}}\big[t' - \tau_{\mathrm{f},a}(t')\big]\Big\rfloor\Big]}_{=0}\Bigg) \\ &= 4\nu_{\mathrm{A}} f_{\mathrm{m}}\big[\tau_{\mathrm{f},b}(t') - \tau_{\mathrm{f},a}(t')\big] \end{aligned} \qquad \text{[Hz] (A.60)}$$

and

$$\begin{aligned} f_{\mathrm{b},ab}^{-}(t') &= \left[\nu_{\mathrm{A}}\mathrm{tri}\Big(f_{\mathrm{m}}\big[t' - \tau_{\mathrm{f},a}(t') - T_{\mathrm{m}}\big]\Big) + \nu_{\mathrm{c}}\right] - \left[\nu_{\mathrm{A}}\mathrm{tri}\Big(f_{\mathrm{m}}\big[t' - \tau_{\mathrm{f},b}(t')\big]\Big) + \nu_{\mathrm{c}}\right] \\ &= 4\nu_{\mathrm{A}}\Bigg(-f_{\mathrm{m}}\big[\tau_{\mathrm{f},b}(t') - \tau_{\mathrm{f},a}(t')\big] - \underbrace{\Big[\Big\lfloor f_{\mathrm{m}}\big[t' - \tau_{\mathrm{f},b}(t')\big]\Big\rfloor - \Big\lfloor f_{\mathrm{m}}\big[t' - \tau_{\mathrm{f},a}(t')\big]\Big\rfloor\Big]}_{=0}\Bigg) \\ &= -4\nu_{\mathrm{A}} f_{\mathrm{m}}\big[\tau_{\mathrm{f},b}(t') - \tau_{\mathrm{f},a}(t')\big]. \end{aligned} \qquad \text{[Hz] (A.61)}$$

Unlike the sawtooth equations in Equations (A.54) and (A.55) the interfering frequencies in Equations (A.60) and (A.61) are one the same period in both cases and there is no need to shift one by T_{m}; the difference of floors also cancels for the same reason as Equation (A.54) in the sawtooth modulation derivations. From Equations (A.60) and (A.61), there is a symmetry that $f_{\mathrm{b}}^{+} = -f_{\mathrm{b}}^{-}$, however, only when the target is stationary. From the relativistic Doppler effect used in radio detection and ranging (RADAR) systems, a Doppler frequency of $f_{\mathrm{d}} = 2v/\lambda_{\mathrm{c}} = v_{\mathrm{opt}}/\lambda_{\mathrm{c}}$ is observed, where v is the velocity of the target [194]; the beam undergoes a single

reflection so $v_{\text{opt}} = 2v$ is the velocity in optical path. After Doppler shifting, the modified beat frequencies

$$f^{+\prime}_{\text{b},ab} = f^{+}_{\text{b},ab} + f_{\text{d},ab}, \qquad \text{[Hz]} \text{ (A.62a)}$$

$$f^{-\prime}_{\text{b},ab} = f^{-}_{\text{b},ab} + f_{\text{d},ab} = -f^{+}_{\text{b},ab} + f_{\text{d},ab}, \qquad \text{[Hz]} \text{ (A.62b)}$$

are produced.

The Doppler shifted beat frequencies from Equation (A.62) are measured, and both the position and velocity may be determined. The position is found from the difference of these frequencies, $f^{+\prime}_{\text{b},ab} - f^{-\prime}_{\text{b},ab} = 2f^{+}_{\text{b},ab}$ and thus the OPD is given by

$$\Lambda_{ab}(t'') = \frac{\text{c}}{8\nu_{\text{A}}} \frac{f^{+\prime}_{\text{b},ab}(t'') - f^{-\prime}_{\text{b},ab}(t'')}{f_{\text{m}}}. \qquad \text{[m]} \text{ (A.63)}$$

The velocity is found from the sum $f^{+\prime}_{\text{b},ab} + f^{-\prime}_{\text{b},ab} = 2f_{\text{d},ab}$ and the $f_{\text{d}} = v_{\text{opt}}/\lambda_{\text{c}}$ above, yielding

$$v_{\text{opt},ab}(t'') = \frac{\lambda_{\text{c}}}{2}\left[f^{+\prime}_{\text{b},ab}(t'') + f^{-\prime}_{\text{b},ab}(t'')\right]. \qquad \text{[m/s]} \text{ (A.64)}$$

Appendix B

Driven Harmonic Oscillator Equations

The following equations are derived for the silica resonator discussed in Section 7.7. A driven harmonic oscillator, is described by the differential equation

$$m\frac{\mathrm{d}^2x(t)}{\mathrm{d}t^2} + b\frac{\mathrm{d}x(t)}{\mathrm{d}t} + kx(t) = F(t), \qquad \text{[N] (B.1)}$$

where m is the mass of the oscillator, b is the frictional damping coefficient, k is the spring constant, F is the driving force, x is the position, and t is time [321, 322]. For all cases in Section 7.7, the driving force is sinusoidal, and Equation (B.1) may be rewritten as

$$\frac{\mathrm{d}^2x(t)}{\mathrm{d}t^2} + \frac{\omega_0}{Q}\frac{\mathrm{d}x(t)}{\mathrm{d}t} + \omega_0^2 x(t) = \frac{F(t)}{m} = \frac{F_0}{m}\cos(\omega t), \qquad \text{[m/s}^2\text{] (B.2)}$$

where ω_0 is the natural frequency, Q is the quality factor, F_0 is the amplitude of the driving force, and ω is angular frequency. Equation (B.2) is often written using $2\zeta\omega_0$ or 2γ instead of ω_0/Q, where ζ is the damping ratio and γ is the damping factor [189,322,323], however, since the topic of Section 7.7 is quality factor characterization, Q is used directly in all equations. A solution to Equation (B.2) is

$$x(t) = \underbrace{\frac{F_0}{m}\frac{1}{\sqrt{(\omega_0^2-\omega^2)^2 + \omega_0^2\omega^2/Q^2}}}_{A(\omega)}\cos\left(\omega t - \underbrace{\arctan\left(\frac{\omega_0\omega/Q}{\omega_0^2-\omega^2}\right)}_{\phi(\omega)}\right), \qquad \text{[m] (B.3)}$$

where A is the displacement amplitude and ϕ is the phase [189, 321].

The total energy, E, is the sum of the potential and kinetic energies [45], and is given by

$$E(t) = \frac{1}{2}kx(t)^2 + \frac{1}{2}m\left[\frac{\mathrm{d}x(t)}{\mathrm{d}t}\right]^2. \qquad \text{[J] (B.4)}$$

Since $\omega_0 = \sqrt{k/m}$, Equation (B.4) may be rewritten using Equation (B.3) to obtain

$$E(\omega) = \frac{1}{2}A(\omega)^2 m\Big[\omega_0^2 \cos^2\big(\omega t - \phi(\omega)\big) + \omega^2 \sin^2\big(\omega t - \phi(\omega)\big)\Big]. \quad \text{[J] (B.5)}$$

The average energy taken over one cycle, $\langle E(\omega)\rangle$, is found by noticing that $\langle \cos^2\theta\rangle = \langle \sin^2\theta\rangle = 1/2$, yielding

$$\big\langle E(\omega)\big\rangle = \frac{F_0^2}{4m}\frac{\omega_0^2 + \omega^2}{(\omega_0^2 - \omega^2)^2 + \omega_0^2\omega^2/Q^2}. \quad \text{[J] (B.6)}$$

The silica resonator in Section 7.7 is known to have a high Q and thus a sharp peak in energy near ω_0. The energy is near zero at all frequencies except those where $\omega \approx \omega_0$, allowing the following approximations to be made:

- $\omega_0^2 + \omega^2 \approx 2\omega_0^2$,
- $\omega_0^2 - \omega^2 = (\omega_0 + \omega)(\omega_0 - \omega) \approx 2\omega_0(\omega_0 - \omega)$,
- and $\omega_0^2\omega^2 \approx \omega_0^4$.

Equation (B.6) can then be written as the approximation

$$\big\langle E(\omega)\big\rangle \approx \frac{F_0^2 Q^2}{2m\omega_0^2}\frac{1}{1 + 4\Big(\frac{\omega_0 - \omega}{\omega_0/Q}\Big)^2} \quad \text{when} \quad Q \gg 1. \quad \text{[J] (B.7)}$$

Using $f = \omega/2\pi$, $f_0 = \omega_0/2\pi$, and the substitution of $\Gamma \approx f_0/Q$, Equation (B.7) may be simplified to

$$\big\langle E(f)\big\rangle \approx \frac{F_0^2}{8\pi^2\Gamma^2 m}\frac{1}{1 + 4\Big(\frac{f_0 - f}{\Gamma}\Big)^2} \quad \text{when} \quad Q \gg 1, \quad \text{[J] (B.8)}$$

where f is the driving frequency in time units, f_0 is the natural frequency in time units, and Γ is the full width at half maximum (FWHM) of the peak. Note that $1/(1 + 4((f_0 - f)/\Gamma)^2)$ is the Lorentzian function [324].

From the substitution made earlier, the quality factor can be estimated by the natural frequency and the width of the profile with $Q \approx f_0/\Gamma$. Recall that this substitution was *approximate*, since a measurement of $\langle E(f)\rangle$ has the peak at the resonant frequency, f_r, not the natural frequency, f_0. For a high Q system, $f_\mathrm{r} \approx f_0$, which can be seen by solving for the frequency which maximizes $A(\omega)$ in Equation (B.3). $A(\omega)$ has extrema at $\omega = 0$ and $\omega = 2\pi f_\mathrm{r}$, where the latter is the resonant angular frequency. The resonant frequency is then given by

$$f_\mathrm{r} = f_0\sqrt{1 - \frac{1}{2Q^2}} \approx f_0 \quad \text{when} \quad Q \gg 1. \quad \text{[Hz] (B.9)}$$

Note that the resonant frequency is not the frequency where the average energy is greatest, $f_{\max\langle E\rangle}$, which from Equation (B.6), can be shown to be

$$f_{\max\langle E\rangle} = f_0\sqrt{\sqrt{4-\frac{1}{Q^2}}-1} \approx f_0 \quad \text{when} \quad Q \gg 1. \qquad \text{[Hz]} \text{ (B.10)}$$

One must appreciate the distinction between f_0, f_r, and $f_{\max\langle E\rangle}$. An ideal, undamped oscillator carries the natural frequency, f_0, while a driven, lightly damped oscillator achieves its greatest displacement amplitude at f_r and maximum average energy at $f_{\max\langle E\rangle}$. The experiment in Section 7.7 measures f_r as the average energy is approximated by the square of the displacement. As will soon be seen, the above distinction is numerically negligible for a high Q resonator having $f_0 \approx f_\mathrm{r} \approx f_{\max\langle E\rangle}$. Keeping with the resonant frequency, Equation (B.9) may be solved for Q to obtain

$$Q = \sqrt{\frac{f_\mathrm{r}^2}{\Gamma^2}-\frac{1}{2}} \approx \frac{f_\mathrm{r}}{\Gamma} \quad \text{when} \quad f_\mathrm{r} \gg \Gamma. \qquad \text{(B.11)}$$

To investigate these equations and approximations, a resonator with parameters resembling those of the system in Section 7.7 was simulated. From the CAD model, the volume of the fused silica proof mass is $\sim$50 mm^3 with density $\sim$2200 kg/m^3 [263], giving a mass of $m \approx 110$ mg. The resonator has experimentally determined $Q \approx 350$ and $\Gamma \approx 1.93$ Hz values with a natural frequency $f_0 \approx 677$ Hz in atmosphere. The driving force can be estimated from $A(\omega)$ by noticing that the maximum value of A

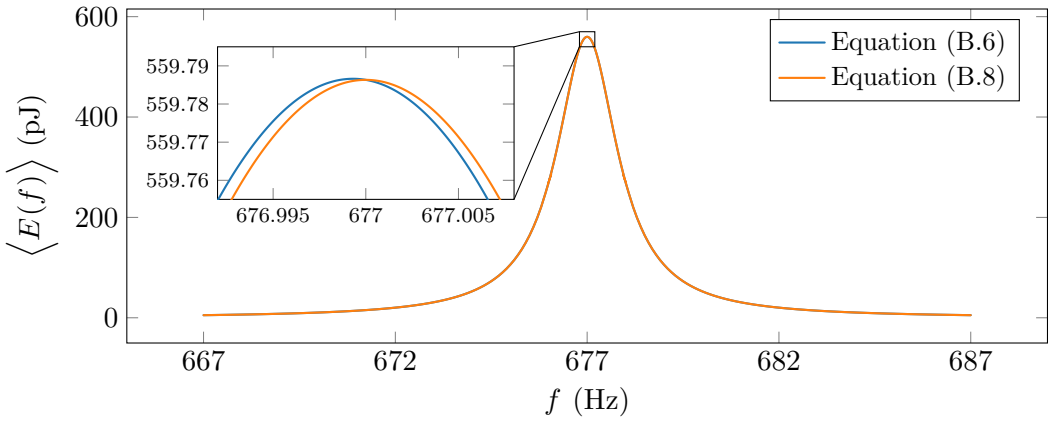

Figure B.1: Simulation of the exact and approximate average energy of an oscillator. The parameters are selected to closely match the silica resonator discussed in Section 7.7 in atmosphere: $m = 110$ mg, $f_0 = 677$ Hz, $Q = 350$, $\Gamma = 1.93$ Hz, and $F_0 = 4$ µN.

occurs when $\omega \approx \omega_0$. Under this condition, the driving force is

$$F_0 \approx \frac{A_{\max} m \omega_0^2}{Q}, \quad \text{when} \quad \omega \approx \omega_0, \qquad \text{[N]} \quad \text{(B.12)}$$

where $A_{\max}$ is the maximum observed displacement amplitude. From the experimental data in Section 7.7, $A_{\max} \approx 750\,\text{nm}$, and Equation (B.12) gives $F_0 \approx 4\,\mu\text{N}$. These parameters are used to produce the simulated plots in Figure B.1 and find $f_\text{r} = 676.9986\,\text{Hz}$ by Equation (B.9). The peak of the curve generated using the exact solution for in Equation (B.6) occurs at 676.9993 Hz, and the same value is found using Equation (B.10). Close agreement of 2 ppm among $f_0 = 677\,\text{Hz}$, f_r, and $\langle E(f) \rangle$ is observed, which shows that Q may be found with acceptable accuracy from the estimate $Q \approx f_\text{r}/\Gamma$ in Equation (B.11).

Appendix C

Parts List

C.1 FMDU Components

Table C.1: Components of the FMDU shown in Figure 4.1.

Component	Description	Table
Digilent Eclypse Z7 [202]	MPSoC Evaluation Board	Table C.2
Digilent Zmod AWG 1411 [204]	DAC	Table C.3
Zmod Scope 1410-105 [205]	ADC	Table C.4
Eblana Photonics EP1550 NLW [186]	LD	Table C.5
Koheron CTL200 [207]	LD Controller	Table C.6
Thorlabs 6015-3-APC [208]	Circulator	—
Thorlabs FGA01FC [209]	Photodetector	Table C.7
Analog Devices AD8009 [210]	Amplifier	Table C.8
Thorlabs ADAFC3 [264], ADABS1 [266]	Mating Sleeves	—
Thorlabs BFCT [325], FSR1 [326]	Fibre Trays	—
Thorlabs AV6/M [327]	Rubber Feet	—

Table C.2: Digilent Eclypse Z7 MPSoC development board specifications [202].

Parameter	Value
MPSoC	
Part Number [201]	XC7Z020-1CLG484C
Logic Slices	13 300
6-input LUTs	53 200
Flip-flops	106 400
Block RAM	630 kB
DSP Slices	220
Internal ADC	Dual-channel, 1 MHz
Processor	Dual-core ARM Cortex A9, 667 MHz
Memory	
RAM	1024 MB, 1066 MT/s, DDR3
Flash	16 MB, QSPI
SD	microSD
Connectivity	
SYZYGY [203]	2 SYZYGY 1.1 interfaces
Pmod [328]	2 Pmod ports
Ethernet	10/100/1000 Mbps
USB	USB micro-AB
Device Port	UART, JTAG
USB OTG Port	Host/Device

Table C.3: Digilent Zmod AWG 1411 DAC specifications [204].

Parameter	Value
Connectivity	SYZYGY 1.1 [203]
DAC Part Number	AD9717 [329]
Channels	2
Resolution	14 bit
Sample Rate	100 MHz
Low Range	
Output Range	±1.25 V
Absolute Resolution	167 µV
High Range	
Output Range	±5 V
Absolute Resolution	665 µV
Accuracy	±0.2 %
Output	Single-Ended
Output Impedance	50 Ω
Slew Rate	180 V/µs (2 V Step)
Analog Bandwidth	
40 MHz	3 dB
20 MHz	0.5 dB
14 MHz	0.1 dB

Table C.4: Digilent Zmod Scope 1410-105 ADC specifications [205].

Parameter	Value
Connectivity	SYZYGY 1.1 [203]
ADC Part Number	AD9648 [330]
Channels	2
Resolution	14 bit
Sample Rate	100 MHz
High Gain	
Input Range	±1 V
Absolute Resolution	134 µV
Low Gain	
Input Range	±25 V
Absolute Resolution	3.21 mV
Input	Single-ended
Input Impedance	1 MΩ ‖ 18 pF
Analog Bandwidth	
70 MHz	3 dB
30 MHz	0.5 dB
20 MHz	0.1 dB

Table C.5: Eblana Photonics EP1550 NLW LD specifications [186]. Some values differ from the specification sheet; device specific values are provided in the characterization report from the manufacturer.

Parameter	Value
Wavelength	1550 nm
Optical Linewidth	99 kHz
Side Mode Suppression Ratio	52 dB
Threshold Current	35 mA
Output Power in Fibre	5 mW
Temperature Tuning Coefficient	0.09 nm/K
Current Tuning Coefficient	3 pm/mA
Slope Efficiency	0.03 mW/mA
Coupling	Single-mode, FC/APC

Table C.6: Koheron CTL200-2-B-200 digital LD controller specifications [207].

Parameter	Value
Current	5 to 225 mA
Current Resolution	5 µA
Current Noise (10 Hz to 1 MHz)	220 nA rms
Current Noise Density (1 kHz)	230 pA/$\sqrt{\text{Hz}}$
Current Modulation Gain	
Low	250 µA/V
Medium	2.5 mA/V
High[1]	25 mA/V
Current Modulation Bandwidth (3 dB)	10 MHz
Temperature Stability	0.002 K/K[1]
Maximum TEC Current	1.2 A

[1] High current modulation gain is used for all applications in this thesis.
[2] Maximum change in laser temperature per unit temperature change of the environment.

Table C.7: Thorlabs FGA01FC InGaAs photodiode specifications [209].

Parameter	Value
Wavelength Range	800 to 1700 nm
Active Area	$0.011\,\mathrm{mm}^2$ ($\varnothing 120\,\mu\mathrm{m}$)
Rise Time	300 ps (5 V, 50 Ω)
NEP	$4.5 \times 10^{-15}\,\mathrm{W}/\sqrt{\mathrm{Hz}}$ (1550 nm)
Dark Current	50 pA (5 V)
Package	Bulkhead, FC/PC

Table C.8: Analog Devices AD8009 operational amplifier specifications [210].

Parameter	Value
Topology	Current Feedback
Slew Rate	5500 V/µs (4 V Step, Gain = +2)
Rise Time	545 ps (2 V Step, Gain = +2)
Large Signal Bandwidth (−3 dB)[1]	
440 MHz	Gain = +2
320 MHz	Gain = +10
Small Signal Bandwidth (−3 dB)[1]	
1 GHz	Gain = +1
700 MHz	Gain = +2
Settling Time	10 ns to 0.1 % (2 V Step, Gain = +2)

[1] Large and small signals are greater than and less than 100 mV, respectively.

C.2 Fibre and Laser Components Used in Experiments

Table C.9: Kurt J. Lesker custom single-pass hermetic fibre feedthrough [267].

Parameter	Value
Flange	KF16
Style	Receptacle, FC/APC
Passes	1× 1310/1550 nm

Table C.10: Kurt J. Lesker custom triple-pass hermetic fibre feedthrough [267].

Parameter	Value
Flange	KF40
Style	Receptacle, FC/APC
Passes	2× 1310/1550 nm, 1× 633 nm

Table C.11: Fitel FRL15DCWD LD specifications [260].

Parameter	Value
Wavelength	1550 nm
Optical Linewidth	<10 MHz
Side Mode Suppression Ratio	45 dB
Threshold Current	15 mA
Output Power in Fibre	40 mW
Coupling	Single-mode, FC/APC

Table C.12: Optiphase PZ1 PZT fibre stretcher specifications [281]. Some values differ from the specification sheet; device specific values are provided in the characterization report from the manufacturer.

Parameter	Value
Fibre	Single-mode
Wavelength Range	780 to 1625 nm
Fibre Length	4.984 m
Fibre Stretch (Mechanical)	0.0441 µm/V
Fibre Stretch (Phase)	0.263 rad/V at 1550 nm
Fibre Stretch (Optical)[1]	64.9 nm/V

[1] Calculated from *Fibre Stretch (Phase)*.

C.3 Optical Test Equipment

Table C.13: Keysight N7744A optical power meter specifications [219].

Parameter	Value
Sensor	InGaAs
Ports	4
Wavelength Range	1250 to 1625 nm
Power Range	−80 to 10 dBm
Averaging Time	1 µs to 10 s
Total Uncertainty[1,2]	4.5 %
Linearity[2]	±0.04 dB ± 5 pW
Polarization Dependent Responsivity[3]	<±0.01 dB
Spectral Ripple Due to Interference[4]	<±0.01 dB
Drift	±9 pW

[1] Single-mode fibre, source linewidth <10 nm FWHM.
[2] Power range −60 to 10 dBm.
[3] FC/PC connector.
[4] FC/APC connector, source linewidth <100 MHz.

Table C.14: EXFO WA-1500-NIR wavemeter specifications [220].

Parameter	Value
Wavelength Range	0.6 to 1.8 µm
Accuracy	±0.2 ppm
Maximum Input Power	2 mW
Coupling	Free space, fibre (FC/PC)

Table C.15: New Imaging Technologies WiDy SenS 640 V-ST InGaAs camera specifications [271].

Parameter	Value
Sensor	InGaAs
Resolution	640 × 512
Pixel Pitch	15 µm
Array Dimensions[1]	9.6 × 7.68 mm
Wavelength Range	900 to 1700 nm
Response	Linear, Logarithmic
Frame Rate	≤230 fps
Exposure Time	10 µs to 1 s

[1] Calculated from *Resolution* and *Pixel Pitch*.

C.4 Fibre Optics Preparation Kit

Table C.16: List of fibre termination supplies for FC/APC and FC/PC finishes described in Section 4.6. Fibres and ferrules are not included.

Component	Description
Thorlabs FTS4 [331]	Furcation and buffer stripper
Thorlabs F112 [332]	Epoxy for fibre optic connectors
Thorlabs MS403-10 [333]	3 cc epoxy syringes
Thorlabs S90R [334]	Ruby fibre optic scribe for manual cleaving
Thorlabs D50-FC/APC [335]	FC/APC polishing puck
Thorlabs D50-FC [336]	FC/PC polishing puck
Thorlabs NRS913A [232]	Rubber polishing pad
Thorlabs LF30D [337]	30 µm diamond lapping film
Thorlabs LF6D [338]	6 µm diamond lapping film
Thorlabs LF3D [339]	3 µm diamond lapping film
Thorlabs LF1D [340]	1 µm diamond lapping film
Thorlabs LFCF [341]	0.02 µm diamond lapping film
Thorlabs FS201 [234]	Fibre inspection microscope

Table C.17: Select specifications for an Inno Instrument View 7 arc fusion splicer [235]. Abbreviations of SM, MM, DS, and NZDS are common abbreviations in the telecommunications industry for single-mode, multimode, dispersion shifted, and non-zero dispersion shifted, respectively.

Parameter	Value
Form Factor	Portable, battery operated
Interface	5” colour touch screen, buttons
Magnification	520×, x and y cameras
Splice	
Simultaneous Fibres	1
Fibre Type	SM, MM, DS, NZDS
Cladding Diameter	80 to 150 µm
Cleaved Length	8 to 16 mm
Time	8 s
Loss (Single-mode, typical)	0.02 dB
Tension Test	1.96 to 2.25 N
Heating Sleeve	
Length	20 to 60 mm
Time	13 s

C.5 Laser Frequency Stabilization Components

Table C.18: Wavelength References $H^{13}C^{14}N$ gas cell specifications [237].

Parameter	Value
Gas	$H^{13}C^{14}N$
Pressure	2.4 Torr (0.13 kPa)
Wavelength Range	1525 to 1565 nm
Path Length	48 cm
Fibre Coupling	FC/APC

Table C.19: Koheron PD100B-DC balanced photodetector specifications [238].

Parameter	Value
Photodiode	
Type	InGaAs
Responsivity (Peak)	0.9 A/W
Wavelength Range	900 to 1700 nm
Maximum Optical Power	1.5 mW
Fibre Coupling	FC/PC and FC/APC
Amplifier	
Coupling	DC
Small Signal Bandwidth	0 to 100 MHz
Transimpedance Gain	3.9 kV/A
Common-mode Rejection Ratio (1 MHz)	35 dB
Input Current Noise Density (1 MHz)	$8\,\mathrm{pA}/\sqrt{\mathrm{Hz}}$
Output Voltage Range	−3.3 to 3.3 V
Connectivity	SMA, female

Table C.20: Koheron PI200-T laser servo controller specifications [239].

Parameter	Value
Control Bandwidth	5 MHz
Slow Integrator	8 mHz t0 8 Hz
Fast Integrator	47 kHz to 4.7 MHz
Loop Delay	20 ns
Output Voltage Noise (0 dB Gain)	$5\,\mathrm{nV}/\sqrt{\mathrm{Hz}}$
Output Voltage Range	−2 to 2 V
Connectivity	SMA, female